Synthesis, Electrical and Electrochemical Behavior of Lanthanum Strontium Cobalt Ferrite for SOFC Cathode Application

Ph.D Thesis

By

SARAT KUMAR ROUT

Department of Ceramic Engineering

National Institute of Technology, Rourkela

Rourkela-769008, India

Synthesis, Electrical and Electrochemical Behavior of Lanthanum Strontium Cobalt Ferrite for SOFC Cathode Application

A Dissertation submitted to

National Institute of Technology, Rourkela

in partial fulfilment of the requirements for the degree of

Doctor of Philosophy

in

Ceramic Engineering

by

Sarat Kumar Rout

(Roll- 507CR004)

under the supervision of

Prof. Swadesh Kumar Pratihar

&

Prof. Santanu Bhattacharyya

Department of Ceramic Engineering

National Institute of Technology, Rourkela

Rourkela- 769008, India

July 2015

DEPARTMENT OF CERAMIC ENGINEERING
NATIONAL INSTITUTE OF TECHNOLOGY, ROURKELA
ODISHA – 769008, INDIA

C E R T I F I C A T E

This is to certify that the thesis entitled '**Synthesis, Electrical and Electrochemical Behavior of Lanthanum Strontium Cobalt Ferrite for SOFC Cathode Application'** being submitted by ***Sarat Kumar Rout*** for the award of the degree of Doctor of Philosophy in Ceramic Engineering is a record of bonafide research work carried out by him under our supervision at Department of Ceramic Engineering. To the best of our knowledge, the embodied work has not been submitted elsewhere for the award of any degree or diploma.

Co-supervisor
Prof. (Dr.) Santanu Bhattacharyya
Professor
Department of Ceramic Engineering
National Institute of Technology
Rourkela- 769008 (Odisha), INDIA
E-mail: santanub@nitrkl.ac.in

Supervisor
Prof. (Dr.) Swadesh Kumar Pratihar
Associate Professor
Department of Ceramic Engineering
National Institute of Technology
Rourkela-769008 (Odisha), INDIA
E-mail: skprathihar@nitrkl.ac.in

Dedication

To my revered parents

Shri Brajabandhu Rout
&
Smt. Kumudini Rout

Acknowledgements

I owe my sincere gratitude to the entity, I always believe to be with me as a universal guiding principle, for making me eligible to write up this thesis; to my parents for their huge patience and sacrifice in pushing me this far.

I would like to express my sense of gratitude to my supervisor Prof. Swadesh Kumar Pratihar for introducing me to a new area of research and edging my knowledge with his subtle feedbacks and intelligence. I cherish the moments of work with him in which I got surplus freedom of expression, admiration for my works and all possible chances of exploration of my technical skills. With a vigor attitude of simplicity, calm and coolness he has been very supportive and friendly to me at any point of time and space.

I thank my co-supervisor Prof. Santanu Bhattacharyya for his encouragement, supportiveness, friendly attitude and hidden appreciation through his pleasant style of talking. I feel proud for having him as one of my supervisors.

I express my thankfulness to the chairman and all the members of the DSC committee for their recognition, appreciation and approval of my work. My special thanks to Prof. J Bera, Prof R Mazumder and Prof. S Behera for their constructive suggestions of incorporation of ideas for the improvement of my thesis.

My sincere thanks to the teachers (Prof J Bera, Prof. S K Pratihar, Prof. B B Nayak & Prof. R Mazumder) under whom I completed the required course works that have been in many ways essentially helpful during the data analysis and compilation of the thesis. I extend my respect and thankfulness to other faculty members, namely, Prof. D Sarkar, Prof R Sarkar, Prof. S Pal, Prof. A Choudhury and others for their collective effort of making the department like a research hub and maintaining a cordial atmosphere of which I had been a part.

My word of thanks to the departmental technicians and staff members, namely, Mr. G Behera, Mr. S Sahu, Mr. L Dhal, Mr. P K Mohanty, Mr. N Barik and others for their support and time to time required help.

I thank my friend Rashmi Ranjan Rout and my PG college senior Tankadhar Mohanta for passing me information to pursue research at NIT Rourkela.

Appreciating her swiftness in work I thank my research colleague, senior and friend Dr (Mrs.) H Patra for rendering me quicker analyses of some portions in this thesis through her earlier related work. I also thank her for the care, appreciation and love she has lend me as a sister.

I convey my gratefulness to my senior research colleagues Ranabhai, Yougojoti, Jyotibhai, Pradeep bhai and Arundhati madam for inheriting many practical and technical skills related to synthesis, software usage and data analysis. I would also like to thank all of them for their love and help when required. I would love to recall the company of my research colleagues Subrat, Ganesh, Sanjay, Bhabani, Abhisek, Sambarta, Nadiya bhai, Geeta, Smrutirekha, Sangeeta, Jayarao and many more for their love, support, respect and afterall

for maintaining a pleasant & motivating atmosphere for work. My special thanks to Jayarao and Abhisek for their readiness of prompt help irrespective of their busy schedule.

I would love to recall the company of my gifted friends Prakash, Subrat, Naresh, Ravi, Pushpendra, Biswanath, Ramesh, Nihar, Upendra, Biswajit and others during my stay at hostel. The splendid lighter moments spent with them not only helped in overcoming the frustrations and worries but also induced fresh motivations and new encouragements in me.

I whole heartedly thank my colleagues Dr. T Badapanda, Dr. S Parida, Dr. (Mrs) H Mohapatra, Dr. A B Panda and others at CV Raman College of Engineering for their unconditional help, support and encouragement. I specially acknowledge the effort and help of Dr. S parida for the analysis of some important data.

I gratefully acknowledge the support of my family members, my brother, sisters and relatives. My token of love and word of thanks to my nephews and nieces; Lutu, Liti, Muna, Muni, Kuna and Doodley; to my well-wisher, sister and friend Ruby; to my cute little friends Chinti, Micky and others for their freshness, simplicity and love that reenergized me from time to time.

Apart from expressing my gratitude to my all-time ideal, well-wisher and brother Bibhuti bhai, I find this moment to wish him a brighter and better future. My sincere gratitude to my music teacher Dr. A K Dutta for his time to time advice and love apart from the invaluable knowledge of music he instilled in me.

I acknowledge the DST Govt. of India and CSIR for financial support through sponsored project and CSIR-SR Fellowship programme respectively.

Sarat Kumar Rout

CONTENTS

List of Figures

List of Tables

ABSTRACT

Mixed ionic and electronic conductive (MIEC) perovskites, particularly $La_{1-x}Sr_xCo_yFe_{1-y}O_{3-\delta}$, have been widely explored to replace the conventionally used $LaSrMnO_3$ (LSM) materials for intermediate temperature SOFC applications. The B-site Co rich compositions have a fairly good electrical conductivity but because of its poor thermal and chemical compatibilities the iron rich composition ($La_{1-x}Sr_xCo_{0.2}Fe_{0.8}O_{3-\delta}$) has usually been a preferred destination. The La-Sr variations on A-site have however a set of scattered data that needs to be optimized. In addition to the MIEC character, cathodes need a microstructural tailoring to enhance the oxygen reduction reaction sites. For this the cathode particles must have a considerably smaller size with high exposed surface area.

In the present work $La_{1-x}Sr_xFeO_{3-\delta}$ perovskites with x=0.0-1.0, have been synthesized. Electrical conductivity and thermochemical stability study as a function of x showed $La_{0.6}Sr_{0.4}FeO_{3-\delta}$ as a potential candidate for cathode application. Iron rich $La_{0.6}Sr_{0.4}Co_{0.2}Fe_{0.8}O_{3-\delta}$ (LSCF) has been synthesized following solution combustion technique using citric acid and glycine as fuel. Different process parameters namely metal cation to fuel ratio (elemental stoichiometric coefficient), extra chelating agent and oxidant addition, and pH of the precursor solution has been optimized. It is seen that a fuel rich precursor solution favored the formation of high surface area (~30m^2/g) LSCF powder. The effect of EDTA in reducing the calcination temperature and that of pH in powder homogenization helps in yielding fine powders. Infra-red spectroscopy (FTIR) study showed the purity of the well dispersed fine powder from the carbon residues. A correlation between the BET specific surface area, the crystallite size and SEM average particle size was established and was seen to be linked with the elemental stoichiometric coefficient. The influence of the processing parameters on the sintering, thermal expansion, thermal stability and electrical conductivity was studied. Thin electrolyte substrates were prepared from the in-house synthesized 8%-yttria stabilized zirconia (YSZ) and samarium doped ceria (SDC) powder. The chemical compatibility of LSCF powder with these electrolytes has also been studied and SDC was observed to be a better candidate in comparison to YSZ. Half electrochemical cells were prepared by screen printing the in-house prepared LSCF ink on YSZ and SDC substrates. For comparison half cells with SDC interlayer were also prepared with thin layer of LSCF electrode. Electrochemical study revealed that the polarization resistance of the half cells, apart from being influenced by the kind of electrolyte used and by the sintering temperature, are also influenced by the powder synthesis conditions. The improved electrochemical properties in case of LSCF electrode was attributed to its fineness at its powder synthesis level and the resulting microstructure. It has also been found that the electrode polarization of LSCF cathode is minimum with SDC electrolytes and maximum with YSZ electrolyte. The study also suggests the use of SDC interlayer on YSZ electrolyte as a potential solution for application of LSCF cathode with YSZ.

Keywords:*IT-SOFC, Cathode material, Combustion Synthesis, Citric acid, Glycine, Nano powder, $La_{0.6}Sr_{0.4}Co_{0.2}Fe_{0.8}O_{3-\delta}$ (LSCF), Electrochemical, Sintering kinetics, Electrical conductivity, AC Impedance*

Chapter-1

Introduction

General Introduction

The urbanization and industrialization of human civilization across the digitally connected fast and competitive world leads to a surge in the global energy utility. The evolution of developing nations with growing economy upsurges the energy consumption at historic rates. International energy statistics (US Energy Information Administration) indicated that in just four years from 2008 to 2012 the total primary energy consumption in the world has increased from 485.7181 to 524.0758 quadrillion BTU [1.1]. Some emerging world economies have an annual energy growth of near 3% [1.2-1.4]. As a consequence in the next decade, the world energy consumption can be predicted to touch 50-60% [1.2]. The reserved non-renewable fossil fuels such as coal, natural gas, and oil, etc. can meet most of these energy requirements. However, the long-term consumption of these fuels by thermal power plants is not safe and advisable. Use of fossil fuel is associated with several environmental issues related to the emission of hazardous pollutants, suspended particles, acid producing- and greenhouse gasses like NO_x, SO_x, CO and CO_2[1.5]. Besides, with the accelerated consumption rates, the dependency on these non-renewable fuel stocks will decrease as these stocks are expected to be exhausted within limited periods.

These scared circumstances of energy scarcity and stringent emission regulation policies [1.6, 1.7] have spurred the development of alternative energy methods. Researchers, manufacturers, governments and industrialists around the globe have been propelled by new research drives for the development of clean and environmental friendly efficient energy technologies.

On this present scenario of the energy crisis, fuel cells spell out as one of the promising solutions. Fuel cells, particularly solid oxide fuel cells (SOFCs) can have an estimated 60-80% of conversion efficiency unlike thermal power plants fueled by coal that has 30-40% efficiency. Apart from being highly efficient, fuel cells are clean and environmental friendly [1.8,1.9].

1.1 Fuel Cells

Fuel cells are devices that convert directly the chemical energy of a fuel into electrical energy by an electrochemical reaction [1.9]. Additional intermediate steps involving generation of heat and mechanical energy are associated with the

conversion of chemical energy to electrical energy by an internal combustion engines. So fuel cells are more efficient than the heat engines and even than these internal combustion engines [1.10]. Also, the utilization of the byproduct heat in these systems adds to the conversion efficiency [1.11] further. Apart from the high conversion efficiency fuel cells are famous for their low emission of environmental pollutants, noises, and hazardous gas products. The internal fuel reforming system in certain kind of fuel cells makes them even more viable as they avoid an extra expensive reforming sub-unit [1.12]. The size of the fuel cells can be adjusted as per the need of energy requirements.

In a fuel cell, an electrolyte phase is sandwiched between a porous anode (fuel electrode) and a porous cathode (air electrode). The electrodes have porous structure whereas the electrolyte is dense and impermeable. Usually hydrogen, hydrocarbon gasses such as ethanol, methanol or gaseous fossil fuels has been used as fuel and air, or oxygen is used as the oxidant. The electrochemical reaction to generate voltage occurs at the triple phase boundary (gas-electrolyte-electrode) [1.8,1.9].

The theoretical concept of fuel cell proposed by Davy [1.13] was carried forward by Grove [1.14] to make it a reality in earlier decades of 19th century. In Grove's cells, the reaction of H_2 and O_2 lead to the formation of water. It was just towards the end of 19th century in which a solid material was used as an electrolyte [1.15] by Nernst in his device 'glower'. This concept leads to the demonstration of the solid oxide fuel cell (SOFC) by Baur and Preis [1.16] during the first half of 20th century. The need of efficient energy conversion leads to the research interests in fuel cells from time to time. In the 1960s, during and the just aftermath of the World War II, uses of fuel cells were limited to spacecraft and submarines [1.17]. During the 1980s, the development of the materials research technology and characterizations lead to new research interests on fuel cells.

There have been classifications of fuel cells on the basis of the electrolyte materials used, fuel and oxidant consideration, use of internal or external reforming and working principle [1.18]. There are five major classes of fuel cells (all named after the use of electrolytes): (i) alkaline fuel cells (AFC), (ii) polymer electrolyte fuel cells (PEMFC), (iii) molten carbonate fuel cells (MCFC), (iv) phosphoric acid fuel cells (PAFC) and (v) solid oxide fuel cells (SOFC). A gist on the

construction and characteristics of different classes of fuel cells has been given in Table 1.1 below [1.8, 1.9].

Table 1.1 Different Classes of Fuel Cells with their characteristics

Cell Components/ Characteristics	Cell Types				
	AFC	PEMFC	PAFC	MCFC	SOFC
Electrolyte	KOH	polymers	H_2PO_4	Li_2CO_3-K_2CO_3	YSZ
Cathode	As-Pt	Pt black	PtC	Li doped NiO	Sr-$LaMnO_3$
Anode	Pt-Pd	Pt black	PtC	Ni-Cr	YSZ-Ni
Operating Temp.	200	80	80-90	600	600-1000
Reaction at cathode	$O_2+2H_2O+4e^- \rightarrow 4OH^-$	$O_2+4H^++4e^- \rightarrow 2H_2O$	$O_2+4H^++4e^- \rightarrow 2H_2O$	$O_2+2CO_2+4e^- \rightarrow 2CO_3^+$	$O2+4e- \rightarrow 2O^{2-}$
Fuels used	Highly pure H_2	Pure H_2	CO free H_2	H_2, CH_4, CO	H_2, CH_4, CO
Efficiency (%)	40	40	40	60	60-80

As the list suggests, the alkaline fuel cells (AFCs) uses KOH as electrolyte and OH^- as a charge carrier. The need for CO_2 free gas limits its use for some specific purposes such as in aircrafts in space [1.8-1.10].

The polymer based fuel cells (PEMFC) operates at low temperature and thus involve the requirement of precious catalysts that raise the overall cell cost. The uses of PEMFCs are also limited by the need of ultra-pure hydrogen fuel. Hydrogen fuel technology is yet under development. Major challenges in this technology lie with the development of an efficient hydrogen energy storage system.

The PAFCs are based on the application of phosphoric acid as an electrolyte. The low operating temperature and the requirement of pure fuels impose constraints for its use and commercialization [1.8-1.10].

Molten carbonate fuel cells (MCFC) work at rather high temperatures around 600°C. Though the low operating temperature related problems could be overcome in this cell, there are new concerns owing to its liquid electrolyte Na /Li/ KCO_3. It is a corrosive liquid that reacts with the electrode and container materials and makes the cell structure complicated. It reduces the mechanical stability of the cell and prone to creep and mechanical flaws [1.8-1.10].

Solid oxide fuel cells (SOFCs) on the other hand have a traditionally higher operating temperature. At the high temperature of operation, SOFCs offer higher efficiency. Moreover they are less sensitive to the purity of fuels, unlike lower operating temperature fuel cells.

1.1.1 Solid Oxide Fuel Cells

SOFCs are all solid components fuel cells with a fast oxygen ion conducting electrolyte that operate at a higher temperature (500^{o}C-1000^{o}C). The use of solid electrolyte doped zirconia (ZrO_2 +Y_2O_3) by Nernst literally marked the beginning of SOFCs. Till date, this is also the most widely used electrolyte in SOFCs. As pointed out in the previous section the credit for the discovery of the first ever working SOFC goes to Baur and Preis. They fabricated and demonstrated the working of SOFC by using stabilized zirconia as electrolyte. Their work was subsequently carried forward by Thomas Bacon whose work was licensed to Apollo spacecraft program [1.17]. The increasingly mounted pressure during the 1960s in the need of an alternative energy conversion device leads to new research motivations. The result was the exploration of materials for SOFC application and that came out with the use of SOFCs for military, space and transport purposes [1.20]. With the advancement of new technologies (processing and fabrication) and characterization techniques, inspired by the growing interests in the energy conversion needs, the research on SOFCs took an accelerating mode during the 1980s. The focus of research interests now shifts to the electrode materials, design and technologies. Almost commercial units of SOFCs started to take shape by leading technology supplier groups across the world [1.21-1.23]. In the past two decades, there have been tremendous demands on the research involving the development of new materials, improvement of design and electrochemical reactions of the cell [1.24-1.27]. This research drive is ongoing in parallel with the production of commercial units of SOFCs.

The SOFC working principle is based on Nernst equation [1.8]:

$$\varepsilon_r = RT/4F \ln \{pO_{2,c}/pO_{2,a}\} \qquad 1.1$$

Where, ε_r is the reversible cell potential; R is the universal gas constant. F is the Faraday's constant; $pO_{2,c}$ and $pO_{2,a}$ are the oxygen partial pressures of feed gasses at the cathode and the anode respectively.

In SOFCs oxygen atoms on the cathode side take up electrons to become oxygen ions at the cathode-electrolyte-gas interface. These oxygen ions move inside the dense ion-conducting electrolyte. At the anode side, these oxygen ions oxidize the fuel by releasing electrons to external circuit [1.5, 1.28, 1.29].

For a SOFC using O_2 as oxidant and H_2 as fuel the electrochemical equations are:

At cathode, $0.5O_2 + 2e^- \rightarrow O^=$

At anode, $H_2 + O^= \rightarrow H_2O + 2e^-$

The overall cell reaction is $H_2 + 0.5O_2 \rightarrow H_2O$

The working of SOFC thus involves the transport and regulation of oxygen ions and the voltage depends on the oxygen ion partial pressures at the electrodes. Therefore, it has higher efficiency than any other energy converting systems. The overall cell reaction shows that no other harmful byproducts or gasses except water could be produced while working with air as oxidant and hydrogen as fuel.

SOFCs consist of a dense ceramic electrolyte for oxygen ion transport. 8% Y_2O_3 doped ZrO_2 (YSZ) usually used as an electrolyte for its high ionic conductivity and almost zero electronic conductivity [1.30, 1.31]. The cathode must offer surplus sites for reduction reaction and should provide a path for the passage of both electrons and ions. Similarly, anode materials must favor oxidation reaction and provide a path for the passage of electron and gasses. Apart from this, the electrode materials must have chemical and structural stability and chemical compatibility with the electrolyte and interconnect material [1.8]. The state of the art material for cathode has been porous LSM (Sr-doped $LaMnO_3$ perovskite) [1.5, 1.8, 1.10] and that for the anode has been a cermet of Ni-YSZ [1.8,1.10].

Among several other features the following virtues of SOFCs make them distinguished and more attractive than other fuel cells:

- It consists of all solid ceramic material that are not as precious as the materials (such as platinum) used in other cells.
- It has a very long-life expectancy of 40,000-80,000h.
- It has a highest conversion efficiency of all fuel cells (more than 50-60%).
- Utilization of waste heat increases the over-all efficiency to over 80%.
- Fuel reforming is possible internally that reduces the cost avoiding the requirement of an extra subunit.

The main hurdle in the development and commercialization of SOFCs is, however, their high operating temperature. At high operating temperature, the material choices are limited [1.5] and hence increases the manufacturing cost of the cell. The assembly of materials consisting of different layers has a question of thermal and chemical compatibility at elevated temperature. High operating temperature also forbids rapid start-up of the cell [1.32]. To overcome the problems associated with the high operating temperature of fuel cell scientists and researchers around the globe were working to reduce operating temperature. The approaches include the development of electrolyte material with high ionic conductivity at low temperature and thus lowering the internal resistance loss of the electrolyte. This approach yielded development of several electrolyte materials with high ionic conductivity in the low-temperature zone. However, these materials either suffer thermal reduction at high temperature under reducing atmosphere or are associated with electronic conductivity. Thus till date application YSZ as an electrolyte has not been replaced. However, the internal resistance of the electrolyte has been compensated by lowering the thickness of the electrolyte with the help of advanced fabrication techniques [1.33-1.35].

The other losses are associated with the slow reaction rate and mass transport of gas at the porous electrode sides, especially at the cathode. These losses can be minimized by careful tailoring of the triple phase boundaries (TPBs). As the majority of this voltage loss occurs at the cathode side for reduction reaction, cathodes need special attention [1.10,1.36]. The other approach to lower the operating temperature of SOFC deals with the development of cathode material with improved characteristics and thus lowering the cathode overpotential.

1.1.2 The SOFC Cathode

The cathode in the SOFC is the positive electrode where reduction reaction of air/oxygen occurs. The oxygen molecules in the oxidant gas get reduced at the cathode-electrolyte interface by the electrons in the external circuit. The oxygen ions so produced are transported through the bulk of the electrolyte following ionic conduction mechanism. To understand the loss the cathode offers to the overall cell voltage one has to know the reaction kinetics involves in the reduction process. The exact reaction mechanism of the whole process is complicated and involves some elementary steps. The reaction mechanism also depends on the

type of cathode material (electronic conducting or mixed conducting) used or the pathway of reaction. The reaction fragments, in general, are the surface diffusion, adsorption, dissociation and transport of oxide ions [1.5,1.8].

Mixed ionic electronic conducting (MIEC) cathode materials allow the bulk transport of the intermediate oxygen species thereby extend the reaction zones over the entire electrode surface. In other simple cases (cathode materials having electronic conductivity only) the reaction sites are limited to the TPBs only. Thus, the length of the TPBs and the extent of TPBs in MIECs are crucial in determining the cathode performance. The length of the TPBs can be enhanced by tailoring the microstructure of the cathode.

Taking into account the roles and working of the cathode in SOFC as discussed above a cathode material should have the following qualities [1.8, 1.37].

- It must be a good electronic as well as adequate ionic conductor.
- It must have good chemical and thermal stability under reducing atmosphere at high temperature
- It must be compatible with the other cell components such as electrolyte and the interconnect

The state of the art material for SOFC cathode is Sr- doped $LaMnO_3$ [1.38]. $La_{1-x}Sr_xMnO_{3-\delta}$ (LSM) [1.39, 1.40] is used as cathodes in high-temperature SOFCs. The intensive research and investigation on the cathode materials in the recent decades has produced a wide variety of other options for the cathode. To list a few, doped $LaCoO_3$ [1.41, 1.42], solid solutions of doped $LaMnO_3$ with $LaCoO_3$ and $LaCrO_3$ [1.43], $Sm_{1-x}Sr_xCoO_3$ [1.44-1.46], $Pb_2Ru_2O_{6.5}$ [1.47] and $La_{1-x}Sr_xCuO_{2.5-\delta}$ [1.48] etc. have been experimented as some popular cathode materials.

The most recent focus on the development in SOFC research is to reduce the operation temperature from high to the intermediate range (500-800^{o}C). At intermediate temperature, the number of choices for electrode materials increases which favors the cell manufacturing cost. The formation of insulating Zr-layer due to the reactions between the electrolyte and electrode that occurs at the higher temperature can be restricted. However, the operating temperature reduction is associated with two main issues. They are (i) the rate of reduction reactions becomes slow and limited, and (ii) the contact between the cathode and

the electrolyte becomes poor as the sinterability is reduced. Because of these the cell voltage drastically reduced down.

MIECs such as $La_{1-x}Sr_xCo_yFe_{1-y}O_{3-\delta}$(LSCF), $Sm_{0.5}Sr_{0.5}CoO_{3-\delta}$, and $Ba_xSr_{1-x}Co_yFe_{1-y}O_{3-\delta}$ (BSCF) have been extensively investigated as IT-SOFC cathode [1.44-1.46, 1.49-1.52]. Use of MIECs as cathodes increases the rate of oxygen reduction at the electrolyte-electrode interface as TPB extends over the electrode surface [1.53]. Among these materials, $La_{1-x}Sr_xCo_yFe_{1-y}O_{3-\delta}$(LSCF) showed a matching thermal expansion coefficient (TEC) with the oxide electrolyte material. LSCF also have high electrical conductivity and good catalytic activity for the oxygen reduction reaction [1.54,1.55].

The literature on $La_{1-x}Sr_xFeO_{3-\delta}$ (x=0.0-1.0) perovskites (LSCF) as a cathode material for SOFC indicated that Sr- substitution at La-site alters the oxygen stoichiometry and consequently the electrical and electrochemical behavior of LSF. The data on the electrical and electrochemical behavior of LSF showed a quite scattering as per the Sr-substitution level at A-site is a concern [1.56-1.60]. $La_{1-x}Sr_xCo_{1-y}Fe_yO_{3-\delta}$ perovskites with Co-rich compositions, particularly $La_{1-x}Sr_xCo_{0.8}Fe_{0.2}O_{3-\delta}$ exhibits improved electrical, electrochemical behaviour [1.61, 1.62]. However, Co-rich perovskites possess high TEC and prone to deleterious reactions with Zr based electrolytes [1.63]. Fe-rich composition especially $La_{1-x}Sr_xFe_{0.8}Co_{0.2}O_{3-\delta}$ has exhibited good thermochemical stability with the SOFC electrolyte [1.64-1.68]. Nanostructured electrode powder is used to avoid the detrimental reaction between the electrode and the electrolyte as they can be sintered at a low temperature. Moreover, the application of nanostructured cathode material also increases the effective triple phase boundary for electrochemical reaction [1.69, 1.70]. The powder preparation method has a significant effect on the microstructure, particle size distribution and the surface area of the resulting particle [1.65, 1.71-1.73]. Morphology of the electrode powder also affects the performance of the electrode.

1.2 Scope and Structure of the thesis

The broad objectives of the present work involve synthesis of $La_{1-x}Sr_x FeO_3$ powder series with x=0-1.0 following combustion technique and optimization of strontium substitution level based on electrical conduction and thermochemical stability. The study also includes the synthesis of nano scale Fe-rich $La_{1-x}Sr_xCo_{0.2}Fe_{0.8}O_{3-\delta}$

(LSCF) powder (with optimized Sr-substitution level) by solution combustion method with different morphology and characterization.

Chapter 1 is a general introduction to the present energy scenario, environmental pollution, and the importance of the development of intermediate temperature cathode materials. There are four other chapters in the thesis. A thorough review of the recent past works on LSF and LSCF materials has been reported in Chapter 2. Analysis of the literature provides motivation and definition of the problem addressed in this thesis. Chapter 3 detailed the procedure for powder synthesis and experimental works involving powder and bulk material characterization. The observations, analysis and results of the work are discussed in Chapter 4. The results and discussion chapter includes the powder synthesis and compositional optimization of $La_{1-x}Sr_xFeO_{3-\delta}$ (LSF) based on phase, thermal and electrical behavior. Synthesis of $La_{1-x}Sr_xCo_{1-y}Fe_yO_{3-\delta}$ (LSCF) powder to tailor particle morphology following solution combustion route as a function of process parameter has been also been included. The synthesized LSCF powder has been characterized with respect to thermal stability, phase purity, microscopy of morphology. Densification behaviour of the sample has also been studied. The electrical conduction behaviour of the bulk samples has been studied as a function of powder synthesis process parameter. The chemical compatibility of the LSCF powder with YSZ and SDC electrolytes has also been studied. The cathodic performance of the LSCF powder has been studied with SDC and YSZ electrolyte with in-house fabricated half cells using impedance spectroscopy. Chapter 5 elaborately describes the summary of the thesis on the basis of results and inferences. It also forwards some future works on the basis of the major findings and describes the scopes.

Chapter-2

Motivations and Objective

2.1 Related works

The research scenario on SOFC cathode has taken a new look at the development of mixed ionic and electronic conducting (MIEC) materials [2.1-2.3]. Conventionally used $La_{1-x}Sr_xMn_yO_{3-\delta}$(LSM) cathode offers high thermo-chemical compatibility and possesses good electrochemical activity. However, for intermediate temperature application it has been practically becoming unimportant for its low oxygen reduction reaction (ORR) sites and pure electronic conductivity [2.4-2.5]. MIECs carry out ORR over its entire surface and increase the performance by neglecting the polarization resistance [2.2]. Further improvement in the SOFC application has been achieved by nanostructuring the cell components by tailoring the structure from the powder synthesis level [2.6-2.7].In this context, the present study has been a result of our insight into the cathode material on the basis of the following important literature works.

2.1.1 Studies on Lanthanum Ferrite ($LaFeO_3$) based perovskites

There has been a growing interest among researchers since past few decades over the development of new materials with perovskite structure. Perovskite with ABO_3 formula unit is a corner-linked BO_6 octahedra, having a larger A-cation in 12-coordinated site. The existence of mixed valence states in the transition metal ions plays a critical role in determining the physical properties of such oxides [2.8]. In perovskites, structural changes introduced by doping in both A and B-sites also play a crucial role, as the B-O bond lengths and B-O-B bond angles are affected throughout the lattice [2.9]. The influence of the crystal structure and the valence of the transition metals brings out a change in its mechanical, thermal and electrical behavior of these perovskite-type oxides. $LaFeO_3$ perovskites have been synthesized using different synthesis routes. Sol–gel auto-combustion method [2.10]; co-precipitation [2.11]; hydrothermal [2.12]; polymerizable complex (PC) method [2.13] based on the Pechini-type reaction; reverse drop co-precipitation method with polyvinyl alcohol as a protecting agent [2.14]; polyethylene glycol and citrate methods [2.15] are explored for the synthesis of perovskite powder. Each technique has its advantages and disadvantages and

yields a wide range of particle size as a function of calcination temperature. In these methods the crystal structure and particle size has been shown to be affected by the synthesis routes [2.10-2.17].

Kindermann *et al* studied the physio-chemical compatibility behavior of $LaFeO_3$ based perovskites with YSZ and found reactive phases. They developed a La-Sr-Fe-M-O based perovskite that is highly chemical compatible with YSZ. Their study also claimed to provide a working hypothesis for the development of improved cathode compositions for solid oxide fuel cells [2.18]. Electrical conductivity and thermal expansion behavior have been studied by Tiez *et al* [2.19]. The work provided a full overview of the quasy-ternary system of a series of perovskites and the distribution of different crystallographic phases in the selected series. It also discussed the effect of phase transform on the DC electrical conductivity and the thermal expansion behaviour.

The use of MIEC perovskites could improve the surface oxygen reduction kinetics [2.20]. The Oxygen reduction kinetics could be predicted from thermodynamic properties such as molar free energies, enthalpies and entropies of oxygen dissolution [2.21]. Thus, MIEC perovskite has been considered as potential candidates for SOFC components.

Perovskite compounds, particularly those based on $LaFeO_3$ have been envisaged as mixed ionic electronic conductors (MIECs) for application as fuel cell electrodes. For these applications, they need to be stable under reducing conditions. The structural changes of the perovskites can be achieved by doping a large number of di, tri and tetravalent cations. For example, partial substitution of La^{3+} by Sr^{2+} in $LaFeO_3$ resulted in significant changes in its structure and catalytic activity. The perovskites structure was changed from orthorhombic in $LaFeO_3$ to nearly cubic in $La_{0.8}Sr_{0.2}FeO_3$. Replacement of La^{3+} by Sr^{2+} induced a positive charge deficiency in the perovskite. The charge compensation takes place by the oxidation of some Fe^{3+} to Fe^{4+} and the generation of oxygen vacancies, which greatly promoted the reducibility of the perovskite [2.8]. $La_{0.8}Sr_{0.2}FeO_3$ perovskite showed enhanced activity in CO oxidation and methane combustion. It has been suggested that the oxygen vacancies accelerate the dissociation of gaseous oxygen on the surface in CO for oxidation and facilitate the diffusion of lattice oxygen from the bulk to the surface.

The structural influence on the physical properties of the perovskites to be used as the cathode in SOFC can be further understood by studying following review of the literature on doped $LaFeO_3$.

2.1.2 Studies on Lanthanum strontium ferrite [$La_{1-x}Sr_xFeO_{3-\delta}$ (LSF)]

$La_{1-x}Sr_xFeO_{3-\delta}$ (x=0–0.3) perovskites with different particle sizes has been prepared by a sol–gel method [2.22]. The influence of the Sr content and particle size on the microstructure and magnetic properties has been investigated. Increasing Sr content has been found to increase the lattice contractions.

The conductivity of the entire solid solution $La_{1-x}Sr_xFeO_{3-\delta}$, where x=0.2, 0.4, 0.5, 0.7 and 0.9, in the oxygen partial pressure range 10^{-19}– 0.5 atm and temperatures between 750°C and 950°C has been reported [2.23]. The partial contributions from different charge carriers and the energetic parameters governing transport of charged species suggest LSF as mixed ion-electron conductors in the low oxygen pressure with high oxygen deficiency. The partial contributions to the conductivity from oxygen ions, electrons, and holes increase with strontium content and attain maximal values at x =0.5. Further increase in doping resulted in charge ordering of oxygen vacancy and deterioration of conducting properties.

The high temperature conductivity of $La_{1-x}Sr_xFeO_{3-\delta}$, (x=0.2, 0.4, 0.5, 0.7 and 0.9) has also been studied over a wide oxygen partial pressures (P_{O2})range (below 10^{-6} atm) as a function of acceptor doping [2.24]. It has been observed that the oxygen vacancy is fully ionized in the p-type region at high $P_{O2.}$ It has also been observed that high Sr substitution level influence of oxygen vacancy as well the electrical conductivity. Fe^{3+} plays a compensating role in conductivity for low Sr-containing samples.

A series of perovskite compounds with the general formula $La_{1-x}Sr_xFeO_{3-\delta}$ (x= 0.2, 0.4, 0.6, and 0.8) have been synthesized by self-combustion route [2.25] using a fuels urea/nitrates. Structural study indicates a phase transition from orthorhombic (x= 0.2) to rhombohedral (x > 0.2) structure. The pseudocubic lattice parameter and <Fe-O> bond lengths were observed to decrease monotonically with increasing x. The decline nature has been attributed to an increase in the mean oxidation state of the transition metals. All reported compounds exhibited semiconductor behavior with temperature described by

hopping conduction model. The monotonic decrease of resistivity with increasing x ($0.2 < x < 0.6$) was correlated to the increase in charge carrier density. Partial substitution of La^{3+} by Sr^{2+} in $LaFeO_3$ resulted in significant changes in its structure and catalytic activity. The perovskites structure was changed from orthorhombic in $LaFeO_3$ to nearly cubic in $La_{0.8}Sr_{0.2}FeO_3$. Replacement of La^{3+} by Sr^{2+} induced a positive charge deficiency in the perovskite. It has also been observed that the substitution of 20% La^{3+} by Sr^{2+} in $LaFeO_3$ changed the crystalline structure from orthorhombic to cubic [2.8]. Structural study as a function of temperature showed that the first-order phase transition from orthorhombic-to-rhombohedral in $La_{1-x}Sr_xFeO_{3-\delta}$ ($x = 0, 0.1$) shifts to lower temperatures with increasing Sr content [2.9]. The observed phase-transition temperature was significantly lower in polycrystalline ceramics as compared with fine powders. This decline in phase-transition temperature has been correlated to the combined effect of stress induced anisotropic thermal expansion and volume contraction due to the phase transition. Rhombohedral $La_{1-x}Sr_xFeO_{3-\delta}$ ($x = 0.3, 0.4, 0.5$) were observed to transform to the cubic perovskite structure during heating. The second-order phase-transition temperature was reported to decrease with increasing Sr content as well as decreasing the partial pressure of oxygen. The observed nonlinear thermal expansion behavour of the samples were correlated to a chemical expansion resulting from a reduction of the higher valence state of Fe.

The conductivity study revealed that the charge carrier density and mobility strongly depend on the A- site cation of perovskite ferrites [2.26]. The carrier densities and the mobilities were found to be high in $SrFeO_{3-\delta}$ than that in $BaFeO_{3-\delta}$. It has also been reported that the mobility rather than the carrier densities decreased with the increase of the amounts of the oxygen vacancy [in the range of $0 < \delta < 0.5$]. The mobilities of $SrFeO_{3-\delta}$ in which the Fe-O-Fe average distance is about 3.86 Å were about 3 times than those of $BaFe0_{3-\delta}$ with the Fe-O-Fe distance of 4.01 Å. Thus, the mobilities remarkably decreased with the increase of the Fe-O-Fe distance. It was concluded that the electrical conductivities of the $SrFeO_{3-\delta}$ and the $BaFeO_{3-\delta}$, at room temperature are mainly determined by the mobility that is affected by the oxygen vacancy and the Fe-O-Fe distance.

Zhang *et al* [2.27] studied the conductivity of La-substituted $SrFeO_3$ ferrite perovskites prepared by citrate combustion from metal nitrate salts as cation

precursors. The maximum conductivity of the undoped $SrFeO_3$ was found to be 72 S cm^{-1}. They attributed the increasing conductivity to the highly abundant electrons formed during reduction. It has also been observed that the conductivity increases with La^{3+} substitution $x = 0.4$ and after that it decrease. The maximum electrical conductivity of 109 S cm^{-1} was observed for $La_{0.4}Sr_{0.6}FeO_3$ resulted from the contribution of the increased charge carriers. The declining value of conductivity in compounds with x ≥0.6 is attributed to the charge order of La^{3+}, Sr^{2+}. The charge ordering localizes the electrons and hence reduces the conductivity. In this work, it has also been suggested that a decrease in the electron double exchange process caused by the increase in the cell volume and bond length M-O and Fe-O distance may decrease conductivity. The decrease in the conductivity also correlated to the higher oxygen vacancy in the crystal lattice created by increased concentration of La^{3+}.

The density of the substituted $SrFeO_{3-\delta}$ is observed to increase with La^{3+} substitution. XRD patterns indicated that the synthesized $SrFeO_3$ materials have a cubic structure and the substituted compounds show orthorhombic structure. The physical, electrical and electrochemical characterization suggests $La_{0.4}Sr_{0.6}FeO_{3-\delta}$ as a suitable green electrode material for electrometallurgy applications.

$La_{0.3}Sr_{0.7}FeO_{3-d}$ (LSF)/CeO_2 cathode supported $Ce_{0.8}Sm_{0.2}O_{2-\delta}$ (SDC) electrolyte was prepared by a simple multilayer tape casting and co-firing method [2.28]. SDC electrolyte slurry and LSF/ CeO_2 cathode slurry were optimized, and the green bi-layer tapes were co-fired at a different temperature. Phase characterizations and microstructures of electrolyte and cathode were studied by X-ray diffraction (XRD) and Scan Electronic Microscopy (SEM). No additional phase peak line was observed in electrolyte and cathode support when the sintering temperature was lower than 1400°C. The cathode support was porous with the electrical conductivity of about 4.21 S/cm at 750°C. Open Current Voltage and maximum power density reached 0.61 V and 233 $mWcm^2$ at 750°C, respectively with Ni/SDC as an anode.

$La_{0.6}Sr_{0.4}FeO_{3-\delta}$ (LSF) has been studied to be a promising material for cathode support application due to its matching thermal expansion coefficient (TEC) of electrolytes and adequate ionic and electronic conductivity [2.24]. The electrical

measurements indicated that porosity of the sample influenced the electronic conductivity of LSF. The properties of the LSF support were altered by sintering temperature, powder compacting pressure and pore former. The study suggested powder compacting pressure of 100MPa and sintering temperature of 1150^{o}C as an optimum fabrication condition for preparation of cathode support.

Anode-supported yttria-stabilized zirconia (YSZ) solid oxide fuel cells with Sr-doped $LaFeO_3$ (LSF) cathode showed improved performance when Sm-doped CeO_2 (SDC) interlayer between the cathode and YSZ electrolyte was incorporated[2.29]. XRD analysis of LSF–YSZ reaction mixtures indicated no reaction associated with the formation of strontium or lanthanum zirconate between these materials even at 1400^{o}C. A significant shift in the LSF diffraction peaks indicating unit cell volume expansion was observed. The change in volume was correlated with the incorporation of Zr^{4+} cations in the perovskite structure which in turn lowers the conductivity of LSF.

Mixed conducting perovskite membranes ($La_{1-x}A_xFeO_{3-d}$ with A = Ca, Sr and x = 0.1–0.2) have also been studied for simultaneous O_2 separation and catalytic oxidation of ammonia to nitric oxide [2.28]. The catalytic oxidation of ammonia over these membranes in the temperature range of 1000–1333 K showed NO selectivity up to 98% with no N_2O production. It has been reported that these membranes do not show any performance degradation on stream during several days of operation.

Structural and electronic transport properties of LFN ($LaFe_{1-z}Ni_zO_3$) and LSCFN ($La_{1-x}Sr_xCo_{1-y-z}$ $Fe_yNi_zO_3$) perovskites synthesized by a modified citric acid method were studied [2.30]. Temperature dependence electrical conductivity showed a strong compositional dependence. Chemical stability studies on $Ce_{0.8}Gd_{0.2}O_{1.9}$ electrolyte revealed a declined stability with increasing Ni concentration associated with the formation of solid solutions in CGO/perovskite composites. The coefficient of TEC of LFN perovskites was found to match that of CGO electrolyte.

Perovskite ferrite $La_{1-x}Sr_xFeO_3$ (x = 0–0.3) nanoparticles were prepared by Lise *et al* using the sol–gel method [2.31]. The influence of the Sr content and particle size on the microstructure and magnetic properties has been investigated. It has been reported that with increasing Sr content causes a lattice contraction.

The properties of $La_{1-x}Sr_xFeO_{3-\delta}$ (x = 0.1, 0.25) mixed conductors have been investigated. A special attention has been given to study the effect of secondary phases due to cation non-stoichiometry (±5 mol% La excess and deficiency) [2.29]. Secondary phases, located at grain boundaries in cation non-stoichiometric materials was found to be increased as compared to single-phase materials. Extensive swelling in the final stage of sintering was observed in all materials, which resulted in micro-porous materials. The swelling was most pronounced in the phase pure and two-phase materials due to La-deficiency, while refractory secondary phases in La-excess materials inhibited both sintering, grain growth and swelling. In La-deficient materials, the formation of molten, secondary phases resulted in rapid swelling due to viscous flow. Their findings demonstrated the effect of sintering temperature and time on the density. It was found that controlling the sintering temperature and time, as well as cation stoichiometry of $La_{1-x}Sr_xFeO_{3-\delta,}$ fully dense and homogenous $La_{1-x}Sr_xFeO_{3-\delta}$ ceramics could be achieved.

Electrical conductivity relaxation experiments were performed on thin specimens of LSF at oxygen partial pressures $P_{O2}= 10^{-1}$ bar in the temperature range 923 to 1223 K [2.32]. The transient response of the electrical conductivity after a sudden change of the ambient oxygen partial pressure was analyzed to identify diffusion-limited and surface exchange-limited kinetics of re-equilibration. The response of specimens indicated diffusion-controlled kinetics at $P_o > 0.03$ bar while surface exchange governs it at $P_o < 0.01$ bar. The chemical diffusion coefficients, D, were found invariant with oxygen pressure. At 1073 K the absolute values were D = 6.5 x 10-6 cm^2 for x = 0.1 and D = 1.1 X 10 cm^2 for x = 0.4 respectively, with activation energies of about 80 kJ/mol. This pressure dependency was interpreted in terms of a slow surface process involving an oxygen molecule and a surface oxygen vacancy and causes the observed sharp transition from diffusion- to exchange-controlled kinetics. The activation energy of k_o was estimated to be110 to 135 kJ/mol.

The thermomechanical properties, oxygen non-stoichiometry and electronic and ionic conductivity of $La_{0.6}Sr_{0.4}FeO_{3-\delta}$ has been reported by Yao *et al* [2.33]. Their study indicated that the electrical conductivity of the sample is a function of the charge carrier concentration. The electron hole mobility was found to decrease

with increasing charge carrier concentration. The chemical diffusion coefficient, D_{Chem}, as determined from electrical conductivity relaxation study was found to be $6.2x10^{-6}$ cm^2s^{-1} at 800°C with an activation energy of 137 kJ mol^{-1}. The surface exchange coefficient was found to decrease with decreasing oxygen partial pressure.

The chemical diffusion coefficient and the chemical surface exchange coefficient of $La_{0.4}Sr_{0.6}FeO_{3-\delta}$ has been measured as a function of oxygen partial pressure (10^{-4} to $10^{-2.7}$ bar) and temperature (700- 900°C) [2.34]. The surface exchange coefficient was found to be proportional to P_{O2} =0.8 at 700°C and P_{O2} =0.7 at 900°C, respectively. The chemical diffusion coefficient was found to be almost independent of P_{O2} at 700°C with values around $2.5x10^{-6}cm^2s^{-1}$. The mechanism for the surface reaction of gaseous oxygen with the solid oxide is interpreted by the adsorption (chemisorption) of negatively charged oxygen molecules on the surface.

Composite electrodes were prepared by adding 40% (by wt) $La_{0.8}Sr_{0.2}FeO_{3-\delta}$ into porous yttria-stabilized zirconia (YSZ) and their performance was studied as a function of time and calcination temperature [2.35]. The XRD studies showed an increase in lattice parameter when calcination was above 1523 K suggesting reaction of Zr with LSF to form a Zr-doped perovskite. LSF and YSZ did not react when calcined at 1373 K. The dependency of ASR was also studied on the current density. ASR was found to be decreasing under both anodic and cathodic polarization. Electrodes calcined at 1373 K showed an ASR of 2.5 Ωcm^2 at 973 K, but this value decreased dramatically under polarization. Scanning electron microscopy images demonstrated that aging at 973 K and calcination at 1373 K cause significant sintering of the $La_{0.8}Sr_{0.2}FeO_{3-\delta}$. The study suggested the deactivation of the electrode to be caused by the morphological changes, rather than solid-state reactions.

2.1.3 Studies on lanthanum strontium cobalt ferrites [$La_{1-x}Sr_xCo_{1-y}Fe_yO_{3-\delta}$ (LSCF)] system

2.1.3.1 Studies based on Co-rich compositions of $La_{1-x}Sr_xCo_{1-y}Fe_yO_{3-\delta}$

The electrical properties of mixed-conducting perovskite $La_{1-x}Sr_xCo_{0.8}Fe_{0.2}O$ samples have been studied as a function of composition, temperature and bias conditions. Attention is focused on the investigation of the grain boundary role in

the conductivity reduction [2.36]. It has been observed that the Sr-substitution leads to an increase of the electronic conductivity of the samples and reduction of the E_a value. The impedance spectra analysis suggested the existence of two different charge carriers i) those which are blocked and ii) those which are non-blocked by grain boundary related processes. It was shown that the increase in grain sizes increases the electrical conductivity of perovskite electronic ceramics. High-temperature phase relation of $La_{0.6}Sr_{0.4}Co_{0.8}Fe_{0.2}O_{3-\delta}$(LSCF) was studied with XRD in controlled atmospheres [2.37]. The electrical conductivity was measured by the four-probe DC method, at temperatures 973–1173 K, in the P_{O2} range of 1–10^{-5}Pa. These properties were discussed in combination with oxygen non-stoichiometry and the diffusion constant of oxide ions. It was found that LSCF has a phase transition from rhombohedral to cubic, at about 773 K. The lattice constant of the high-temperature phase was found to increase with decreasing $P_{O2.}$ The increase in lattice parameter showed the reduction of metallic ions with increased oxygen non-stoichiometry. Although the reduction causes the hole concentration to decrease, hole conduction dominants in the measured P_{O2} range. The ionic conductivity has a maximum value of 0.08 S cm^{-1} at 1073 K, the value is close to that of Gd-doped ceria at the same temperature.

Perovskite-type oxides of $Ln_{0.4}Sr_{0.6}Co_{0.8}Fe_{0.2}O_{3-d}$ (Ln/La, Pr, Nd, Sm, Gd) have been prepared using the solid state reaction of corresponding metal oxides [2.38]. The electrical conductivity of the sintered samples showed semiconductor-like behavior at a lower temperature and metallic behavior at a higher temperature. The reactivity test of these oxides with 8 mol% Y_2O_3 doped zirconia (8YSZ) was studied between 800 and 1000°C for 96 h in air. The perovskite oxides were found to react with 8YSZ to produce Strontium Zirconate phase at 900°C and no reaction product was observed at 800°C. These perovskite oxides showed no degradation of the electrode performance by annealing between 600 and 800°C. A large thermal expansion mismatch between these perovskite oxides and 8YSZ is also observed. The conversion of the tetravalent state of Co and Fe to the trivalent state causes the precipitation of Sr at higher temperatures resulting in the reaction of Sr with ZrO_2 to produce Strontium Zirconate.

The catalytic and electrocatalytic behaviour of the $La_{0.6}Sr_{0.4}Co_{0.8}Fe_{0.2}O_3$ (LSCF) perovskite deposited on yttria-stabilized zirconia (YSZ), was studied during the

reaction of methane oxidation [2.39]. Experiments were carried out at atmospheric pressure, and at temperatures between 600 and 900°C.When, instead of co-feeding with methane in the gas phase, oxygen was electrochemically supplied as O_2, considerable changes in the methane conversion and product selectivity were observed. The non-faradaic effects (NEMCA) were also studied and compared to those observed with metal catalysts. $La_{0.8}Sr_{0.2}Co_{0.8}Fe_{0.2}O_3$ (LSCF), substituted by Sr and Fe at the A and B sites, was prepared using the sol–gel (SG) method in the work of Liu *et al* [2.40]. The powder followed by heating at 900°C for 4 h. Scanning electron microscopy showed that the LSCF structure is highly porous, facilitating gas transfer and maximizing the number of active sites for the oxygen reduction reaction (ORR) at the cathode of a solid oxide fuel cell. The kinetics of the ORR of (SG-derived) LSCF deposited by screen-printing on a samarium-doped ceria (SDC) electrolyte was studied using electrochemical impedance spectroscopy and cyclic voltammetry at temperatures ranging from 400 to 700°C. The study showed that the LSCF cathode is stable and exhibits a high exchange current density (and low charge transfer resistance), yielding an apparent activation energy for the ORR of cathode 120 kJ/mol. It was also found that the LSCF on SDC cathode was one order of magnitude more active than standard manganite-based composite cathodes, deposited on yttria stabilized zirconia, studied under otherwise identical operating conditions. With increasing Fe content, the TEC decreases, but the lattice energy increases and the ionic conductivity decreases monotonously. On the other hand, increasing the Sr content increases the LSCF conductivity, with a maximum at a Sr content of 0.5.

Pure-phase $La_{0.4}Sr_{0.6}Co_{0.8}Fe_{0.2}O_{3-\delta}$ (LSCF) nanocrystallites were synthesized by the combustion method [2.41]. The studied process uses glycine as fuel and complexing agent, and ammonium nitrate as combustion trigger. The morphological and structural characterization of the LSCF nanopowders was performed. The synthesized LSCF nanopowder was found to have interconnected nanocrystallites (~45 nm) forming a sponge-like structure with meso and macropores. The specific surface area of the synthesized powder was around 10 $m^2\ g^{-1}$. Crystalline structural analyzes showed LSCF nanopowder have cubic crystal structure in the Pm-3m space group. Symmetrical cells with different

electrode crystallite size (45 and 685 nm) were fabricated on $La_{0.8}Sr_{0.2}Ga_{0.8}Mg_{0.2}O_{3-\delta}$ (LSGM) electrolyte using spin coating technique and different thermal treatments. Electrochemical impedance spectroscopy of the symmetric cells was performed as a function of temperature and p_{O2}. The area specific resistance of the nanostructured sample (45 nm) decreases by two orders of magnitude (values as low as 0.8 Ωcm^2 at 450°C) with respect to the sub micro structured sample (685 nm). This improvement is attributed to the cathode morphology optimization in the nanoscale. The enlargement of the exposed surface area and shortening of the oxygen diffusion paths was attributed to the reduced polarization resistance and is associated with the surface exchange and O-ion bulk diffusion process.

The oxygen reduction reaction on YSZ solid electrolytes has been investigated by Baumann *et al* [2.42] using thin film microelectrodes employing perovskite-type mixed conductors such as $La_{0.6}Sr_{0.4}Co_{0.8}Fe_{0.2}O_{3-\delta}$, $Ba_{0.5}Sr_{0.5}Co_{0.8}Fe_{0.2}O_{3-\delta}$ and $Sm_{0.5}Sr_{0.5}CoO_{3-\delta}$ as electrode materials. Comparison of electrochemical material parameters revealed that the Fe/Co ratio in $La_{0.6}Sr_{0.4}Co_{0.8}Fe_{0.2}O_{3-\delta}$ has only little effect on the resistance associated with the surface oxygen exchange. $Ba_{0.5}Sr_{0.5}Co_{0.8}Fe_{0.2}O_{3-\delta}$ thin films exhibit very low surface-related polarization resistances. Strongly decreased resistances can also be observed in Co-rich $La_{0.6}Sr_{0.4}Co_{1-x}Fe_xO_{3-\delta}$ electrodes after a cathodic voltage pulse treatment of several tens of seconds. It has been reported that area specific resistances below 0.1 Ωcm^2 at 700°C could be achieved using such activation.

Dense thin film microelectrodes of $La_{0.6}Sr_{0.4}Co_{0.8}$ $Fe_{0.2}O_{3-\delta}$ have been prepared by pulsed laser deposition and standard photolithographic techniques on yttria-stabilised zirconia substrates [2.43]. Impedance spectroscopy of the sample as a function of temperature and dc bias has been analyzed to study the electrochemical behaviour of these electrodes. The electrochemical resistance was found dominated by the oxygen exchange reaction at the surface of the electrode. A minor contributions from the electrode/electrolyte interface and the ohmic resistance of the electrolyte under zero or small dc bias as also found to contribute to electrochemical resistance. The main capacitive process is associated with oxygen stoichiometry changes in the bulk of the electrode (chemical capacitance) while an additional electrode/electrolyte interfacial

capacitance is also present. The temperature and dc bias dependencies of these processes are discussed in terms of defect chemistry.

$La_{0.8}Sr_{0.2}Co_{0.8}Fe_{0.2}O_3$ (LSCF) nanopowders, has been studied as low-temperature solid oxide fuel cells (SOFCs) cathode material. The powders have been prepared by citric acid gel combustion method [2.44]. Phase pure LSCF perovskite powder with an average particle size of less than 30 nm was achieved on calcination at 700°C. The anode-supported single cell has been prepared with the synthesized LSCF powder as a cathode. Cathode sintered at 700°C showed high electrical performance with the maximum power density of 771 $mWcm^{-2}$ at 600°C. The study suggested that the synthesized LSCF nanopowders have the potential to be applied as cathode material for low temperature SOFCs.

Iron- and cobalt-containing perovskites, $La_xSr_{1-x}Co_yFe_{1-y}O_{3\pm\delta}$, (x = 0.8; 0.6 and y = 0.8; 0.2) were synthesized via solid state reaction method [2.45]. It was revealed that formation of the perovskite structure occurs at temperatures above 900°C. Mixing LSCF powder with gadolinia doped ceria (GDC) in 50:50 wt% ratio, composite materials were prepared. Conductivity measurements were carried out with circle-shaped samples. The highest conductivity at the target temperature of 600°C was observed on composite $La_{0.6}Sr_{0.4}Co_{0.8}Fe_{0.2}O_{3-\delta}$-GDC samples. Study of a fracture surface of compacted samples has shown that adding GDC enhances both conductivity and sinterability of powders changing the fracture mechanism of cathode material from intergranular to the cleavage one.

Baque *et al* studied the effect of electrode morphology on the electrochemical performance of $La_{0.4}Sr_{0.6}Co_{0.8}Fe_{0.2}O_{3-\delta}$ (LSCF) [2.46]. An acetic acid-based chemical route, a hexamethylenetetramine chemical route and spray pyrolysis technique has been used to produce different morphology LSCF powders. The cathode films were fabricated by spin coating inks, starting from these powders, onto $Ce_{0.9}Gd_{0.1}O_{1.95}$ ceramic substrates. They found that all methods can obtain nanostructured LSCF samples, but with different morphologies. In particular, spray pyrolysis method allows the attainment of LSCF cathode films with a typical microstructure (i.e. spherical particle shape, nanometric grain sizes and large and open porosity). They also showed in their work that the electrochemical properties of LSCF cathode films strongly depend on microstructure and morphology. The

cathode polarization resistance can decrease considerably with optimized synthesis parameters.

$La_{0.6}Sr_{0.4}Co_{0.2}Fe_{0.8}O_{3-\delta}$ (LSCF) and $Ba_{0.5}Sr_{0.5}Co_{0.8}Fe_{0.2}O_{3-\delta}$ (BSCF) materials were synthesized by spray pyrolysis and characterized by the electrical conductivity relaxation technique [2.47]. The electrical transport and the oxygen exchange properties of these mixed conducting materials between 600 and 800°C has been compared. The study showed that LSCF has the higher electrical conductivity (257-412 Scm^{-1} between 450 and 900°C), on the other hand, BSCF has faster oxygen exchange kinetics and diffusion. The thermal expansion behaviour study of this material showed that the expansion of both materials follows a nonlinear behaviour. The TEC was found to be 27.3 and 15.5 ppmK below 700°C for BSCF and LSCF, respectively.

Ethylene diamine N,N,N',N'-tetra N-acetyl diamine (EDTNAD) was used as a chelating agent for synthesis of $La_{0.6}Sr_{0.4}Co_{0.8}Fe_{0.2}O_{3-\delta}$ (LSCF) perovskite powder for dense membrane application [2.48]. EDTNAD formed complexes of the four metal ions simultaneously as a ligand thereby provided a facile one-step combustion process. Oxidative coupling of methane (OCM) reaction showed a C2 selectivity of 100% and C2 yield of 5.01% at 1153K using LSCF disk in the atmospheric membrane reactor and over the temperature range of 1073-1173K.

Nanocrystalline powders of $La_{1-x}Sr_xGa_{1-y}Mg_yO_{3\pm\delta}$ (x = 0.10 to 0.15; y =0.10 to 0.15) (LSGM) as electrolyte, $La_{0.8}Sr_{0.2}Cr_{0.7}Mn_{0.3}O_{3\pm\delta}$ (LSCM) as anode, porous $La_{0.8}Sr_{0.2}Co_{0.8}Fe_{0.2}O_{3\pm\delta}$ (LSCF) or $LaNi_{1-x}Fe_xO_{3\pm\delta}$ (x=0-0.5) (LNF) as cathode and substituted $LaCrO_3$ as interconnect were synthesized by various wet chemical methods to fabricate all perovskite IT-SOFCs [2.49]. The wet chemical methods used are metal-carboxylate gel decomposition, hydroxide co-precipitation, sonochemical and regenerative sol-gel process. For densification microwave sintering of the powders have been performed. Optimized microwave sintering parameters were obtained by varying the sintering time, and temperature to achieve a higher density of LSGM pellets. The microstructural study revealed the average grain size of these perovskites was ~ 22 nm range. The conductivity of the sintered electrolyte pellets was found to be ~0.01- 0.21 S/cm at 550-1000°C. The conductivity of the electrodes was 1.5-100 S/cm at 25-1000°C.

Ammonium nitrate assisted combustion synthesis method was successfully used for the synthesis of $La_{0.4}Sr_{0.6}Co_{0.8}Fe_{0.2}O_{3-\delta}$ (LSCF) perovskite [2.50]. The morphology of the powder showed a presence of meso and macropores in a sponge-like structure with interconnected nanosized crystallites (size 45 nm) with a specific surface area of $8 m^2 g^{-1}$. Cathode performance studies on LSCF4682 on $La_{0.8}Sr_{0.2}Ga_{0.8}Mg_{0.2}O_{3-\delta}$ (LSGM) electrolyte in the intermediate temperature range between 400°C-700°C showed that the polarization resistances R_p were 0.067 and 0.035 Ωcm^2 at 600°C and 700°C, respectively. The long-term behavior has also been studied by applying an accelerated aging at 800°C. A degradation rate of $1/R_P(dR_P/dt) = 0.002\ h^{-1}$ raised the R_p to 0.1 Ωcm^2 at 700°C after 500 h of aging. The study reported achievement of a maximum power density of 1.23 Wcm^{-2} at 650°C with LSCF cathode deposited on a porous SLT-LSGM supported multilayer cell.

The electrochemical performance of Ni-YSZ, Ni-GDC, and Ni/Ru-GDC hydrogen electrodes and LSM-YSZ, LSCF, and LSF oxygen electrodes were studied [2.51]. The operating parameter studied includes variation in the ratio of H_2O/H_2 and CO_2/CO (50/50 to 90/10), the operating temperature (550-800°C), and the applied voltage. It has been reported that the activity of Ni-YSZ electrodes during H_2O electrolysis significantly lowered as compared to that for H_2 oxidation. Ni-GDC and Ni/Ru-GDC electrode showed comparable activity for operating between the SOEC and solid oxide fuel cell (SOFC) modes. The study also indicated that the activity of all the O_2 electrodes as an SOFC cathode was higher than that as SOEC anodes. The electrochemical performances of the perovskite on Ni-YSZ anode-supported SOFC containing YSZ electrolyte (~10 μm) with CGO interlayer (~15 μm) are studied in the temperature range 700-800°C using H2 as fuel and oxygen as the oxidant. The study indicated that $La_{0.5}Sr_{0.5}Co_{0.8}Fe_{0.2}O_3$ perovskite showed the highest current density of 1.7 A/cm^2 at 800°C.Precipitation of nanocrystalline grains over the core grains in the porous microstructure of this cathode is attributed for the observed cell performance.

2.1.3.2 Studies based on Fe-rich compositions of $La_{1-x}Sr_xCo_{1-y}Fe_yO_{3-\delta}$

2.1.3.2.1 Studies based on synthesis

Different synthesis methods have been compared for the preparation of $La_{0.2}Sr_{0.8}Co_{0.2}Fe_{0.8}O_{3-\delta}$ (LSCF) powders [2.52]. Among all the technique studied the

solid state reaction method was ascribed as the most easily controlled and effective method for LSCF powder synthesis. The study proposes a mathematical model in consideration of membrane bulk diffusion and surface reaction to simulate the performance of the dense disk-shaped membranes for oxygen permeation. The study indicated that oxygen permeation flux of the LSCF membrane increases with the decreasing downstream oxygen partial pressure. The oxygen permeation flux through a 2 mm LSCF membrane was found 0.32 cm^3/cm^2 min (STP) at 1123K and P_{O2} of 0.21-1×10^{-3} atm. The characteristic thickness (L_c) of the LSCF membrane was estimated to be 1.8 mm both by simulation and experimental study.

Three synthesis methods were compared for the preparation of $La_{0.2}Sr_{0.8}Co_{0.2}Fe_{0.8}O_{3-\delta}$ (LSCF) powders. It was found that the solid state reaction method is the most easily controlled and effective [2.53]. A mathematical model in consideration of membrane bulk diffusion and surface reaction has been proposed to simulate the performance of the dense disk-shaped membranes for oxygen permeation. The experimental results showed that oxygen permeation flux of the LSCF membrane increases with the decreasing downstream oxygen partial pressure. The oxygen permeation flux through a 2 mm LSCF membrane was found about 0.32 cm/min (STP) at 1123K .The characteristic thickness (L) of the LSCF membrane was estimated to be 1.8 mm by modeling and experimental study.

Fine and uniform $Ln_{0.6}Sr_{0.4}Co_{0.2}Fe_{0.8}O_{3-\delta}$ (Ln = La, Pr, Nd, Sm) powders with a perovskite phase were produced using a glycine–nitrate process [2.54]. The structure, electrical conducting and thermal expansion properties of the resulting ceramics were investigated. The results indicated that replacing La^{3+} by smaller lanthanide cations lead to a change in crystal structure from rhombohedral to orthorhombic symmetry and a decrease of the pseudocubic lattice constant. It was found that the electrical conducting properties decrease with reducing lanthanide cation size. Compared with $La_{0.6}Sr_{0.4}Co_{0.2}Fe_{0.8}O_3$, the degradation of the electrical conducting properties of $Pr_{0.6}Sr_{0.4}Co_{0.2}Fe_{0.8}O_3$ and $Nd_{0.6}Sr_{0.4}Co_{0.2}Fe_{0.8}O_3$ is not pronounced, whereas the electrical conducting properties of $Sm_{0.6}Sr_{0.4}Co_{0.2}Fe_{0.8}O_3$ declined to an unsatisfactory level. The study showed that there was an increase in thermal expansion at high temperatures for all the

compositions. This inclined thermal expansion is attributed to a chemically induced lattice expansion due to oxygen loss and formation of oxygen vacancies. $Pr_{0.6}Sr_{0.4}Co_{0.2}Fe_{0.8}O_3$ and $Nd_{0.6}Sr_{0.4}Co_{0.2}Fe_{0.8}O_3$ present relatively low thermal expansion coefficient values of 14.2×10^{-6} and 13.2×10^{-6} K^{-1} averaged between 100–750 and 100–700◦C, respectively.

Ammonia nitrate was applied as an oxidizer and combustion trigger to modify the normal combined EDTA-citrate complexing method into a process with auto combustion and low ignition temperature properties [2.3]. The effect of NH_4NO_3/metal ions to organic mole ratios and the heating temperature on the auto combustion behavior and the properties of the powders derived were investigated in detail. The critical amount of NH_4NO_3 for the auto combustion to occur was identified at the NO^{3-} to citric acid to EDTA mole ratio of around 10:2:1. After the experimental optimization, well-crystallized nanostructured $La_{0.6}Sr_{0.4}Co_{0.2}Fe_{0.8}O_{3-\delta}$ (LSCF) powder with a specific surface area as high as $21m^2/g$ was obtained. The study suggested that the properties of the powders could be tailored for different applications by adjusting the combustion parameters. For example nano-grained dense membrane for oxygen separation membrane and porous cathode for fuel cells and sensors.

Nano-crystalline $La_{0.6}Sr_{0.4}Co_{0.2}F_{0.8}O_{3-d}$ (LSCF) powder with a specific surface area of $22.9m^2\ g^{-1}$ and an average particle size of 175 nm was prepared by a nitrate-glycine solution combustion method and subsequent ball-milling [2.55]. The LSCF pre-calcined at 800◦C (LSCF-800) shows very good low-temperature sintering activity, and can well adhere to electrolyte after sintering at 700◦C and above. The single cell Ni–YSZ/YSZ/LSCF- 800 with the cathode sintered at 750◦C demonstrates the lowest polarization resistance and good electrical generation performance, but poor cathode microstructure stability. The sintering activity of LSCF cathode can be tailored through the control of the pre-calcination temperature of the precursor powder. Pre-calcining of LSCF powder at 900◦C (LSCF-900) increases the optimum sintering temperature of the cathode to 850◦C and improves the microstructure stability. The cell Ni–YSZ/YSZ/LSCF-900 with this cathode demonstrates excellent generation performances with the maximum power density greater than $1.0Wcm^{-2}$ and the power density of above $0.80Wcm^{-2}$ at 0.7V under operation at 700◦C. Low-temperature processing of the interlayer-

free LSCF cathode with good microstructure is beneficial to simplifying the cell structure and improving fuel cell performance.

$La_{0.6}Sr_{0.4}Co_{0.2}Fe_{0.8}O_{3-\delta}$ powder was synthesized by a combined EDTA-citrate complexing process via low-temperature auto-combustion synthesis with NH_4NO_3 as an oxidizer and combustion trigger [2.56]. The catalytic performance of the powder was also examined in the decomposition of peroxide hydrogen. The study showed that catalytic combustion and asymmetric precursor route derived powder were advantageous in terms of crystallite size, specific surface area, the valence state of B-site ion, sintering ability and catalytic performance.

$La_{0.6}Sr_{0.4}Co_{0.2}Fe_{0.8}O_{3-\delta}$ powder was synthesized by a combined EDTA-citrate complexing process via low-temperature auto-combustion technique with NH_4NO_3 as an oxidizer and combustion trigger [2.57]. The as-prepared pure LSCF powder itself can be used as a catalyst to facilitate the auto-combustion and to improve the powder characteristics. To further reduce the NH_4NO_3 addition, the concept of asymmetric sol–gel technique was also applied to provide the precursor powder with various concentrations of NH_4NO_3 in a vertical orientation. The study reported that the LSCF powder synthesized via low-temperature auto-combustion are better in terms of crystallite size, specific surface area, B-site valence state, sintering ability and catalytic performance in peroxide hydrogen decomposition. Given its simplicity and many unique features, the study suggested that this method is useful for low-cost mass production of perovskite powders.

$La_{0.6}Sr_{0.4}Co_{0.2}Fe_{0.8}O_{3-d}$ (LSCF) oxide powder was synthesized by a facile auto combustion process based on a modified glycine nitrate process (GNP) using cellulose fiber as micro-reactor [2.58-2.60]. As compared with the normal GNP, this technique allows the combustion to proceed in a much more environmentally friendly and controllable way. Transmission electron microscopy study revealed that the derived powder have a particle size in the range 15–20 nm. Suppression of impurity like $SrCO_3$ is attributed to the homogeneous dispersion of metal ions in cellulose–GN precursor. These nano powders showed a performance improvement of the cathode in solid-oxide fuel cells (SOFCs). The interfacial resistances of only B=0.70 and B=0.36 cm^2 at 600 and 650^oC under air, respectively, were observed, which was about two times better than the LSCF cathode derived from the normal GNP.

The high exothermal nature of above reaction created a high temperature and ensured the LSCF phase formation.

$La_{0.6}Sr_{0.4}Co_{0.2}Fe_{0.8}O_{3-\delta}$ (LSCF) perovskite nanostructures were synthesized using a 42 kHz ultrasound-assisted synthesis technique [2.61]. Synthesized LSCF was studied as electrodes in the intermediate and/or low-temperature solid oxide fuel and electrolysis cells (SOFCs/SOECs). The obtained nanomaterials were dried at 110°C followed by calcination in a normal atmosphere at various temperatures from 400 to 1000°C for 2h. Crystal structure, thermal decomposition, particle size and morphology of the powder were characterized. The formation of uniform equiaxial shape particles was confirmed by transmission electron microscopy (TEM) study and the growth of the nanostructures with respect to the calcination temperature till 800°C was also reported. The structural and chemical analyzes confirmed the existence of LSCF and $CoFe_2O_4$ phases in the powder.

A mechanical process was used to synthesize $La_{0.6}Sr_{0.4}Co_{0.2}Fe_{0.8}O_3$ (LSCF) perovskite by using a high-speed attrition-type mill [2.62]. The properties of the synthesized powder together with the electrochemical performance of the resultant cathode were studied. The study reports successful synthesis of LSCF perovskite at a short 20 min duration mechanical processing without any external heating. The method was suggested as a simple and energy-saving technique for producing high-quality LSCF particles for application as a solid oxide fuel cell (SOFC) cathode material on the basis of the electrochemical properties of the resultant cathode.

Mimuro *et al* [2.63] obtained Lanthanum strontium cobalt ferrite (LSCF) by the citrate complex method adding oleic acid as a surfactant. The powder was obtained from the precursor by calcining at a low temperature of 500°C. Dynamic laser scattering measurements suggested that precursor exhibited high dispersibility in the solution with an average diameter less than around 20 nm. The crystallite size decreased, and the total specific area increased as the calcination temperature was decreased from 800 to 500. °C. It was found that the oleic acid functioned as a surfactant to form fine homogeneous precursor, and then assisted in the crystallization of LSCF even at a low calcination temperature of 500°C. The study suggested that low-temperature synthesis suppressed the agglomeration and growth of LSCF particles. As a result, fine powders with a

particle size less than 20 nm were synthesized. $La_{0.6}Sr_{0.4}Co_{0.2}Fe_{0.8}O_3$ (LSCF) were synthesized by a combination of citrate and hydrothermal methods [2.64]. As-prepared and calcined powders were studied with different material characterization techniques. LSCF films were applied on gadolinium doped ceria electrolyte substrates (CGO) after sintering at 1200°C. The microstructure and electrochemical performance of the electrodes were studied by scanning electron microscopy and impedance spectroscopy respectively as a function of sintering conditions. An (LSCF/CGO/LSCF) symmetrical cell configuration was used for the electrochemical characterization in the temperature range 650 to 800°C. The area specific resistance (ASR) of the electrode showed a strong relationship with microstructure. The study reported a best electrochemical behavior (0.18 Ωcm^2 at 800°C) with the cathode fabricated with sintering dwell time of 2h. $La_{0.7}Sr_{0.3}Co_{0.5}Fe_{0.5}O_3$ (LSCF) powders were prepared by the solid-state reaction [2.65]. The effect of synthesis parameters (calcination temperature, milling conditions and sintering temperature) on the structural, morphological and electrical properties of LSCF was studied. The thermogravimetric study indicated that the minimum temperature for the carbonate decomposition and formation of perovskite phase is 800°C. A loose and porous structure of the powder materials was revealed from the SEM analysis. The milling parameters such as grinding balls: sample ratio, rotational speed, and milling time were found to influence the structural properties. The study suggested that grinding balls: sample ratio of 8:1, 500 rpm and 4 h of milling as an optimum milling condition to obtain pure LSCF phase. The porosity of the pellets was found to decrease with the increasing sintering temperature from 950 to 1100°C. Electrical conductivities measured at 400-1000°C were correlated with sintering temperature. A combination of citrate and hydrothermal technique of powder synthesis was adapted to synthesize $La_{0.6}Sr_{0.4}Co_{0.2}Fe_{0.8}O_{3-\delta}$ (LSCF) powders [2.66]. Simultaneous TG-DTA was used to study the thermal decomposition behavior of the as-prepared powder. LSCF/CGO/LSCF screen-printed symmetrical cells sintered in the temperature range 1150-1200°C were studied by impedance spectroscopy to assess the cathode kinetics for the oxygen reduction reaction. Rietveld refinement of XRD data indicated the formation of perovskite LSCF phase with a crystallite size of 53 nm at 900°C. The area specific resistance (ASR) measured in the static air was

found to be 0.34 Ωcm^2 at 750°C. The study suggested that the citrate-hydrothermal method as an effective process for the synthesis of cathode materials for SOFC. Surface modification through impregnation with Pr-containing solution into the cathode further enhanced the performance of the cathode with an increase in area specific resistance to 0.17 Wcm^2 at 750°C.

Lanthanum based iron and cobalt-containing perovskite have high electrocatalytic activity at a relatively low operating temperature. Iron and cobalt containing perovskite material has a high potential for a cathode material in intermediate temperature solid oxide fuel cells (IT-SOFCs) (700-800°C). Jin *et al* [2.67] adapted a complex method using carbon black (CB) and an aqueous dispersion of carbon black (AqCB) as inorganic nano-dispersants to synthesize nanocrystalline $La_{0.58}Sr_{0.4}Co_{0.2}Fe_{0.8}O_{3-\delta}$ (LSCF) material. They reported that the surface areas of LSCF powder increased from 25 m^2g^{-1} to 40 m^2g^{-1} when AqCB was used as dispersants. The LSCF cathode prepared with CB and sintered at 800°C showed polarizations of 0.10 Ωcm^2 and 0.28 Ωcm^2 at 700°C and 650°C respectively. On the other hand, the polarizations of LSCF prepared with AqCB were 0.08 Ωcm^2 and 0.13 Ωcm^2 at 700°C and 650°C respectively. The increment in the surface area of AqCB derived LSCF has been attributed to the decrease in cathode polarization resistance and a higher electrocatalytic activity. The study also suggested that the aqueous dispersion of CB has a potential as an inorganic dispersant for the synthesis of nanocrystalline cathode materials in views of enhanced catalytic activity and lowered contamination.

Zhou *et al* [2.68] introduced a simple in situ sol-gel derived carbon templating process to synthesize nano-sized $La_{0.6}Sr_{0.4}Co_{0.2}Fe_{0.8}O_{3-\delta}$ (LSCF) and $La_{0.8}Sr_{0.2}MnO_{3-d}$ (LSM) oxides. They observed the formation of nano-sized LSCF-carbon and LSM-carbon composites first with a grain size of 20-30 nm. Further, after calcination of the obtained composites under air they found nano-sized pure-phase perovskites with the crystalline size of as small as 14 nm. Such a decrease in crystalline size of perovskite via the indirect calcination process was ascribed to the suppressing effect of carbon in the grain growth of perovskite. Furthermore, when the in situ created carbon was applied as a template for pore forming, a highly porous perovskite sintering body packing from the nano-sized perovskite oxide was obtained.

Zhu *et al* [2.69] presented a comparative study of a low-temperature auto-combustion process and an EDTA (ethylene diamine tetra acetic acid)-citrate sol-gel process for the synthesis of $La_{0.6}Sr_{0.4}Co_{0.2}Fe_{0.8}O_{3-\delta}$ (LSCF). The samples were characterized by XRD, SEM, BET, TGA and instant temperature analysis. The iodometric titration was used to determine the average valence of Co and Fe ions and the oxygen nonstoichiometry of the prepared powders. The catalytic properties of the synthesized powders were investigated by the hydrogen peroxide catalytic decomposition. The pure-perovskite structure was formed by both synthesis methods. The oxygen nonstoichiometry of the samples prepared by the auto combustion process is larger than that by the sol-gel process. The catalytic activities of the powders from two synthesis processes also differed largely due to the different oxygen nonstoichiometry, surface area and crystalline sizes.

A modified combustion synthesis using ethylene diamine tetraacetic acid (EDTA)-citrate complexing method with NH_4NO_3 as combustion aid has been used to synthesize $La_{0.6}Sr_{0.4}Co_{0.2}Fe_{0.8}O_{3-\delta}$ (LSCF) perovskite membrane for oxygen separation application [2.70]. It has been reported that the combustion of the gel proceeds results in self-propagating combustion, volumetric combustion or smothering combustion depending on the relative amount of NH_4NO_3 used during the synthesis. The electrical conductivity and oxygen permeation fluxes of LSCF membrane were found to increase with the sintering temperature (1000-1300^{o}C) of the membrane. The LSCF powder prepared from self-propagating combustion showed the highest sintering ability, electrical conductivity, and oxygen permeability among all the three modes of combustion. It has also been reported that the derived membrane exhibited the permeation fluxes comparable to that of LSCF membrane prepared from the normal EDTA-citrate complexing method under optimized conditions.

Normal combined EDTA-citrate complexing method has been modified into an auto combustion process with low ignition temperature using ammonia nitrate as an oxidizer and combustion trigger [2.71]. The properties of the powders derived by this process have been studied as a function of NH_4NO_3/metal ions to organic mole ratios and the heating temperature. NO_3^- to citric acid to EDTA mole ratio of around 10:2:1 has been suggested as the critical amount of NH_4NO_3 for the auto

combustion to occur. The $La_{0.6}Sr_{0.4}Co_{0.2}Fe_{0.8}O_{3-\delta}$ (LSCF) powder synthesized by this optimized condition have well-crystallized nanostructured with a specific surface area as high as 21 m^2/g. The morphology of the derived powder could be tailored to suite different application such as nanograined dense membrane for oxygen separation membrane, and porous cathode for fuel cells and sensors by adjusting the combustion parameters. $La_{0.6}Sr_{0.4}Co_{0.2}Fe_{0.8}O_{3-\delta}$ (LSCF) precursor powder was synthesized by a nitrate-glycine solution combustion method [2.72]. The synthesized LSCF powders have perovskite structure with a specific surface area of 22.9 m^2g^{-1} and an average particle size of 175 nm. The non-isothermal sintering study suggested that the synthesized LSCF powder possessed good low-temperature sintering activity. Ni-YSZ/YSZ/LSCF exhibited a maximum power density of 0.97 Wcm^{-2} at 0.7V under operation at 700°C when the cathode sintered at 800°C for 2 h. The study demonstrated low-temperature processing of the interlayer-free LSCF cathode on YSZ electrolyte. Microwave assisted sol-gel (MWSG) method has been used for the synthesis of nano-crystalline $La_{0.8}Sr_{0.2}Co_{0.5}Fe_{0.5}O_{3\pm\delta}$ powder [2.73]. An irradiating the precursor at 700 W for 3 min was found to form $La_{0.8}Sr_{0.2}Co_{0.5}Fe_{0.5}O_{3\pm\delta}$ perovskite powder. However, well-crystalline $La_{0.8}Sr_{0.2}Co_{0.5}Fe_{0.5}O_{3\pm\delta}$ perovskite powder was obtained at 700 W for 35 min irradiation. Morphological and specific area analysis revealed that the synthesized powder has a surface area of 38.9 m^2/g with the particle size of ~23 nm. Electrochemical properties of pure LSCF cathode on YSZ electrolyte at intermediate temperatures showed a low area specific resistance (0.077 Ωcm^2 at 1073K and 0.672 Ωcm^2 at 953K).The study suggested the MWSG method as an extremely facile, time-saving and energy-efficient process to synthesize LSCF powders.

Pechini-type gel combustion technique was followed for the synthesis of $La_{0.8}Sr_{0.2}Cu_{0.95}Fe_{0.05}O_{2.5-\delta}$ (LSCuF) powder for SOFC application [2.74]. The combustion behavior of the gel as analyzed by a differential scanning calorimetry and thermogravimetry analysis (DSC/TG) revealed the igniting temperature of the gel at 190°C. The derived LSCuF powder has a single phase orthorhombic perovskite structure, with lattice parameters a, b and c of 0.548430, 1.037549 and 0.384504 nm, respectively when heat treated at 900°C. Chemical stability study showed the formation of a secondary phase of $La_{0.75}Sr_{0.25}CuSmO_4$ at 1100°C

When LSCuF was cofired with $Ce_{0.8}Sm_{0.2}O_{1.9}$ (SDC). The electrical conductivity of LSCuF sintered at 1000°C was found to be more than 450 Scm^{-1}. $La_{0.6}Sr_{0.4}Co_{0.4}Fe_{0.6}O_{3-\delta}$ (LSCF) perovskite oxides have been synthesized by modified citrate process [2.75]. The chelation process, phase formation behaviour, the morphology of the derived powder, and oxygen permeability of sintered LSCF oxides were studied as a function of pH of the precursor solution. The chelate processes for pH = 1 and 3 were found different from those for pH = 5, 7, and 9 from the analysis of the FT-IR patterns. The study revealed that the phase formation and morphology of LSCF oxides dependents on the precursors solution pH. Crystallinity and oxygen permeability of LSCF oxide could be tailored by controlling the pH values in this synthesis process. Citric synthesis route and subsequent media agitating milling were adapted to synthesize $La_{0.6}Sr_{0.4}Co_{0.2}Fe_{0.8}O_{3-\delta}$ (LSCF) powder [2.76]. The derived powder particle size reduced to 0.66 and 0.53 μm, on milling for 1.5 and 3 h respectively. The starting particle size, as well as sintering temperature of the LSCF cathode, influenced the cathode performance strongly. The smallest cathode polarization for both 700 and 800°C operations was obtained with a fine powder (0.53 μm) sintered at 850°C and is correlated to the cathode morphology.

Sol-gel derived $La_{0.8}Sr_{0.2}Co_{0.5}Fe_{0.5}O_3$ (LSCF) nanometer powder has been studied for IT-SOFC cathode [2.77]. The authors showed a detailed process through a series of reaction steps. Water from the precursor solution was removed first, then followed citric acid and nitrates decomposition processes and carbonates formation processes. LSCF phase began to form at 500°C. Nitrate ions decomposed completely at 600°C. A single phase of LSCF perovskite was obtained at 800°C. The derived powder has typical mean particle diameters and specific surface are 34.2 nm and 28.2 m^2/g respectively when powders sintered at 800°C for 2 h.

A sol-gel synthesis process has been adopted for the preparation of $La_{0.6}Sr_{0.4}Co_{0.2}Fe_{0.8}O_{3-\delta}$ (LSCF) nanoceramic powders for SOFC cathode application [2.78]. For chelation and dispersion, the researchers have used citric acid and ethylene glycol respectively. Pure crystalline perovskite peaks with broad peak width were observed from the XRD patterns. The SEM revealed particle size of the LSCF powders to be in the range of 50-200 nm. Porosimetry study revealed a

decrease in the surface area from 26 to 3 m^2/g as a result of an increase in the calcination temperature. After 500°C, no weight loss has been seen from the TG analysis confirming complete combustion.

2.1.3.2.2 Studies based on Characterization

The cathode behaviour at temperatures below 600°C has been explained from the classical triple-phase-boundary model as the contribution of mixed conductivity was low. The O_2 reduction reactions on LSM and LSCF electrodes in air with and without the presence of gaseous Cr species has been studied in the temperatures 700 -900°C [2.79]. Surface dissociative adsorption and diffusion, charge transfer, and oxygen ion migration into the zirconia electrolyte phase has been identified as the reaction steps for an O_2 reduction on the LSM electrode. The study suggested that the O_2 reduction reaction is controlled by the dissociative adsorption and diffusion at LSM electrode surface at low temperatures and the oxygen ion migration/diffusion into zirconia electrolyte at high temperatures. The reaction steps on LSCF electrodes have also been identified from the comparison of the electrode behavior of LSM and LSCF in the absence and presence of chromium-forming alloy under identical experimental conditions. The study suggested that that surface and bulk diffusion processes play important roles in the overall reaction kinetics for the O_2 reduction on LSCF electrodes.

$La_{1-x}Sr_xCo_{1-y}Fe_yO_{3-d}$ perovskite materials have been considered as potential cathodes for solid oxide fuel cells operating at intermediate temperatures [2.80]. The effect of temperature, ambient oxygen partial pressure and composition on the extent of oxygen deficiency was electrochemically investigated using solid electrolyte coulometry. It was found that the degree of oxygen non-stoichiometry increases with increasing temperature, decreasing oxygen partial pressure and increasing Sr or Co content. Transient re-equilibration experiments showed that the time needed for re-equilibration increases with increasing oxygen deficiency. The oxygen uptake and release of $La_{1-x}Sr_xCo_{1-y}Fe_yO_{3-\delta}$ (x=0.2, 0.4; y=0, 0.8, 1) perovskite powders was examined with temperature programmed techniques. In addition to the commonly used temperature-programmed reduction (TPR), temperature-programmed oxidation (TPO) was used to examine oxygen adsorption on the perovskites that had previously been partially reduced [2.81]. While perovskite reduction started slowly at an offset temperature of about 300°C,

the re-oxidation already started below 100°C resulting in a distinct re-oxidation peak. The measured oxygen stoichiometry changes were in the range of δ=0.03–0.19. For the re-oxidation process, surface-controlled kinetics was assumed, allowing the application of conventional temperature-programmed desorption (TPD) procedures to determine the activation energy of the adsorption process. Simulation of the peak profiles confirmed the predominant surface kinetics. The determined activation energies were in the range of 0.46–0.63 eV. The study concluded that $La_{0.6}Sr_{0.4}Co_{0.2}Fe_{0.8}O_{3-\delta}$ should be a superior cathode material to $La_{0.8}Sr_{0.2}Co_{0.2}Fe_{0.8}O_{3-\delta}$ or $La_{0.8}Sr_{0.2}FeO_{3-\delta}$.

A-site-deficient LSCF based oxides of the compositions $La_{0.6}Sr_{0.4}Co_{0.2}Fe_{0.8}O_3$ was prepared and characterized. The crystal structure, electrical conductivity and thermal expansion of these oxides were studied using X-ray diffraction, four-point DC and dilatometry, respectively [2.80-2.83]. The electrical conductivity increased with temperature up to about 600°C and then decreased due to the loss of lattice oxygen. The charge compensation mechanism in these A-site-deficient perovskites was attributed to the formation of oxygen vacancies rather than the oxidation.

$(Ln_{0.6}Sr_{0.4})_{0.99}Fe_{0.8}Co_{0.2}O_{3-\delta}$, (Ln=La, Pr, Sm or Gd) has been synthesized and studied using powder XRD, dilatometry, 4-point DC conductivity measurements, and electrochemical impedance spectroscopy [2.84]. XRD revealed that only the La-containing perovskite was hexagonal while the Pr and Sm perovskites were orthorhombic. The gadolinium-based perovskite has a two-phase system consisting of an orthorhombic and a cubic perovskite phase. The thermal expansion coefficient (TEC) increased systematically with a decrease in the size of the A-site cation until the gadolinium-containing perovskite where the TEC decreases abruptly. The total electric conductivity was found to be highest for La-based perovskite and it was lowest for Gd-based perovskite as determined by 4-point DC conductivity measurements. A clear correlation between the size of the A-site cation and the electrochemical performance was revealed, as the area specific resistance (ASR) was the lowest for the compounds with the smallest A-site cation. The change in A-site cation type in Fe-Co based perovskites showed a remarkable influence on the performance of the Fe-Co based cathodes for oxygen reduction. An increase in performance of around two decades is achieved

for the reduction of oxygen by lowering the size of the A-site cation. Best performance is achieved by the composition $(Gd_{0.6}Sr_{0.4})_{0.99}$ $Fe_{0.8}Co_{0.2}O_{3-\delta}$ with an ASR value as low as 0.89 Ω cm^2 at 600 °C measured on a cone-shaped electrode. The effect of thermal treatment on the structure and electrical characteristics of $La_{1-x}Sr_xF_{1-y}Co_yO_3$ (LSCF) electrodes on gadolinia doped ceria (CGO) electrolytes has been investigated [2.85]. Low calcination temperature and short sintering times lead to the formation of a cubic A-site deficient perovskite. Higher calcination temperature and longer sintering time lead to the incorporation of strontium, derived from the decomposition of Strontium carbonate into the perovskite structure, producing a stoichiometric rhombohedral perovskite. Electrodes containing a larger proportion of the stoichiometric perovskite had a higher resistance than those consisting largely of the A-site deficient perovskite.

Lanthanum strontium cobalt iron oxides, with the perovskite structure, were synthesized using citrate and glycine complexation methods. Low-temperature calcination of the precursor phases leads to the formation of cubic perovskites, which on high-temperature calcination transformed to rhombohedral distorted perovskites [2.84]. The cubic phase is identified as a perovskite, with a large degree of strontium deficiency (x = 0.20 to 0.25).The chemical reactivity of perovskite oxide SOFC cathodes and yttria stabilized zirconia (YSZ) solid electrolyte was also studied [2.82].

Ceramics can play a remarkable role in the engineering of intermediate temperature solid oxide fuel cells (IT-SOFCs) capable of meeting the ambitious targets of reduced cost and improved lifetime. Mixed ionic–electronic conductors such as $La_xSr_{1-x}Co_yFe_{1-y}O_{3-d}$ are being used as volumic cathodes to increase the catalytic performance of these components. It has also been reported that microstructure of the electrode plays an important role for optimal performance, particularly at lower operating temperatures. $La_{0.6}Sr_{0.4}Co_{0.2}F_{0.8}O_{3-d}$ films on $Ce_{0.9}Gd_{0.1}O_{2-d}$ substrates were deposited by electrostatic spray deposition (ESD) and characterized [2.55]. Variation of ESD deposition parameters (nozzle-to-substrate distance (15, 30, 43, 45, and 58 mm), solution flow rate (0.34 and 1.5mL/h), and substrate temperature (300, 350, 400 and 450°C)) lead to development of wide variety of microstructures. These include dense to porous, with particular features such as reticulation and micro-porosity. The correlation

between deposition parameters and resulting microstructures was systematically studied and put into evidence.

$La_{0.6}Sr_{0.4}Co_{0.2}Fe_{0.8}O_{3-\delta}$ (LSCF-6428) has been considered as both the anode and cathode in solid oxide fuel cells (SOFCs) operating at intermediate temperatures (550–700°C) [2.86]. The oxygen non-stoichiometry of LSCF-6428 has been measured as a function of temperature and ambient oxygen partial pressure using solid electrolyte coulometry (SEC). The kinetic data relating to oxygen transport in cathodes were correlated with the material oxygen vacancy concentration. The catalytic activity towards methane oxidation, and susceptibility to deactivation through carbon deposition have both been investigated by temperature programmed methods and compared with data for the conventional Ni/YSZ anode material.

The development of high-performance cathodes is a critical issue to reduce solid oxide fuel cells (SOFCs) operation temperature to the 600-800°C range or less [2.87]. CeO_2-based composite cathodes were found very attractive to such operational temperatures. $La_{0.6}Sr_{0.4}Co_{0.2}Fe_{0.8}O_3$ (LSCF) and $Ce_{0.8}Sm_{0.2}O_{1.9}$ (SDC) powders synthesized by different synthesis methods were mechanically mixed to prepare LSCF-SDC composite cathodes. LSCF-SDC/CGO/LSCF-SDC symmetrical cells prepared by screen-printing and sintered at 1150°C for 4 h were characterized by electrochemical impedance spectroscopy in static air. The composite cathodes containing SDC powder synthesized by modified Pechini and microwave-assisted combustion methods were found to show area specific resistance values of 0.72 and 2.77 Ωcm^2 at 800°C, respectively. Lanthanum-based iron- and cobalt-containing perovskite has been studied as cathode material due to its high electrocatalytic activity at a relatively low operating temperature (700-800°C) in SOFCs [2.88]. A complexing method consisting of chelants and inorganic nano dispersants was used for the synthesis of nanocrystalline $La_{0.6}Sr_{0.4}Co_{0.2}Fe_{0.8}O_{3-\delta}$ (LSCF) materials to enhance the electrocatalytic reduction of oxidants. The surface area of the LSCF powder was found to increase from 18 to 88 m^2g^{-1} on the addition of inorganic dispersants in the synthesis process. The observed enhanced electrocatalytic behavior is correlated with the surface areas of the starting electrode powder. The study also demonstrated that the performance of a unit cell of an SOFC with the synthesized

nanocrystalline LSCF powders to increase by 60%, from 0.7 to 1.2 W cm^{-2}. $La_{0.7}Sr_{0.3}Co_{0.5}Fe_{0.5}O_3$ (LSCF) porous materials have been studied extensively for intermediate temperature solid oxide fuel cells (IT-SOFC) cathode [2.89]. The effect of different propellants (urea, glycine, citric acid and sucrose) on the characteristics of LSCF powders syhtesized by combustion method has been reported. The study also includes the influence of the sintering temperature on the porosity, and electrical conductivity of the synthesized LSCF powder. The low weight loss for the sample prepared with glycine observed in TGA profiles of the as-prepared samples is ascribed to the higher combustion temperature. The XRD study revealed characteristic reflections of LSCF perovskite with a trace amount of secondary phases. The crystallite size of the powder was found in the range of 9-20 nm. SEM analysis revealed the loose and porous structure of the powder materials. Densification studies within 950-1100^oC showed a decrease in porosity with increasing sintering temperature. Observed electrical conductivity measured in the temperature range 300-800^oC has been correlated with the densification temperature. $La_{0.8}Sr_{0.2}Co_{0.5}Fe_{0.5}O_{3-\delta}$ (LSCF) nano-powders has been synthesized following a polymer-assisted synthesis method using glucose and acrylamide with metal at pH=8~10 [2.90]. The authors studied LSCF as cathode materials for intermediate temperature solid oxide fuel cells (IT-SOFC). The effect of the ratio of glucose and acrylamide to metal nitrates on the particle size has been studied in detail. The study showed that the particle size of LSCF decreased with the increasing ratio of glucose and acrylamide to metal nitrates. The polarization resistance of the cathode was found to be 0.72 Ωcm^2 and 0.11 Ω cm^2 at 700 and 750^oC, respectively.

Thin $La_{0.8}Sr_{0.2}Co_{0.2}Fe_{0.8}O_{3-\delta}$ (LSCF) membrane was deposited on a porous a-alumina substrate by electrostatic spray deposition (ESD) technique [2.91]. The spray mode was varied from the dripping mode to the cone-jet mode together with increasing applied voltage between the nozzle and the substrate. The morphology of the deposited LSCF membrane was found to be affected by the substrate temperature. The study suggested an optimum substrate temperature of 340^oC, followed by annealing at 1000^oC under O_2 atmosphere for deposition of a crack-free membrane. The ESD, drying, and annealing were repeated to get a rigid, crack-free membrane structure. After three coatings, the LSCF layer was about 3

μm in thickness. These thin films were characterized using SEM, DTA-TGA, XRD and EDX in addition to helium permeation tests, which showed that thin LSCF membranes were pin-hole (or crack) free.

Cotton fibers was used as the micro-bioreactor to synthesise nano-crystalline $Sm_{0.2}Ce_{0.8}O_{1.9}$ (SDC), $Gd_{0.2}Ce_{0.8}O_{1.9}$ (GDC), $La_{0.6}Sr_{0.4}Co_{0.2}Fe_{0.8}O_{3-\delta}$ (LSCF) and NiO (65 wt.%)-GDC powders for solid-oxide fuel cells applications [2.92]. The process was claimed to be a more environmental-friendly process as compared with the conventional glycine-nitrate (GN) combustion method. The small particle size of powders obtained by this process was attributed to the blocking effect of cellulose on suppressing the particle contact during synthesis. The SDC powder synthesized by this process showed a particle size as small as 10 nm, which was sintered to dense electrolytes at 1350°C.

$La_{0.6}Sr_{0.4}Co_{0.2}Fe_{0.8}O_{3-\delta}$ (LSCF) has been studied for the effect of A-site deficiency introduced intentionally into the structure to create additional oxygen vacancies [2.93]. The lattice parameters and oxygen content of $La_{0.6}Sr_{0.4}Co_{0.2}Fe_{0.8}O_{3-\delta}$ gradually increased and decreased with increasing Sr-deficiency suggesting creation of additional oxygen vacancies in the lattice. These additional oxygen vacancies were expected to improve the oxide ionic conductivity and catalytic property for oxygen reduction of the samples. The electrical property of Sr-deficient samples showed p-type semi-conduction regardless of the deficiency, whereas its conductivity was strongly affected by a subtle change in deficiency over a wide range of $P_{O2.}$

$La_{0.6}Sr_{0.4}Co_{0.2}Fe_{0.8}O_{3-\delta}$ perovskite powders have been studied for permeation application by Richardson *et al* [2.94]. The various methods they studied through were solid-state reaction, co-precipitation, drip pyrolysis and citrate gel derived. They reported that use of oxalic acid or aqueous ammonia as a precipitating agent could not be able to produce phase pure powder. Phase pure perovskite powder was produced by the other technique studied. Surface areas ranging from 0.6 to 17.4 m^2 g^{-1} were obtained depending upon the synthesis process. Powder morphology also varied as a function of synthesis technique. The citrate gel product showed large surface area and has been correlated to the convoluted network morphology of the powder obtained. Membranes prepared with citrate derived gel showed oxygen permeation rates in the range 0.1 to 0.3 $\mu molcm^{-2}s^{-1}$

at 1273K. The catalytic behavior of the LSCF tubes towards methane oxidation was favored by combustion reactions, with smaller amounts of partial oxidation and oxidative coupling products.

The electrochemical performance and stability of $La_{0.8}Sr_{0.2}MnO_3$ (LSM) and $La_{0.6}Sr_{0.4}Co_{0.2}Fe_{0.8}O_3$ (LSCF) cathodes in interconnect/cathode/YSZ electrolyte half-cell configuration at 800°C for 500h has been studied [2.95]. Deconvolution of electrochemical impedance spectroscopy (EIS) results has been utilized to study the Ohmic and polarization resistance of the cathodes. The LSM cathode has reported showing much higher resistance than the LSCF electrode even although over the long term thermal treatment the respective cathode resistance either decreases or stays stable. It has been noticed that a dramatic elemental distribution changes influence the electrochemical behaviour of the cathodes during the 500 h thermal treatment. Segregation of Sr away from La and Mn at triple phase boundaries (TPBs) of LSM electrode was observed and correlated with the chromium diffusion from interconnects. On the other hand, Sr and Co-segregation were found dominant for the LSCF cathode. A mechanism governing the fundamental processes at the TPBs are also proposed. LSCF was suggested as a preferred cathode material due to its smaller resistance for the 500h thermal treatment. $La_{1-x}Sr_xCo_{1-y}Fe_yO_{3-\delta}$ perovskites have been studied as cathode materials for solid oxide fuel cells (SOFC). A combination of citrate and hydrothermal methods has been used to for the synthesis of $La_{0.6}Sr_{0.4}Co_{0.2}Fe_{0.8}O_{3-\delta}$ powder [2.64]. Symmetrical cell (LSCF/CGO/LSCF) has been prepared by depositing LSCF films on gadolinium doped ceria substrates (CGO) after sintering at 1200°C. The electrochemical characterization was assessed using the fabricated symmetrical cell in the temperatures range 650 to 800°C. The area specific resistance of the electrode showed a strong dependence on the morphology of the electrode. The study achieved as best electrochemical behavior (0.18 Ωcm^2 at 800°C) with the electrode sintered for 2 h.

$La_{0.6}Sr_{0.4}Co_{0.2}Fe_{0.8}O_{3-\delta}$ (LSCF) as cathode for IT-SOFC has been studied under CO_2/H_2O-containing atmosphere [2.96]. The stability of LSCF against CO_2 and H_2O at high and low temperature was found to be different. LSCF showed an excellent electrochemical performance and high stability against the corrosion of CO_2 and H_2O at 750°C and was correlated to the weak reactivity of LSCF with CO_2. However,

LSCF showed a serious degradation at 600°C under O_2-CO_2 (2.83%)-H_2O(2.64%) atmosphere. The enhanced degradation was attributed to the impeded oxygen activation and oxygen surface diffusion by surface carbonates and formation $SrCO_3$ phases on LSCF surface. LSCF reacts with CO_2 atmosphere to yield $SrCO_3$ phases in 400-680°C under CO_2(5%)-H_2O(2.81%)-He. H_2O was found to aggravate the chemical reaction between CO_2 and LSCF. The study suggested that LSCF cathode is stable under operation with O_2-CO_2(2.83%)-H_2O(2.64%) in 680-800°C, whereas it is unstable below 680°C taking into account of $SrCO_3$ phase formation on LSCF. Moreover, the study also indicated that the degradation of LSCF may be caused by CO_2 and H_2O in air during long-term operation below 680°C.

Screen-printed LSCF/CGO/LSCF symmetrical cells were studied by impedance spectroscopy to assess the cathode kinetics for the oxygen reduction reaction [2.66]. The electrodes were sintered in the temperature ranges 1150-1200°C. The best area specific resistance (ASR) value was found to be 0.34 Ωcm^2 at 750°C, measured in static air. The study suggested that the enhancement of cathode performance by additional surface modification through impregnation with a Pr-containing solution. It showed an ASR value 0.17 Ωcm^2 at 750°C. The activation energy of the PrO_x-impregnated cathode was 83.4 kJ/mol, much lower than 123.8 kJ/mol for barred cathode [2.98]. Electrochemical oxygen reduction behavior of $(La_{0.6}Sr_{0.4})(Co_{1-y}Fe_y)O_{3-\delta}$ (LSCF) on an oxygen excess type Al-doped lanthanum silicate $[La_{10}(Si_{5.8}Al_{0.2})O_{26.9}$ (ALSO)] solid electrolyte was reported. The polarization resistance, R_P was found to depend largely on y. y = 0.2 composition showed a minimum R_P value. The R_P value was found 0.3 Ωcm^2 at 1073K in ambient air [$P(O_2) = 2.1 \times 10^4$ Pa] for y = 0.2. Silver nano-particles have been incorporated into the LSCF particles to improve the performance. Ag-modified LSCF showed R_P 0.08 Ωcm^2 at 1073K. DC polarization study showed a cathodic overpotential of 18 mV at 0.1 Acm^{-2} at 1073K [2.98]. The influence of microstructure, temperature, and pO_2 on the electrochemical behaviour of $La_{0.6}Sr_{0.4}Co_{0.2}Fe_{0.8}O_{3-\delta}$ (LSCF) cathodes has been studied. Electrochemical impedance spectroscopy of symmetric LSCF/CGO/LSCF cells was investigated to study oxygen reduction reaction. The spectroscopic data has been characterized by the presence of three contributions in the high (HF), medium (MF) and low frequency (LF) ranges. The LF response showed the strongest dependence on oxygen partial pressure. The resistance and

capacitance values calculated in this range increased with decreasing pO_2. The resistance associated with the HF response was observed to be constant as a function of p_{O2} while there was a slight dependence found in the MF response. The HF, MF and LF contributions were ascribed to the ionic transfer at the cathode/electrolyte interface, bulk diffusion of oxygen species and oxygen surface exchange. An increasing contribution of oxygen gas-phase diffusion with temperature was suggested at low p_{O2} from the analysis of the LF response. The electrochemical behaviour of $La_{0.6}Sr_{0.4}Co_{1-y}Fe_yO_{3-\delta}$ cathodes with y = 0.2 and 0.8 was studied using impedance spectroscopy in the temperature range 400 and 600°C at OCV in the air [2.99]. The morphology of the cathode (microstructure) and chemical composition of the cathodes were found to have a significant influence on the impedance responses. The cobalt-rich composition with cracked microstructure showed the lowest cathode polarization resistance value 0.6 $\Omega.cm^2$ at 600°C. The enhancement of the cathodic performance is correlated with the increase in cathode surface of the porous film as well as the improvement of both the bulk diffusion and surface exchange phenomena due to increasing cobalt content. The study suggested that the cathode reaction is limited by bulk diffusion and surface exchange. The oxygen nonstoichiometry of $La_{0.6}Sr_{0.4}Co_{1-y}Fe_yO_{3-\delta}$ (LSCF) has been studied as a function of oxygen partial pressure and temperature by thermogravimetry and coulometric titration. LSCF perovskite oxides were classified into two groups based on oxygen non-stoichiometry [2.100]. The cobalt-rich compounds (y=0, 0.2, 0.4) showed a sharp decrease in oxygen content with reducing atmosphere. The iron-rich compounds (y=0.6, 0.8, 1) the oxygen vacancy concentration increased more smoothly as compared to the other. The measurement of the oxygen content of LSCF samples with y=0.5 showed no transitional behaviour. It showed a similar behaviour as for the cobalt-rich compounds. The thermochemical stability of LSCF was little affected by the iron dopant content except for y=1. [2.101]. Crystallization and electrochemical performance of $La_{0.6}Sr_{0.4}Co_{0.2}Fe_{0.8}O_{3-\delta}$ - $Ce_{0.8}Gd_{0.2}O_{1.9}$ (LSCF-CGO) composite thin film has been studied. The thin films were obtained by spray pyrolysis of a single precursor solution followed by annealing at temperatures 500-900°C. It has been reported that the films annealed at 600°C possess a mixture of amorphous and crystalline of fine 5 nm crystallites size. The ratio of crystalline to amorphous

material increases while annealing was performed above 600°C. High-temperature annealing led to a segregation of the films into distinct LSCF and CGO phases and promoted grain growth. The studies on the electrical behaviour of the films showed a dependence on the annealing temperature. The polarization resistance of films with lower annealing temperatures was found to be large as compared to that annealed at temperatures in the low-temperature region (below 400°C). However, in the high-temperature region (above 500°C) the polarization resistance of films with lower annealing temperatures was found to be equal or lower than the polarization resistance of films prepared with higher annealing temperatures. The study suggested that bulk diffusion to be the rate-limiting step in the films prepared with lower annealing temperatures and oxygen dissociation to be the rate-limiting step in the films prepared with higher annealing temperatures.

Electron-blocked alternating current impedance analysis technique was utilized to study the ionic conductivities of $La_{0.54}Sr_{0.44}Co_{0.2}Fe_{0.8}O_{3-\delta}$ and $La_{0.6}Sr_{0.4}Co_{0.2}Fe_{0.8}O_{3-\delta}$ [2.102]. It has been observed that the oxygen ion conductivity of $La_{0.54}Sr_{0.44}Co_{0.2}Fe_{0.8}O_{3-\delta}$ is nearly five times higher than that of $La_{0.6}Sr_{0.4}Co_{0.2}Fe_{0.8}O_{3-\delta}$. The enhanced electrochemical behaviour of $La_{0.54}Sr_{0.44}Co_{0.2}Fe_{0.8}O_{3-\delta}$ is correlated to the extension of the electrochemical reaction region from the interface between the cathode and the electrolyte to the whole surface of the cathode grains. XRD analysis showed that both $La_{0.54}Sr_{0.44}Co_{0.2}Fe_{0.8}O_{3-\delta}$ and $La_{0.6}Sr_{0.4}Co_{0.2}Fe_{0.8}O_{3-\delta}$ reacts with 8YSZ at 850°C. Moreover, $La_{0.54}Sr_{0.44}Co_{0.2}Fe_{0.8}O_{3-\delta}$ showed a faster reaction rate. The thermal expansion study revealed that the two LSCFs have approximate thermal expansion coefficients 14×10^{-6} - 15×10^{-6} K^{-1} from 500°C to 700°C.

The electrochemical behaviour of a $La_{0.8}Sr_{0.2}Co_{0.2}Fe_{0.8}O_{3-\delta}$ (LSCF)on CGO interlayered YSZ electrolyte has been studied in the temperatures zone 600-850°C at oxygen partial pressures ranging from 0.07 to 21 kPa by cyclic voltammetry [2.103]. A reversed hysteresis was observed. A high current was observed in the backward scan than in the forward scan, with increasing oxygen partial pressure and decreasing temperature. The electrochemical redox of B-sites and the associated stoichiometry change in the presence of gaseous oxygen is attributed to the observed hysteresis. The electrochemical performance of LSCF cathode was

studied using voltage-current density curves and impedance spectroscopy at different cell voltages as a function of temperature and cathode gas condition [2.104]. The study indicates that the cell impedance spectroscopy has at least four semicircles among them two are partially dependent on the cathode gas conditions. It has also been reported that the historical effects also played a role in the impedance spectra. With the increase in temperature and as the cathode gas conditions are switched from air to O_2-He mixture, the cell ohmic resistance was found to decrease. Under pure O_2 the cell ohmic resistance was found to be higher than the O_2-He mixture. Interfacial resistances were found to be a significant portion of the total ohmic resistance of the cell ohmic. The ASR of the electrode decreases with the increase in temperature. ASR was also found to increase with as the cathode gas conditions were switched from air to the O_2-He mixture and pure O_2. It has been observed that the peak frequency of the largest semicircle observed at high frequency had a linear dependence on the applied voltage. This behavior is related to the charge transfer that occurs in the high-frequency range. The electrochemical reaction rates are enhanced as more current flows through the cell. Microwave assisted sol-gel (MWSG) method has been used to synthesize $La_{0.8}Sr_{0.2}Co_{0.5}Fe_{0.5}O_{3\pm\delta}$ nano-crystalline powder [2.73]. LSCF/YSZ/LSCF symmetrical cell has been prepared to study the electrochemical behaviour of pure LSCF cathode on YSZ electrolyte at intermediate temperatures using AC impedance analyzer. The study showed a low area specific resistance 0.077 Ωcm^2 at 1073K and 0.672 Ωcm^2 at 953K. The study suggested that MWSG method as a time-saving and energy-efficient route to synthesize LSCF powders. $Ba_{0.5}Sr_{0.5}Co_{0.8}Fe_{0.2}O_{3-\delta}$ (BSCF) and $La_{0.6}Ba_{0.4}Co_{0.2}Fe_{0.8}O_{3-\delta}$ (LBCF) have been synthesized using combined citrate-EDTA method and studied as IT-SOFCs cathode materials [2.105]. The cathode performance of the interfaces between the porous electrode (BSCF or LBCF) and GDC electrolyte was studied in the temperatures range 500-700^oC using AC impedance spectroscopy. The study showed that the cathode performances of the BSCF and LBCF electrodes were sensitive to the powder preparation conditions. The best performance was achieved with the BSCF electrode prepared from the precursor solution with a pH value of 8 showed low polarization resistance. The area specific resistances (ASR) were 1.1, 0.15 and 0.035 Ωcm^2 at 500, 600 and 700^oC, respectively. It has also

been observed that the cathode polarization resistances of the LBCF electrode were slightly higher than that of the BSCF electrode.

Esquirol *et al* [2.106] studied $La_{0.6}Sr_{0.4}Co_{0.2}Fe_{0.8}O_{3-\delta}$ as intermediate-temperature solid oxide fuel cell cathode application. The observed change in cathode behaviour at temperatures around 600°C was interpreted in terms a mixed ionic-electronic conductivity of LSCF at temperatures above around 600°C. The oxygen reduction reaction is correlated to the formation of oxygen vacancies with increasing cathode overpotential.

Zheng *et al* [2.107] have studied the behavior of $La_{0.6}Sr_{0.4}Co_{0.2}Fe_{0.8}O_{3-\delta}$ as oxygen selective membrane. The effect of sintering temperature has been elaborately studied on the basis of its impact on the microstructure, electrical conductivity, phase formation behavior and non-stoichiometry of oxygen. They have shown that the sintering temperature has a negligible effect on oxygen non-stoichiometry and phase structure but has a considerable impact on the conductivity, microstructure and hence on oxygen permeability. The increase in the sintering temperature leads to the growth of the grains and enhancement of the electrical conductivity. They have also shown the grain boundary have much less contribution to the conductivity than that of the bulk materials. The increasing in sintering temperature of the membrane lowers the activation energy of oxygen permeation.

$La_{0.6}Sr_{0.4}Co_{0.2}Fe_{0.8}O_{3-\delta}$ (LSCF), perovskite powder has been investigated for SOFC applications in the operating temperature range of 600-800°C [2.108]. Fine LSCF powder with a surface area of 88 m^2g^{-1}, was printed as cathode onto the electrolyte of an anode supported cell. A comparative study of this in situ sintered LSCF cathode with an LSCF cathode sintered at 780°C was reported. The current density of the in situ sintered SOFC was found to be 0.51 Acm^{-2} at 0.9 V and 730°C, which the authors have seen comparable with sintered SOFC with sintered LSCF. As the conventional ex-situ sintered cathode requires heat treatment process and time consuming they recommended the in situ sinterable nano crystalline LSCF for the fabrication of a cost effective and simple SOFC.

Lu *et al* (2011) tested anode-supported SOFCs in three different cathode environments: stagnant air, flowing air, and flowing oxygen at temperatures from 550°C to 750°C. Electrochemical impedance spectroscopy performed under a

series of operating voltages revealed features that have not been well documented [2.109]. In flowing oxygen, the polarization resistance decreased considerably with the current density. The ohmic-free over-potential of the fuel cell calculated from the polarization resistance and the corresponding current density showed a linear relationship with the logarithm of the current density. An additional arc related to diffusion of molecular oxygen arose in the low-frequency end of the spectrum at high current densities in the air. This arc increased its size as the current density was further increased due to the low oxygen partial pressure at the interface of the cathode and the electrolyte. Optimization of the microstructure of the cathode or employment of a new cathode design that can mitigate the oxygen diffusion problem might enhance cell performance significantly.

LSCF–infiltration of LSCF fabricated GDC cathodes into GDC scaffolds [2.110]. The GDC scaffold firing temperature was found to be important, with the polarization resistance minimized for 1100-1200°C firing. Polarization resistance decreased with increased LSCF loading. A low LSCF infiltrate firing temperature of 800 °C was reported to be important for achieving a nano-scale (~50 nm) LSCF network structures. The polarization resistance was 0.24 Ω cm^2 at an operating temperature of 600°C. These results indicate that controlled firing conditions of the GDC scaffold and the LSCF infiltrate, and thereby their nano/micro-structures, was important for achieving low polarization resistance. Preliminary stability tests at an operating temperature of 650 °C indicated that the cathode polarization resistance was stable over ~300 h.

$La_{1-x}Sr_xM_{1-y}Co_yO_{3-\delta}$, where $x \leq 0.5$ and $y \leq 0.8$ (M is transitional metal = Mn or Fe), perovskite have been synthesized for SOFC cathode application. Combustion synthesis using alanine as fuel is used to synthesize the powder at a relatively low temperature [2.111]. X-ray powder diffraction study indicated 47-96% phase purity of the as-synthesized powder. The powder calcined at 825°C showed the presence of single-phase nanocrystalline perovskite with crystallite size in the range 19-24 nm.

2.1.4 Studies on nano LSCF and nano structured SOFC

Robust Development SOFCs with high efficiency for commercialization requires active cathodes and anodes with high catalytic activity values. The microstructure

should enable the cathode with faster O_2 reduction. This section highlights the contribution of the microstructure to the performance of the SOFC on the basis of nanostructuring.

Nanostructured conducting materials have many more advantages than their coarse counterparts. The studies of Zhang *et al* [2.112-2.113] suggest that nano-structured materials can increase the specific surface area dramatically. Enhanced specific surface area in turn enhances the electrocatalytic reaction at the electrode and hence increases the catalytic activity for oxidant reduction. Nano-structuring of materials also enables them high sintering activity and sufficiently reduce the effective sintering temperature [2.54, 2.114-2.116]

Kim *et al* [2011] used nanostructured $La_{0.6}Sr_{0.4}Co_{0.2}Fe_{0.8}O_{3-\delta}$ (LSCF) as a cathode material in SOFCs at a relatively low temperature (700-800^oC) [2.71]. The use of high surface area (reportedly 88m^2/g) LSCF powder as cathode increases its electrocatalytic activity. The performance of the cell was reported to be increased by 60% from 0.7 to 1.2Wcm^{-2}in terms of power density.

The importance of cathode and cell nanostructuring was thoroughly reviewed in the recent work of Young [2.117]. it also illustrates that the researchers have favored the nanocrystalline materials with a high surface area as cathode materials.

Zhao *et al* [2008] synthesized $Sm_{0.5}Sr_{0.5}CoO_{3-\delta}$ (SSC) nanowires from nanobeads of size less than 50nm [2.118]. They fabricated anode-supported SOFCs with a novel nano-networking out of this SSC cathode and investigated it for intermediate operating temperature (500-600^oC) range. They reported remarkably high performance of the cell: the cell demonstrated a peak power density of 0.44Wcm^{-2} at 500^oC and displayed excelled with cell operating time. The exceptionally high performances were attributed to the nano-structuring of the cell. Cathode grains with nano dimensions exhibits high surface area and porosity, the affording straight path for oxygen ion and electron transportation. Nanostructure also results in high three-phase boundaries and consequently shows higher electrocatalytic reactions.

San Ping Jiang [2012] reviewed the nanostructuring of electrodes in SOFCs. Metal salt solution impregnation or infiltration method eliminates the TEC mismatch and suppresses the detrimental reactions between the electrode and the electrolyte

[2.119]. He has shown some remarkable enhancement of cathode and subsequently cell performances by the use of nanostructured cells.

The approach was aimed at increasing the overall cell performance of the SOFC by promoting the nano-structuring of the cathode layers [2.120]. The idea was to avail abundant surface area (TPBs) by forming a large number of pores with nanometer scale. The nanostructuring of cells facilitates the electrocatalytic processes occurring on the air electrode. The authors aimed at synthesizing the thermally stable mesoporous particles and depositing them as microporous films by screen printing over the electrolyte. They also have suggested the production of nanostructured films of regularly-arranged nano-sized particles of electrocatalytic materials over the dense electrolyte. There was electrochemical characterization for the complete anode (Ni-YSZ) supported SOFC with YSZ electrolyte.

Lai *et al* [2011] discussed the nano-structuring of fuel cells by fabricating functional micro-SOFCs with thin film oxide components [2.121]. Films of $La_{0.6}Sr_{0.4}Co_{0.8}Fe_{0.2}O_{3-\delta}$ (LSCF) were used both as cathode and anode on $Y_{0.08}Zr_{0.92}O_{1.96}$ (YSZ) electrolyte. The electrodes, particularly the anode, reported not to react with the YSZ electrolyte and to show good lattice and microstructural stability with it. The open circuit voltage and peak power density were reported to be 0.18V and 210 Wcm^{-2} respectively at 545^{o}C.

Synthesis, characterization and effect of nanopowders on the powder morphology and microstructure has also been reported in many other studies [2.120]. Nanocrystalline cathode powders have high sintering activity, enhanced electrocatalytic reduction towards oxygen fuel. Moreover, the sintering activity can be modified during powder synthesis by adjusting the levels of additive organics compounds such as fuel and chelating agents [2.116] [2.123 - 2.125].

Nano-crystalline Al_2O_3 powder has been synthesized by a pyrophoric chemical reaction using an ammonia-citric acid route [2.122]. The pH was varied and was shown to be an important morphology controller. Low pH (pH=2,4,6) found to yield flaky powder morphology that was subsequently desegregated by increasing the pH to a higher value (pH=10). The authors attributed the change of morphology of the pH controlled precursor to the sluggish and rapid rate of

decomposition. As prepared powder was amorphous that became crystalline after calcination.

2.2 Motivations & Problem statement

I. There are numerous works on $La_{1-x}Sr_xFeO_{3-\delta}$ (x=0.0-1.0) perovskites (LSCF) as a cathode material for SOFC. The properties of LSCF vary with the substitution of aliovalent cations at A-site [2.24]. Sr- substitution at La-site leads to alter the level of oxygen vacancy in the material and consequently the electrical and electrochemical behaviour of LSF. However, it has been observed that the property of LSF varies from literature to literature. For example in some work [2.23], the conductivity of the member with x=0.5, $La_{0.5}Sr_{0.5}eO_{3-\delta}$, has been reported to be maximum. Whereas, in some others the best candidate on the basis of conductivity was $La_{0.4}Sr_{0.6}FeO_3$ (x=0.6) [2.27] with a maximum conductivity of 109 S cm^{-1}. Consideration of the overall properties leads to choosing $La_{0.3}Sr_{0.7}FeO_{3-\delta}$ as the best candidate for electrode application in some works [2.28] [2.26]. Whereas in some others $La_{0.8}Sr_{0.2}FeO_3$ has been chosen as a potential candidate [2.28, 2.35] [2.26, 2.34]. On the basis of electrical and electrochemical behavior $La_{0.6}Sr_{0.4}FeO_3$ has been used as a promising candidate in few other literature [2.126, 2.11]. *Thus, the conductivity and electrochemical data as a function of Sr substitution level at A-site in LSF perovskite are quite scattered in the literature.*

II. In the mixed conducting (MIEC) $La_{1-x}Sr_xCo_{1-y}Fe_yO_{3-\delta}$ perovskites with Co-rich compositions, particularly $La_{1-x}Sr_xCo_{0.8}Fe_{0.2}O_{3-\delta}$ has shown improved electrical properties [2.36, 2.37, 2.46] . Co-rich compositions also have remarkable low polarization resistance and studied for SOFC cathode at intermediate temperature. For example in some work [2.50] $La_{0.4}Sr_{0.6}Co_{0.8}Fe_{0.2}O_{3-\delta}$ with $La_{0.8}Sr_{0.2}Ga_{0.8}Mg_{0.2}O_{3-\delta}$ (LSGM) electrolyte showed a polarization resistance (R_p) of values 0.067 and 0.035 Ωcm^2 at 600°C and 700°C respectively. The electrocatalytic behavior of $La_{0.6}Sr_{0.4}Co_{0.8}Fe_{0.2}O_{3-\delta}$ with YSZ was shown to be quite impressive [2.39]. A lot of other works with Co-rich B-site composition have reported its high conductivity value at intermediate temperature (500-800°C) [2.41,2.44,2.45,2.48]. Higher Co content in $La_{1-x}Sr_xCo_{1-y}Fe_yO_{3-\delta}$

perovskites, however, deteriorate the mechanical strength of the cell because of the TEC mismatch. $La_{1-x}Sr_xCo_{1-y}Fe_yO_{3-\delta}$ perovskites with Co-rich compositions showed deleterious reactions with Zr based electrolytes. Co-rich LSCF materials are reported to react with YSZ electrolyte at temperature 900°C and above [2.38].

On the basis of change in oxygen stoichiometry Mai et al [2.81] concluded that $La_{0.6}Sr_{0.4}Co_{0.2}Fe_{0.8}O_{3-\delta}$ is superior cathode material as compared to that of Co-rich composition ($La_{0.8}Sr_{0.2}Co_{0.8}Fe_{0.2}O_{3-\delta}$). Many recent works [2.47, 2.52, 2.54, 2.56 -2.60] on cathode materials have reported iron-rich compositions ($La_{0.8}Sr_{0.2}Co_{0.2}Fe_{0.8}O_{3-\delta}$) as a potential candidate for SOFC cathode at intermediate temperature. Moreover, the Fe-rich compositions are thermochemically stable over the Co-rich compositions.

III. Nanostructured conducting materials have been more advantageous than their coarse counterparts. Zhang *et al* [2.112- 2.113] has shown that nanostructured materials can increase the specific surface area dramatically. The enhanced surface area in turn enhances the electrocatalytic reaction at the electrode-electrolyte interface and hence increases the catalytic activity for oxygen reduction. Nano-structuring of materials also enables them high sintering activity and drastically reduce the effective sintering temperature [2.54, 2.114-2.116]. Kim *et al* used nanostructured $La_{0.6}Sr_{0.4}Co_{0.2}Fe_{0.8}O_{3-\delta}$ (LSCF) as a cathode material in SOFCs at a relatively low temperature (700-800°C) [2.88]. The performance of the cell was reported to be increased by 60% from 0.7 to 1.2 Wcm^{-2} in terms of power density. Similar conclusions were outlined by Zhao *et al* [2.118] where, it has been demonstrated an achievement of a peak power density of 0.44 Wcm^{-2} at 500°C. Nanostructure also results in high three-phase boundaries [2.118-2.120] and consequently shows higher electrocatalytic reactions. Some other works also suggests the application of nanostructured components by synthesizing them from advanced powder synthesis techniques [2.120].

Advantages of nanomaterials processing and technology can be used in reducing the sintering temperature of the electrode over the electrolyte, thereby can restrict the detrimental reactions at the electrode-electrolyte interface that leads to the formation of insulating layers.

IV. The literature also covered a wide variety of different synthesis techniques for the preparation of the LSCF perovskites. Solid state [2.53, 2.65], glycine-nitrate [2.54], modified auto combustion [2.3,2.56-2.60, 2.69,2.70,2.72,2.49,2.75,2.76] ,ultrasound assisted synthesis technique [2.61] , high-speed attrition-type milling technique [2.62] , citrate complexion method [2.63], hydrothermal methods [2.64,2.66] , sol-gel derived carbon templating method [2.68] and microwave assisted sol-gel [2.73] to name a few. The literature showed the synthesis technique has a great influence on the powder morphology and hence on the properties of the powder. Combustion synthesis technique has the extra advantage of changing the morphology and sinterability of the powder by the adjustment of the levels of organic compounds such as fuel and chelating agents [2.3,2.56-2.60, 2.69,2.70,2.72,2.49,2.75,2.76]. This technique is simple and cost-effective and has the potential for upscaling. The advantages of combustion synthesis technique can be taken in synthesizing cathode material with high surface area powder.

The summary of the literature suggests optimizing the Sr-substitution label in LSF materials based on electrical and thermochemical stability. The study also includes synthesis and characterization of nano-size iron rich perovskite oxide, $La_{1-x}Sr_xCo_{0.2}Fe_{0.8}O_{3-\delta}$ (LSCF), with the optimized Sr-substitution level at A-site for intermediate temperature SOFC.

Figure 2.1 gives an overview of the research demand of nano LSCF as the cathode material. The plotted data are the year-wise publications in international journals. There is a substantial surge in the publications on the nano LSCF as cathode material for SOFC application. Thus, it provides one motivation to investigate the wide unexplored areas still hindered by it.

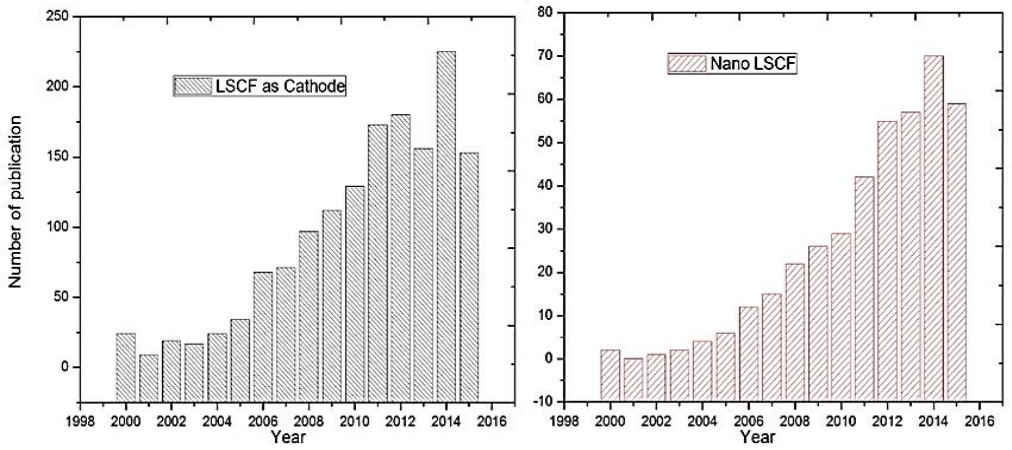

Figure 2.1 A plot of number of publications on LSCF

2.3 Objectives of research

With the motivations as supporting background the broad objectives of the present work are as follows:

- Synthesis of $La_{1-x}Sr_x FeO_3$ powder series with x=0-1.0 following combustion technique and optimization of strontium substitution level based on electrical conduction and thermochemical stability.
- Synthesis of nanoscale Fe-rich $La_{1-x}Sr_xCo_{0.2}Fe_{0.8}O_{3-\delta}$ (LSCF) powder (with optimized Sr-substitution level) by solution combustion method with different morphology and characterization.

The present study on LSCF system include

- Synthesis of LSCF powder of different morphology by varying the process parameters of solution combustion technique.
- LSCF powder characterization on the basis of phase purity, purity from carbon contamination, structure, morphology, thermal stability and chemical compatibility with electrolyte.
- Bulk characterization of LSCF material including sintering kinetics, microstructure, thermal stability, thermal expansion behavior, electrical conductivity
- Synthesis and characterization of SDC and YSZ electrolyte powder and fabrication of electrolyte substrate.
- Studying the electrochemical behavior of the LSCF powder on SDC and YSZ electrolyte as a function of powder morphology, and processing parameter.

Chapter-3

Materials Synthesis & Experimental Works

3.1 Synthesis of Powder Samples

All the powders samples, namely the electrode powders, $La_{1-x}Sr_xFeO_{3-\delta}$(LSF, x=0.1-1.0), $La_{0.6}Sr_{0.4}Co_{0.2}Fe_{0.8}O_{3-\delta}$(LSCF); and the electrolyte powders, 8% Yttria doped Zirconia (YSZ) and Samarium doped Ceria ($Ce_{0.8}Sm_{0.2}O_{2-\delta}$-SDC) have been synthesized by a modified gel combustion synthesis. Combustion synthesis is considered suitable for its many advantages over other traditional methods such as the homogeneity in the particle size, requirement of low calcination temperature, low contamination and high purity etc [3.1].The LSF powder has been synthesized by a conventional combustion synthesis method [3.2,3.3] from the corresponding metal nitrates with citric acid as fuel. For the synthesis of nano powders of LSCF, YSZ and SDC the combustion technique is modified with the consideration of elemental stoichiometric coefficient and addition of extra chelating agent and additional oxidizer.

3.1.1 Synthesis of LSF

The nitrate metal salts of La and Sr were weighed in a molar ratio (1-x) : x and were dissolved in two separate beakers in deionized water (Millipore) to get transparent solutions. These two types of solutions were poured into another beaker containing pre-estimated solution of $Fe(NO_3)_3.9H_2O$ so as to maintain the molar stoichiometry of $La_{1-x}Sr_xFeO_3$. The nitrate solution of these three cations was stirred thoroughly by a magnetic stirrer. Anhydrous Citric acid ($C_6H_8O_7$) was added to the above mixture with a molar ratio of 1:2 with the total metal cations. Now the entire solution was placed over the hot plate and stirred thoroughly with a simultaneous constant heating. After some time the solution started to become viscous and subsequently a gel was formed. Proceeding with time with no supplement of extra heat, the gel started to self-ignite and finally burnt with some black ash as residue. A flow diagram of the whole method has been shown in figure 3.1.

The product obtained in the form of black ash has been ground to fine powder by agate mortar and heat treated in a programmed furnace. Usually powders of the $La_{1-x}Sr_xFeO_{3-\delta}$ series have been heat treated in the temperature range 600^oC to 1000^oC with a moderate heating rate of 3^oC min^{-1} phase purity is achieved.

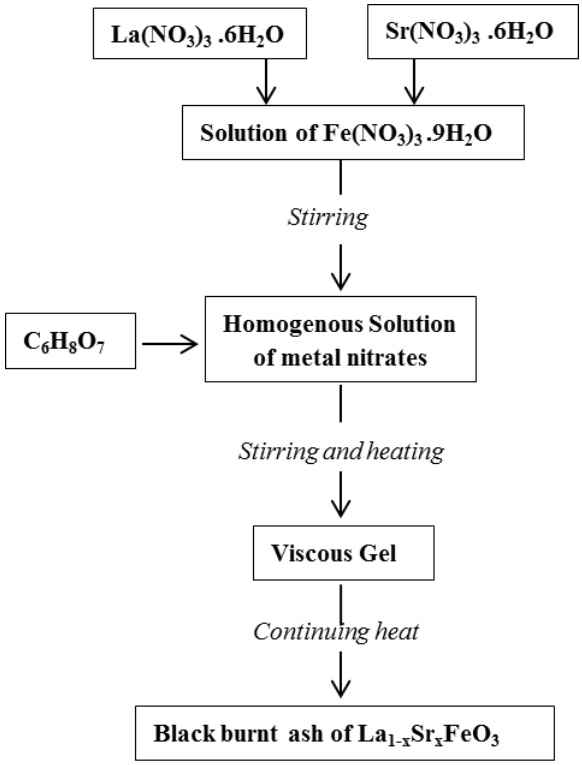

Figure 3.1 Flow diagram showing the formation of $La_{1-x}Sr_xFeO_3$ by a typical combustion technique.

3.1.2 Synthesis of LSCF, YSZ and SDC

The combustion syntheses of LSCF, YSZ and SDC nano powders involve calculated amount of metal salts, fuels and other process parameters such as extra chelating agent and additional oxidizer in the precursors mixture on the basis of the elemental stoichiometric coefficient (ϕ_e) [3.4,3.5]:

$$\phi_e = \frac{\sum(coefficients\ of\ oxidising\ elements\ in\ the\ spefic\ formula \times oxidising\ valence)}{(-)\sum(coefficients\ of\ reducing\ elements\ in\ the\ specific\ formula \times reducing\ valence)} \quad \ldots\ldots (3.1)$$

The specific formulae of each component in the stoichiometric mixture for the synthesis of a molecule say $A_mB_nO_3$, has been calculated as follows [3.6]. Suppose the molecule is obtained from the combustion synthesis of the corresponding metal nitrates $A(NO_3)_3$ and $B(NO_3)_2$ with citric acid ($C_6H_8O_7$) as fuel such that the molar ratio of metal cation to citric acid is, say 1:2. Then the respective specific formula for $A(NO_3)_3$, $B(NO_3)_2$ and $C_6H_8O_7$ are given by

$A_{1\times m}N_{3\times m}O_{9\times m}=A_mN_{3m}O_{9m}$,

$B_{1\times n}N_{2\times n}O_{6\times n}= B_nN_{2n}O_{6n}$ and $C_{6\times 2}H_{8\times 2}O_{7\times 2} =C_{12}H_{16}O_{14}$ ...(3.1(i))

Thus the subscripts in the specific formula denote the molar absolute values by which the elements are involved in the precursor mixture. In our calculation as also has been taken elsewhere [3.6,3.7], O has been taken as positive valence whereas C, H, La, Sr, Co and Fe are taken as negative valences and N as usual has been taken as neutral. The water of crystallization included in the nitrate salts are not taken into consideration as they are not taking part in the chemical reaction.

3.1.2.1 Synthesis of LSCF

Nano LSCF has been synthesized in two different methods of combustion. The first method involves citric acid as fuel and the second involves glycine as fuel. In both cases metal nitrates namely $Fe(NO_3)_3.9H_2O$, $Sr(NO_3)_2$, $Co(NO_3)_2.6H_2O$ and $La(NO_3)_3$ were used as precursor chemicals. Purity of all the chemicals used in this study is greater than 99.5%. $La(NO_3)_3$ and $Sr(NO_3)_2$ were dissolved in deionized water separately in two beakers in a molar ratio 3:2. Pre-estimated solutions of $Fe(NO_3)_3.9H_2O$ and $Co(NO_3)_2.6H_2O$ were poured into a beaker in molar ratio 4:1 followed by the addition of the above salt solutions. The mixture was stirred by a magnetic stirrer constantly.

For citrate method calculated amount of citric acid - anhydrous ($C_6H_8O_7$) was added to the above prepared mixture. Additional chelating agent EDTA ($C_{10}H_{16}N_2O_8$) and/or additional oxidizer ammonium nitrate (NH_4NO_3) were added subsequently for different powder morphology. The pH of the precursor was controlled by the addition of ammonia ($NH_3.H_2O$). The solution was heated with a simultaneous stirring over a hot plate maintained at 90-100^oC temperature. After dehydration, the gel self- ignited to produce the final product as black colored ash.

For glycine method, calculated amount of glycine ($C_2H_5NO_2$) was added to the salt solution. Solutions with metal cation to glycine fuel ratio 1:2, 1:3 and 1:4 were prepared. In this method powders with different morphology were obtained with a starting neutral solution (pH 7). The subsequent other steps are similar to that of citrate method.

A flow chat depicting the methodology has been shown in figure 3.2.The details of the symbols used in the flow chats are listed separately in table-3.1.

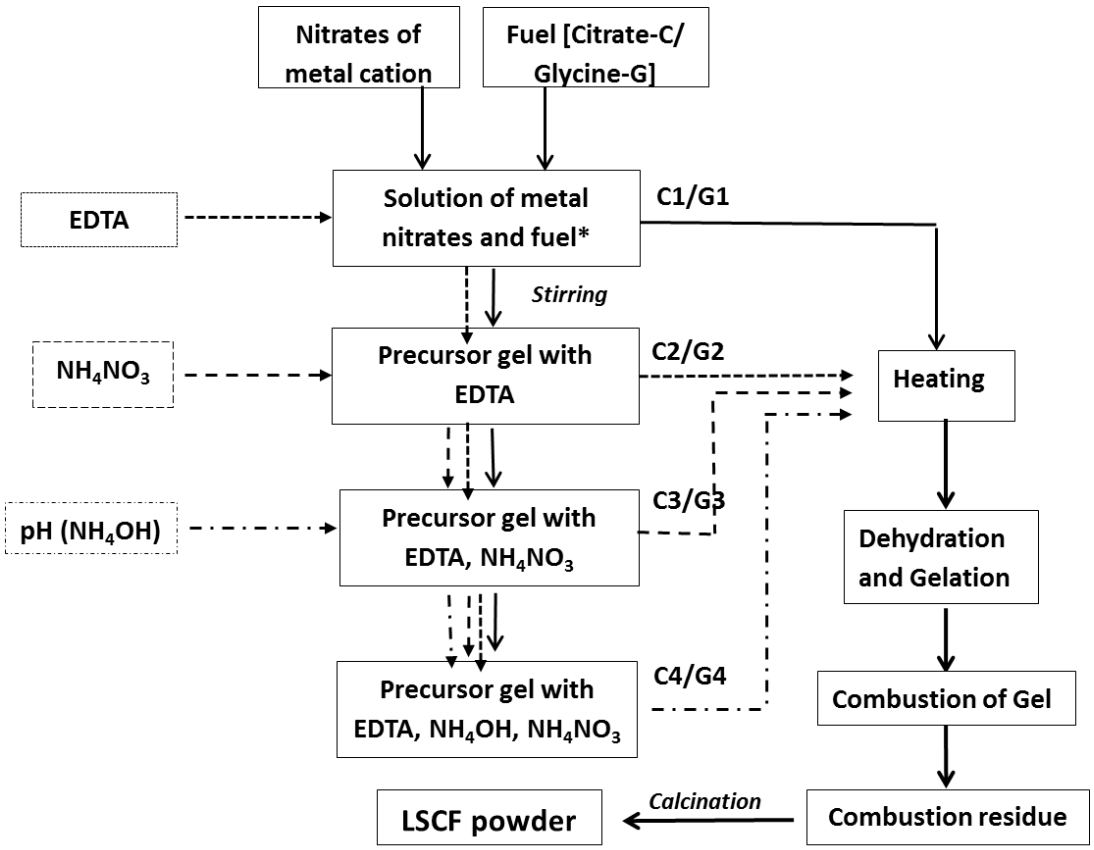

Figure 3.2 Flow diagram showing the formation of $La_{0.6}Sr_{0.4}Co_{0.2}Fe_{0.8}O_{3-\delta}$ by a modified combustion technique using citric acid/glycine as fuel.

* For glycine fuel the initial pH has been kept 7

Table 3.1: Description of symbols used in the flow chats, fig 3.2

Symbol Used	Detail Description	Symbol Used	Detail Description
C1	metal cation : citric acid = 1:2	G1	metal cation : glycine = 1:4, pH 7
C2	C1:EDTA = 1:0.5	G2	G1 :EDTA= 1:0.5
C3	C2 : NH_4NO_3= 1:0.5	G3	G2 : NH_4NO_3= 1:0.5
C4	C3 with pH 9	G4	G3 with pH 9

3.1.2.2 Synthesis of YSZ and SDC

To start with $ZrOCl_2.8H_2O$ was added with HNO_3 and heated to get a transparent solution. Complete removal of chloride was subsequently confirmed by using silver nitrate solution. The solution was cooled to room temperature. In a separate beaker a similar nitrate solution of Y_2O_3 was prepared, for which HNO_3 was added to Y_2O_3, heated with continuous stirring until a transparent solution was obtained.

Both solutions were mixed, with the stirring goes on, citric acid was added followed by $NH_3.H_2O$ so as to make the pH of the solution 8. The precursor solution is now heated with the continuous stirring. As the dehydration process goes on a whitish- grey gel was formed which on further heating leads to burning and YSZ ash was formed. The ash after soft grinding and subsequent heat treatment give rise to YSZ powder. The flow chart of the whole process has been shown in figure 3.4.

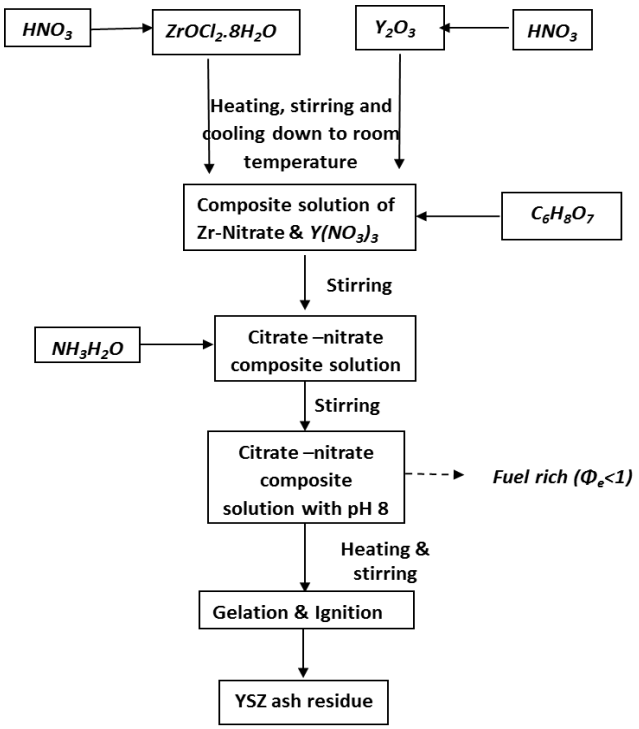

Figure 3.3 Flowchart showing the synthesis of 8% Yttria doped Zirconia by a combustion technique using citric acid as fuel.

Synthesis method of SDC is very similar to that of YSZ the flowchart for which has been given in the figure 3.4. Ammonium ceric nitrate $(NH_4)_2Ce(NO_3)_6$ and $Sm(NO_3)_3$ were mixed in the form of solutions with continuous stirring. Calculated amount of citric acid was added followed by $NH_3.H_2O$ to adjust the pH of the solution to 7. The precursor solution was maintained fuel rich keeping ϕ_e <1. The solution of citrate-nitrate stirred continuously with simultaneous heating. The dried gel subsequently ignited to yield yellowish white powder of $Ce_{0.8}Sm_{0.2}O_{2-\delta}$. As it is prepared the powder is phase pure but to tackle the usual untraceable residual carbon impurities it has again been calcined after crushing.

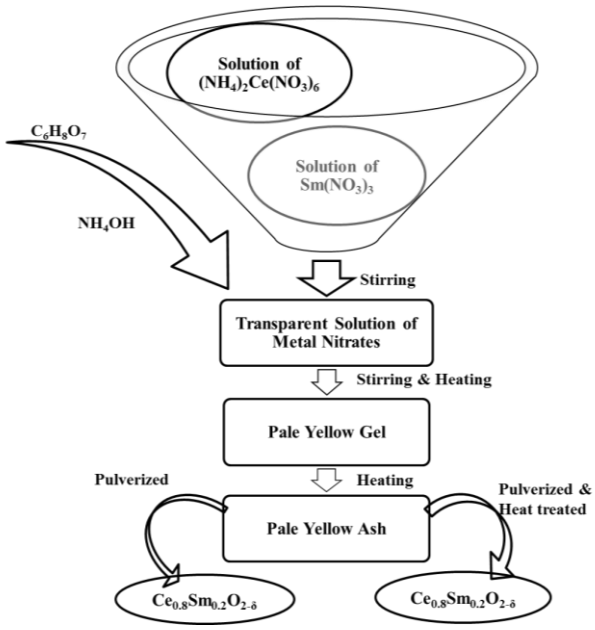

Figure 3.4 Flowchart showing the synthesis of $Ce_{0.8}Sm_{0.2}O_{2-\delta}$ by a combustion technique using citric acid as fuel.

3.2 Characterizations of the precursor gel and the powder

3.2.1 Calorimetry (DSC) of the precursor gel

Differential scanning calorimetry (DSC) has been performed to study the thermal decomposition of the complexes formed during the synthesis of $La_{0.6}Sr_{0.4}Co_{0.2}Fe_{0.8}O_{3-\delta}$ (LSCF). For this, during final stage of the synthesis, for both the methods, dried gels were collected from each of the four different precursors for each of the variations. Similar gels were collected from the second method during the final stage of the synthesis before burning. A pinch ((~10 mg) of this gel was mounted in the sample holder of the instrument. In our study DSC/TG (NETZSCH STA 409C) has been used to record the scans in the temperature range of 25 ^{o}C -800^{o}C at a rate of 10^{o}C min^{-1}.

In DTA (differential thermal analyzer) device the sample is usually exposed to the same heating schedule as that of a reference. For any transformation the sample undergone the instrument detects a change through the reference as to whether it is cooler or hotter than the sample. The change is marked by either an endothermic of exothermic peak [3.8].

3.2.2 General powder characterization

3.2.2.1 Phase formation behavior

The phase formation behavior of the calcined powder has been studied from the X-Ray diffraction patterns, in a x-ray diffractometer (Philips PW-1830 PANalytical, Netherland) using Cu- K_α radiation ($\lambda = 0.15418$ nm) at a scan rate of 0.025 degree per second. For this the powder samples are packed in a sample holder and scanned continuously for about 40 minutes for the range 20^o- 80^o of 2θ. The accelerating voltage and current were maintained at 35 kV and 30 mA respectively.

The XRD pattern of a material is the fingerprint of the periodicity of its atomic arrangement. The incident X-ray beams scatter from each set of the atomic planes at specific angles and interfere constructively to generate a peak for that particular position (angle). The relation is known as Bragg's diffraction condition [3.9]:

$$2d\sin\theta = n\lambda \quad \ldots\ldots\ldots\ldots\ldots \quad (3.2),$$

where d is the inter planer separation, θ is the angle of diffraction/incident, n is the order of diffraction and λ is the wavelength of radiation.

The phase analysis for each sample was carried out by the help of X'Pert HighScore Plus software, basically, by comparing the peak intensity and position of the given data file with the known JCPDS files.

3.2.2.2 Crystal structure and crystallite size

The crystal structure of the phase pure powder samples YSZ, SDC and LSCF has been refined by Rietveld analysis by the computer program Fullprof_Suite (version 2006). The software uses a least square minimization technique for the refinement of the complete structure that includes the atomic position, occupancy and lattice parameters. For the refinement the powder samples were scanned in a step scan mode with each step size being 0.2^o min^{-1} and the XRD data was collected for the 2θ range of 20-80^o. For the background refinement a six coefficient polynomial function was used. With Brag-Brentano diffraction geometry both the instrumental and sample intrinsic profiles were described by a

pseudo-Voigt profile function (the convolution of Lorentzian and Gaussian components).

For YSZ and SDC samples cubic symmetry with space group Fm-3m was assumed. It was further assumed that Y atoms in YSZ and Sm atoms in SDC randomly occupy the Zr and Ce sites subject to the stoichiometry of the composition.

The crystallite size of the powder particles has been calculated either by using Williamson-Hall equation (for refined data) (3.3) or from Scherrer formula (3.4) [3.9]:

$$\frac{1}{\tau} + \frac{2\epsilon sin\theta}{\kappa\lambda} = \frac{\beta cos\theta}{\kappa\lambda} \qquad \text{..... (3.3)}$$

$$\tau = \frac{\kappa\lambda}{\beta cos\theta} \qquad \text{..... (3.4)}$$

Where τ is the crystallite size, κ is the shape factor (usually has value 0.9), λ is the wavelength of X-ray, β is the full width at half maxima, θ is the angle of diffraction (for Scherrer formula it is the position of the most intense peak) and ε is the lattice strain.

3.2.2.3 Fourier Transform Infra-red Spectroscopy (FTIR)

FTIR has been carried out for all the LSCF, YSZ and SDC samples to check their purity from carbonous contamination which is very common for combustion synthesis. For this characterization a pinch of the powder samples was mixed with analytical grade of KBr and was pressed into a thin pellet. This pellet was scanned by the spectrometer (Perkin Elmer FTIR Spectrophotometer) to obtain spectra over the wavenumber range 4000cm^{-1}-400cm^{-1}. The resolution of the spectrometer being kept 4cm^{-1}.

FTIR technique is used basically to determine the different functional groups present in organic molecules. The stretching and bending of bonds due to the IR incident radiation appears as discrete emission or absorption spectra as the bond energy for a given molecule is quantized.

3.2.2.4 BET Surface area analysis

The specific surface area of the phase pure LSCF, YSZ and SDC powder has been determined by a multi-point BET (Brunauer, Emmet and Teller) surface area

technique. A few mg of the powder samples was kept in an oven to keep it dry and moisture free. It was degased at low temperature (200-300^{o}C) and measurements were taken in a multi-point BET surface area analyzer (Quantachrome, Autosorb-1). The analyzer uses a low temperature Nitrogen adsorption technique in which the adsorbate (nitrogen) forms a monolayer over the particle surface. The surface area was calculated considering the weight of gas adsorbed at a particular relative pressure.

The equivalent particle size can be calculated by assuming the spherical shapes of particles from the following formula.

$$d_{BET} = \frac{6}{\rho \sigma_v} \qquad \text{..... (3.6),}$$

where, d_{BET} is the equivalent particle size/diameter, ρ is the material density and σ_v is the specific surface area (surface area per unit mass).

3.2.2.5 Electron Microscopy (SEM and FESEM)

The microstructures of the powder samples LSCF, SDC and YSZ have been investigated with a field emission scanning electron microscope (Nova Nanosem 450). In order to avoid presence of external impurities such as dust particles and other contaminations the sample was prepared with extra care. A few of the powder samples was dispersed thoroughly in a non-aqueous medium such as acetone by ultrasonication. A drop of the dispersed powder then was transferred to the surface of a pre-cleaned glass slide and dried under IR lamp to get a thin layer of deposition. As the samples are insulating in order to avoid space charge formation the slide was coated with platinum by a sputter coater.

In a scanning electron microscope high energy electron beams are incident on the sample surface that scans it line by line. The resolution and intensity of the beam and hence the image quality is controlled by adjusting various parameters such as incident angle, generator voltage and current.

3.2.2.6 Particle size distribution by image analysis

The particle size of the nano powder has been measured by the use of a computer program Image-J. The particle size distribution histogram (size~ frequency) was generated by quantitative image analysis techniques. For this the selected image was processed by filtering (applying FTT bandpass filter) and was threshold. The

circularity factor for all the samples was kept in the range 0.6-1.0 for all samples except for those which are cubic (such as YSZ). The area distribution was converted into size (diameter) distribution and plotted in as a histogram in the program Origin (Origin Pro 8).

3.3 Preparation of Bulk samples

To study the bulk properties of the materials bulk samples were prepared in the form of disc shaped pellets and rectangular bars according to the requirement. For this all the powder samples have been added with a liquid binder (3 wt. % PVA) and ground to uniform mixture by a mortar. The dried powders were molded by a programed pellet press (CARVER) by means of a die punch. For YSZ and SDC discs were obtained from a die punch of dimension16mm diameter by applying a uniaxial pressing of 4 MPa and rectangular bars of 15 mm x 5 mm x 4 mm by applying the same pressure with a dwell time of 90s. Similar rectangular bars were obtained for all the LSF and LSCF samples. The green pellets and bars were sintered in the in the temperature range of 1100-1300^{o}C for the electrode samples (LSF and LSCF) and in the range of 1450-1600^{o}C for the electrolyte (YSZ and SDC) samples for different soaking times. A constant heating rate of 3^{o}C min^{-1} has been maintained throughout for all the samples except for a dwell time of 30-60mins at 650^{o}C for the removal of binder.

3.4 Characterization of Bulk samples

3.4.1. Measurement of bulk density

The density of all the bulk samples (ρ_{bulk}) has been calculated by Archimedes principle in kerosene medium from the following formula:

$$\rho_{bulk} = \frac{\rho_{liq} W_{dry}}{(W_{soak} - W_{susp})} \quad \text{..... (3.7),}$$

where ρ_{liq}, W_{dry}, W_{soak} and W_{susp} are the density of the liquid medium (here it is kerosene), dry weight, soaked weight and suspended weight of the bulk sample respectively.

The theoretical density (ρ_{th}) has been determined by the formula [3.10] below:

$$\rho_{th} = \frac{\sum_i n_i A_i}{NV} \quad \text{..... (3.8),}$$

where, n is the number of atoms per unit cell, A is the atomic weight of the corresponding atom, N being the Avogadro's number and V, the unit cell volume as determined from the XRD by using the lattice parameters.

3.4.2 Densification and Thermal expansion behavior

The densification behavior of the materials has been studied by a Dilatometer (NETZSCH DL 402 C). The samples with a linear dimension (fraction of a rectangular bar samples prepared above) were heated in air atmosphere with different heating rates 5°C-15°C min^{-1} to a temperature of 1000°C.

The thermal expansion coefficient of the sintered bars has been obtained from the dilatometer study by running the samples in the temperature range 30°C to 800°C in air at the rate of 10°C min^{-1}.

In a dilatometer the specimen is placed in contact with a spring-loaded push rod and the other end is butted to the wall of the casing [3.8]. The push rod therefore senses the linear expansion or contraction and the fraction (change in length per original length) can be plotted with temperature. By taking the slope of the trace, the instrument determines expansion coefficient.

3.4.3 Morphology and Microstructure

The microstructures of the sintered samples have been studied under a scanning electron microscope (SEM- JEOL JSM-6480LV l). For the surface topology the pellets and bars were polished by graded SiC papers and were thermally etched after a thorough cleaning in an ultrasonic bath. As described in section 3.2.2.5, the sample surfaces were made conducting. The samples were scanned with different magnification while the instrument was maintained at 15 kV.
Similar image analysis has been carried out by the Image-J software for the grain size determination and distribution, as has been described in section 3.2.2.6.

3.4.4 DC electrical conductivity

The DC electrical conductivity of the electrode samples LSF and LSCF has been measured with temperature by a DC four probe technique in the range 30°C to 900°C in air atmosphere. Four equidistant grooves were carved out on the bar samples used for the measurement by a diamond file and were silver pasted for good electronic contact. The self-assembled experimental set up used for it

consists of a furnace with a sample holder in the form of a horizontal cylindrical alumina tube with four platinum wire leads. Two of these leads are connected to a constant power supply and the other ends to the outer grooves of the sample in the furnace.

A digital multimeter (Agilent 34970A) interfaced with the furnace records the instantaneous resistance with temperature. The detail of the set up with a sample mounted on it has been shown in the figure 3.6. The dc conductivity (σ) was calculated from the recorded resistance values by the following formula:

$$\sigma = \frac{L}{AR} \qquad \text{..... (3.8)}$$

where, A is the cross-sectional area, L is the distance between the voltage leads, and R is the resistance.

In four probe method a constant current is supplied to the material across its length. The voltage drop is measured from any two of the points over it. This variable voltage predicts the conductivity as per the formula 3.8.

3.4.5 AC Impedance spectra of Electrolyte material

The ac impedance of the electrolyte materials YSZ and SDC has been measured in open circuit conditions in air. The AC electrochemical impedance of the symmetrical cells were measured in the temperature range 650-850°C using an impedance/gain phase analyzer (Solartron SI 1260) coupled with electrochemical interface (Solartron SI 1287) with excitation potentials of 10 mV over a frequency range 0.1-100 kHz..

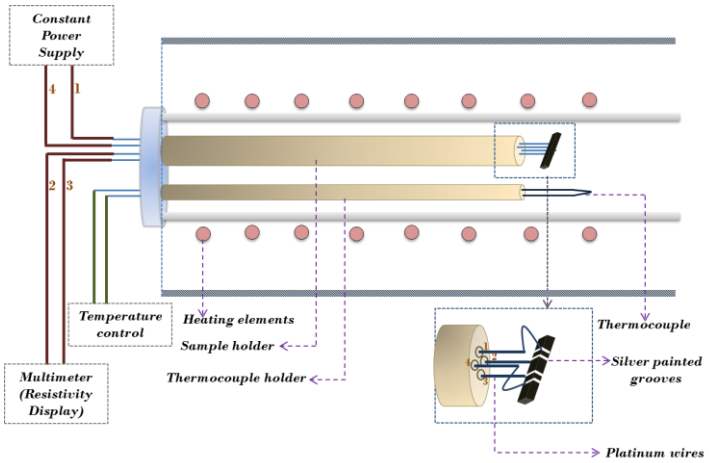

Figure 3.5 Schematic diagram for a four probe DC conductivity set up with a rectangular bar specimen mounted on.

Sintered circular discs were polished, thoroughly cleaned and both sides were painted with silver paste. The pellet with silver electrode paste was dried 550°C for 30mins

3.5 Fabrication of symmetric cell

3.5.1 Preparation of YSZ and SDC electrolyte substrate

The YSZ and SDC substrates have been prepared from the corresponding nano powder synthesized by the above mentioned way (section 3.1.2.2). For YSZ the prepared green circular discs were sintered in two stages: In the first stage it was sintered at 1000°C for 2h and was ground by SiC paper to make it as thin as 0.5mm, in the second stage it was sintered again at 1550°C for 4h to achieve a final thickness of 0.3-0.4mm. The sintered thin substrates were again polished and washed thoroughly by ultra sonication before use.

3.5.2 Preparation of electrode and buffer layer inks

First of all a composite organic vehicle was prepared [3.11] out of Isopropyl alcohol (IPA) (Merck), Polyethylene glycol (PEG)-400 (Qualigens) and glycerol (Merck) by mixing them thoroughly. PEG acts as binder in the mixed solvent of Isopropyl alcohol and glycerol.

For buffer layer SDC ink, SDC powder was added to the vehicle in a weight proportion of 4:6 and thoroughly ground by a planetary ball mill for 1h.

For electrode ink, LSCF powder was added to the vehicle with the similar proportion and thoroughly mixed by the planetary ball mill for 1 h.

3.5.3 Cell fabrication

SDC paste was painted on either side of YSZ electrolyte and kept in the drier for 2 h. Then the other side was painted, kept in the drier for 2 h and then sintered at 1400°C for 4 h. The electrode (LSCF) pastes were then screen-printed symmetrically on both sides of SDC buffer layered YSZ electrolyte and sintered at 1000°C for 2 h. For half cells the printing is limited to one side only. The electrode thickness was approximately in the range of 20-30 µm. Silver paste was painted on the electrodes and fired at 550°C for 1 h for electroding purpose.

3.6 Characterization of symmetric cell

3.6.1 Electron microscopy of the half cell

The surface of the half cells so produced has been coated with platinum by sputter coater and scanned to obtain the microstructural image. The images were later used by the Image-j programme to determine the porosity.

3.6.2 Electrochemical characterization

Symmetrical electrochemical cells consisting of porous LSCF electrodes and dense YSZ electrolyte with a SDC buffer layer (on both side of the electrolyte) were fabricated to test the electrochemical characteristics. The impedance of the cathode in symmetric cell was measured in open circuit conditions in two electrode configuration under air. The AC electrochemical impedance of the symmetrical cells were measured in the temperature range 650-800^{o}C using an impedance/gain phase analyzer (Solartron SI 1260) coupled with electrochemical interface (Solartron SI 1287) with excitation potentials of 10 mV over a frequency range 0.1-100 kHz. Fig. 3.7 represents schematic diagram illustrating AC impedance measurement.

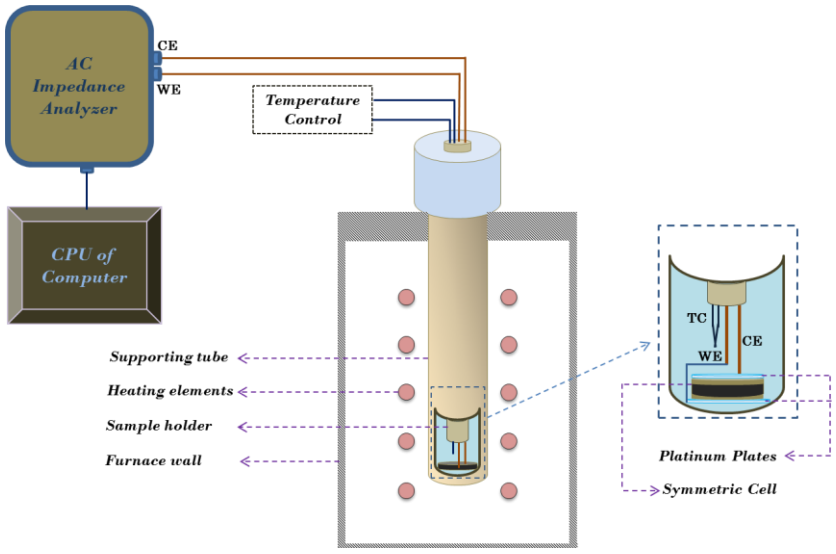

Figure 3.6 Schematic diagram for AC Impedance measurement set up with a symmetric cell mounted on.

Chapter-4

Results and Discussion

4.1 Synthesis and Characterization of $La_{1-x}Sr_x FeO_{3-\delta}$

The optimization of A-site in $La_{1-x}Sr_xFeO_3$ perovskite requires a thorough study of its phase formation behavior and characterizations related to its structure thermochemical and electrical response. Thus $La_{1-x}Sr_xFeO_3$ (LSF; x= 0.0-1.0) series of compounds has been synthesized following combustion synthesis technique and is followed by some characterization in this section. The detail flow diagram has been given in Chapter 3 (Fig. 3.1). The detail of the characterization techniques has been given in chapter 3 also. The observations and important inferences drawn from the powder and the sintered pellets were discussed below.

4.1.1 Thermal decomposition behavior of the precursor gel

Thermal decomposition behavior of the citrate-nitrate gel precursor has been shown in Fig.4.1.1.

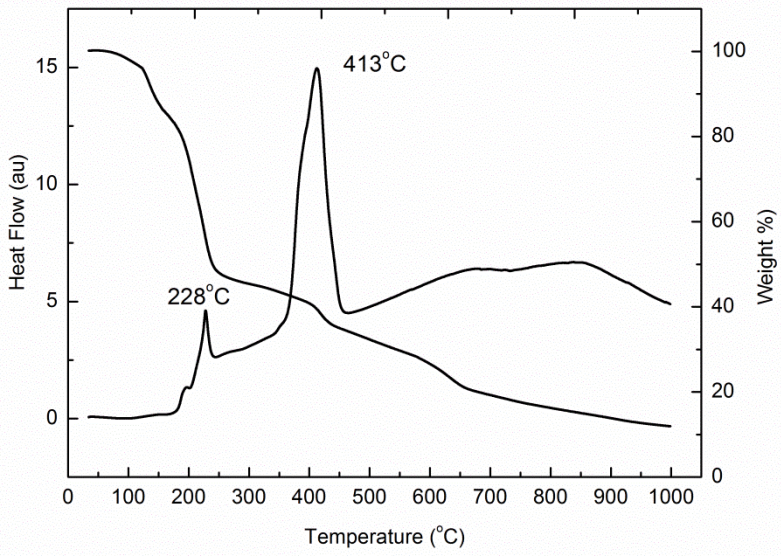

Fig. 4.1.1. DSC-TG of LSF precursor gel

DSC curve of the gel showed one small endothermic peak at 179°C as well as two exothermic peaks at 228°C, and 413°C respectively. The small endothermic peak at 179°C is due to combined effect of charring of the gel as well as the loss of hydrated water [4.1]. The exothermic peak at 228°C may be attributed to the decomposition/oxidation of the metal-citrate-nitrate chelates. The strong exothermic peak at 413°C indicates the pyrolysis of metal nitrate – citrate complexes. The calculated heat evolved during this stage is 6234 Jgm^{-1}. The TG curve also showed a maximum weight loss (80.2%) in two well-separated steps in

the temperature zone (150-450°C). The study thus confirms that the decomposition and combustion of the metal nitrate – citrate - EDTA complex took place in two stages. However, it can be seen that there is a gradual weight loss in the temperature zone 600-850°C. This weight loss is attributed to the removal of carbonaceous bi-products (residue) formed during the combustion process.

4.1.2. Phase evolution of LSF powder

The phase evolution of LSF powder has been studied from the XRD patterns collected as a function of calcination temperature (800-1000°C at an interval of 100°C). The XRD patterns of LSF (with x= 0.4) powder as a function of calcination temperature is shown in Fig.4.1.2.

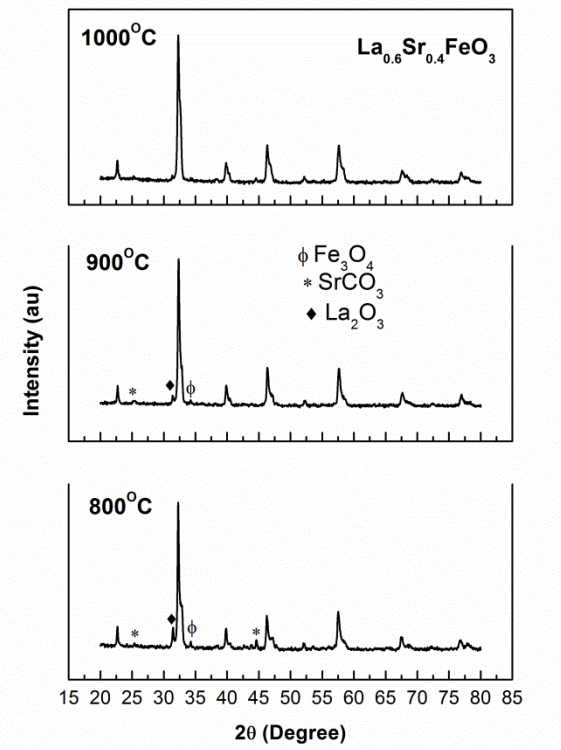

Fig.4.1.2 XRD patterns of $La_{0.6}Sr_{0.4}FeO_3$ powder as a function of calcination temperature

The phases identified in the samples calcined at 800°C are identified to be associated with impurity phases like Fe_3O_4, $SrCO_3$, La_2O_3 along with desired LSF phase. The intensity of the impurity phases was observed to decrease with the increase in calcination temperature. The formation of LSF perovskite phase even in the low-temperature calcined powder (800°C) is attributed the exothermic nature of the pyrolysis reaction of metal nitrate citrate complex. The heat evolved

during this pyrolysis stage is 6234 Jgm^{-1} (as measured from DSC study) helps the formation of perovskite LSF phase during the combustion stage itself. The formation of LSF from citrate-nitrate precursor follows the chemical reaction as provided below [4.2]. The combustion reaction involves the evolution of by-product of gasses such as CO_2, N_2, O_2, and H_2O.

$$(1-x)La(NO_3)_3 + xSr(NO_3)_3.6H_2O + Fe(NO_3)_3.9H_2O + C_6H_8O_7 \rightarrow La_{1-x}Sr_xFeO_3 + 6CO_2 + 19H_2O + 3N_2 + 7/2\,O_2 \quad \ldots\ldots\ldots\ldots\ldots\ldots (4.1.1)$$

The formation of impurity phases like Fe_3O_4, $SrCO_3$, La_2O_3 indicates that the phase formation involves the formation of intermediate phases. At a high calcination temperature, the intermediate phases dissociate/disappear. Phase pure LSF perovskite is obtained at 1000°C having a well-indexed perovskite structure with a lattice parameter of 4.74Å, which is in good agreement with the literature [4.3]. The samples prepared in the $La_{1-x}Sr_xFeO_3$ (x= 0.0-1.0) series showed the similar observation.

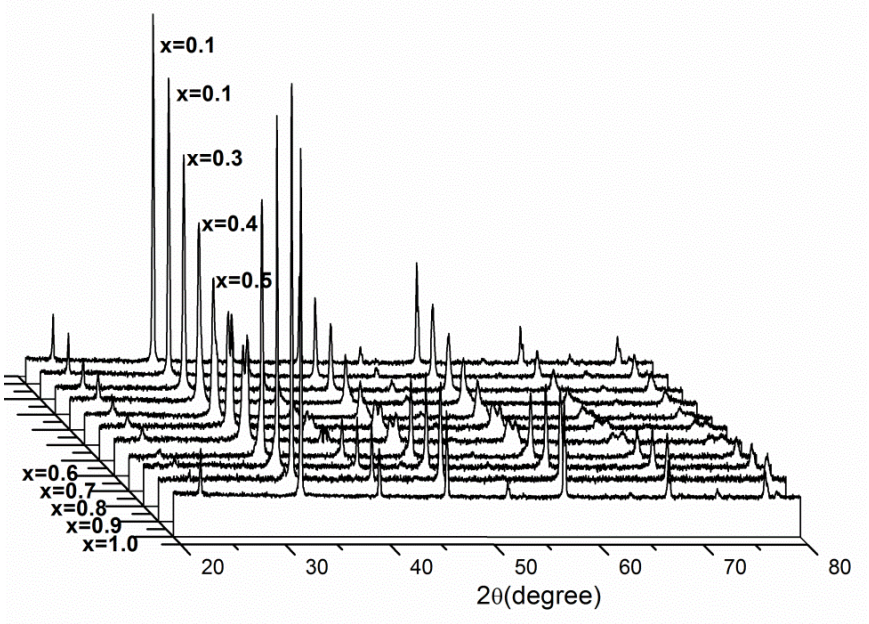

Fig. 4.1.3 XRD patterns of $La_{1-x}Sr_xFeO_3$ powder calcined at 1000°C

XRD pattern of the 1000°C calcined powder of the $La_{1-x}Sr_xFeO_3$ (x= 0.0-1.0) series is shown in Fig.4.1.3. It could be seen from the figure that all powder patterns show distinct peaks indicating high crystallinity of $La_{1-x}Sr_xFeO_3$ powder. Thus, the powder prepared were crystalline and phase pure when the combustion residue

was calcined at 1000°C for 4 hours. Phases identified at room temperature with increasing strontium content in $La_{1-x}Sr_xFeO_3$ are displayed in Table 4.1.1. The phase is cubic (space group **Pm-3 m**) for $LaFeO_3$. For x = 0.1–0.3, the XRD patterns are refined using an orthorhombic phase in the space group **Pnma**. A rhombohedral phase (space group **R-3c**) is observed for x = 0.4–0.9. A phase transition to cubic (**Pm-3 m**) occurs when x = 1.0. The observed structural changes seem to follow Roth's rules [4.4]. Perovskite ceramics with large A-site and small B-site ions in $A^{3+}B^{3+}O_3$ configuration have stable rhombohedral symmetry.

The unit cell volumes of these samples were calculated from the XRD data and are illustrated in Table 4.1.1. The pseudo-cubic lattice constant calculated on the basis of the cube root of unit cell volume per ABO_3 has also been included in the figure 4.1.4.

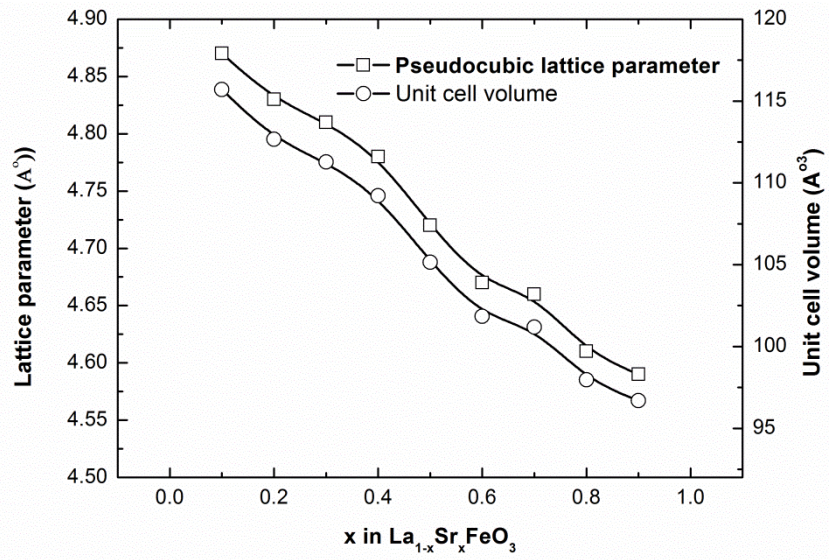

Fig. 4.1.4 Lattice parameter and unit cell volume of $La_{1-x}Sr_xFeO_3$ powder as a function of x

It is worthy to note that the crystal structure gradually changes from cubic to orthorhombic to rhombohedral and then to cubic with increasing Sr substitution at A site. This behavior is similar to that observed for the $LaFeO_3$-$SrFeO_3$ system [4.5]. It could be seen from the Figure that the unit cell volume and hence the pseudo-cubic lattice parameter decreases with increasing Sr content. Thus, the replacement of La^{3+} by Sr^{2+} leads to lattice contraction. The substitution of La^{3+} ($r_{CN:12}$ = 1.36 Å) by Sr^{2+} ($r_{CN:12}$= 1.44 Å) [4.6] in $La_{1-x}Sr_xFeO_3$ increased the averaged radius of A-site ions and caused a charge imbalance. Some trivalent B-site ions

oxidized to form B^{4+} to maintain electrical neutrality, which resulted in a net decrease in the average radius of the B ions. This effect also leads to an increased covalency between the iron and oxygen ions. Also, according to Pauling's rules for bond strength [4.7] the tetravalent Fe ions will strengthen B-O bonds in the BO_6 building block of the perovskite lattice. The bond length of Fe–O decreases due to the formation of Fe^{4+} ions [4.8]. As a result, both the size of the BO_6 octahedra and the dimensions of the ABO_3 unit cell decrease with increasing Sr content. As a result the volume of the unit cell decreases.

Table 4.1.1 Variation of lattice parameter and unit cell volume

Sample (x)	Lattice parameter a (in Å)	Unit cell volume V ($\times 10^{-3}$nm^3)	Crystal symmetry (space group)
0	3.94	61.16	Cubic (Pm-3m)
0.1	4.87	115.71	Orthorhombic (Pnma)
0.2	4.83	112.67	Orthorhombic (Pnma)
0.3	4.81	111.28	Orthorhombic (Pnma)
0.4	4.78	354.12	Rhombohedral (R-3c)
0.5	4.72	109.22	Rhombohedral (R-3c)
0.6	4.67	101.85	Rhombohedral (R-3c)
0.7	4.66	101.19	Rhombohedral (R-3c)
0.8	4.61	97.97	Rhombohedral (R-3c)
0.9	4.59	96.7	Rhombohedral (R-3c)
1	4.12	69.93	Cubic (Pm-3m)

4.1.3. Thermogravimetric analysis (TG) analysis

The weight loss behavior of $La_{1-x}Sr_xFeO_3$ (x = 0.2 and 0.6) while heating up in the air has been shown in Fig.4.1.5. The weight loss was found to increase with an increase in Sr^{+2} content at A-site. In perovskite oxides, the most stable oxidation state of B-site cations is +3, and the oxide achieves high stabilization energy when tolerance factor is around 1 [4.9]. The XRD study discussed above showed that a small decrease in pseudocubic lattice parameter with an increase in Sr^{+2} content at A-site. The decrease in lattice parameter has been attributed to the decrease in average metal–oxygen bond distance. The decrease in the bond distance in turns increase the electron density around the B-site cations resulted in an increase in average oxidation state of the B-site cations. Higher valence state B-site cations are more prone towards thermal reduction at high temperature as compared to their lower valence counterpart.

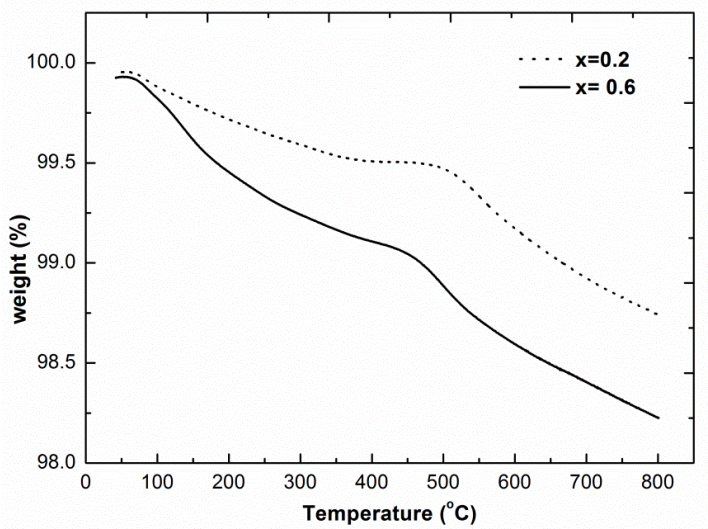

Fig. 4.1.5 Thermogravimetry of $La_{1-x}Sr_xFeO_3$ powder samples as a function of x

At moderate temperature range (usually 200-600°C), the oxygen desorption usually associates with the reduction of high valence state Fe^{+4} to $Fe^{+3.}$ Thus, Sr^{+2} enriched A-site $La_{1-x}Sr_xFeO_3$ samples showed higher weight loss due to the presence of more fractions of B-site cations at higher oxidation state.

4.1.4. Thermal Expansion Behavior

The thermal expansion behavior of $La_{1-x}Sr_xFeO_3$ as a function of temperature measured under air atmosphere has been shown in Fig.4.1.6. The thermal expansion curves showed a nonlinear expansion behavior in the temperatures ranges 500 to 800°C irrespective of the Sr^{+2} content. This nonlinear thermal expansion behavior of the samples can be correlated with the lattice oxygen loss and formation of oxygen vacancies with an increase in temperature and could be supported by the thermogravimetry data. The lattice oxygen loss or the formation of vacancies in turn reduces the oxidation state B-site cations following equations (4.1.2) to maintain the charge neutrality.

$$2Fe_{Fe}^{\bullet} + O_O^X \rightleftarrows 2Fe_{Fe}^X + V_o^{\bullet\bullet} + \frac{1}{2}O_2(g) \qquad (4.1.2)$$

The ionic radii of lower valence states are greater than their respective higher valence state counterparts. The increase in ionic radii leads to an increase in TEC value at high temperature. The lattice parameter was found to decrease with increase in Sr^{2+} content. It is expected that the TEC value should decrease with increase in Sr^{+2} content at A site. However, the samples showed an increase in

TEC value with an increase in Sr^{+2} content. It is worthwhile to note that the TEC value does not follow any regular trend with an increase in Sr^{2+} content.

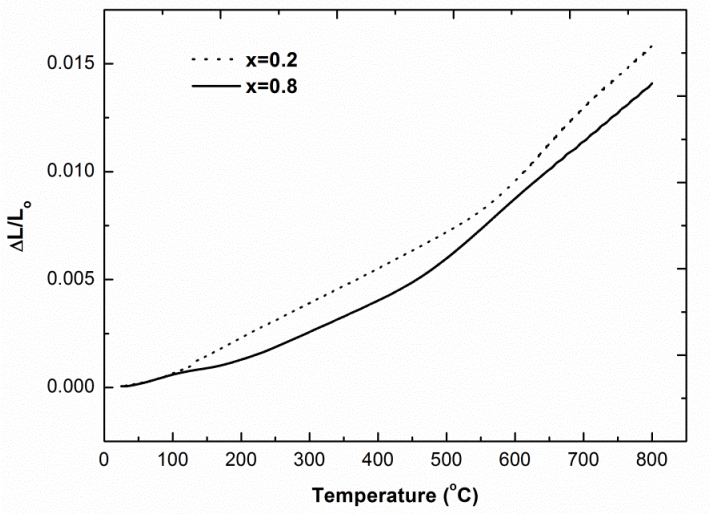

Fig. 4.1.6 Thermal Expansion behaviour of sintered $La_{1-x}Sr_xFeO_3$ samples as a function of x

As discussed earlier the average oxidation state of B-site cations increases with increase in Sr^{+2} content at the A-site. The reduction of Fe form higher oxidation state to their lower oxidation state became more active with the increase in Sr^{2+}-content at the A-site and accounted for the higher thermal expansion in the samples. The higher thermal expansion in the samples with increasing Sr^{+2} content is because of more lattice oxygen loss. The TEC change in these materials is governed by the change in oxidation state of B-site ions at high temperature associated with the corresponding weight loss and is not by the absolute valence of the B-site ion.

4.1.5. Microstructural study

SEM micrographs of the $La_{0.6}Sr_{0.4}FeO_3$ samples sintered at 1150°C and 1250°C for 4h has been shown in Fig 4.1.7. It could be seen that both the samples are dense in nature. The grain size of the sample sintered at 1150°C is smaller as compared to that sintered at 1250°C. The increase in grain size is attributed to the grain growth of the material, which is quite obvious. Both the samples shows the presence of small grains along with few large grain. The formation of large grain is correlated to the presence of agglomerate in the starting powder.

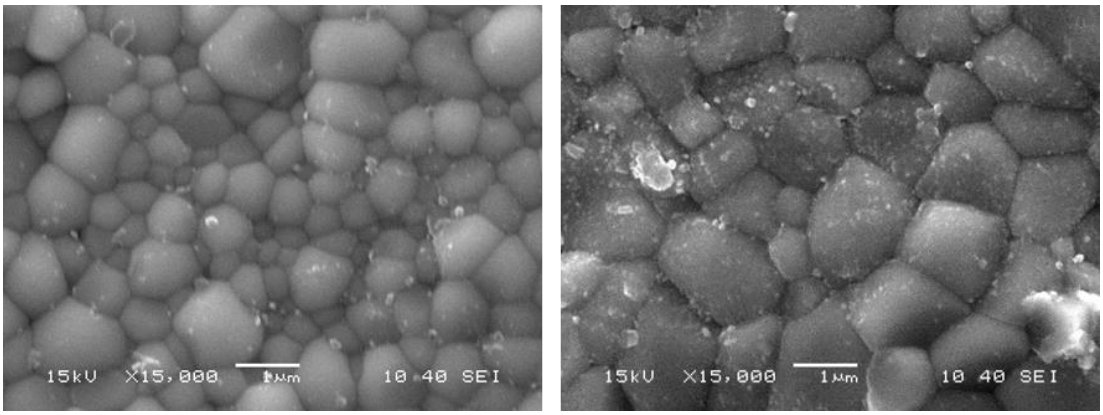

Fig. 4.1.7 SEM micrograph of $La_{0.6}Sr_{0.4}FeO_3$ sintered sample (A) 1150°C/4h and (B) 1250°C/4h

4.1.6. Electrical conduction behavior

The existence of both ionic and electronic conductivity in the $La_{1-x}Sr_xFeO_3$ samples could be explained by the consideration of the electrovalent equilibrium. The charge compensation in these oxides on replacement of La^{3+} by Sr^{2+} at A-site cause the following. i) the change in oxidation state of B-site transition-metal ions from trivalent to tetravalent state and ii) oxygen deficiency in samples from the loss of lattice oxygen [4.10]. The oxidation state change of B-site cation introduces electronic conductivity (electron holes by $B^{4+} \Longrightarrow B^{3+\bullet}$) following Eqn. (4.1.3). Thus, the material showed electronic conductivity.

$$Fe_{Fe}^{X} \rightleftarrows Fe_{Fe}^{'} + h^{\bullet} \qquad (4.1.3)$$

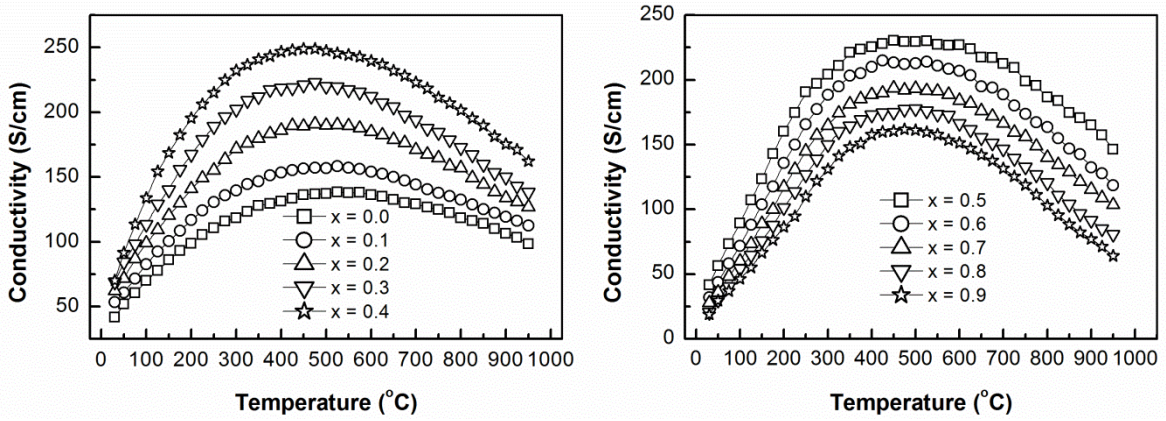

Fig. 4.1.8 Temperature dependent electrical conductivity of $La_{1-x}SrxFeO_3$ samples as a function of Sr substitution

On the other hand, the lattice oxygen loss in due to charge compensation in turn generates oxygen vacancy ($V_O^{\bullet\bullet}$) (following Eqn. 4.1.4) in the samples. These samples showed ionic conductivity due to the existence of oxygen vacancies.

$$O_o^X \rightleftarrows \frac{1}{2}O_2(g) + V_o^{\bullet\bullet} + 2e' \qquad (4.1.4)$$

The ionic conductivity of mixed ionic and electronic conductors (MIECs) is usually several orders of magnitude lower than the electronic conductivity [4.11, 4.12]. Therefore, the measured conductivity values mainly refer to the electronic conductivity.

The temperature dependence electrical conductivity of $La_{1-x}Sr_xFeO_3$ (x = 0.0-0.9) samples has been shown in Fig. 4.1.8.

All the curves showed a similar temperature dependent conductivity. The temperature dependent electrical conductivity of the samples was found to increase with temperature through a maximum about 300 - 600˚C and then decreased. Below this characteristic temperature (temperature showing maximum conductivity) the electrical conduction behavior of $La_{1-x}Sr_xFeO_3$ could be ascribed by a p-type, small polaron hopping mechanism where, charge carriers hopped between $B_B^{\bullet} - O - B_B^x$ [4.13]. The small polaron conduction behavior could be observed more predominately from the Arrhenius plots of conductivity not shown. These plots were nearly linear in low temperature range (< 300˚C). The temperature dependent conductivity in this region could be expressed as:

$$\sigma = \left(\frac{A}{T}\right)\exp\left(-\frac{E_a}{KT}\right) \qquad (4.1.5)$$

Where, the pre-exponential factor A is a material constant, which depends on the site fraction of charge carriers and the probability that neighboring ions are available to participate in the hopping conduction process. E_a is the hopping conduction activation energy, K is the Boltzmann's constant and T is the temperature [4.13-4.16]. The electrical conductivity of the $La_{1-x}Sr_xFeO_3$ samples was found to decrease with temperature in the temperature region 600-950°C. As mentioned above, the lattice oxygen loss of $La_{1-x}Sr_xFeO_3$ samples at high temperatures would result in the formation of oxygen vacancies as expressed in Eq. (4.1.3). The electrons thus liberated annihilate electron holes leading to the decrease in electrical conductivity. Moreover, the oxygen vacancies act as

scattering centers or random traps of electrons and would cause a decrease in the concentration of electron holes [4.17]. Thus, the electrical conductivity decreased with increase in temperature in the high-temperature region.

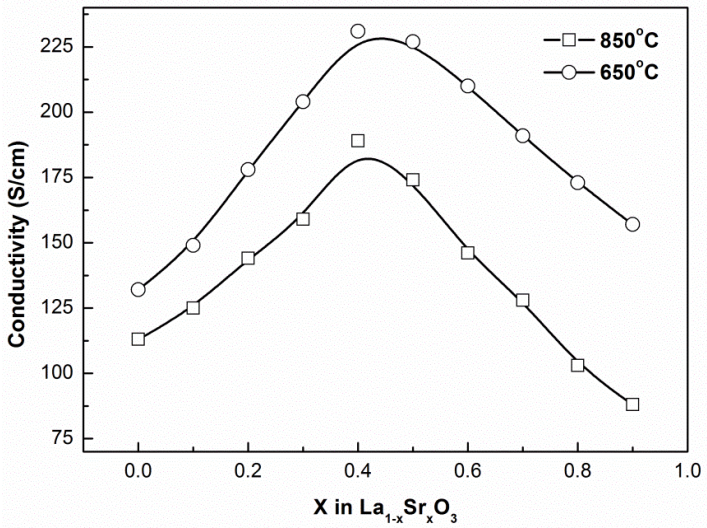

Fig. 4.1.9 Electrical conductivity of $La_{1-x}Sr_xFeO_3$ samples as a function of Sr substitution

Electrical conductivity as a function of x in $La_{1-x}Sr_xFeO_3$ is shown in Fig 4.1.9. It could be observed from Fig. 4.1.9 that the conductivity of $La_{1-x}Sr_xFeO_3$ samples increases with increase in Sr^{+2} content at the A-site up to x= 0.4 after that it decreases. The conductivity of the samples was more at 650°C than that at 850°C and could be explained, in the same way, as discussed earlier.

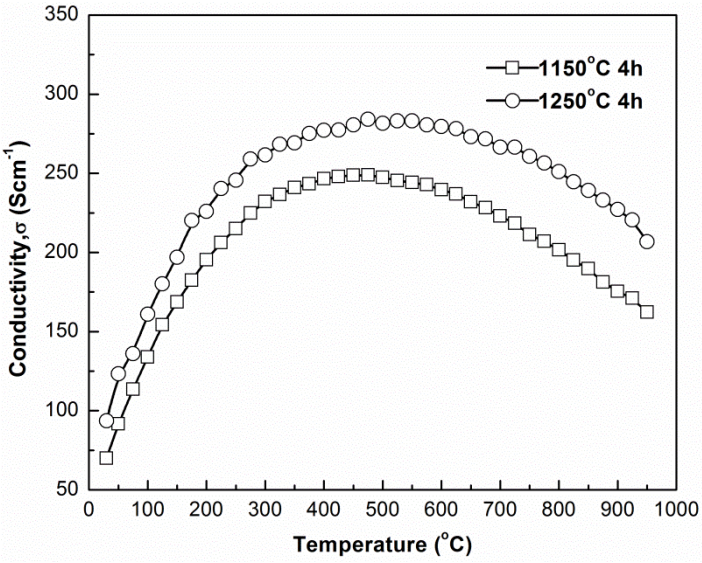

Fig. 4.1.10 Temperature dependent electrical conductivity of $La_{0.6}Sr_{0.4}FeO_3$ as a function of sintering temperature

It has been discussed earlier that addition of Sr^{2+} to $LaFeO_{3-\delta}$ creates a charge imbalance that is compensated by the formation of Fe^{4+} or oxygen vacancies (Eqn. 4.1.2 and 4.1.4). At a high substitution level (x >0.4), the annihilation of the hole by electron may cause a decrease in the electrical conductivity.The temperature dependent electrical conductivity of the $La_{0.6}Sr_{0.4}FeO_{3-\delta}$ sample as a function of sintering temperature is presented in Fig.4.1.10.It could be observed that the conductivity of the sample increases with increase in sintering temperature. The microstructural study revealed that the grain size of the sample increases with increase in sintering temperature. Thus, the increase in conductivity with increase in sintering temperature is correlated to grain growth in the sample with an increase in sintering temperature.

Summary

$La_{1-x}Sr_xFeO_3$ powder series with x=0.1-1.0 has been synthesized by solution combustion route with citric acid as fuel. The powder shows a phase purity when calcined at 1000°C. However, depending on the level of doping phase transformations have been observed from cubic ($LaFeO_3$) to orthorhombic (x=0.1-0.3) to rhombohedral (x=0.4-0.9) to again cubic ($SrFeO_{3-\delta}$). There has been a cell volume contraction and reduction in the pseudo cubic lattice parameters with the increase in the Sr content. The weight loss has been found to increase with the Sr content and was ascribed to the induction of more fractions of B-site cations to higher oxidation state. There has been a non-linear behavior in the thermal expansion of the sample with irrespective of the Sr content. The electrical conductivity for all samples has a similar trend of increasing for lower temperature range reaching a maximum and then decreasing. The behavior has been described to be due small p-type polaron hopping at the lower temperature as well as to the oxygen ion loss at higher temperature. The electrical conductivity increases with Sr content up to x=0.4 and then decrease. $La_{0.6}Sr_{0.4}FeO_{3-\delta}$ has been observed to have maximum conductivity.

4.2. Combustion Synthesis and characterization of nano $La_{0.6}Sr_{0.4}Co_{0.2}Fe_{0.8}O_{3-\delta}$: Citric acid as fuel

Chemical homogeneity is of prime concern in the preparation of multicomponent materials. Solution combustion synthesis is one of the preferred approaches to

synthesizing these materials. The advantage of combustion synthesis lies with the homogenization of all the cations present in various components on a molecular scale. Powder synthesized in this route undergoes a low-temperature densification as compared to that synthesized by conventional ceramic processing involving two or more oxide powders. Solution combustion technique is a versatile process leading to the synthesis of single phase, solid solutions, composites as well as complex compound oxide phase in homogeneous form. This process has the advantage of choosing a wide variety of fuels, rapid cooling leading to nucleation of crystallites without any appreciable growth and also has the potential for scale up. Because of the evolution of gaseous products of combustion, larger particles or agglomerates could be disintegrated during the process resulting in very fine products. Friable agglomerates are obtained that could easily be ground to obtain a much finer particle size. This method shows some advantages due to its relatively low cost as compared to alkoxide based sol-gel technique and better control of stoichiometry in comparison to the co-precipitated method while producing powders in the nanometer range. Solution combustion route is based on the gelling and subsequent combustion of an aqueous solution containing salts of the desired metals (usually nitrates) and some organic fuel. The fuels are urea, carbo-hydrazide, oxalic hydrazide, citric acid, glycine, alanine, etc. The combustion results from an exothermic redox reaction between nitrate ions and the fuel. The morphology of the powder prepared in this technique strongly depends on the following. Oxidant to fuel ratio, or more preciously the elemental stoichiometric ratio. The amount of chelate addition governs the degree of complex formation. The intensity of the redox reaction could be tailored by the addition of additional oxidant and pH of the precursor solution. The following section discusses the effect of fuel to oxidant ratio (elemental stoichiometric ratio), chelating agent, etc. on the morphology of LSCF powder prepared by solution combustion technique.

$La_{0.6}Sr_{0.4}Co_{0.2}Fe_{0.8}O_{3-\delta}$ powders have been synthesized following solution combustion technique using citric acid as fuel. An attempt has been made to synthesize nano LSCF powder with high specific surface area by optimizing oxidant to fuel ratio (metal cation to citric acid ratio; (M:C). Effect of the additional chelating agent (EDTA in this case), additional oxidant $NH_4(NO_3)$, and precursor

solution pH on the derived powder characteristics, have also been optimized. The powder samples prepared in this study along with their characteristics has been presented in Table 4.2.1.

4.2.1. Optimization of Metal Cation to Citric Acid (M:C) Ratio

To avoid the phase separation during the final stage of gelation, the process of chelation in combustion synthesis is of prime importance [4.18]. A typical quantity of chelats ensures the formation of phase pure powder at a relatively low temperature. Citric acid plays a dual role in the solution combustion synthesis process. It acts as a fuel as well as a chelating agent. The molecular structure of citric acid along with complex formation is schematically shown in Fig. 4.2.1.

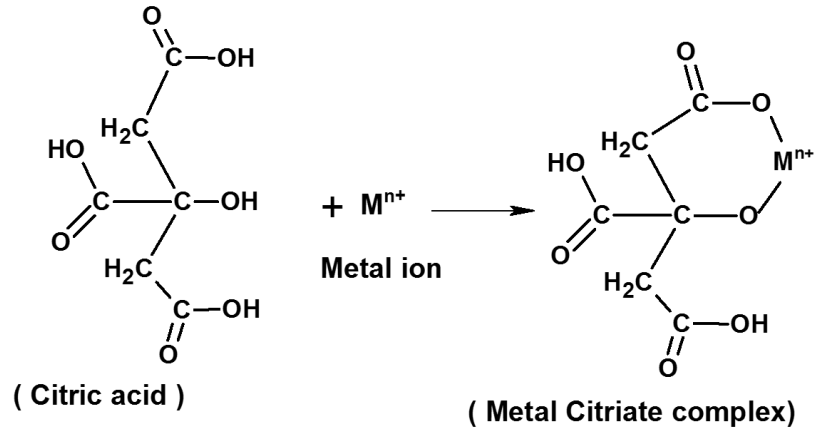

Fig. 4.2.1 Molecular structure of citric acid and chelation of a metal cation to form metal-citrate complex

Citric acid is chosen here for this purpose in the present study. Precursors with three different metal cation to the citric acid (M:C) molar ratio (C1, C1A, and C1B) were prepared. The effect of citric acid on the phase formation behavior of LSCF powder has been studied. The elemental stoichiometric coefficient (ϕ_e) corresponding to the different precursor batches has been calculated using eq. (3.1). The ϕ_e values thus calculated are listed in Table 4.2.1. It could be noted that the sample prepared with M:C ratio 1:1 is fuel lean, M:C ratio 1:1.5 stoichiometric and M:C ratio is fuel rich by nature.

The thermal decomposition behavior of the gel as a function of cation to citric acid (M:C) ratio are shown in Fig. 4.2.2. All the DSC patterns consist of an exothermic peak followed by a small endothermic peak irrespective of the M:C ratio. The TG

patterns show a gradual weight loss followed by two-step weight losses. The endothermic peak below 100°C associated with a small weight loss is attributed to the dehydration of the gel. In this step removal of physically absorbed water present in the gel occur. The exothermic peak associated with a sharp weight loss corresponds to the combustion of the citrate-nitrate gel and is the indication of the redox reaction. The combustion peak was found to shift from 148°C to 160°C with an increase in M:C ratio. Moreover, the peak intensity decreases with increase in citric acid content in the precursor solution. As stated earlier, the precursor solution (C1A) with M:C ratios 1:1, ϕ_e = 1.23, exceeds to unity; a fuel lean situation. In this fuel lean situation, the redox reaction occurs at a faster rate. Thus, a strong explosive combustion reaction is expected. Precursor solution (C1) prepared with M:C = 1:2. ϕ_e= 0.87. This fuel rich situation leads to a slow and sluggish redox reaction. Thus, a less explosive combustion is expected [4.19-4.20].

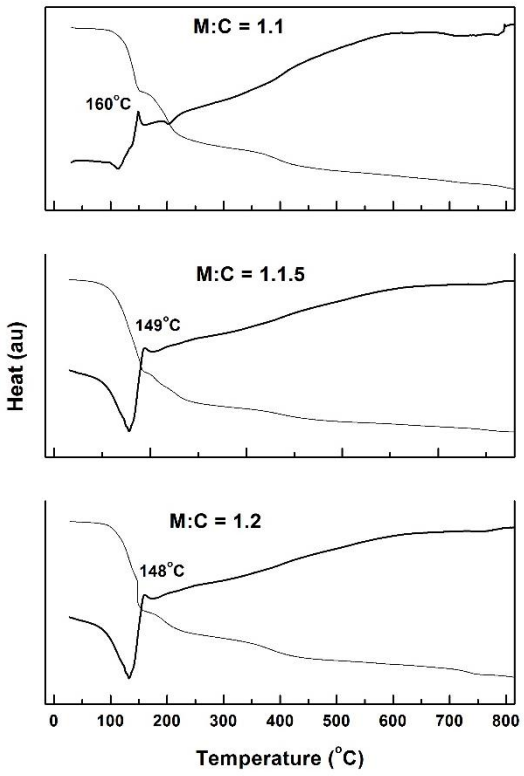

Fig. 4.2.2 **Thermal decomposition behavior of the precursor gel as a function of metal cation to citrate (M:C) ratio.**

On the contrary, solution precursor (C1B) consists of M:C = 1:1.5, ϕ_e =0.99 is stoichiometric in nature. In this stoichiometric situation, the redox reaction will have an intermittent rate. Thus, an intermediate combustion reaction is expected. The decrease in exothermic peak intensity with the increase in M:C ratio is thus quite expected. The citric acid used in the present study act as a chelating agent also. The high-temperature shift of the combustion reaction is attributed to the formation of a more stable complex with the increase in citric acid content in the precursor solution. The gradual weight loss in the high-temperature zone is ascribed to the removal of carbonaceous residue present is ash formed after combustion of the gel.

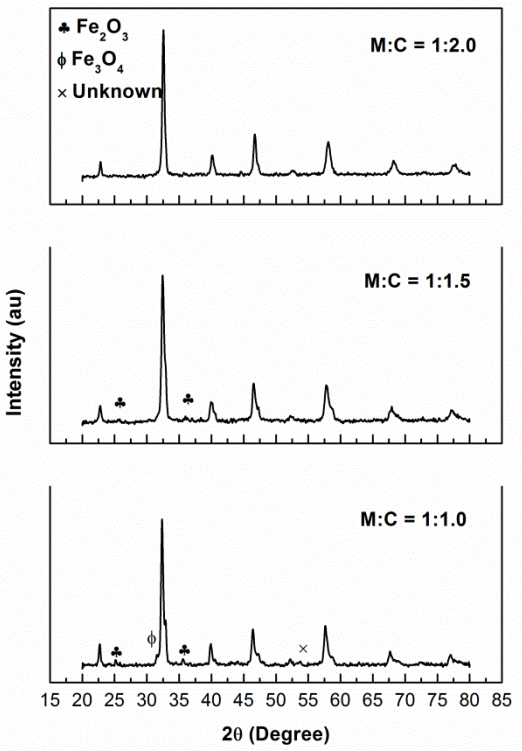

Fig. 4.2.3 XRD pattern of the powder samples calcined at 850°C as a function of metal cation to citrate ratio of the precursor solution

The XRD pattern of the powder calcined at 850°C as a function of metal to the citric acid molar ratio in the precursor solution has been shown in Fig. 4.2.3. The powder synthesized from stoichiometric (C1B) and fuel lean (C1A) precursor solution are associated with a trace amount of impurity phases like Fe_2O_3. The

powder prepared from fuel rich (C1) precursor solution are phase pure when calcined at 850°C. No other phases could be detected in the XRD pattern of the powder synthesized from a fuel rich precursor solution. Thus, the fuel rich (C1) situation could yield a better powder.

Figure 4.2.3 shows the XRD pattern of powder with C1 precursor solution as a function of the calcination temperature. It could be observed from the pattern that the powder calcined at a low temperature below 850°C is associated with impurity peaks like Fe_2O_3 and $Sr_2Fe_2O_3$ etc. The formation of impurity phases in the low-temperature calcined powder is attributed to the phase separation during the final stage of gel formation as well as with the dissociation of the citrate–nitrate complex into several intermediate phases.

These intermediate phases further react together at high temperature and form phase pure LSCF powder at 850°C. The citric acid used in the present study acts as chelating agent. The existence of impurity phases in the powder sample prepared with C1A and C1B precursor while calcined at 850°C is attributed to the incomplete complex formation leading to phase separation during the final stage of gelation.

4.2.2. Optimization of additional chelating agent (EDTA) content (M:C:E)

In an attempt to restrict the phase separation during the final stage of gel formation, EDTA (ethylene diamine tetra acetic acid) was used as an additional chelating agent in the present study. EDTA is a hexadentate ligand having two amines and four carboxylates. EDTA can bind a central cation at six different points.

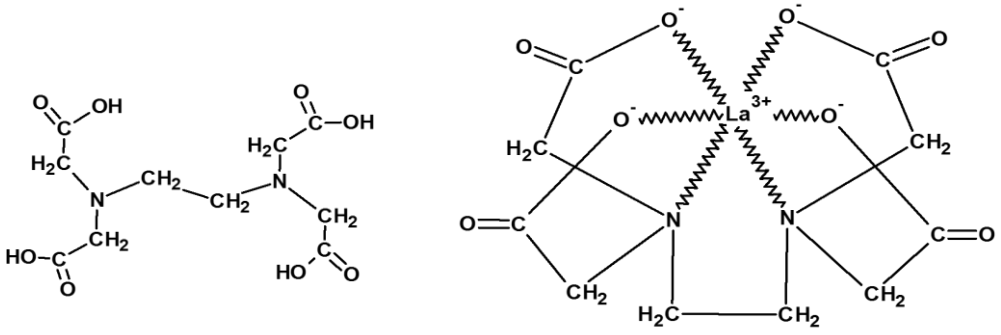

Fig. 4.2.4 Molecular structure of EDTA and its chelating action with a tri-valent metal cation (here La^{3+}) forming a metal-EDTA complex

EDTA forms least stable complexes with alkaline metal ions, stable complexes with alkaline earth cations and very stable complexes with transitional metal ions [4.21]. The EDTA complexes with +3 and +4 valence state metal ions are ultra-stable [4.22]. The molecular structure of EDTA and its chelating action with trivalent metal cation is schematically shown in Fig. 4.2.4.

The DSC pattern of the M:C = 1:2 precursor gel with extra EDTA addition is shown in Fig.4.2.5.

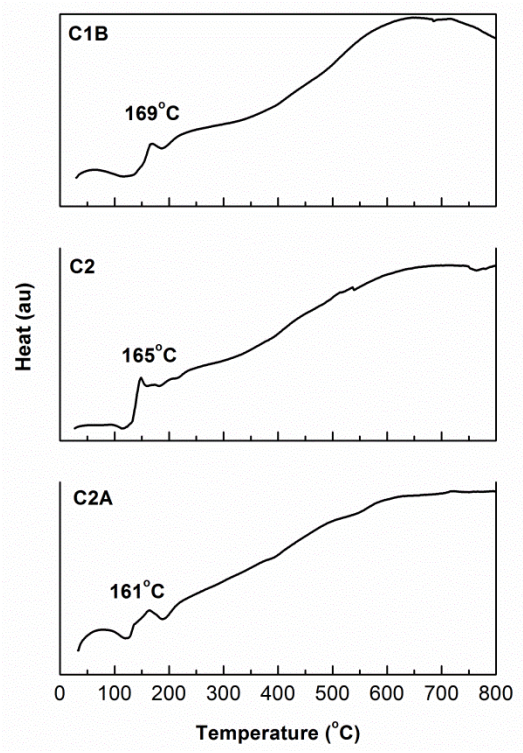

Fig. 4.2.5 Thermal decomposition behavior of the precursor gel prepared with metal cation to citrate (M:C) ratio 1:2 as a function of EDTA addition

Effect of EDTA was studied with a fuel rich (M:C = 1:2, ϕ_e=0.87) precursor solution (C1). Three different batches (C2, C2A, and C2B) has been studied with different EDTA addition in the present investigation. It is worthy to note that EDTA variation studied, does not change the fuel rich (ϕ_e <1) situation of the precursor solution. The low-temperature endothermic peaks observed in the DSC patterns are attributed to the dehydration of the precursors gel, and the high-temperature exothermic peaks are correlated to the combustion process. A substantial shift of the exothermic peaks towards the high temperature was observed with increase

in EDTA content in the precursor solution. The increase in combustion temperature with increase in EDTA content is attributed to the formation of more stable and strong citrate-EDTA-nitrate complexes.

The XRD pattern of the powder calcined at 650°C is shown in Fig.4.2.6 as a function of EDTA addition.

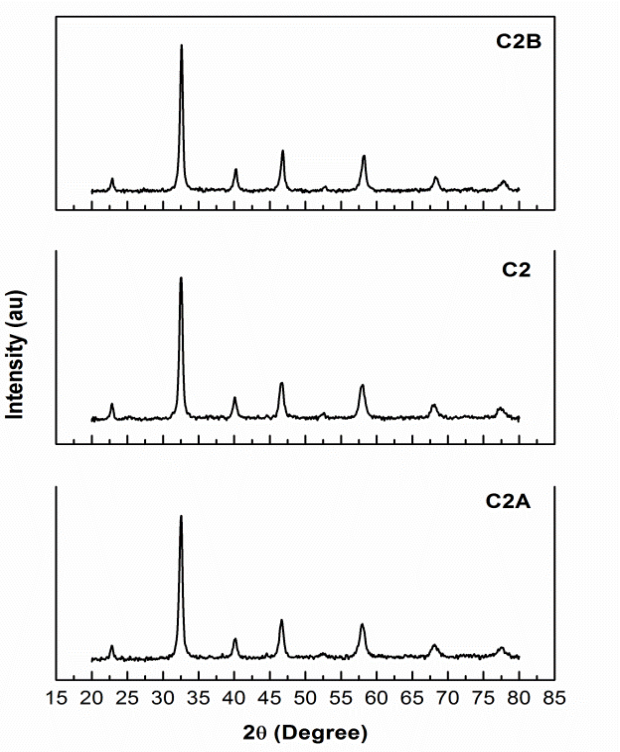

Fig. 4.2.6 XRD patterns of LSCF powder calcined at 650°C prepared with metal cation to citrate (M:C) ratio 1:2 as a function of EDTA addition

The powder obtained from the precursor solution with the metal cation: citric acid: EDTA ratio (M:C:E) =1:2:0.25 (C2A) is associated with impurity phases. The pure rhombohedral $La_{0.6}Sr_{0.4}Co_{0.2}Fe_{0.8}O_{3-\delta}$ powder was obtained in the other two ratios studied (C2, and C2B). Thus, the use of EDTA as a chelating agent not merely restricts the purity of the powder but significantly reduces the calcination temperature by 200°C. The low calcination temperature restricts the powder particles from being agglomerated together, which would otherwise, happened at higher temperature due to the availability of thermal energy and relaxation time. As a result of the reduction of calcination temperature the specific surface area of the powder increases as has been seen from the BET specific surface area

analysis. The presence of Impurity in the powder sample prepared with M:C:E=1:2:0.25 (C2A) precursor solution is correlated to the incomplete complex formation.

In this case, the amount of EDTA is still insufficient to hinder the complete phase separation during the final stage of gelation and thus unable to yield pure phase at 650°C. The powder prepared from the other two batches with ratio M:C:E=1:2:0.50 (C2) and M:C:E=1:2:0.75 (C2B) yielded phase pure powder when calcined at 650°C. Thus, the study indicates that the addition of EDTA 0.5 molar ratio is optimum to arrest phase separation during the final stage of gelation. Further study has been performed with a precursor solution containing M:C:E=1:2:0.50.

4.2.3. Optimization of additional oxidizer (M:C:E:A)

An additional oxidizer in the precursors solution has been introduced to get rid of the problems of agglomeration to which the nano powders are keenest. Ammonium nitrate (NH_4NO_3) being an oxidizer makes the rate of combustion fast and provides a less combustion time to the powder particles to agglomerate [4.23].

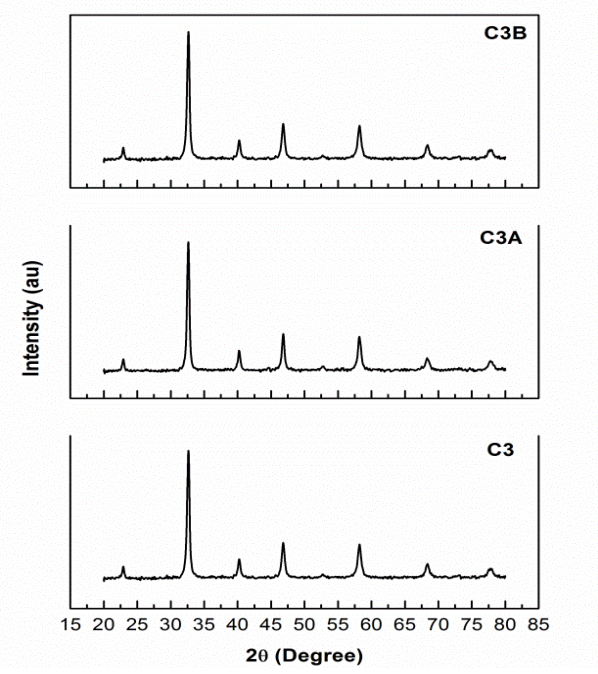

Fig. 4.2.7 XRD patterns of LSCF powder calcined at 650°C as a function of NH_4NO_3

However, the addition of excessive ammonium nitrate may increase the thermal energy of the system to a value that would be sufficient for the particles to agglomerate among themselves. Increasing NH_4NO_3 content also increases the ϕ_e value (though it is with a slow rate) which may lead to the explosive reaction with the consequent increase in the particle size. Thus, good powder quality requires a compromise between the quantity of NH_4NO_3 introduced and the size of the powder particles. Moreover, the increase of NH_4NO_3 increases the toxicity associated with the emission of NO_x during combustion [4.24].
In this study, the amount is fixed to the molar ratio 0.5 with the previously obtained value, i.e. M:C:E:A = 1:2:0.5:0.5. More amount of NH_4NO_3 leads to the decrease in the specific surface area of the powder.

With this value the elemental stoichiometric coefficient (ϕ_e) was calculated to be 0.72, a situation of fuel rich. Though the other variations (M:C:E:A = 1:2:0.5:0.25 and M:C:E:A = 1:2:0.5:0.75) have nearly the same values of ϕ_e (0.71 and 0.72 respectfully),they have no significant contribution to the reduction of the particle size. Using still more quantities of ammonium nitrate the specific surface area value decreases and hence the particle size increases. The XRD pattern of all these compositions calcined at 650^{o}C is shown in the Fig.4.2.7 that shows pure rhombohedral $La_{0.6}Sr_{0.4}Co_{0.2}Fe_{0.8}O_{3-\delta}$ peaks in all the three patterns. i.e. phase purity is independent of the addition of extra oxidizer at the same calcination temperature.

4.2.4. Optimization of pH of the precursor solution

The powder morphology, particularly the dispersion of the powder particulates, is highly influenced by pH of the precursors [4.25-4.27].The introduction of $NH_3.H_2O$ to increase the pH enhances the interaction of the metal species as a result of complete dissociation of the citric acid. The citrate ligands participate in the chelating process that is preserved by the molecular level mixing of the metal ions [4.28]. This effect combined with the effect of dissolution of the EDTA in the solution, make the dispersion of meta-nitrate-citrate-EDTA complex more homogenous. Thus, the resulting powder is well dispersed with uniformly distributed particles of high homogeneity.

The DSC of the precursor gel prepared with C3 solution as a function of pH is shown in the Fig.4.2.8. The exothermic peaks associated with the combustion of the complexes formed during gelation shifts towards the higher temperature side and the shift are now more prominent as compared to the case of variation of EDTA. The combustion peak shifting towards high temperature is attributed to the formation of stronger metal-citrate-EDTA complex. The stability of the complexes increases with the increase in the pH of the precursor as a result of the participation of more ligands during chelation as mentioned above [4.28].

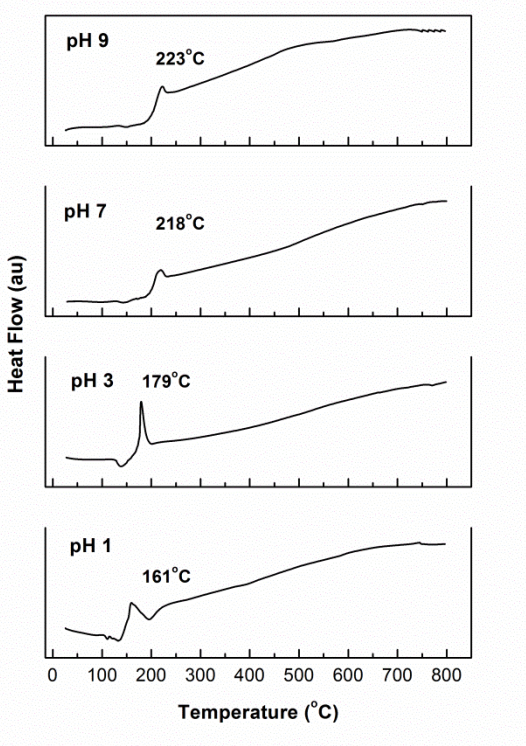

Fig. 4.2.8 Thermal decomposition behavior of the precursor gel prepared with metal cation to citrate to EDTA to ammonium nitrate (M:C:E:A) ratio 1:2:0.5:0.5 as a function of pH of the precursor

The XRD pattern of the powder calcined at 650°C for 4 hours is shown in Fig 4.2.9. The Clear crystalline rhombohedral phase of $La_{0.6}Sr_{0.4}Co_{0.2}Fe_{0.8}O_{3-\delta}$ is obtained from the precursor with different pH. The XRD peaks become wider and consequently the crystallite size reduced with an increase in pH though the change is not so significant. As result particle size decreases further. A very similar kind of observation has been reported by Guoqing Xu *et al.* on the powder synthesis of $BaFe_{12}O_{19}$ though they have increased the pH up to 11 [4.29]. In particular the

number of the dissociated divalent and trivalent citrate ions rises with the increase in the pH. A number of cations such as La^{3+}, Sr^{2+}, Fe^{3+} etc take part in the formation of stable metal citrates at high pH. As a result the homogeneity increases and the crystallite size decreases. As pH of the precursor solution increases, the combustion process becomes more intense but takes less time for its completion. Due to this steady and sluggishness of the gradual intensive combustion reaction the specific surface area of the powder increases. Powder with pH 9 has the highest value of specific surface area of 36.65 m^2/g.

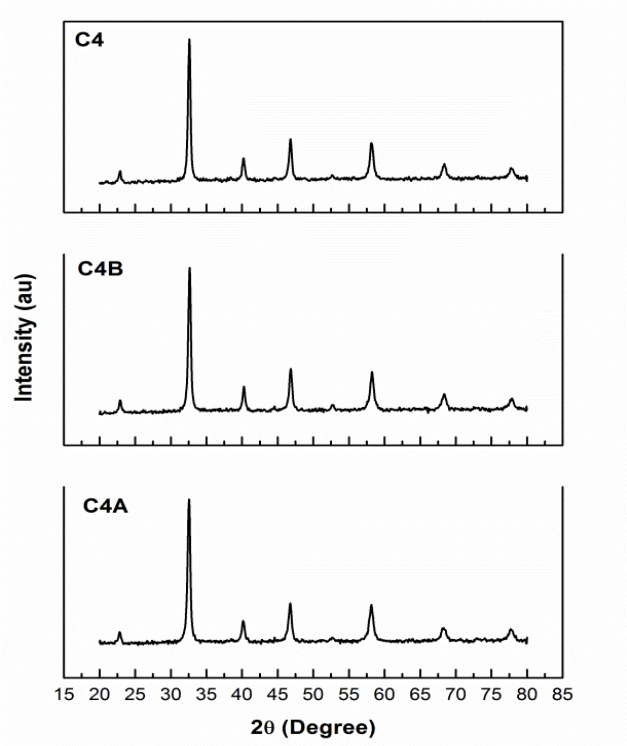

Fig. 4.2.9 XRD patterns of the LSCF powder calcined at 650°C prepared with metal cation to citrate to EDTA to ammonium nitrate (M:C:E:A) ratio 1:2:0.5:0.5 as a function of pH of the precursor

4.2.5. SEM (morphology) of the LSCF powder

The SEM micrograph of the powder profile has been shown in the Fig.4.2.10. C1 has highly hard and agglomerated powder. The morphology has been changing as a function of powder processing parameters as one goes from C1 to C4. Well segregated powder particles seen scattered in C4. The magnified version of C4 has been given for comparison that shows well dispersed particles of the order of

few tens of nanometer. Apart from this C4 have powder particles with spherical shapes with a uniform distribution proving the homogeneity of the powder.

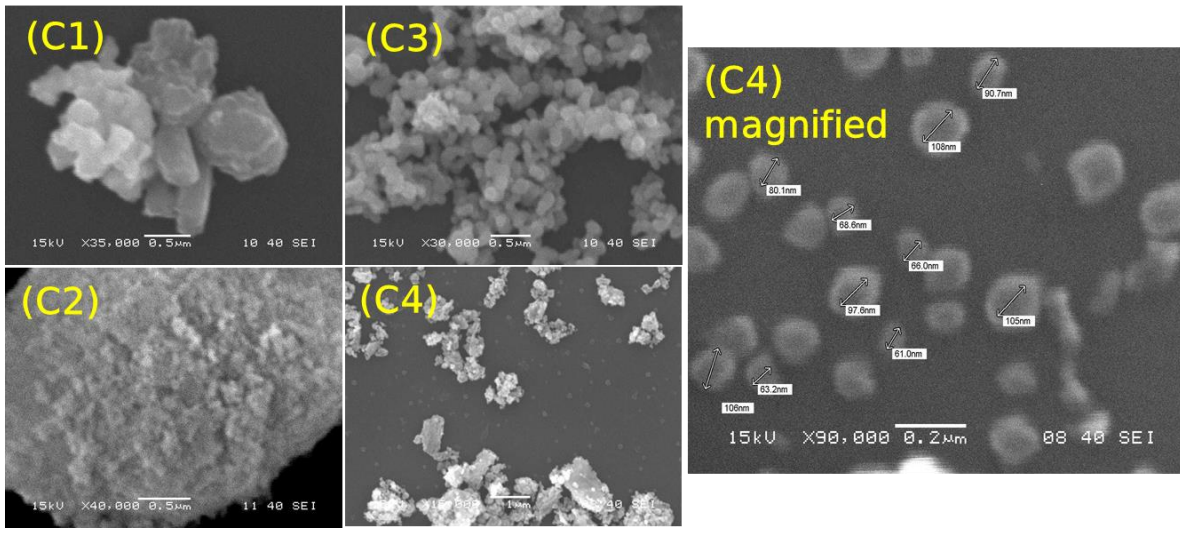

Fig. 4.2.10 SEM micrographs of LSCF powders C1, C2, C3, C4 and magnified image of C4

4.2.6 The degree of agglomeration and purity of the powder

The quantitative summary of the powder morphology is given in Table 4.2.1. Column V shows a significant increase of the BET specific surface area from the initial value 8.34m^2/g of C1 (LSCF powder with M:C =1:2, calcined at 850^{o}C) to the final value 36.65m^2/g of C4 (LSCF powder with M:C:E:A =1:2:0.5:0.5,pH 9,calcined at 650^{o}C). The surface area value achieved are as close as to one (~40m^2/g) reported by Azad *et al* for a spray pyrolysis technique [4.30]. The difference may be due to the different routes of synthesis. Column VII gives the quality of the powder in terms of the degree of agglomeration (ratio of the equivalent BET particle/agglomerate size to the crystallite size). A significant decreasing trend in the degree of agglomeration of the powder ensures the improvement of the powder quality as a function of the synthesis aids. The value unity (1.08) of the degree of agglomeration of the final powder confirms a rich compositional homogeneity and desegregated powder profile. The SEM micrograph shown in Fig.4.2.9 is a direct evidence indicating that the fineness of the powder gradually increases with the addition of the processing parameters. Though the SEM particle/agglomerate size predicted in the list differs from those of the BET average sizes, the sequence of variation in both cases are similar.

4.2.7 Purity of the Powder

In the present work, the purity of the powder has been considered from the two points of view: the phase purity and the purity of the powder from the presence of residual carbon. The XRD pattern of the all optimized samples shows clear crystalline peaks of rhombohedral $La_{0.6}Sr_{0.4}Co_{0.2}Fe_{0.8}O_{3-\delta}$. The FTIR pattern of the calcined powder as a function of the processing parameters is shown in the Fig. 4.2.11.

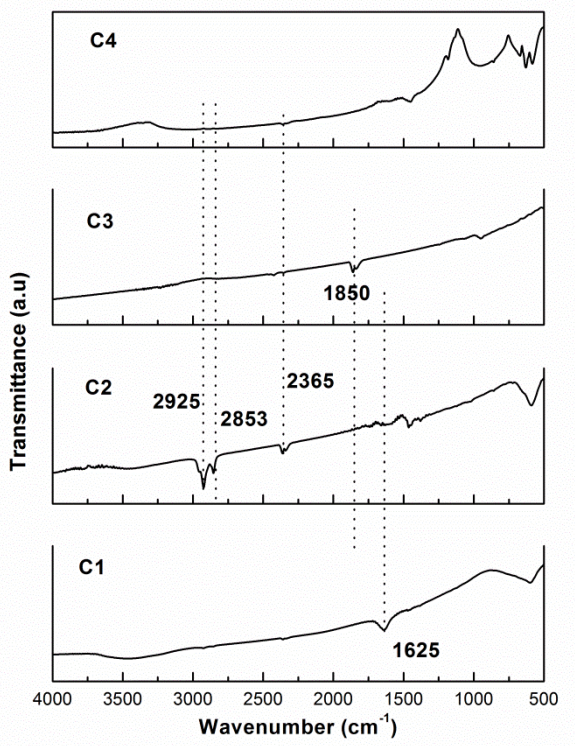

Fig. 4.2.11 FTIR pattern of $La_{0.6}Sr_{0.4}FeO_3$ powder as a function of processing parameter

The peaks at 2925 and 2853 cm^{-1} correspond to C-H stretching, at 2365 cm^{-1} corresponds to ambient CO_2 [4.31]. The peak at 1625 cm^{-1} corresponds to CO_3 vibrations [4.32]. These contaminated phases are because of the presence of some unburnt residues of combustion even after calcination [4.33]. Sample C2 is seen to have more such contaminated peaks because of the introduction of C-rich EDTA. This is one of the reasons of why EDTA amount more than M:C:E = 1:2:0.5 molar ratio has not been encouraged. The addition of the oxidizer NH_4NO_3 minimizes of these residues (noticed by reduction the peak intensities in the fig.) because of its strong oxidizing action. On the viewpoint of incomplete combustion,

the sample C1 should contain more contaminated peaks of carbonate and nitrate. The absence of hydrocarbon peaks in the sample C1 is due to higher calcination temperature (200°C higher than C2). The impurity peaks observed in samples C2 and C3 has been minimized in case of C4.

Table 4.2.1 Quantitative summary of LSCF powder morphology synthesized by combustion method by using citric acid as fuel

Sample Code	Precursor solution		Stoichiometry coefficient	Calcination temp (°C)	BET surface area (m^2gm^{-1})	Particle/ crystallite size(nm)		Degree of agglomeration (d_B/t_C)	agglomerate SEM size (µm/nm)
	M:C:E:A	pH	ϕ_e			BET	XRD		
C1A	1:1:0:0	1	1.23	-	-	-	-	-	-
C1B	1:1.5:0:0	1	0.99	-	-	-	-	-	-
C1	**1:2:0:0**	**1**	**0.87**	**850**	**8.34**	**111**	**25.8**	**4.30**	**0.5µm**
C2A	1:2:0.25:0	1	-	-	-	-	-	-	-
C2	**1:2:0.5:0**	**1**	**0.70**	**650**	**24.6**	**37.6**	**25.8**	**1.45**	**~**
C2B	1:2:0.75:0	1	-	-	-	-	-	-	-
C3A	1:2:0.5:0.25	1	-	-	-	-	-	-	-
C3	**1:2:0.5:0.5**	**1**	**0.72**	**650**	**26.47**	**35.0**	**23.7**	**1.47**	**0.1-0.2µm**
C3B	1:2:0.5:0.75	1	-	-	-	-	-	-	-
C4A	1:2:0.5:0.5	3	0.72	650	-	-	23.7	-	-
C4B	1:2:0.5:0.5	7	0.72	650	-	**-**	**23.0**	**-**	**-**
C4	**1:2:0.5:0.5**	**9**	**0.72**	**650**	**36.65**	**24.4**	**22.5**	**1.08**	**70nm**

Summary

It can be seen that a fuel rich combustion favors the formation of pure phase and fine $La_{0.6}Sr_{0.4}Co_{0.2}Fe_{0.8}O_{3-\delta}$ powder in all cases of processing aid alterations. Mainly on the basis of pure phase formation the metal ion to citric acid molar ratio was kept fixed at 1:2. The addition of EDTA with a molar ratio M:C:E=1:2:0.5 was seen to reduce the calcination temperature by 200°C. As a result, the particle size has been found to decrease, and the specific surface area increased to nearly thrice than that of the initial value. The additional oxidizer NH_4OH with ratio M:C:E:A =1:2:0.5:0.5 was observed to promote the combustion reaction and consequently reduced further the particle size. Increasing the pH of the solution resulted in the powder uniformity and increased the specific surface area of the powder. The precursor with pH 9 produced homogenous carbon free nano particles with high

specific surface area. The FTIR spectroscopy of the powder showed evidence of reduction of residual carbons gradually from C1 to C4.

4.3. Combustion Synthesis and characterization of nano $La_{0.6}Sr_{0.4}Co_{0.2}Fe_{0.8}O_{3-\delta}$: Glycine as fuel

The synthesis of LSCF using citric acid as fuel indicated that the following two factors leads to the formation of the desegregated LSCF nanoparticles. They are (i) amount of fuel in the precursor solution for a fuel rich stoichiometry (Φ_e<1) and (ii) optimization of the pH of the precursor solution. However, the total process is promoted by intermediate steps of addition of extra chelating agent (EDTA) and additional oxidizer (NH_4NO_3).

Glycine being oxidized by nitrate ions is a good fuel [4.25] for combustion synthesis. It has high combustion reaction enthalpy (13.0 kJ/g) than that of citric acid (10.2 kJ/g) [4.34]. It has been a preferable choice for faster and explosive combustion reaction. The presence of the amino group at one end and the carboxylic acid group at the other (zwitterionic) makes glycine a perfect complexing agent to many metal cations with various ionic radii [4.25, 4.35,4.36].

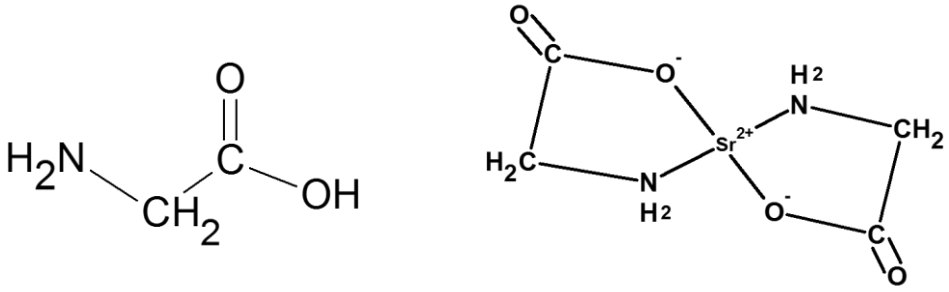

Fig. 4.3.1 Glycine molecule and its complexing action with a divalent cation (Sr^{2+}) forming a metal-glycine complex

Glycine molecule along with its complexing action is presented schematically in Fig. 4.3.1. Thus, even though the Φ_e value does not meet the fuel rich criteria, synthesis of LSCF can be expected with the less amount of glycine in comparison to the amount of citric acid. So to study the effect of fuel amount in the combustion process the starting precursors with three different Φ_e values have been prepared. The study includes a precursor solution consisting of metal ion to glycine ratio (M:G) 1:2, 1:3 and 1:4 respectively. It was observed from section 4.2 that pH of

the solution is a leading and necessity factor for morphology control and compositional homogeneity of the synthesized powder. The precursors have been prepared with a high pH value from the initial step in the present study. Particularly pH 7 is the most favorable choice because glycine dissociates to zwitterion in neutral to basic pH medium (pH 7- pH 9) [4.37]. The successive addition of extra chelating agent and oxidizer have been carried out to study the effect on the morphology of the powder. The detail parameter alterations have been presented in Table 4.3.1.

4.3.1 Optimization of metal cation to glycine fuel ratio (M:G)

Precursors G1A (M:G=1:2; Φ_e=1.27), G1B (M:G=1:3; Φ_e=1.00) and G1C (M:G=1:4; Φ_e=0.87) with three different elemental stoichiometric coefficients have been prepared. Separately G1 was prepared by adding NH_4OH to G1C until its pH becomes 7. The thermal decomposition behavior of the G1 gel has been studied from the DSC/TG pattern given in the Fig. 4.3.2. four exothermic combustion peaks were observed on the DSC curve. The endo-thermic peak at 86^{o}C is associated with the dehydration of the precursor gel. The burning of the glycine corresponds to the peak at 178^{o}C. This sharp peak in glycine case shows a vigorous combustion of the complexes because of high combustion enthalpy of glycine as compared to that of citric acid. Other exothermic combustion peaks appearing at 300^{o}C and 450^{o}C are associated with the burning of the residual nitrates and carbonates after the redox reaction. The peak at 650^{o}C is the crystallization of the LSCF compound [4.36]. The TG curve shows weight changes in four different stages. The maximum weight loss of about 65% in the temperature range 25-180^{o}C may be due to the dehydration of the gel. The loss of about 15% in the temperature range 180^{o}C-300^{o}C and that of about 10% in the range 300^{o}C-500^{o}C is correlated to the charring of nitrates and carbonates. The remaining asymptotic part of the curve from temperature 500^{o}C onwards shows a gradually slow weight loss. The nature of the DSC/TG curve for the gel derived from precursor solutions of G1A, G1B, and G1C also showed very similar in nature.

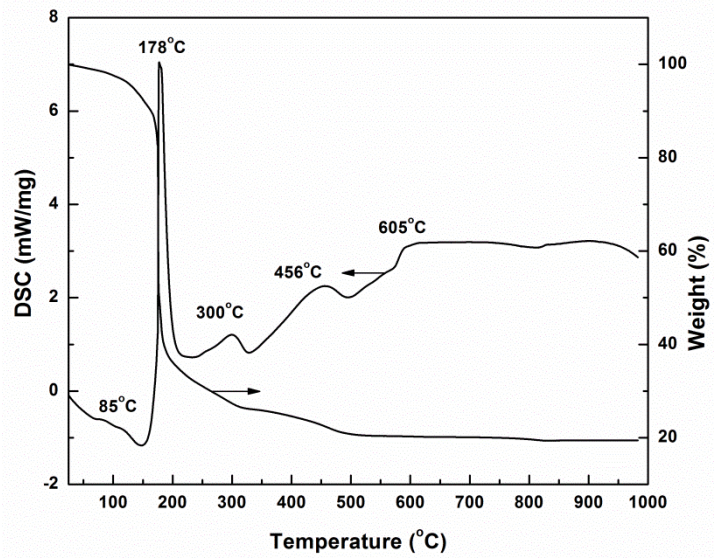

Fig. 4.3.2 Thermal decomposition behavior of glycine-nitrate precursor gel (G1)

The phase formation behavior of the powder as a function of powder processing parameters has been shown in Fig. 4.3.3. The powders were calcined at a temperature of 650°C for 4h. The XRD patterns show the formation of crystalline LSCF peaks in all the three compositions G1A, G1B and G1C along with some intermediate impurity phases. The impurity peaks were identified to be oxides and carbonates of metal such as $La_xSr_{2-x}CoO_4$, $SrCo_3$, and Fe_2O_3. Two obvious reasons may be ascertained by the presence of these impurity peaks. The first one is the constituents might not chelate sufficiently due to the presence of an inadequate amount of chelating agent in the fuel lean mixture and thus eventually ended up with the partly formed compounds as impurity peaks. The second one is the inhomogeneity in the molecular level mixing of the metal cations due to improper chelation for which some part of the precursor undergo local reaction to form these undesired oxide and carbonate peaks.

The XRD pattern of G1C precursor derived powder calcined at a higher temperature of 750°C is shown in the Fig. 4.3.4 (a). It could be seen from the figure that crystalline LSCF is formed at 750°C calcined for 4 h. Similarly, pure LSCF phase could also be obtained from G1C precursor at pH7 (Fig 4.3.4 (b)) while calcined at a low temperature of 650°C for 4 h.

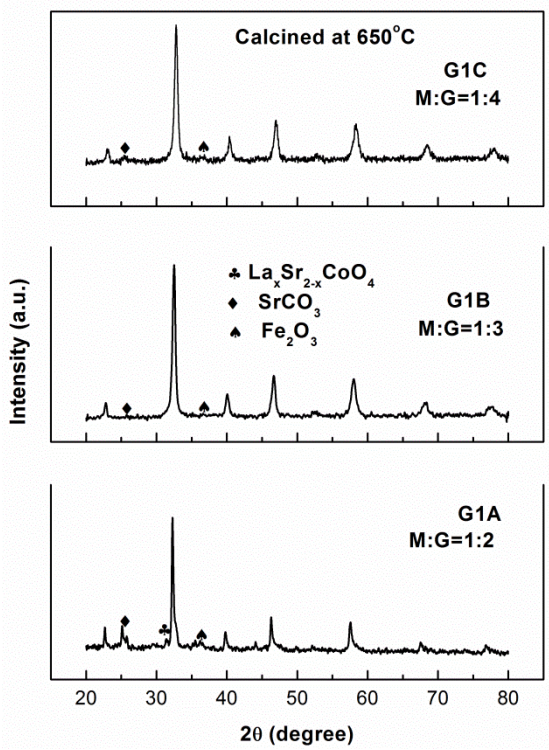

Fig. 4.3.3 XRD patterns of LSCF powder as a function of Glycine content (G1A, G1B, and G1C) calcined at 650°C for 4h

The impurities such as $SrCo_3$ gets dissolved as a result of homogenization due to dissociation of the ligand and phase pure LSCF is formed at 650°C. It agrees with the work by Zhou et al. [4.36] in which it was shown that $SrCO_3$ phases dissolve in the main pattern. Phase pure powder could be obtained from other glycine containing precursor solution G1A and G1B at 750°C. The requirement of high calcination temperature could be justified from the consideration of the fuel deficiency and lack of homogeneity in these precursor gels.

Thus, a very similar conclusions can be drawn for the glycine assisted combustion case as that achieved in the case of citric acid combustion synthesis. Fuel rich value of Φ_e favors the formation of phase pure powder at a low temperature. The role of NH_4OH is significant for homogenizing the precursor. The works of the literature also support these analogies [4.36].

The addition of NH_4OH in the precursor solution acts as a combustion aid and hence reduces the calcination temperature because of intense combustion. The calcination temperature was found to be reduced by 100°C. The crystallite size calculated from the XRD patterns was observed to decrease (from 30 nm in G1C

derived powder to 26 nm in G1 derived powder) because of lowering down of the calcination temperature. The change of the value of stoichiometry coefficient by the addition of NH_4OH is insignificantly small and can practically be ignored.

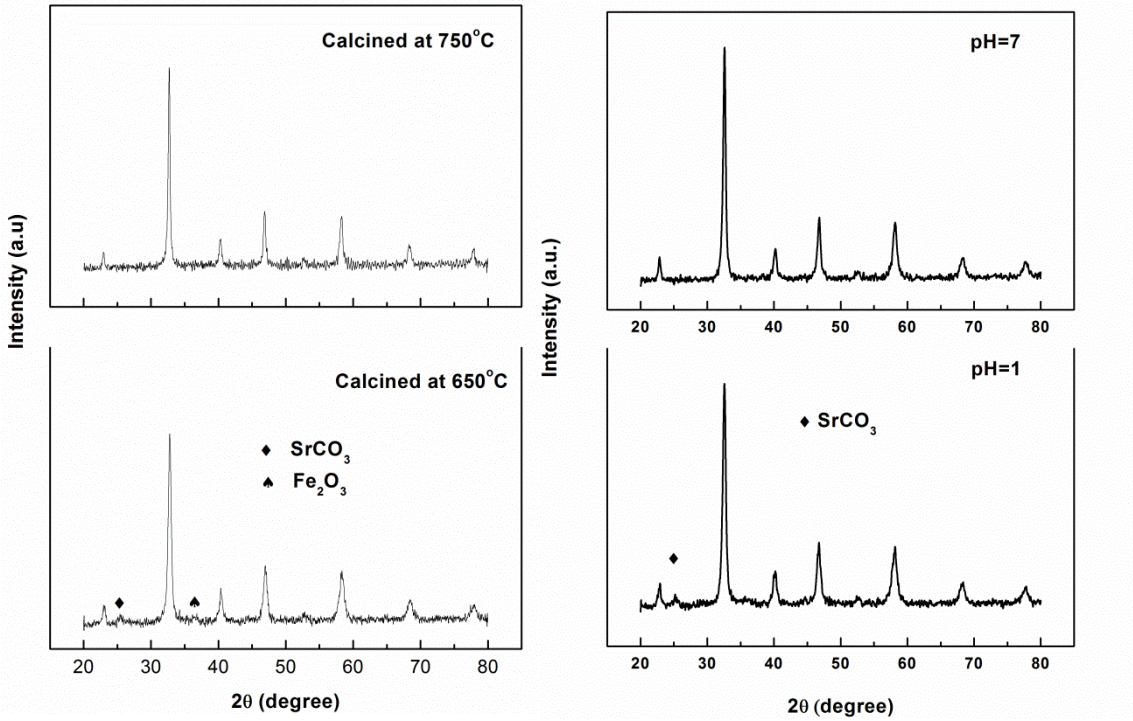

Fig. 4.3.4 XRD patterns of LSCF powder (G1C) as a function of (a) calcination temperature and (b) pH calcined at 650°C.

4.3.2 Optimization of EDTA content (M:G:E)

Effect of the EDTA addition with glycine on the phase formation behavior of LSCF powder has also been studied. Three precursor solutions G2A, G2, and G2C have been prepared with different EDTA content (M:G:E) for the study. The Φ_e value for all the compositions studied has been given in the Table 4.3.1. All values indicate that the precursors are of fuel rich stochiometry. The DSC of G2 precursor derived gel is plotted in Fig. 4.3.5 along with the other gels (G1, G3, and G4). The graph shows two exothermic peaks one at 185°C and the other at 300°C. The first exothermic peak corresponds to the burning of EDTA-glycine complex. The second exothermic peak at 300°C is attributed to the burning of residual nitrates. The apparent shift of the combustion peak from 178°C for G1 derived gel to a higher temperature side 185°C for G2 derived gel indicates the formation of stable and stronger complex by the EDTA. Because of the chelation properties of EDTA [4.38]

the number of other combustion peaks that leads to the formation of intermediate phases was also seen to be limited. The thermal decomposition behaviors of the dried gels with different EDTA content are quite similar consisting of multiple exothermic peaks followed by the dehydration peak. It is because of the same kind of chemical reactions the EDTA involves with the other constituents as discussed earlier.

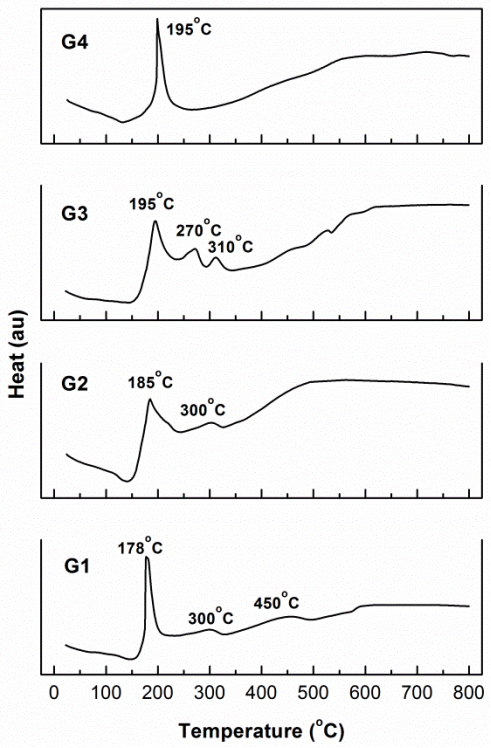

Fig. 4.3.5 **Thermal decomposition behavior of glycine-nitrate gel as a function of precursor solution constituent**

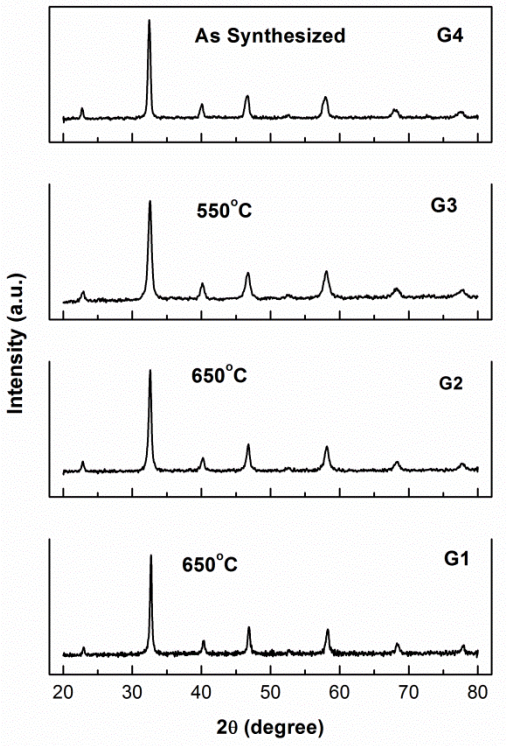

Fig. 4.3.6 **XRD patterns of G1, G2, G3 and G4 calcined powder**

The XRD pattern in Fig. 4.3.6 shows crystalline phase pure rhombohedral peaks of LSCF for G2 derived powder calcined at 650°C for 4h. The addition of EDTA in the case of glycine as a fuel does not further decrease the calcination temperature unlike that observed in the case of citric acid. The result correlates the pre-homogenization of the precursor by the elevated pH whereby the impurity intermediate phases get dissolved. In other words, EDTA has a uniform dissociation in a neutral pH medium of the precursor. The uniform distribution of ions and hindrance of the phase separation leads to the development of smaller

particles as revealed from the broadening of XRD peaks. The addition of more amount of EDTA has no significant effect on the particle size reduction or phase formation temperature (Table 4.3.1). Because of the optimal surface area for the ratio M:G:E=1:4:0.5, G2 has been considered for further morphological modification.

4.3.3. Optimization of additional oxidizer (M:G:E:A)

To further reduce the particle size and desegregate the powder structure additional oxidizer is required [4.23]. NH_4NO_3 has been used as an oxidizer with the fuel glycine. In a parallel argument with the section in citric acid combustion, the amount of NH_4NO_3 content has been fixed for the precursor G3. The precursor is fuel rich with M: G: E: A=1:4:0.5:0.5 and Φ_e=0.75. The addition of NH_4NO_3 in the precursor with glycine is also of particular importance because the nitrate ions oxidize it.

The thermal decomposition for the G3 gel has been shown in the Fig. 4.3.5. In addition to the usual combustion peak for the decomposition of the glycine-EDTA-nitrate complex, there are two other prominent peaks at 270^{o}C and 310^{o}C. The peaks are attributed to some intermediate redox reactions of NH_4NO_3 forming some compounds of nitrates and carbonates and is related to the presence of some residual nitrates in the precursor[4.36].

The phase formation behaviour of LSCF powder as a function of ammonium nitrate addition could be observed from the Fig. 4.3.6 The XRD pattern showed the presence of rhombohedral LSCF phase in the powder calcined at 550^{o}C for 4h. The peaks are even broader than those obtained from the precursor containing EDTA and glycine in the previous step. The broadening of the XRD peaks is accounted for the decrease in the crystallite size of the synthesized LSCF powder. The BET specific surface area of the powder was found to increase to a value of 25 m^2/g from a value of 19 m^2/g.

4.3.4 Optimization of pH of the precursors solution

Because of the enhanced number of nitrate ions produced by the addition of NH_4NO_3 the dissociation of both glycine and NH_4NO_3 might require an increase in the pH value. The pH of the precursor gel G3 was increased to 9. The thermal decomposition behaviour has been shown in the same Fig. 4.3.5. It has a single exothermic peak at 195^{o}C that represent the single stage burning of the complex

formed by glycine with the metal cations, EDTA and ammonium nitrate at a pH value 9 [4.36]. No other exothermic peaks could be observed in the DSC pattern of the gel prepared at pH 9. The study showed an interesting result, which indicate that no other intermediate phases are formed in the precursor G4. The exothermic peaks corresponding to the redox combustion reaction of the complex have been shifted towards the higher temperature side from 178°C to 195°C through 185°C. The peak shifting towards high temperature is attributed to the formation of successively stronger and stable glycine-EDTA-nitrate complex.

The phase formation behavior has been shown in the Figure 4.3.6 along with the patterns for other compositions G1, G2, and G3 for comparison. The crystalline peaks are obtained in the as synthesized (G4) powder and are identified to be of rhombohedral structure. The XRD peaks are now even broader than that of G3 that leads to the decrease in the crystallite size (Table 4.3.1). It may mainly be attributed to the low-temperature synthesis because of single stage combustion [4.39]. Single stage combustion resulted in the formation of the crystalline phase in less time and thus hindered the growth of the particles leading to the formation of larger agglomerates [4.40]. Thus, desegregated fine particles can be obtained in the powder by single step combustion using glycine as fuel [4.41]

4.3.5 FTIR analysis of the powder

The FTIR pattern of the set of phase pure LSCF powders has been shown in the Fig.4.3.7. The low wave numbered peak (at 587 cm^{-1}) is due to the vibration of the metal ion bonds and are characteristic peaks for perovskites [4.42]. Peaks at 854 cm^{-1} and 1462 cm^{-1} are the characteristic vibration of NO_3^- and CO_3^{2-} respectively [4.42,4.43] and are seen to be present in almost all samples. The peak at 1385 cm^{-1} is a significant peak that corresponds to NO_3^- vibration [4.43] and is seen in most of the samples except G4. The suppression of NO_3^- peak in G4 samples indicates that the gel is optimized with the chelating agent, oxidizer, and pH. The optimization leads to the minimization of residual phases formation because of homogeneity in the molecular level mixing and complete burning during single step combustion. The CO_3^{2-} peaks are however still present though suppressed in G4 to some extent in comparison to others. The presence of this nitrate peaks in other samples is attributed to the partial burning of the precursor that is still in the fuel lean state.

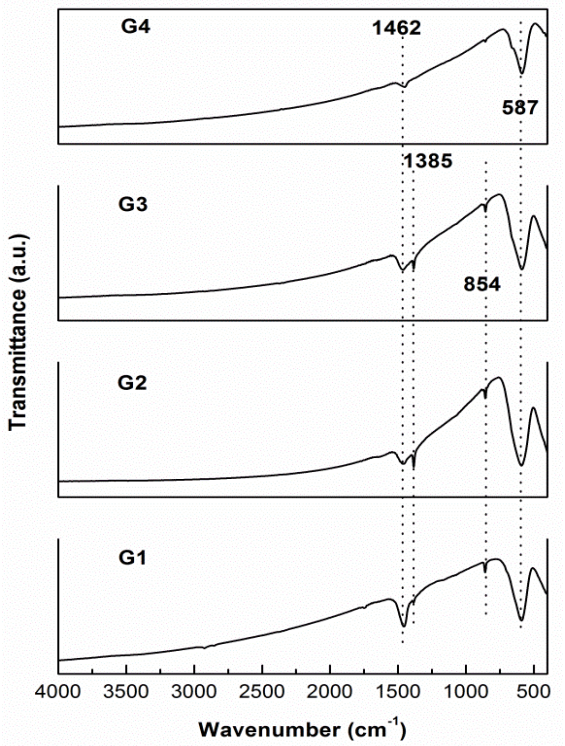

Fig. 4.3.7 FTIR patterns of calcined phase pure G1, G2, G3 and G4 powders

4.3.6 Microstructural and numerical data analysis

Figure 4.3.8 shows the scanning electron microscopic images of all the final powder (G1, G2, G3, and G4). The morphology of G1 (M: G= 1:4; pH 7) powder is highly agglomerated with agglomerates in the range of microns. A significant improve in the morphology of the powder is clearly observed from the micrographs as one goes from G1 to G4. G2 powders are seen to have agglomerates that are smaller than those of G1 powder. The decrease in agglomerate size is related to the effect of EDTA addition, as observed in the case of citric acid. The powder is seen to be very porous and light in the case of G3. It is because of the oxidizing action of the added NH_4NO_3 that enhances the quality of redox combustion reaction. Th ammonium nitrate addition leads to the evolution of the high volume of gasses during burning because of the reactions with metal cations and subsequent decompositions [4.38]. G4, as was expected consisted of desegregated fine particles. The exact agglomerate/particle size is however not matching with that of the BET size.

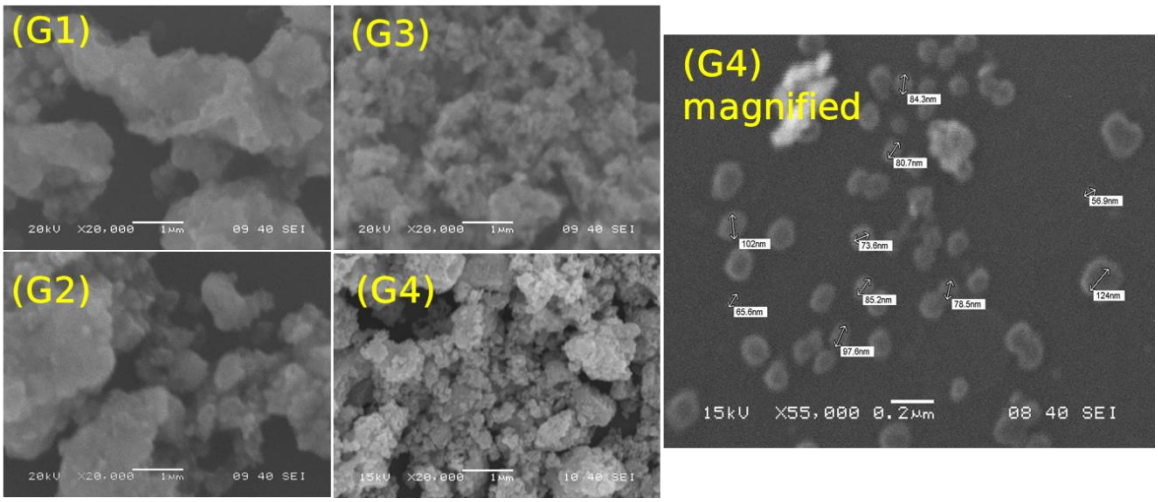

Fig. 4.3.8 SEM micrographs of calcined powders of G1, G2, G3, G4 and magnified image of G4

The Table 4.3.1 summarizes the powder characteristics of glycine derived powder. Considering the XRD profiles and the column III of the Table, it is evident that a fuel rich value of the precursors (ϕ_e<1) favors the formation of phase pure particles. Column IV shows the decrease of the calcination temperature as a result of the addition of combustion parameters.

Table 4.3.1 Quantitative summary of LSCF powder morphology synthesized by using glycine as a fuel in combustion technique

Powder Type	Precursor solution		Stoichiometry Coefficient	Calcination Temperature (°C)	BET surface area (m^2/g)	Particle/Crystal lite size (nm)		Degree of agglomeration (d_B/t_C)	SEM particle size (µm /nm)
	M: G:E:A	pH	ϕ_e			BET	XRD		
G1A	1:2:0:0	1	1.27	-	-	-	-		-
G1B	1:3:0:0	1	1.00	-	-	-	-		-
G1C	1:4:0:0	1	0.87	750°C	6.25	-	30	-	9µm
G1	**1:4:0:0**	**7**	**0.87**	**650°C**	**14.23**	**62.9**	**26**	**2.42**	**~5 µm**
G2A	1:4:0.25:0	7	0.84	650°C	18.7	-	25.2	-	-
G2	**1:4:0.5:0**	**7**	**0.72**	**650°C**	**19.4**	**46.2**	**25.2**	**1.83**	**~3µm**
G2B	1:4:0.75:0	7	0.68	650°C	19.4	-	25.2	-	-
G3	**1:4:0.5:0.5**	**7**	**0.75**	**550°C**	**25.3**	**35.4**	**24.8**	**1.43**	**0.3 µm**
G4	**1:4:0.5:0.5**	**9**	**0.75**	**As Synthesis**	**32.5**	**27.5**	**24.3**	**1.13**	**80nm**

The specific surface area of the powder, as measured by BET technique, has a successively increasing trend and a consequent decreasing nature in the equivalent particle size as one goes from G1 to G4. The crystallite size has a similar decreasing trend.

The degree of agglomeration for G4 has the smallest value of 1.13 which indicates that the tendency of agglomeration for this powder is minimum, and the morphology is desegregated. Lei *et al.* [4.44] also adopted a similar synthesis method with glycine as fuel. The powder found to require a calcination temperature of 800^{o}C. After subsequent ball milling, a surface area of 22.9 m^2/g with a particle size of 175 nm was achieved in that work. Thus, the result obtained in this study is quite significant.

Summary

The use of zwitterionic glycine as fuel has similar inferences as those of citric acid. A fuel rich value of the stoichiometric coefficient of the precursor with the only glycine as the combustion aid has been found favorable for the phase pure powder formation. Glycine fuel in a neutral pH medium works well that has seen to reduce the phase formation temperature by 100^{o}C. The reduction in phase formation temperature is described to the complete dissociation of glycine. The specific surface area of the powder has seen to increase with the addition of processing aids as one goes from G1 to G4. The addition of EDTA has no effect on the reduction of the calcination temperature, but it decreases the crystalline size. NH_4NO_3 as an oxidizer has a role in decreasing the calcination temperature and a further decrease in the crystallite size. It was attributed to its supplement of NO_3 required for combustion with glycine as a fuel. Further increasing pH has a positive effect that resulted in a single step combustion because of homogeneity. The ‘as synthesized’ LSCF powder was found to be phase pure due to single step combustion. The particle size of the powder was found to decrease significantly. The degree of agglomeration of the final powder G4 has a good agreement with the SEM powder morphology. The FTIR analysis shows a significant decrease of the residual carbon and nitrates.

4.4. Structural and Thermal Behavior of $La_{0.6}Sr_{0.4}Co_{0.2}Fe_{0.8}O_{3-\delta}$ Powder

During fabrication of SOFCs, its components are subjected to heat treatment at different temperature regime. Perovskite cathode materials may have phase transition when undergoing temperature change [4.45, 4.46]. Thus, the structural study of the powder is of vital importance. Also for an understanding of its electrical conduction behavior and stability against stringent temperature regime the thermal stability study of the powder is necessary. The study can sketch in general the oxygen adsorption and desorption mechanism inside the material. Depending on the structure of the powder and the synthesis method the properties may vary.

4.4.1. Structural analysis

The crystal structure of LSCF powder has been reported in the literature [4.45-4.50]. The crystal structure of the powder often depends upon the synthesis route. Several synthesis routes have been adopted for LSCF powder synthesis. There are many possible arguments regarding the structure of the LSCF powder. For example powders prepared by an EDTA-citrate method has been observed to be cubic [4.45] and remains the same without any phase transition (or lattice distortion) during the whole course of temperature. Powders prepared by a Pechini method by Waller e*t al* [4.46] reported cubic phase at a lower temperature and shown to transit to rhombohedral at a higher temperature. Several other literature [4.47-4.49] also suggest low-temperature rhombohedral structures of the LSCF powder. To clarify these gaps, we have provided a Rietveld structural analysis of the powder synthesized in our study.

Rietveld refinement of the XRD pattern of LSCF (C4) powder sample calcined at 650^{o}C for 4 h has been performed assuming rhombohedral phase symmetry with space group R3-C. The analyzed pattern has been presented in Fig. 4.4.1. The scattered points are the measured data. The calculated/refined pattern has been presented as solid lines. The differential plot has been presented at the bottom of the figure. The calculated Bragg peak positions have been plotted as vertical lines. The calculated peak positions have been presented between the XRD patterns. Rietveld analysis parameters and outputs have been given in Table 4.4.1.

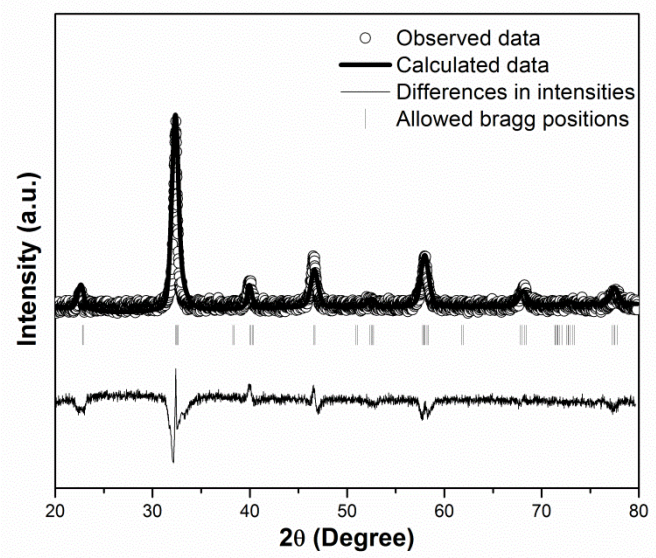

Fig. 4.4.1 Rietveld analysis of LSCF (C4) powder calcined at 650°C for 4 h

Table 4.4.1 Rietveld analysis data of LSCF powder (C4) showing crystal structure and other parameters

Atom	x	y	z	Occupancy	Biso
La	0.00000	0.00000	0.25000	0.60000	0.78960
Sr	0.00000	0.00000	0.25000	0.40000	0.78960
Co	0.00000	0.00000	0.00000	0.20000	0.48160
Fe	0.00000	0.00000	0.00000	0.80000	0.48160
O	0.45800	0.00000	0.25000	1.00000	1.80020

Fitting Detail		Cell Info (Lattice parameter)
Bragg R-factor	17.95	a 5.525258
RF-factor	10.235	b 5.525258
Space group	R -3c	c 13.423898
Rp	45.0	
Rwp	70.1	α 90.00°
Rexp	36.46	β 90.00°
χ^2(GOF)	3.70	γ 120.00°

The χ^2 value (3.70), also known as the goodness of fitting has a reasonably acceptable value, indicating a quality fitting. The lattice parameters calculated has a good agreement with the works of Qing Xu *et al* [4.50] and other reported literature [ref]. The R-values also has an agreement with reported literature

[4.30], and the differences may be because of the heat treatment temperature and powder synthesis method. The lattice parameters are seen to be matching with the values 5.4951Å, 5.4951Å and 13.4092Å respectively reported by Xu *et al.* [4.50].

4.4.2 Thermogravimetric analysis (TG) analysis

The thermal stability of the materials has been analyzed using thermogravimetric analysis. The weight loss behavior of LSCF (C4 and G4) powder during heating in the air has been presented in Fig. 4.4.2. All other samples (C1-C3 and G1-G3) also showed the similar behavior. The TG profile shows a gradual slow weight loss in the temperature range 30-400˚C. The desorption of physically adsorbed water and carbon dioxide occurs in the temperature region (30-200˚C). Oxidation of Co^{3+} and Fe^{3+} is reported to occur in the temperature zone (200-400˚C) [4.51-4.53].

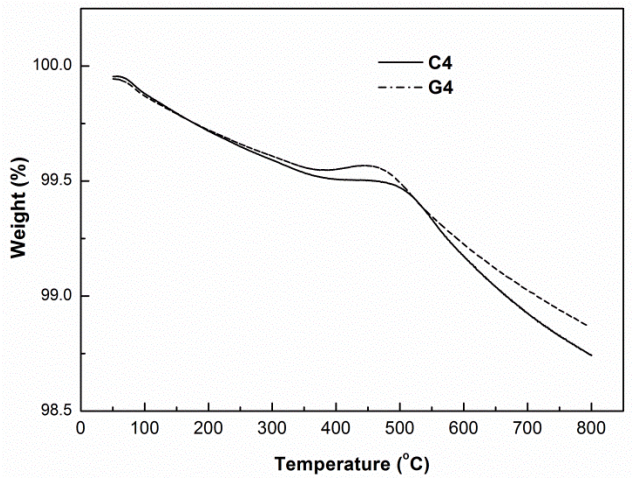

Fig. 4.4.2 Thermogravimetric analysis of $La_{0.6}Sr_{0.4}Co_{0.2}Fe_{0.8}O_{3-\delta}$ powders under air atmosphere

Thus, a small gain in weight in this temperature range is correlated with the oxidation of Co^{3+} and Fe^{3+}. The weight loss rapidly increases in the temperature range 400-800˚C. This weight loss is ascribed to the lattice oxygen loss governed by the following equations [4.5.1 and 4.5.2]:

$$2Co_{Co}^{\bullet} + O_O^X \rightleftarrows 2Co_{Co}^X + V_o^{\bullet\bullet} + \frac{1}{2}O_2(g) \quad (4.5.1)$$

$$2Fe_{Fe}^{\bullet} + O_O^X \rightleftarrows 2Fe_{Fe}^X + V_o^{\bullet\bullet} + \frac{1}{2}O_2(g) \quad (4.5.2)$$

Where, $V_o^{\bullet\bullet}$ and O_o^X represent oxygen vacancy and oxygen ion respectively. Beyond 500˚C, more and more oxygen vacancies are formed because of thermally induced lattice oxygen loss. At the same time, to maintain the electrical charge neutrality the valence state of Co and Fe ions changed from IV to III valence state. The equilibrium of the above equation shifts towards the right as the temperature increases [4.51, 4.52] resulting an enhanced weight loss in the samples. The small difference in the weight loss pattern of the C4 and G4 powder may be correlated to the nonstoichiometry of the starting powder.

Summary

Rietveld refinement has been carried out of the sample assuming rhombohedral symmetry with R-3c space group and the lattice parameters were determined. The goodness of the fit and the lattice parameters have acceptable values. The TG profile shows a gradual slow weight loss in the temperature range 30-400˚C and rapid weight loss in the range 400-800˚C. These losses are ascribed to the desorption of water and carbon dioxide, the oxidation of Co^{3+} and the lattice oxygen loss.

4.5. Sintering and Grain Growth Kinetics of $La_{0.6}Sr_{0.4}Co_{0.2}Fe_{0.8}O_{3-\delta}$ Perovskite

Sintering is an important processing step from all ceramic materials. Sintering is associated with the heat treatment of ceramic materials at an elevated temperature. This heat treatment reduces the porosity of the ceramic compact and is associated with a certain amount of shrinkage of the body. Particles are transformed to grains during the sintering process. The electrical conductivity of materials often depends on the grain size, and its distribution [4.51, 4.52]. The sintering profile controls the size of the grain and pores in the microstructure and hence has a strong effect on the temperature dependence of conductivity [4.53]. The sintering and the grain growth rate is different for different powder morphology. The sintering study is also important to optimize the sintering profile.

4.5.1 Effect of process parameters on sintering behavior

The constant rate heating sintering behavior of powder compact prepared by varying the different process parameters has been shown in the Fig.4.5.1.

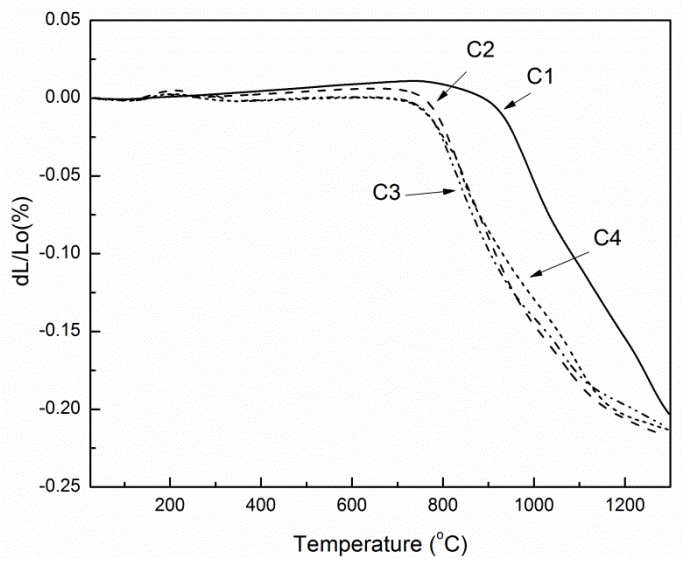

Fig. 4.5.1 Constant rate heating sintering behavior of LSCF powder compact prepared by varying different process parameters (C1, C2, C3 & C4)

The highest shrinkage in the LSCF (C4) sample is correlated with the high surface area of the powder (Table 4.2.1). The onset of densification was found to decrease with process parameter increase (C1-C4). The decrease in onset temperature could be correlated to the surface area of the powder. The surface area of the powder decreases with the increase in process parameters (C1-C4). The increase in surface area could also be seen from the morphology of the powder. However, the onset temperature for densification was found to be independent of the process parameter variations (C2-C4) and for these samples the shrinkage starts in the temperature range 650 - 750°C.

4.5.2. Initial stage sintering kinetics

The typical constant rate heating sintering of LSCF (C4) samples as a function of heating rate has been shown in Fig. 4.5.2. It could be seen that the samples sintered at a low heating rate has higher shrinkage as compared to that at a fast heating rate. Thus, the heating rate had a strong influence on the densification behavior of the LSCF samples. Identical observations were also found for the samples prepared with different process parameters [LSCF (C1-C4, G1-G4) samples]. Thus, slow heating rate may be beneficial for achieving high density in these samples.

An attempt has also been made to identify the densification mechanism of LSCF powder during the initial stage of sintering. It has been well studied that

dilatometric data (below 3% shrinkage) could be well fitted by the following equation (4.5.1-2):

$$\frac{\left(\frac{\Delta L}{L_0}\right)}{T} = Constant\ X \exp\left(-\frac{nE_a}{RT}\right) \qquad (4.5.1)$$

Where, $\frac{\Delta L}{L_0}$ is the relative shrinkage at temperature T, E_a is the activation energy, and n is constant; describes the sintering mechanism (n = 1, 0.5, 0.33 and 0.4 for viscous, surface diffusion, grain-boundary diffusion and volume diffusion respectively). Equation 4.5.1 can be rewritten as follows:

$$\ln\left[\frac{\left(\frac{\Delta L}{L_0}\right)}{T}\right] = \ln(Constant) - \frac{nE_a}{RT} \qquad (4.5.2)$$

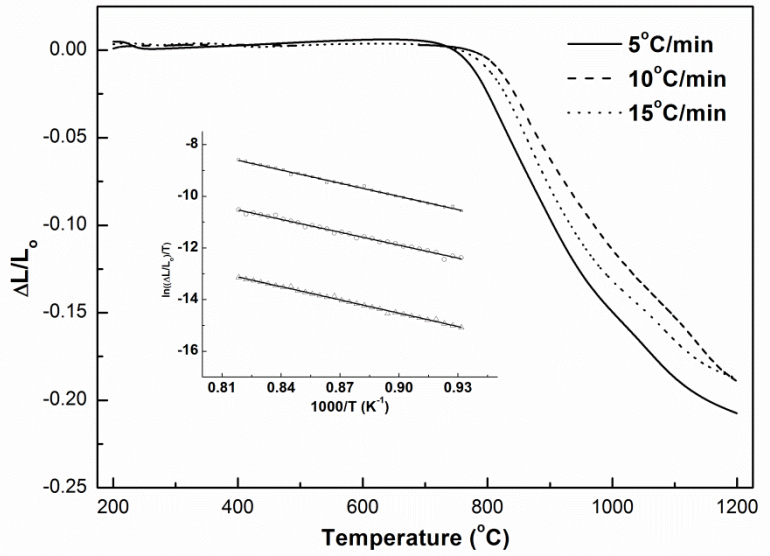

Fig. 4.5.2 Constant rate heating sintering behavior of LSCF (C4) sample as a function of heating rates

Hence, the plot of $ln\left[\frac{\left(\frac{\Delta L}{L_0}\right)}{T}\right]$ vs $\frac{1000}{T}$ will be a straight line. The slope of the straight line has been used to calculate nE_a. Here, the temperature range will be limited only to the initial stage of sintering (in the present investigation it is 850–950°C). The plot of $ln\left[\frac{\left(\frac{\Delta L}{L_0}\right)}{T}\right]$ vs $\frac{1000}{T}$ has been shown as an inset in the Fig.4.5.2. The symbols represent the experimental values as a function of heating rates. A set of parallel lines were obtained, which indicates a constant slope for the entire heating rate studied. The slope has been used to calculate densification parameter nE_a.

Isothermal densification behavior of the LSCF samples has also been studied at 850°C and 950°C to identify the densification mechanism. The typical isothermal densification behavior at a low-temperature range (850°C) and high-temperature range (950°C) for LSCF has been shown in Fig. 4.5.3. It could be seen that the densification takes place more rapidly at high temperature (950°) as compared to that at low temperature (850°C). The densifications of samples were found to have strong temperature dependence rather than time.

The sintering rate equation of isothermal shrinkage during initial stage of sintering could be given as (4.5.3):

$$\left(\frac{\Delta L}{L_0}\right) = K\, t^n \qquad (4.5.3)$$

Where, K is a temperature dependent constant, and n is the sintering exponent; describes the sintering mechanism as stated earlier.

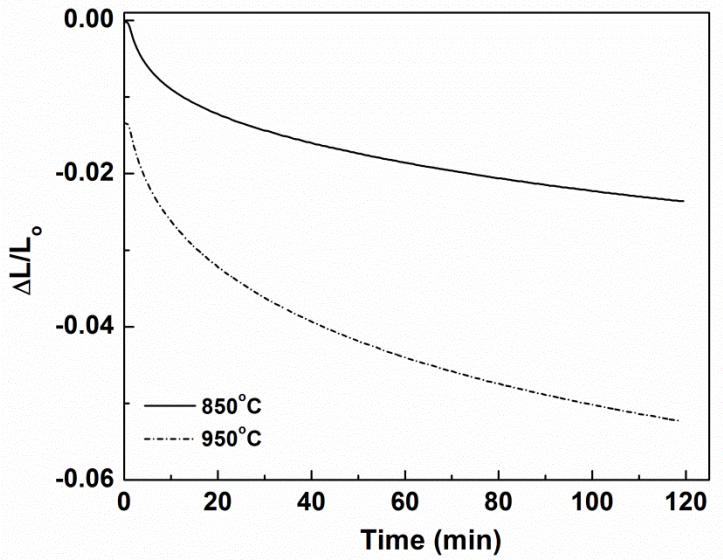

Fig. 4.5.3 Isothermal densification behavior of LSCF (C4) sample at 850°C and 950°C.

The experimental data has been fitted with the Eq. 4.5.3, using nonlinear curve fitting technique. The 'n' value was found to be 0.4113. As mentioned earlier, the 'n' value of 0.4 corresponds to volume diffusion. Thus, the present study confirms that the densification of LSCF sample is dominated by volume diffusion in the studied temperature region during the initial stage of densification. The activation energy for densification has also been calculated using the 'n' value obtained from the isothermal study and nE_a value calculated from constant rate heating sintering

study. The activation energy was found to be 165.81 kJmol^{-1}. Thus, the study suggests that the densification of LSCF samples is governed by volume diffusion of oxygen vacancies during the initial stage of sintering [Ref].

4.5.3 Microstructure of sintered LSCF sample

It has been reported earlier that the sintering profile could affect the microstructure of perovskite ceramics [4.54, 5.8]. The microstructural study has been conducted on sintered LSCF samples. The samples were sintered in the temperature 1150-1250˚C for 4 h. The SEM micrographs of LSCF (both C1-C4 and G1-G4) samples has been shown in the Figs. 4.5.4-4.5.7 respectively.

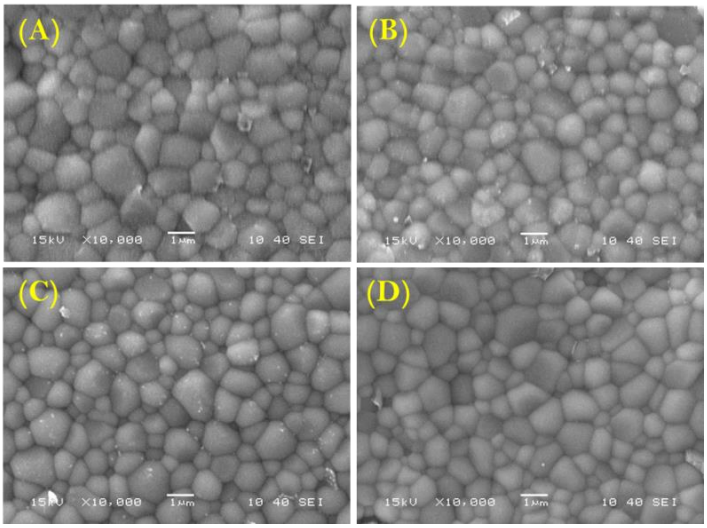

Fig. 4.5.4 Microstructure of LSCF compact (A) C1, (B) C2, (C) C3 and (D) C4 sintered at 1150°C/4hr

A dense microstructure with clear grain boundaries could be observed for all the samples. The grain size of the samples has also been calculated with the help of the computer programmed software *image J* and has been presented in Table-4.5.1. Also, the grain size distribution pattern generated from the software has been plotted in Fig. 4.5.8 (for selected samples). It could be seen that the grain size of the samples increases with increase in sintering temperature and is well understood from the consideration of grain growth kinetics. For 1150°C, the average grain size of samples vary from 1.31±0.05 µm of C1 derived samples to 0.78±0.03 µm of C4 derived samples.

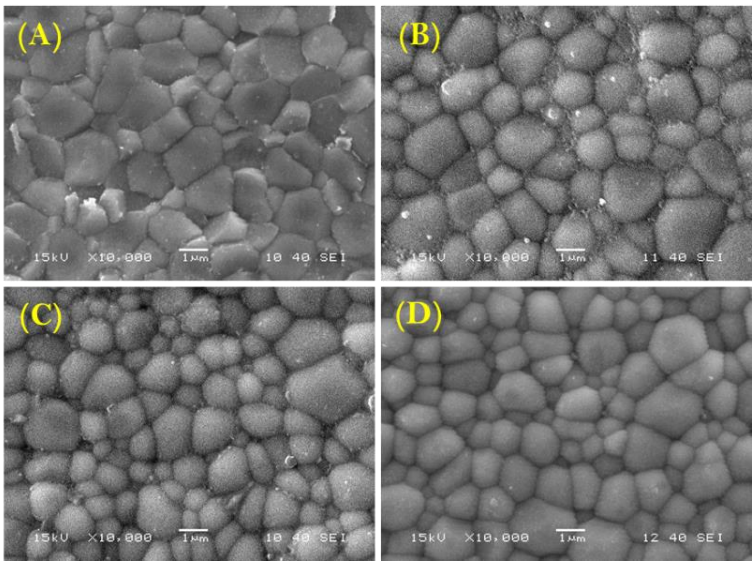

Fig. 4.5.5 Microstructure of LSCF compact (A) C1, (B) C2, (C) C3 and (D) C4 sintered at 1250°C/4hr

The increase of sintering temperature promotes the grains to increase in size: average grain size for C1-C4 derived samples at sintering temperature 1250°C are seen between 1.81±0.05 μm and 1.32±0.07μm.

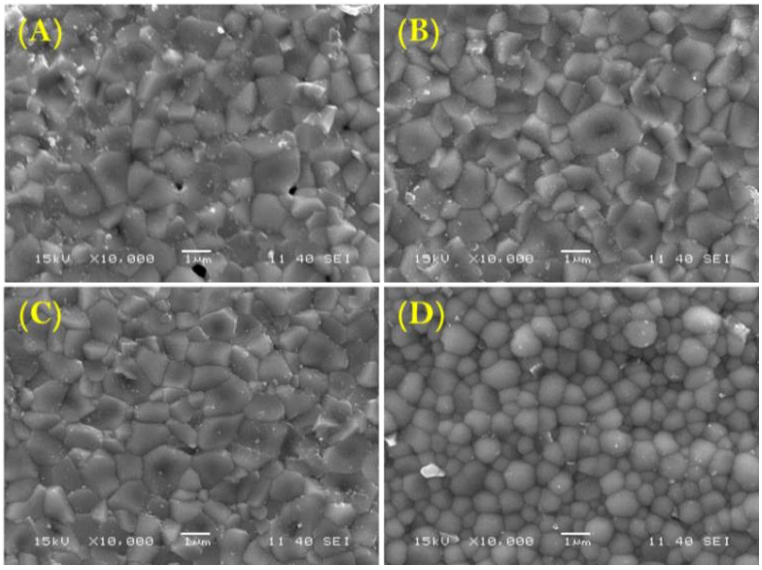

Fig. 4.5.6 Microstructure of LSCF compact (A) G1, (B)G2, (C) G3 and (D) G4 sintered at 1150°C/4hr

The sintering temperature effects on the grain growth for glycine fuel assisted powders are identical to those of the C1-C4 series.

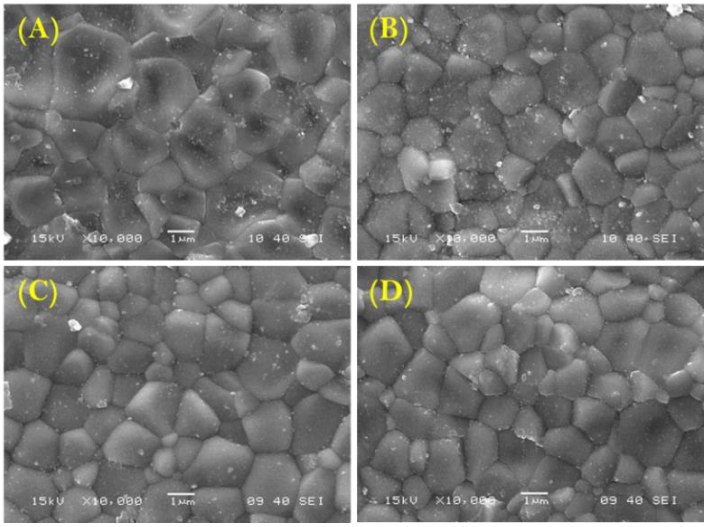

Fig. 4.5.7 Microstructure of LSCF compact (A) G1, (B) G2, (C) G3 and (D) G4 sintered at 1250°C/4hr

The microstructure of G1-G4 series at sintering temperature 1150°C has been shown in Fig. 4.5.6.

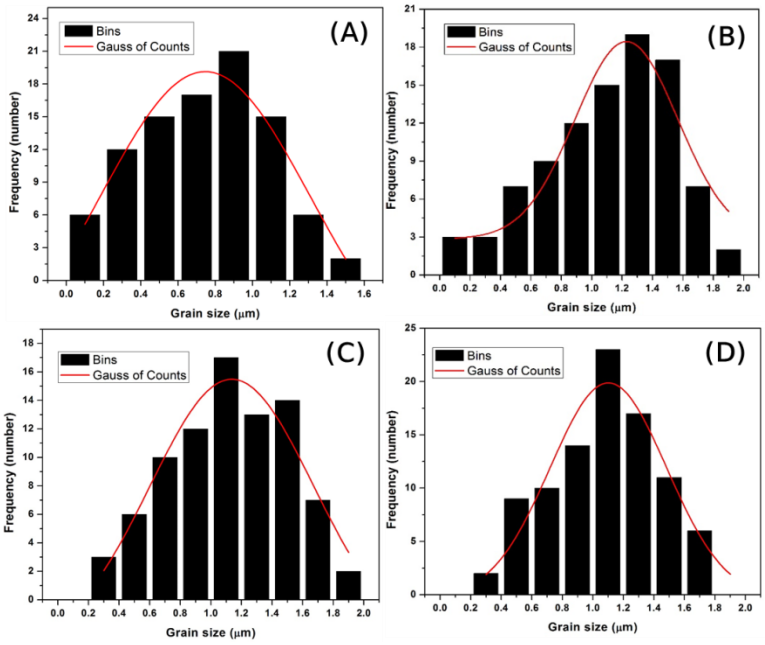

Fig. 4..5.8 Grain size distribution measured by Image J (A) C4 sintered at 1150°C, (B) C4 sintered at 1250°C, (C) G4 sintered at 1150°C and (D)G4 sintered at 1250°C all for 4h.

G1 has been found to have small pores and an average grain size of 1.24±0.05 μm. The sample G4 has a comparatively dense structure with spherical grains of the average diameter of 1.10±0.07 μm. The increase of the sintering temperature

to 1250°C facilitates the grain growth to have an average size of 2.06±0.03 µm for G1 derived samples and 1.12±0.07 µm for G4 derived samples respectively.

Table 4.5.2 Summary of grain size distribution of LSCF sintered compacts

Samples	Av. Grain size (µm)		Samples	Av. Grain size (µm)	
	Sintered at 1150°C/4h	Sintered at 1250°C/4h		Sintered at 1150°C/4h	Sintered at 1250°C/4h
C1	1.31(0.05)	1.81 (0.05)	G1	1.28(0.05)	2.06 (0.03)
C2	1.13(0.04)	1.63 (0.05)	G2	1.22(0.08)	1.44 (0.05)
C3	1.11(0.05)	1.42 (0.04)	G3	1.20(0.05)	1.41 (0.04)
C4	0.78(0.03)	1.32(0.07)	G4	1.10(0.07)	1.12(0.07)

4.5.4 Thermal expansion behavior

The thermal expansion behavior of $La_{0.6}Sr_{0.4}Co_{0.2}Fe_{0.8}O_{3-\delta}$ (C4 and G4) samples sintered at 1150°C for 4 h under air atmosphere has been shown in Fig.4.5.9. The curves show a linear expansion behavior in the temperature range (30 – 500°C). However, they showed a nonlinear expansion behavior in the temperature zone (500 – 800°C). The nonlinear thermal expansion behavior of the samples could be correlated with the lattice oxygen loss leading to the formation of oxygen vacancies with an increase in temperature. This behavior could also be supported by the thermogravimetric results discussed in the previous section. The lattice oxygen loss or the formation of vacancies in turn reduces the higher valence B-site cations to their lower valence state following Eqs. (4.5.1 and 4.5.2) to maintain the charge balance.

The ionic radius of an atom at its lower valence state is greater than its higher valence state counterpart. The ionic radii of Co^{+2}, Co^{+3}, Co^{+4} are 0.088 nm, 0.075 nm and 0.068 nm respectively [4.55 5.15]. The loss of oxygen ion from the lattice generates a repulsive force between the mutually exposed cations. On the other hand, the B-site cations undergo valence state change to maintain the charge neutrality thereby increases the size of the cations. The observed abnormal lattice expansion could be explained by the consideration of the repulsion force as well as the size change of cations. A very similar mechanism has been reported for cobalt containing perovskite materials [4.52, 4.56,4.57 5.13, 5.16, 5.17].

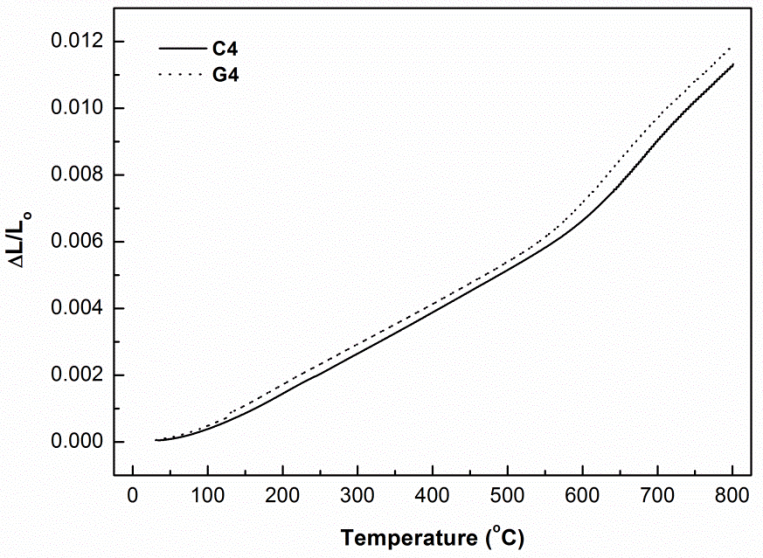

Fig. 4.5.9 Thermal expansion behavior of LSCF (C4 and G4) sample

The calculated specific TEC values are 14.92, 20.67, and 16.44 (x 10^{-6} K^{-1}) in the temperature 30 - 300, 300 – 600, and 30 - 800˚C respectively. The small difference in the thermal expansion behavior of the C4 and G4 derived sample is attributed to the initial non-stoichiometry of the starting powder arising from the very nature of the processing technique. The exact TEC values of LSCF have scattered data and varies from literature to literature depending on the temperature range of measurement and the microstructure of LSCF. The TEC in the temperature range 100-400°C is reported to be 16.8×10^{-6} K^{-1} [4.47], between 30-1000°C it is 21.4×10^{-6} K^{-1} [4.58]. The TEC value of LSCF samples was found to be similar with those reported earlier [4.47,4.50, 4.59].

4.5.5. Electrical conductivity of LSCF as a function of sintering temperature and soaking period

Figure 4.5.10 shows the temperature dependent electrical conductivity of LSCF samples as a function of powder processing parameters (C1-C4) for citric acid as fuel. A similar plot for glycine has also been shown in the Fig. 4.5.11. Both show a similar pattern of conductivity with temperature: increase first up to certain temperature (400-500°C), makes a flat peak with near constant value in the region 400°C-600°C and the starts to decrease. The electrical conductivity of LSCF can be accounted for due to two main sources, ionic and electronic contributions.

The ionic contribution arises because of the generation of an oxygen vacancy ($V_O^{\bullet\bullet}$) due to lattice oxygen loss as per the following defect equation (Eq. 4.5.4)

$$O_o^X \rightleftarrows \frac{1}{2}O_2(g) + V_o^{\bullet\bullet} + 2e' \qquad (4.5.4).$$

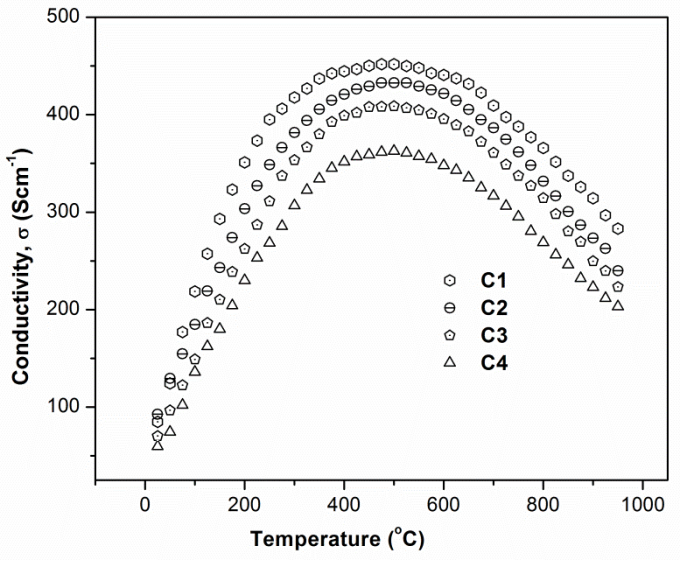

Fig. 4.5.10 Temperature dependence electrical conductivity of LSCF samples (C1-C4) obtained from the combustion synthesis using citric acid as fuel.

On the other hand, the electronic contribution part of the conductivity arises due to the change in oxidation state of the B-site cation. The presence of divalent A-site cation induces the B-site transition-metal ions to remain at a higher valence state [4.10]. In the present case of LSCF MIEC, the following defect equations (Eq. (4.5.5) and (4.5.6)) govern the mechanism:

$$Co_{Co}^X \rightleftarrows Co_{Co}' + h^{\bullet} \qquad (4.5.5)$$

$$Fe_{Fe}^X \rightleftarrows Fe_{Fe}' + h^{\bullet} \qquad (4.5.6)$$

In MIECs, the electronic conductivity is, in general, several orders of magnitude higher than the ionic conductivity [4.12, 4.13]. Therefore, it can be assumed that the values of conductivity for LSCF are mainly due to the electronic contributions.

The electrical conduction behavior of LSCF in lower temperature side could be described by a p-type small polaron hopping mechanism where charge carriers hopped between $B_B^{\bullet} - O - B_B^x$ [4.13]. The temperature dependent conductivity in this region could be expressed as:

$$\sigma = \left(\frac{A}{T}\right)\exp\left(-\frac{E_a}{KT}\right) \qquad (4.5.7)$$

Where, *A* *is* a material constant that depends on the site fraction of charge carriers and the neighboring ions probability of participating in the hopping process. E_a is the activation energy, k is the Boltzmann's constant and *T* is the absolute temperature [4.12, 4.16].

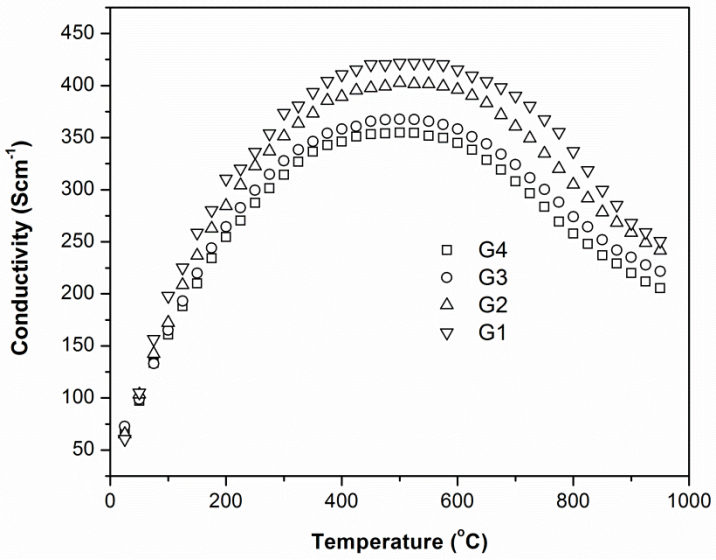

Fig. 4.5.11 Temperature dependence electrical conductivity of LSCF samples (G1-G4) obtained from the combustion synthesis using Glycine as fuel.

In high-temperature region, the electrical conductivity of LSCF was found to decrease with temperature. The decrease in conductivity is attributed to the formation of oxygen vacancies because of lattice oxygen loss as described in Eq. (4.5.4). The electrons so liberated would lead to the annihilation of hole-electron pairs. Now the formed oxygen vacancy acts as an electron trap and would cause a decrease in the hole-electron concentration resulting a decrease in the conductivity [4.17]. The reported values of conductivity for samples obtained here (~ 450 Scm^{-1}) are closely matching with the reported one in the literature [4.50].

It could also be observed that the conductivity of LSCF samples depends on the powder synthesis parameter as well as sintering temperature (Fig. 4.5.12). The conductivity of LSCF sample increases from 350 Scm^{-1} to 450 Scm^{-1} with an increase in sintering temperature. The grain size of C4 sample was found to be 0.78±0.03 µm, and 1.31±0.05 µm while sintered at 1150 and 1250°C respectively. A similar report has also been observed in the literature [4.45]. It has been

reported that with the increase in sintering temperature, the grain size increases, and the effective grain boundary area decreases. Both these two contributed to the conductivity and resulted in an increase in conductivity of the material.

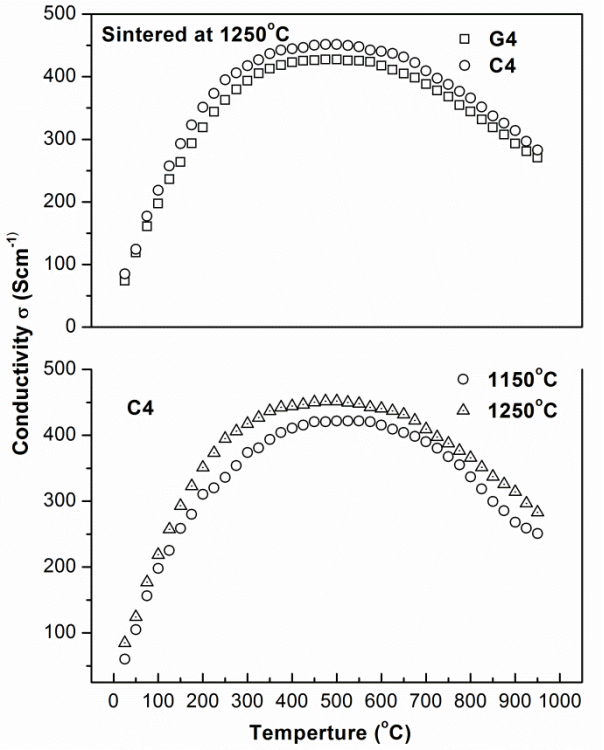

Fig. 4.5.12 Temperature dependence electrical conductivity of LSCF, (top) variation with fuel type and (bottom) with the sintering temperature of C4.

Finally, there is a comparative study of the conductivity of C4 with that of G4 sintered at 1250°C. The variations in the conductivity values are found to be insignificant. It is because of the similar grain sizes of both the samples. If we consider the grain size effect as the only reason for the variation of the conductivity, then G4 should have more conductivity values than C4 at a particular temperature. However, as seen from the Figure C4 possesses more conductivity (though the difference is very small) than G4. It may be attributed to the grain shape, grain size distribution and non-stoichiometry of the sample [4.60].

Summary

The constant rate heating sintering study shows highest shrinkage for the compact that has a high surface area in the powder state. The onset of

densification was found to decrease with process parameter increase (C1-C4) and was correlated with the surface area of the powder. The densification of LSCF samples was found to be governed by volume diffusion mechanism of oxygen vacancies during the initial sintering stage. It was observed that the initial stage of sintering was more a temperature dependent phenomenon than a time dependent one. The increase in sintering temperature increases the grain size and reduces pores in the sample. The average grain size maintains the same trend as in powder state of the sample after sintering: the grain size of C1/G1 is larger than that of C4/G4. The thermal expansion coefficient has a non-linearity with temperature and has an average value of 16.44 x 10^{-6} K^{-1}. The temperature dependent conductivity has been found to be governed by two principles, namely, polaron hopping for lower temperature zone and the creation of oxygen vacancy for higher temperature zone. The conductivity has also been found to be affected by the extent of grain boundary area.

4.6. Synthesis and characterization of SDC and YSZ electrolyte

Stabilized zirconia (8% Y_2O_3 doped Zr_2O_3 known as YSZ) has high ionic conductivity and desirable thermochemical properties under oxidizing as well as reducing atmospheres. It is well studied as electrolyte material for SOFC application [4.61]. To enhance the sinterability and ionic conductivity nanocrystalline YSZ has been synthesized and studied for several applications [4.60, 4.62, and 4.63]. The sintered electrolyte substrates are usually made very thin to reduce the electrolyte internal resistive loss. Application of YSZ electrolyte together with cobalt containing perovskite has been restricted due to the reaction between the cobalt-containing perovskite electrode and the YSZ electrolyte. Application of a thin buffer layer of GDC (Gd-doped ceria) or SDC (Sm-doped ceria) between YSZ and cobalt containing cathode is used to overcome the detrimental effect of the reaction [4.64].

SDC (20% Sm-doped CeO_2) is also widely studied as an intermediate temperature SOFC electrolyte due to its high ionic conductivity [4.65, 4.66]. However, these materials have some limitations as compared to YSZ electrolytes [4.67, 4.68] especially the thermal reduction under reducing atmosphere. Nanocrystalline YSZ and SDC have been widely used in intermediate temperature SOFCs as electrolyte applications [4.63]. The electrochemical behavior of the synthesized LSCF

material has been studied on SDC and YSZ electrolyte in the present study. This section deals with the electrolyte (YSZ and SDC) powder synthesis and electrolyte substrate fabrication.

4.6.1 Synthesis of YSZ powder and preparation of substrate

4.6.1.1 Phase formation

YSZ powders were synthesized by solution combustion route with citric acid as fuel. The detailed procedure has been described in Chapter - 3 in the Fig. 3.2.0 as a flow chart. The powder was calcined at 650°C for 4h. The XRD pattern of calcined powder is shown in the Fig. 4.6.1.

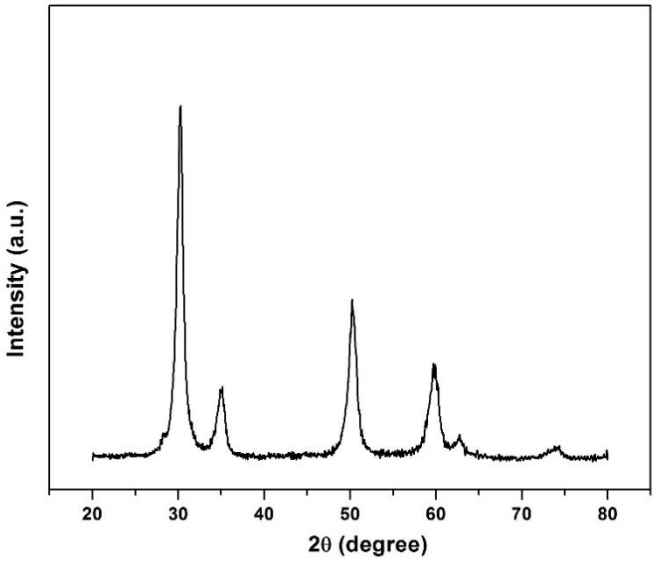

Fig. 4.6.1 XRD pattern of the YSZ powder calcined at 650°C for 4h

Well crystalline cubic YSZ peaks could be revealed from the pattern. No other impurity peaks could be detected. The study thus confirms the YSZ phase formation a temperature as low as 650°C. The broadening of the XRD peaks suggested the formation of fine crystalline YSZ powder by the synthesis technique adopted in the present study. The crystallite size calculated using Scherer's formula showed a value of 9 nm.

4.6.1.2 Phase purity

The powders synthesized by solution combustion techniques are very prone to contamination with carbon impurities. Usually, combustion synthesized powders are associated with unburnt carbon during combustion and even after calcination. The presence of these impurities often reduces the sinterability and reactivity of

the powder. Thus, along with the phase purity, powder quality also requires less contamination with carbon residues.

Figure 4.6.2 shows the FTIR pattern of the YSZ powder calcined at 650°C for 4h.

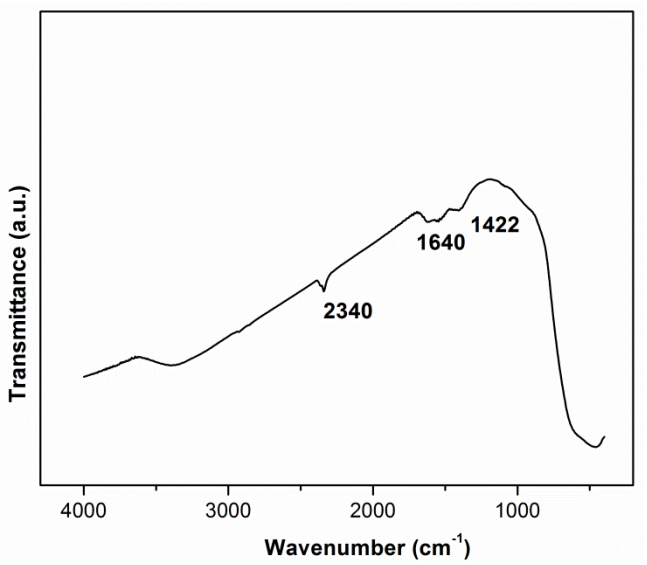

Fig. 4.6.2 FTIR Spectra of YSZ powder calcined at 650°C for 4h

Apart from the lower wavenumber side, a sharp peak that corresponds basically to the metal cation vibrations [4.6.10], there are three less prominent peaks at 2340cm^{-1}, 1640 cm^{-1}, and 1430 cm^{-1}. These peaks correspond to carboxyl group complexed with Zr and Y ions formed due to the reaction of the metal nitrate with hydroxyl carboxylic group during the preparation of precursor [4.6.2]. The less intensity of these peaks is attributed to the optimized fuel content because of the selected (fuel rich) value of Φ_e during combustion followed by the heat treatment during calcination.

4.6.1.3 Powder morphology

Figure 4.6.3 (A) shows the picture of a just calcined YSZ powder in a ceramic crucible. The FE-SEM image of the calcined powder is shown adjacent to it in Fig. 4.6.3 (B). The Powder morphology showed well-dispersed cuboid shaped powder particles of the order of few nanometers, the largest being hardly of one tenth of a micron. The distribution also reveals that the larger cuboid grains are produced at the expense of the smaller ones during the heat treatment. Thus, the YSZ powder synthesized in the present work have nanosized agglomeration free particles.

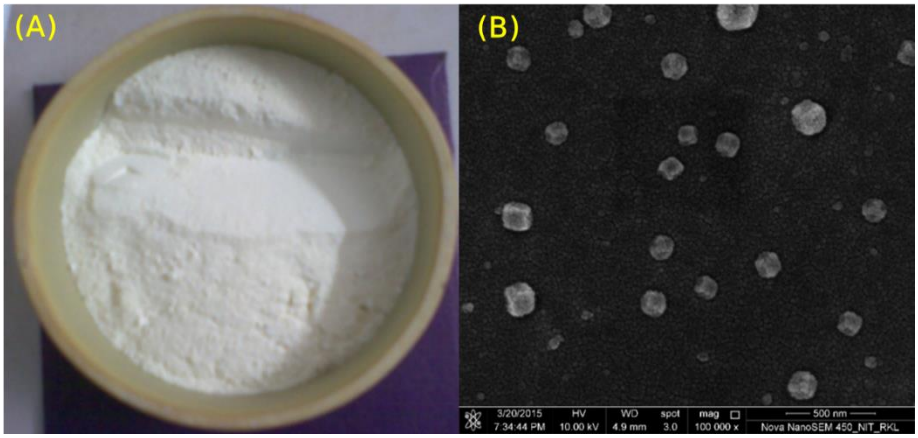

Fig. 4.6.3 (A) Calcined powder of YSZ (B) FE-SEM image of calcined YSZ powder (calcined at 650°C for 4h)

4.6.1.4 Substrate fabrication

The powders thus obtained above are mixed with a binder and pressed into circular discs and subsequently sintered at high temperature. The detailed fabrication technique has been as mentioned in the previous chapter. Thin electrolyte substrates were obtained by grinding the pre-sintered YSZ discs and upon subsequent sintering at a high temperature of 1550°C for 4h. The detailed procedure has been mentioned in sec. 3.5.1. The Archimedes densities of the sintered discs were measured to be > 97%.

The XRD of the sintered disc of YSZ has been shown in the Fig. 4.6.4. The sharp peak shows the high crystalline nature of the sintered powder compact. The pattern has been compared with the XRD pattern of the calcined powder. No other peaks could be revealed in the sintered pattern. Thus, the study confirms that YSZ powder synthesized in the present study remains stable while sintered at high temperature (1550°C). The only differences observed in the patterns is the broadening of the peaks, which is very low in the sintered samples as expected. Figure 4.6.5(A) shows the photograph of the thin YSZ substrates prepared in the present study. The yellowish colour observed in the thin circular hard substrates and typical characteristics features of YSZ. The SEM images of the surface of the pellets with different magnification are shown in Fig. 4.6.5 (B) & (C). The SEM images show the close packing surface structure of the sintered pellets with the hexagonal grain having a clearly distinct boundary.

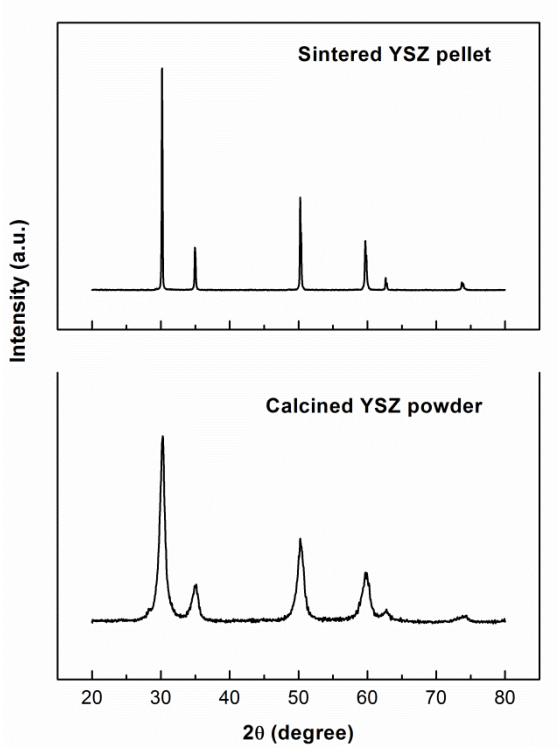

Fig. 4.6.4 **XRD pattern of YSZ pellet (top) sintered at 1550°C for 4h and the XRD of powders for comparison**

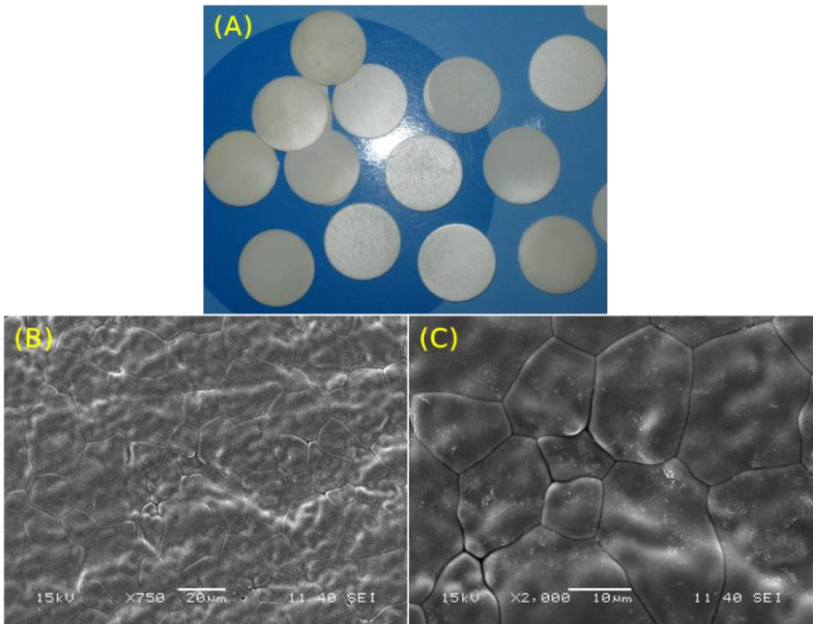

Fig. 4.6.5 **Pictures of thin YSZ substrates (A) and corresponding SEM images with different magnification ((B) and (C))**

The hexagonal shape of grains appears from a closed packed green powder system on sintering. This powder compact results dense microstructure on sintering. A very dense electrolyte is an essential requirement for cell fabrication. Thus the powder is suitable for electrolyte application. The minimum grain size is about 8µm and maximum of about 20µm was achieved.

4.6.2 Synthesis of SDC powder and characterization

SDC has been prepared by a similar solution combustion route by taking citric acid as fuel. The detailed procedure has been described in Chapter - 3 in the flow diagram Fig.3.2.5. The precursors have been prepared with fuel rich stoichiometry.

4.6.2.1 Phase formation

The XRD pattern of the powder is shown in the Fig. 4.6.6. The powder has been calcined at 550°C for 4h.

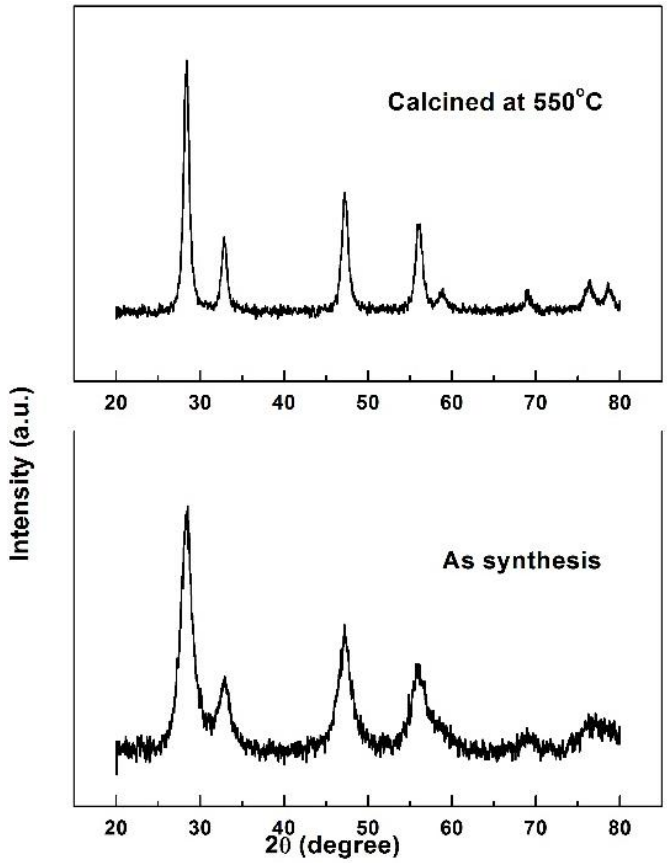

Fig. 4.6.6 XRD pattern of the SDC powder as a function of calcination temperature

This pattern shows the presence of pure cubic SDC phase in the calcined powder. The study confirms the formation of well crystalline SDC powder by calcining the powder at 550°C for 4h. The broad peaks show the formation of nanocrystalline powder with a crystallite size of 12nm.

4.6.2.2 Phase purity

To check the purity of the powder FTIR analysis has been carried out, and the pattern has been shown in the Fig. 4.6.7. The pattern consists of peaks at positions 2340 cm^{-1}, 1640cm^{-1} and 1365 cm^{-1} apart from the smaller wavelength peaks. These peaks may be attributed to the carboxylic group vibrations [4.6.2]. The peak intensities are however very small indicating that undetectable carbon residues were formed due to unburnt residues even after calcination. Thus, the synthesized powder has a minimum amount of carbon impurities. The lower wavelength peaks are attributed to metal oxide vibrations.

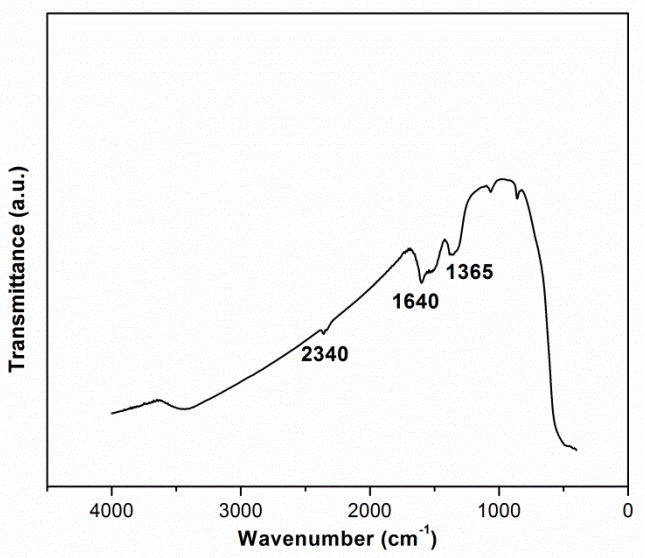

Fig. 4.6.7 *FTIR Pattern of calcined SDC powder (550°C)*

4.6.2.2 Powder morphology

The physical appearance of the calcined SDC powder has been shown in the Fig. 4.6.8 (A) showed whitish colour. Figure. 4.6.8 (B) shows the SEM micrograph of the calcined SDC powder. Agglomerated nanopowder particles could be revealed from the micrographs. The agglomerate sizes varied from 100 nm to few microns.

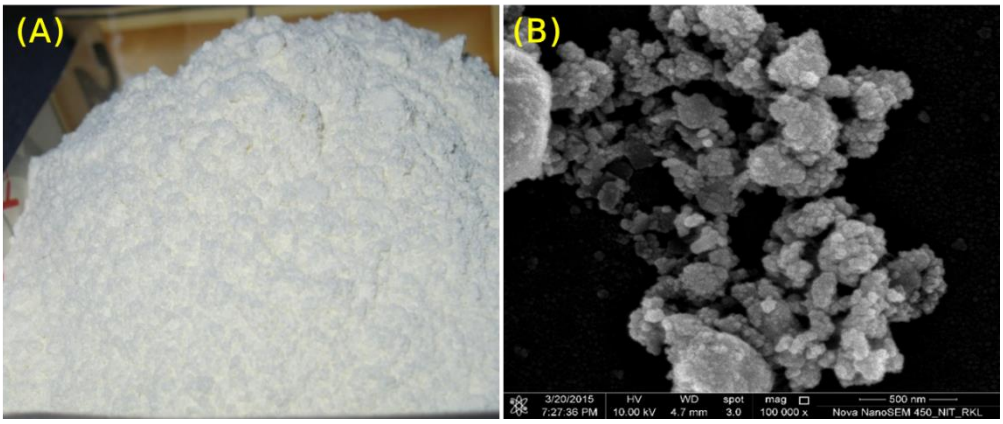

Fig. 4.6.8 (a) Picture of SDC calcined powder (b) FESEM image of SDC powder calcined at 650°C

4.6.2.4 Substrate fabrication

The powder was added to the binder, and circular discs were prepared as mentioned in the Chapter - 3 (sec. 3.21). The discs were sintered at 1500°C for 4h. The sintered discs were polished to have thin electrolyte substrates (sec. 3.2.1).

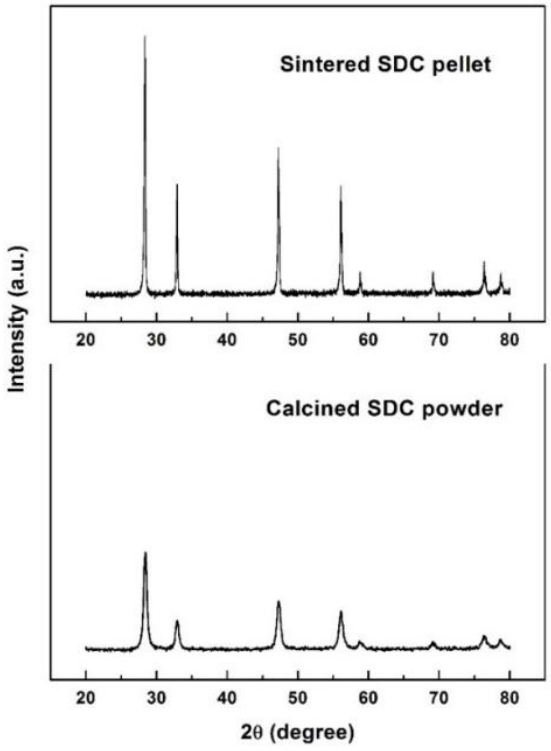

Fig. 4.6.9 XRD Patterns of SDC sintered pellets and calcined powder

The XRD of the sintered SDC pellet is shown in the Fig. 4.6.9. The XRD pattern of the calcined powder has also been incorporated in the figure for comparison. The

patterns are identical in all respects except the broadening nature of the peaks observed in calcined powder. The presence of sharp peaks in the pattern obtained from sintered sample indicated the polycrystalline nature of the sample. Identical peak position confirms the stability of the powder while sintered at high temperature.

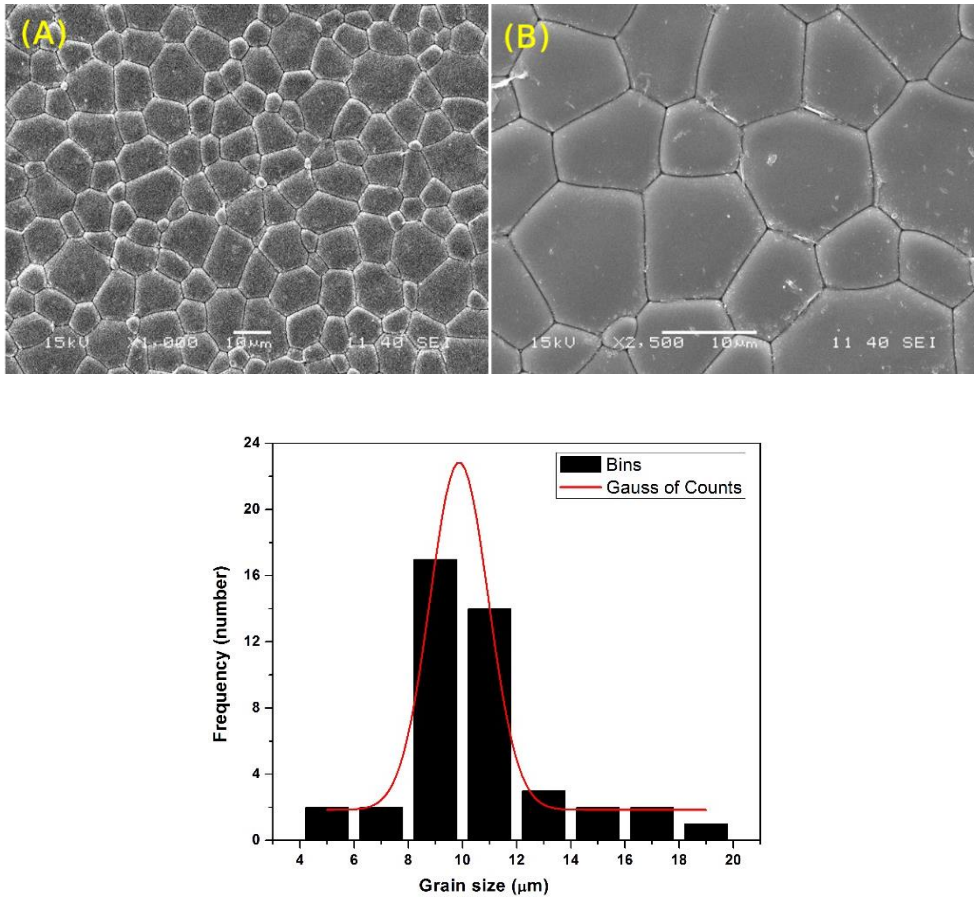

Fig. 4.6.10 **SEM micrographs of SDC pellets (A) 1000× magnification and (B) 2,500× magnification; (C) Grain size distribution of the sintered pellet**

The SEM images of the sintered pellets and the grain size distribution of sintered SDC pallets have been shown in Fig. 4.6.10. The sintered pellet consists of large grains with defined thick grain boundary. The grains are hexagonal in shape, and thus the packing is close. This accounts for a dense structure of the material. The density determined from the Archimedes principle is above 96%. As seen from the grain size distribution curve the minimum size around 5 µm and the maximum around 19 µm. There is a Gaussian sharp peak around 10 µm showing that maximum numbers of grains are around 10 µm in size. The large grains observed

in the samples are due to the growth of the nanopowders while sintered at high temperature.

Summary

Nano-sized YSZ and SDC powder synthesized by combustion method were seen to be phase pure and with a minimum carbon residue. Powder compacts in the form of circular discs wee sintered at 1550^{o}C to obtained density above 96% for both types of pellets. The SEM of the sintered pellets showed grains of hexagonal shape with a closed packing. The grain sizes vary from 8 μm to 20 μm in both cases. The larger grains were formed out of small particles because of high sintering temperature and may be because of the longer dwelling time of sintering. Thin substrates were prepared with a thickness of 0.3-0.4 mm by grinding the sintered discs over a SiC paper.

4.7. Chemical Compatibility of LSCF with YSZ and SDC

LSCF being an MIEC has high catalytic activity towards oxygen ion reduction [4.69]. However, when applied to YSZ electrolyte, it forms insulating layers because of chemical reactions at higher temperatures [4.70, 4.71]. The LSCF-YSZ interfacial reactive layers deteriorate the performance of the cell [4.70-4.72]. Fine powders are more prone to these reactions. For the application point of view as SOFC components powders must, therefore, be chemically compatible.

To test the suitability of these powders as intermediate SOFC component application, the phase analysis of the mixture of these powders have been carried out. Individually the powder mixtures were prepared with 50-50 weight % from each and heat treated at different temperatures (the detail of the mixture processing has been given in Chapter - 3). XRD pattern has been taken from each mixture at different temperature interval. The XRD of SDC+LSCF powder mixture has been shown in the Fig. 4.7.1 as a function of the treated temperature.The peak positions for LSCF has been denoted by L and those for SDC have been denoted by S. The figure shows that none of the graphs at 100^{o}C intervals of temperature shows phases other than LSCF and SDC. Thus, it is confirmed that no reactions occur between SDC and LSCF up to 1050^{o}C. The study suggests that SDC can be used as an electrode for LSCF cathode within fabrication temperature range 1050^{o}C.

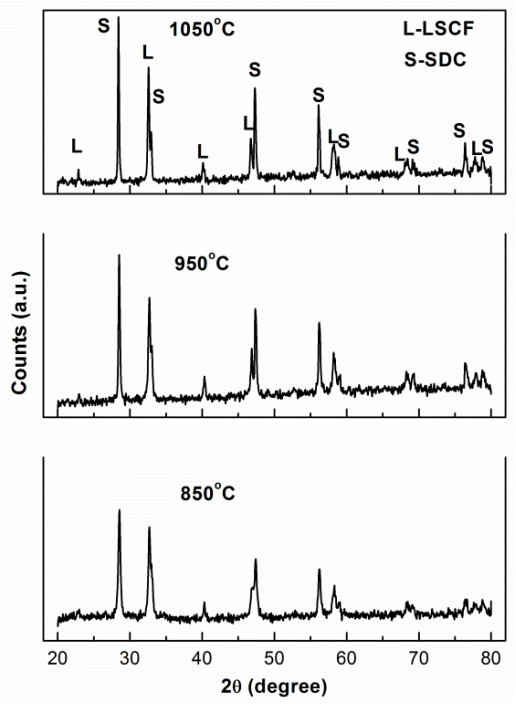

Fig. 4.7.1 XRD patterns of powder mixture of LSCF (C4) & SDC (50-50% by wt) indicating no reaction upto 1050°C.

The XRD of the YSZ+LSCF powder mixture as a function of temperature has been shown in the Fig. 4.7.2.

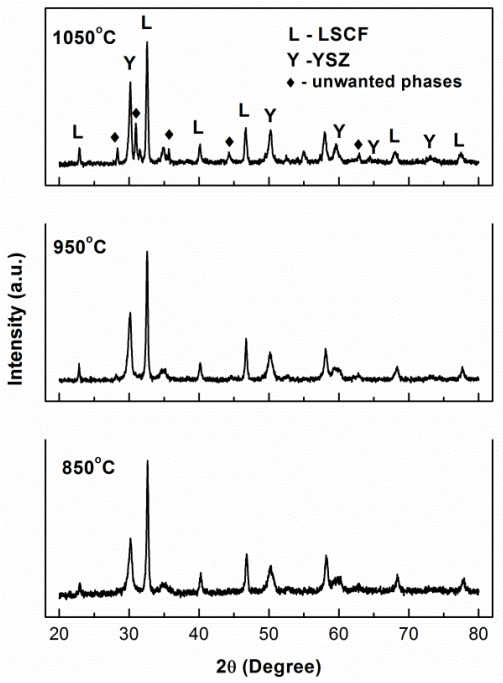

Fig. 4.7.2 XRD pattern of a powder mixture of LSCF (C4) & YSZ (50-50% by wt) showing reactions at 1050°C.

The peaks were denoted by Y and L respectively for YSZ and LSCF. It is seen from the figure that none of the temperatures, 850°C and 950°C, has a peak other than the LSCF and YSZ phase. It confirms that no reaction takes place between YSZ and LSCF up to 950°C temperature. However, at 1050°C the XRD pattern has unwanted impurity phases. The impurity phases have been identified to be those of $SrZrO_3$ and $La_2Zr_2O_7$. Many other pieces of literature also have found the similar conclusions [2.70-4.2]. The resistive reaction peaks forbid the use of LSCF with YSZ as the electrolyte at/above 1050°C fabrication temperature requirement. The study confirmed that YSZ can be used as an electrolyte material for LSCF electrode below 1050°C.

Summary

SDC and LSCF powder mixture heated together and analyzed by XRD for phase. It has been shown that the powder are chemically non-reactive up to temperature 1050°C. Whereas, the powder mixture of YSZ and LSCF heated together showed reactive phases of $SrZrO_3$ and $La_2Zr_2O_7$. Thus, it was concluded that SDC can be used as an electrolyte in association with the LSCF cathode up to 1050°C whereas there are chances of reaction for YSZ with LSCF electrode in that temperature application.

4.8. Fabrication of Symmetric Cell and AC Impedance Studies

As mentioned earlier in section 3.210 the in-house prepared inks were printed over the electrolyte substrates for the fabrication of half-cells. Three types of cells were fabricated: LSCF on (i) SDC electrolyte (ii) YSZ electrolyte and (iii) SDC interlayered YSZ electrolyte substrate. For the electrode application, LSCF should have the requisite amount of porosity (30-40%) for a charge (ion-electron) transport processes [4.73, 4.74] and thus, for the conductivity of the cell. Along with the volume percentage of the pores, the shape of pores also plays an important role in cell performance. The pores with irregular shape and random distribution are of particular importance for SOFC application [4.75]. These requirements have been taken into consideration during the processing and fabrication of the electrode.

4.8.1 Microstructure of LSCF electrode

Figure 4.8.1 shows the SEM image of the screen printed LSCF electrode on SDC electrolyte as a function of sintering temperature and powder processing. Figure

4.8.1 (a) shows the morphology of the LSCF electrodes were prepared with screen printing ink containing C4 and G4 LSCF powder at sintered at 950°C for 4h. It could be revealed from the micrographs that the electrode morphology consists of interconnected grain network with pores of random shape and distribution. The grain size and its distribution in both the samples are nearly identical. The magnified image of C4 shows clearly the formation of open pores. The interconnected pores occupy 30% of the volume as could be calculated from the stereology of the image.

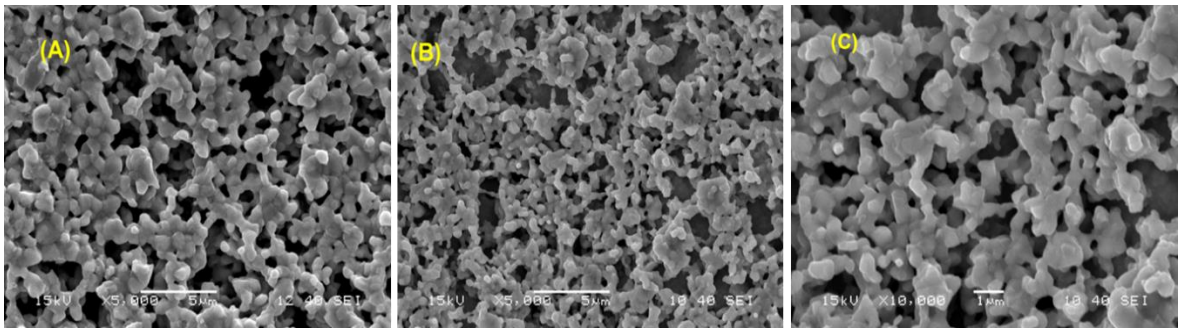

Fig. 4.8.1 (a) SEM image of electrodes (A) C4, (B) G4 and (C) C4 (magnified) printed on YSZ substrate sintered at 950°C

Figure 4.8.1 (b) shows the morphology of the LSCF electrode prepared with C1 and C4 powder to show the effect of initial particle characteristics on the porosity. The electrode prepared with fine particle morphology powder (C4- (B)) had relatively high volume fraction pore as compared to that prepared with coarse particles (C1- (A)). The interconnection between grains are matured [Fig (B)] and have a fine network of the pores.

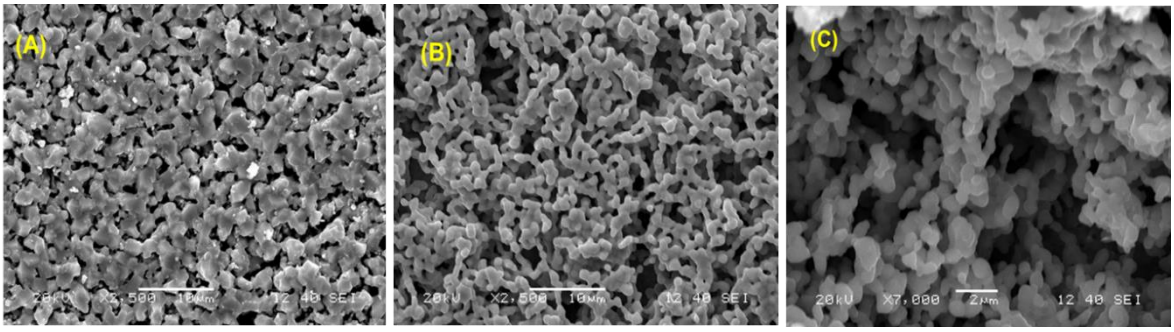

Fig. 4.8.1 (b) SEM image of electrodes (A) C1, (B) C4 and (C) C4 (magnified) printed on YSZ substrate sintered at 1050°C

The magnified image (C) showed the interconnected porosity formed by the sample prepared with C4 powder. The porosity of the sample has been calculated from Image analysis, and the calculated value is 40%. A comparison of the micrographs prepared with C4 powder indicated that there is no appreciable grain growth in the LSCF electrode as a function of sintering temperature. However, in both the cases pore showed a random shape and distribution required for fuel cell application.

4.8.2 AC impedance studies

The performance of an electrochemical cell depends on the polarization resistance $R_{p.}$ The polarization is obtained from the difference in the intercepts of the high- and low-frequency arcs with the X-axis (real component) offered by the electrode [4.76]. The electrochemical impedance spectroscopy is highly influenced by the microstructure of the electrode [4.76] . The grain size of the electrode, the measurement temperature, and the measuring environment play a crucial role in deciding the electrode polarization resistance [4.76, 4.77,4.78]. The present work aims to study the effect of powder synthesis parameter and hence, the powder morphology on the electrochemical behavior of the electrode. The polarization resistance also depends on the electrolyte used and the interlayer between the electrode and the electrolyte.

4.8.3 Effect of sintering temperature of the electrode

The impedance spectra of LSCF electrode (prepared with C4 powder) on SDC electrolyte as a function of sintering temperature is shown in Fig. 4.8.2. The spectra have been measured at 650^{o}C. The plausible equivalent circuit has also been included.

The presence of two arcs in the impedance spectra indicates the possibility of two electrode processes for oxygen reduction reaction. The high-frequency arc has been attributed to the charge transfer polarization. Whereas, the low-frequency arc corresponded to the oxygen adsorption/desorption processes on the electrode surface and related to the diffusion of the oxygen ions [4.10, 4.11, 4.79]. The different electrical contributions are as follows. (i) Electrolyte contribution, including the electrolyte resistance, as well as the DC resistance of leads and electrode (R_s). (ii) Inductance (L), arising from the inductive processes in the Pt

current/voltage probes or the experimental instrument at high temperature. Moreover, (iii) the polarization processes simulated by two R–Q elements (R_1, Q_1, R_2 and Q_2). All these electrical contributions have been taken into account in the equivalent circuit employed for fitting the experimental data. The electrolyte contribution has been eliminated while plotting the impedance spectra. In the impedance spectra, the symbols represent the experimental data, and the solid line represents the fitted data.

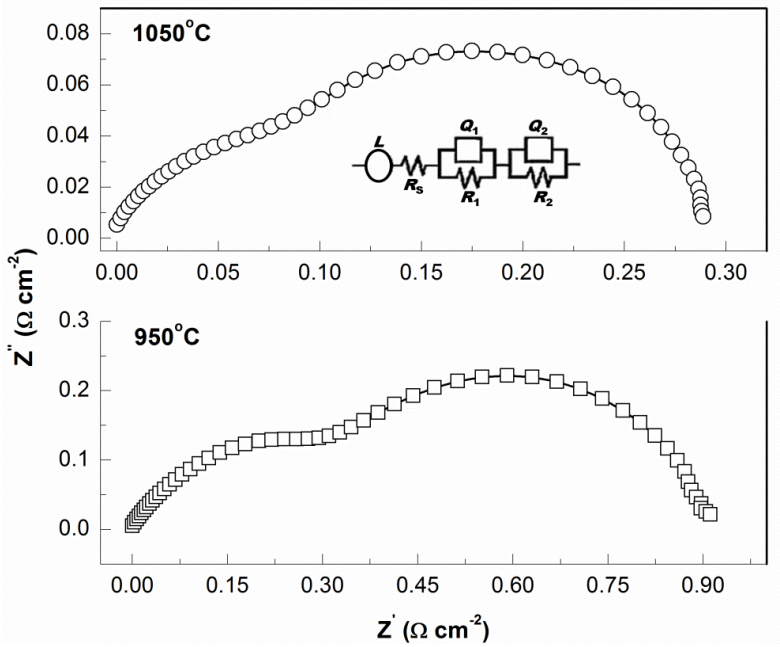

Fig. 4.8.2 Impedance spectra of LSCF (C4) electrode on SDC electrolyte as a function of sintering temperature

It could be seen from the impedance spectra that the polarization resistance of the LSCF electrode decreases with increasing sintering temperature of the electrode. It could also be seen from the micrograph (Fig. 4.8.1) that the electrolyte electrode (SDC-LSCF) contact area increases with increase in sintering temperature of the electrode. The increase in contact area between electrolyte-electrode eventually increases the current carrying capacity of the electrode. Thus, the electrode sintered at 1050°C showed low polarization resistance as compared to that sintered at low temperate (950°C).

The impedance spectra of LSCF electrode (prepared with C4 powder) on SDC electrolyte as a function of measurement temperature is shown in Fig. 4.8.3. The electrode was sintered at 1050°C for 4h. It could be seen from Fig. 4.8.3 that the polarization resistance decreases with increase in measurement temperature. It

has been observed earlier that the conductivity of the sample increases with increase in temperature. Thus, the decrease in polarization resistance in the sample with increasing measurement temperature is attributed to the decrease in charge transfer resistance as well as the decrease in diffusion resistance, which is very much expected.

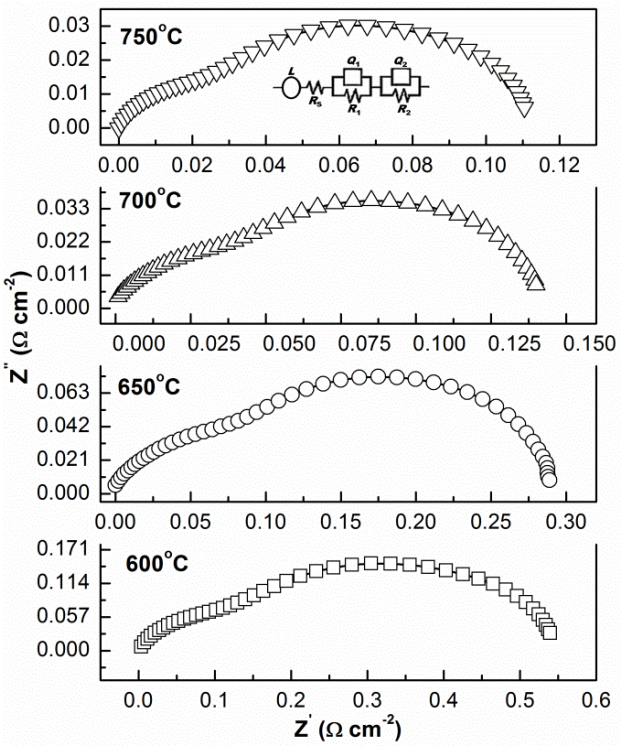

Fig. 4.8.3 Impedance spectra of LSCF electrode on SDC electrolyte as a function of measuring temperature

The different electrical parameters have also been calculated from the measured impedance data with the help of Z-view software and their Arrhenius plots have been displayed in Fig. 4.8.4. The contribution arising from the electrochemical reaction at an electrode-electrolyte interface is R_1 and is interpreted as charge transfer resistance. The polarization resistance associated with oxygen adsorption/desorption processes is R_2 and is related to the oxygen ions diffusion at the electrode [4.79, 4.80]. The polarization resistance R_p consists of charge-transfer resistance R_1 (at high-frequency) and the diffusion resistance R_2 (at low-frequency) as presented in the equivalent circuit.

The total polarization resistance (R_p) of LSCF electrode was found to decrease with increase in sintering temperature of the electrode (Fig. 4.8.4 (a)). The results

exhibited in Fig. 4.8.4 (b) and (c) indicates that the decrease in diffusion resistance R_2 played the key role in lowering total polarization resistance R_p. As mentioned above, R_2 has been attributed to the oxygen adsorption/desorption and is related to the oxygen ions diffusion. Porosity and the grain boundary hinder the oxygen diffusion process. The electrolyte electrode contact area increases with increasing sintering temperature of the electrode. Thus, with the increase in sintering temperature the oxygen ion diffusion in the samples increases. The increase in oxygen diffusion is attributed to the reduced diffusion resistance R_2. The decrease in R_p with an increase in measurement temperature is attributed to the enhancement of kinetics of both the charge transfer and diffusion processes associated with polarization.

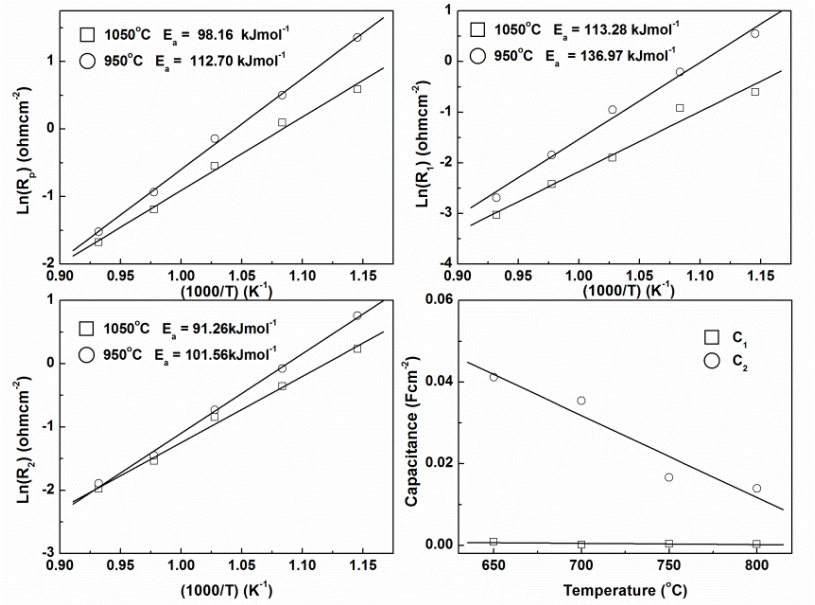

Fig. 4.8.4 **Temperature dependence electrode polarization contributions of LSCF electrode on SDC electrolyte: polarization resistance Rp (a), charge transfer resistance (R1) (b), diffusion resistance (R2) (c), and capacitance (d).**

The activation energy for oxygen diffusion has also been calculated from the Arrhenius plots of R_2 for the electrode. The value of activation energy was found to be 101.56 kJmol$^{-1,}$ and 91.26 kJmol^{-1} for the electrodes sintered at 950°C and 1050°C respectively. The decrease in activation energy with an increase in sintering temperature is related to the effective increase in contact area between the electrolyte-electrode interfaces of the electrode.

In order to clearly understand the relevant oxygen reduction process, the capacitance (C) for each electrode processes has also been calculated according to the equation given below [4.10, 4.80]:

$$C_i = \frac{(R_i Q_i)^{\frac{1}{n_i}}}{R_i} \qquad (4.8.1)$$

Where, C_i is interfacial capacitance. Q_i is constant phase element that represents time-dependent capacitive elements. R_i is cathode polarization resistance, and n_i is Q_i's similarity to a true capacitor of the individual electrode processes.

The temperature dependence capacitance of LSCF (C4 powder) electrode sintered at 1050°C for 4h for each process has been shown in Fig. 4.8.4 (d). The value of capacitance C_1 is found to be in the order of 10^{-4} Fcm^{-2}. This low value of capacitance can be related to oxygen ion as well as electron transfer processes [4.10, 4.80]. On the other hand, the value of the capacitance C_2 is found to be in the order of 10^{-2} Fcm^{-2} and decreases with measurement temperature. Thus, this process can be related to molecular oxygen dissociation and diffusion process [4.10, 4.80].

The exchange current, i_0, the intrinsic oxygen reduction reaction (ORR) rate, has also been calculated from the polarization resistance R_p [4.80] following equation (4.8.2).

$$i_0 = \frac{1}{R_p}\frac{RTv}{nF} \qquad (4.8.2)$$

Where, R_p is the cathode polarization resistance. R is the universal gas constant. T is the absolute temperature. F is the Faraday's constant. v reflects the number of times the rate-determining step occurs for one occurrence of the full reaction, and n is the total number of electrons passed in the reaction.

Four electrons are required for one molecule of oxygen reduction. The rate limiting step would likely have a stoichiometry of 1 for the oxygen reduction reaction. Thus for the ORR, n and v are assumed to be 4 and 1, respectively. The i_0 value thus, calculated at various temperatures has been listed in Table 4.8.1. It has been observed that i_0 in the samples sintered at 1050°C for 4 h increases from 4.56 $mAcm^{-2}$ to 34.39 $mAcm^{-2}$ with an increase in measurement temperature from 600

to 750°C. This increase in i_0 is quite obvious and is correlated to the increase in diffusivity with temperature.

Table 4.8.1: Intrinsic oxygen reduction reaction rate i0 (mAcm-2) of $La_{0.6}Sr_{0.4}Co_{0.8}Fe_{0.2}O_{3-\delta}$ as a function of temperature.

Sintering temperature (°C)	Temperatures (°C)			
	750	700	650	600
1050	34.39	18.10	12.23	4.56
950	22.91	11.33	2.5	1.04

4.8.3 Effect of starting powder morphology

The Impedance spectroscopy of the LSCF electrode (papered with LSCF C1-C4 powder) on SDC electrolyte measured at 650°C has been shown in Fig. 4.8.5 and that prepared with LSCF G1-G4 powder has been shown in Fig. 4.8.6 respectively.

The samples were sintered at 1050°C for 4h. It could be seen from the figure that the starting powder morphology influences the impedance of the sample. The polarization resistance was found to increase with the starting powder morphology. It could be seen from Fig. 4.2.1 that the agglomeration size of the LSCF powder decreases with as one move from C1 to C4 powder. The surface area of the powder and the particle size (Table 4.2.1) also revealed the similar behaviour. It could also be seen from the Fig. 4.8.1 (b) that the morphology of the electrode was quite different when the electrodes were prepared with C1 and C4 LSCF powder. The polarization resistance was found to decrease from 1.69 Ωcm^2 to 0.29 Ωcm^2 in the samples prepared with C1 and C4 powder respectively when measured at 650°C. The observed decrease in polarization resistance is attributed to the change in morphology of the precursor LSCF powder.

The sample prepared with G1-G4 precursor electrode powder also showed a very similar behaviour as that with LSCF C1-C4 powder (Fig. 4.8.5). The morphology of the precursor LSCF powder (Fig. 4.3.9) showed that the agglomeration size decreases from G1-G4. The surface area and particle size of powder also follow the similar trend. Moreover, the morphology of the electrode(Fig. 4.8.1) also influenced by precursor powder characteristics. The polarization resistance of the prepared with G1 and G4 powder was found to be 0.81 Ωcm^2 and 0.37 Ωcm^2

respectively when measured at 650°C. Thus, the observed polarization value is correlated to the morphology of the precursor powder.

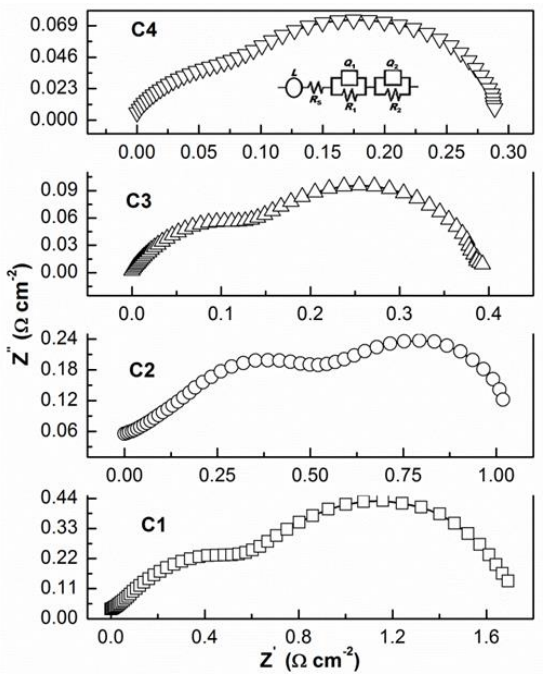

Fig: 4.8.5 **Impedance spectra of LSCF electrode on SDC electrolyte as a function of processing parameters (C1- C4**

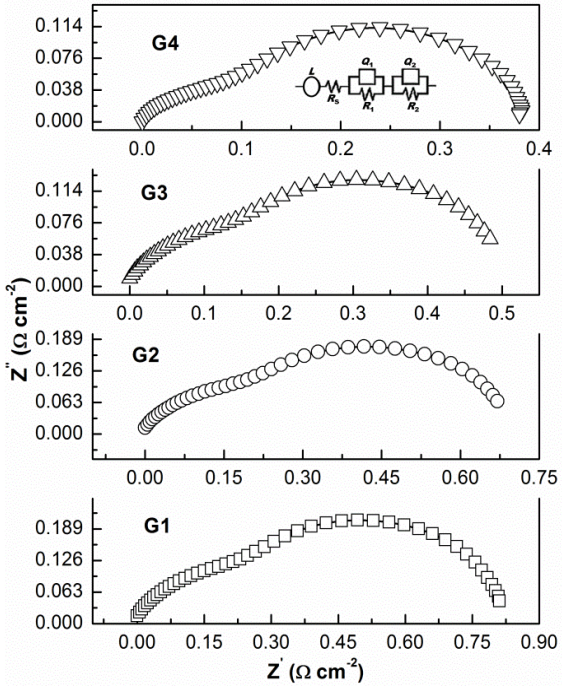

Fig: 4.8.6 **Impedance spectra of LSCF electrode on SDC electrolyte as a function of processing parameters (G1- G4)**

4.8.4 Effect of electrolyte

The impedance spectra of the LSCF (C4 precursor powder) electrode on SDC and YSZ electrolyte are shown in Fig. 4.8.6. Both the electrode were sintered at 950°C for 4 hr. The impedance spectra have been measured at 650°C. The LSCF electrode on YSZ electrolyte has not been sintered at a higher temperature as the chemical compatibility study showed the formation of different phases at 1050°C (Fig. 4.7.2). The impedance spectra showed two distinct contributions as discussed earlier. The polarization resistance was found to be 0.91 Ωcm^2 and 1.46 Ωcm^2 on SDC and YSZ electrolyte respectively. The spectra indicate an increase in polarization resistance on switching the electrolyte. The increase in polarization resistance with YSZ electrolyte is attributed to the chemical reaction between YSZ and LSCF leading to the formation of insulating phases at the electrode-electrolyte

interface. Compatibility study did not show the formation of any impurity phase when YSZ powder was heat treated with LSCF powder at 950°C (Fig. 4.7.2). The increase in polarization resistance thus indicates the formation of insulating phases at the interface although it has not been detected by XRD study.

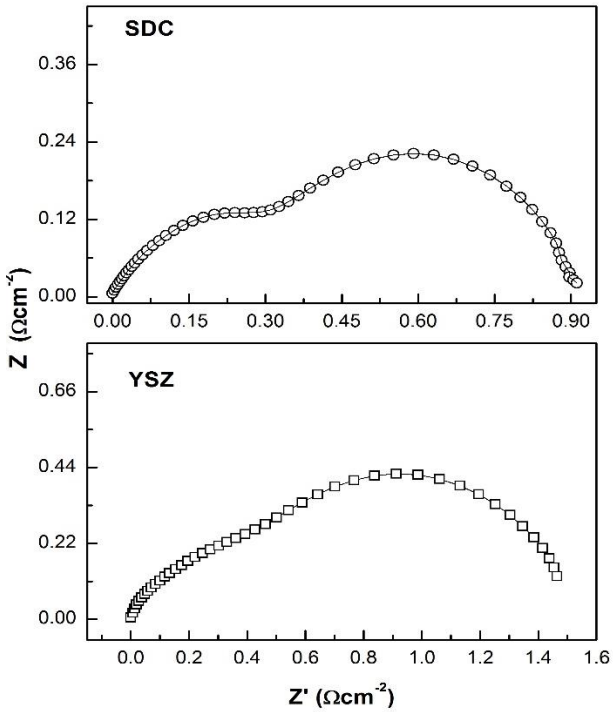

Fig. 4.8.6 Impedance spectra of LSCF (C4) electrode on YSZ and SDC electrolyte measured at 650°C

4.8.4 Effect of interlayer

An attempt has been made to use LSCF electrode on YSZ electrolyte with an application of SDC interlayer between LSCF and YSZ. SDC interlayer was screen printed on YSZ electrolyte followed by sintering at 1600°C. LSCF electrode was then screen printed on the SDC interlayered YSZ electrolyte followed by sintering at 1050°C for 4h. The impedance spectra of LSCF (C4) electrode on SDC interlayered YSZ electrolyte measured at 650°C has been presented in Fig. 4.8.7.

The impedance spectra of LSCF (C4) electrode on SDC electrolyte are also included in the figure for comparison. Two distinct electrode contributions could easily be revealed from the spectra and could be explained in the same line as discussed earlier. The polarization resistance of the SDC interlayered YSZ electrolyte was found to be 0.33 Ωcm^2 when measured at 650°C. The value was

0.29 Ωcm^2 on SDC electrolyte measured in a similar condition. Thus, the study showed that the polarization resistance of SDC interlayered YSZ electrolyte is comparable to that of SDC electrolyte. The use of the interlayer had arrested the reaction between YSZ and SDC, and thus, the polarization resistance decreased. Hence, the study indicated that application of SDC interlayer is effective for application of LSCF electrode with YSZ electrolyte.

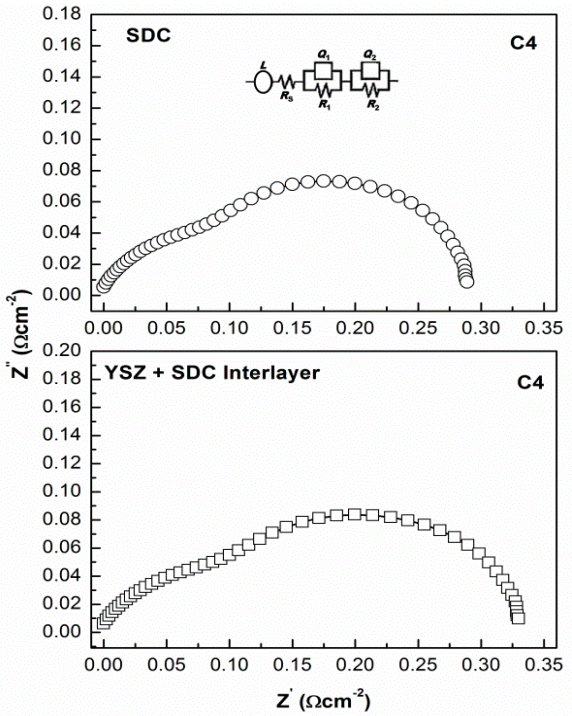

Fig. 4.8.7 **Impedance spectra of LSCF (C4) electrode on YSZ with an SDC interlayer and on SDC electrolyte measured at 650°C**

Summary

The impedance spectra have two arcs that indicate the possibility of two electrode processes for oxygen reduction reaction. The high-frequency arc has been attributed to the charge transfer polarization and the low-frequency one for oxygen adsorption/desorption processes on the electrode surface and related to the diffusion of the oxygen ions. The polarisation resistance (R_p) of LSCF electrode has been seen to decrease with an increase in the sintering temperature. It is attributed to the good contact as a result of sintering. Thus the charge transfer resistance and the diffusion resistance undergoes a decrease as the sintering temperature increases. The polarisation resistance decreases as a result of

increase in measurement temperature. It is attributed to the decrease in charge transfer resistance as well as the decrease in diffusion resistance. The value of activation energy was found to decrease from 101.56 $kJmol^{-1}$ to 91.26 $kJmol^{-1}$ as a rise in the electrode sintering temperature from 950^{o}C and 1050^{o}C. The decrease is related to the effective increase in contact area between the electrolyte-electrode interfaces of the electrode.

The exchange current i_0 in the samples sintered at 1050^{o}C for 4 h increases from 4.56 $mAcm^{-2}$ to 34.39 $mAcm^{-2}$ with an increase in measurement temperature from 600 to 750^{o}C. This increase in i_0 is quite obvious and is correlated to the increase in diffusivity with temperature. The polarization resistance was found to decrease from 1.69 Ωcm^2 to 0.29 Ωcm^2 in the samples prepared with C1 and C4 powder respectively when measured at 650^{o}C. The observed decrease in polarization resistance is attributed to the change in morphology of the precursor LSCF powder. Similar observations were found in case of Glycine powders.

The polarization resistance for YSZ electrolyte is larger than that of SDC. This indicates the formation of insulating phases at the interface although it has not been detected by XRD study. The use of the interlayer had arrested the reaction between YSZ and SDC, and thus, the polarization resistance decreased. Hence the study indicated that application of SDC interlayer is effective for application of LSCF electrode with YSZ electrolyte.

Chapter-5

Conclusions and Scope

5.1 Conclusions

The broad objective of the thesis was the preparation and characterization of Fe-rich $La_{1-x}Sr_xCo_{0.2}Fe_{0.8}O_{3-\delta}$ perovskites with optimized Sr-content for intermediate temperature SOFC. Study of the electrical and thermochemical behaviour of $La_{1-x}Sr_xFeO_3$was utilized for optimization of Sr-substitution level. The following conclusions could be achieved from the present study.

Studies on $La_{1-x}Sr_xFeO_3$ (LSF) powder series with x=0.1-1.0 resolved the following: Phase pure perovskite powder could be synthesized in LSF system at high-temperature calcination (1000°C) using solution combustion synthesis technique. XRD study revealed that Sr-substitution at La-site in lanthanum ferrite causes a structural change. The structure was found to be cubic (space group Pm-3 m) for $LaFeO_3$, which changes to orthorhombic (space group Pnma) for x = 0.1–0.3. A rhombohedral structure (space group R-3c) is obtained for x = 0.4–0.9 which changes to cubic (Pm-3 m) when x = 1.0. The structural change as a function of Sr substitution follows Roth's rule. The unit cell volume and hence the pseudo-cubic lattice parameter of LSF decreases with increasing Sr content and could be explained by the consideration of the ionic sizes of the A-site cations and its consequent effects.

LSF samples are prone to thermal reduction at high temperature with increasing Sr-substitution. Nonlinear thermal expansion of LSF is correlated with the lattice oxygen loss at high temperature associated with the change in oxidation state of the B-site cation.

The electrical conductivity of LSF samples increases with temperature in the low-temperature range attains a maximum and then decreases with temperature in the high-temperature zone. The electrical conduction behavior in the low-temperature zone could be described by p-type small polaron hopping mechanism. The decrease in conductivity observed in the high-temperature zone is correlated to the annihilation of charge carriers by the electrons liberated due to lattice oxygen loss. The electrical conductivity of LSF increases with Sr substitution up to x=0.4 and then decreases is attributed to the thermal reduction of higher valent B-site cations. Among the compositions studied $La_{0.6}Sr_{0.4}FeO_{3-\delta}$ exhibited a maximum conductivity.

Studies on LSCF powder synthesis using citric acid as fuel resolves the following: Elemental stoichiometric coefficient ϕ_e plays an important role on the combustion behavior of the gel. Fuel rich precursor (ϕ_e <1.0) favors the formation of phase pure and fine $La_{0.6}Sr_{0.4}Co_{0.2}Fe_{0.8}O_{3-\delta}$ powder. Precursor solution with ϕ_e = 0.87 yield an LSCF powder with surface area 8.34 m^2/gm. The addition of EDTA with a molar ratio M: C:E=1:2:0.5 was found to be effective in reducing the calcination temperature by 200°C to get a phase pure LSCF powder. The specific surface area of the LSCF powder prepared with EDTA addition increases to 24.6 m^2/gm. The combustion reaction was found to be promoted by the addition of extra oxidizer $NH_4(NO_3)$ resulting enhancement of surface area of LSCF powder. Precursor solution pH was found to affects the surface area of the LSCF powder and helps to reduce the residual carbon in the synthesized powder. The LSCF powder synthesized with precursor solution at pH 9 produced homogenous carbon free nano particles with a high specific surface area of 36.65 m^2/gm. The morphological study suggested the reduction of the agglomerate size of LSCF powder with the increasing processing steps.

Studies on LSCF powder synthesis using glycine as fuel resolves the following:

The use of zwitterionic glycine as fuel has similar inferences as those of citric acid. A precursor solution with fuel rich stoichiometric coefficient has been found favorable for the synthesis of phase pure LSCF powder. Glycine fuel in a neutral pH medium works well that has seen to reduce the phase formation temperature by 100°C. The reduction in phase formation temperature is described to the complete dissociation of glycine. The specific surface area of the powder has seen to increase with the addition of processing aids (as one goes from G1 to G4). The addition of EDTA has no effect on the reduction of the calcination temperature, but it decreases the crystalline size. $NH_4(NO_3)$ as an oxidizer has a role in decreasing the calcination temperature and a further decrease in the crystallite size. $NH_4(NO_3)$ may be attributed as a supplement of NO_3 required for combustion with glycine as a fuel. Further increasing pH has a positive effect that resulted in a single step combustion leading the formation of crystalline LSCF powder in as synthesized ash. The morphological study suggested that the agglomeration of the LSCF powder decreases with the additional processing steps. The FTIR analysis

showed a significant decrease of the residual carbon and nitrates with the increase in the additional processing step.

Characterization of LSCF samples resolves the following:

Rietveld refinement of the XRD pattern of LSCF powder suggests the presence of rhombohedral phase with R-3c space group in the synthesized powder. Thermal stability of LSCF powder showed a rapid weight loss in the range 400-800˚C. These loss are ascribed to the thermal reduction of higher valent B-site cation and the associated lattice oxygen loss.

The constant heating rate sintering study showed the highest shrinkage for the LSCF compact that prepared with high surface area powder. The onset of densification was decreased with the increase in powder synthesis process parameter (C1-C4) and was correlated with the surface area of the powder. The combination of constant rate heating sintering and isothermal sintering study indicated that the densification of LSCF samples was governed by volume diffusion mechanism of oxygen vacancies during the initial sintering stage. The densification of LSCF samples depends strongly on temperature rather than a time. The increase in sintering temperature increases the grain size and reduces pores in the sample. The average grain size maintains the same trend as that of the precursor powder. The LSCF samples showed nonlinear thermal expansion behaviour with temperature and have an average TEC value of $16.44 \times 10^{-6} K^{-1}$. The temperature dependent conductivity of LSCF was governed by small polaron hopping mechanism in the low-temperature zone. The electrical conductivity of LSCF sample decreases with increase in temperature in the high-temperature zone and is correlated with the consequent effect of lattice oxygen loss due to thermal reduction at high temperature. The electrical conductivity of LSCF sample depends on the grain size. It increases with increase in grain size.

Nano-sized YSZ and SDC powder synthesized by combustion method were seen to be phase pure and with a minimum carbon residue. Powder compacts in the form of circular discs were sintered at 1550°C to obtained density above 96% for both types of pellets. The SEM of the sintered pellets showed grains of hexagonal shape with a closed packing. The grain sizes vary from 8 μm to 20 μm in both

cases. The larger grains were formed out of small particles because of high sintering temperature as well as long dwell time.

Chemical compatibility study of SDC and LSCF powder mixture showed that the powders are chemically non-reactive up to temperature 1050°C. On the other hand YSZ reacts with LSCF at 1050°C leading to the formation of $SrZrO_3$ and $La_2Zr_2O_7$ phases. The study suggests that SDC can be used as an electrolyte in association with the LSCF cathode up to 1050°C whereas there are chances of reaction for YSZ with LSCF electrode in that temperature application.

The impedance spectra of LSCF on SDC electrolyte have two arcs that indicate the two electrode processes involved in oxygen reduction reaction at the cathode. The high-frequency arc is attributed to the charge transfer polarization and the low-frequency one for oxygen adsorption/desorption processes on the electrode surface and related to the diffusion of the oxygen ions. The polarization resistance (R_p) of LSCF electrode decreases with an increase in the sintering temperature of the electrode. The increase in sintering temperature of the electrode provides a good contact between electrode and electrolyte and the reduced porosity of the electrode. Thus, the polarization resistance decreases with increase in sintering temperature. The polarization resistance decreases with increasing measurement temperature and is correlated to the thermal activation of the both the electrode process involved. The value of activation energy was found to decrease from 101.56 $kJmol^{-1}$ to 91.26 $kJmol^{-1}$ as a rise in the electrode sintering temperature from 950°C and 1050°C. The decrease is related to the effective increase in contact area between the electrolyte-electrode interfaces of the electrode.

The exchange current i_0 for oxygen reduction increases from 4.56$mAcm^{-2}$ to 34.39 $mAcm^{-2}$ with an increase in measurement temperature from 600 to 750°C in the samples sintered at 1050°C for 4 h. This increase in i_0 is quite obvious and is correlated to the increase in diffusivity with temperature.

The polarization resistance of LSCF electrode is influenced by the starting electrode powder morphology. The polarization resistance was found to decrease from 1.69 Ωcm^2 to 0.29 Ωcm^2 in the samples prepared with C1 and C4 powder respectively when measured at 650°C. The observed decrease in polarization

resistance is attributed to the change in morphology of the precursor LSCF powder. Similar observations were found in the case of Glycine powders.

The polarization resistance of LSCF electrode on YSZ electrolyte is large than that with SDC electrolyte when the electrode was sintered at 950^{o}C/4h. The observed increase in polarization indicates the formation of insulating phases at the interface although XRD study has not detected it.

Studies on polarization resistance of LSCF electrode on SDC interlayered YSZ electrolyte ended up with almost similar polarization resistance as that observed with SDC electrolyte. Thus, the study suggests that application of SDC interlayer had arrested the reaction between YSZ and LSCF. The study indicated the application of SDC interlayer between YSZ electrolyte and LSCF electrode has the potential for application of LSCF electrode with YSZ electrolyte.

5.2 Scope of future work

The work reported here, needs few more other characterizations that were not included in this thesis. For example, the TEM images of the powder morphology could have revealed more detail about the distribution of the fine particles.

The effect of cathode layer thickness of on the electrochemical behavior can be studied by depositing more layer of LSCF over the electrolyte.

LSCF as a cathode material can be studied more appropriately by fabricating a cell with a different anode material. The cell can be studied under simultaneously reducing and oxidizing atmospheres.

Composite electrodes of nano $La_{0.6}Sr_{0.4}Co_{0.2}Fe_{0.8}O_{3-\delta}$ infiltrated LSGM could be studied for a potential cathode application. The cell performance could be enhanced by the incorporation of nano particles due to increasing in the TPBs. The process parameters for infiltration need to be optimized.

Mechanical behaviour of the thin film electrodes needs to be studied. The electrochemical performance of the cell may dependent on the thermal stress. The above issue may be addressed in as a future study.

References

Chapter-1

1.1 http://www.eia.gov/cfapps/ipdbproject/IEDIndex3.cfm?tid=44&pid=44&aid=2

1.2 **Department of Energy and IEA,** World energy Outlook 2004.

1.3 Birol F, Argiri M., **World Energy prospects to 2020** Energy 24 (1999) 905

1.4 Stambouli A B, Traversa E, Solid oxide fuel cells (SOFCs) **"A review of an environmentally clean and efficient sources of energy"** Renewable & Sustainable Energy Reviews 6 (2002)433.

1.5 Minh N Q, and Takahashi T, **Science and Technology of Ceramic Fuel Cells**, Elsevier, (1995)

1.6 Pan Z, Segal M, Arritt R W, Takle E S, **On the potential change in solar radiation over the US due to increases of atmospheric greenhouse gases** Renewable Energy 29 (2004) 1923

1.7 Stainforth D A, et al., **Uncertainity in predictions of climate response to rising levels of greenhouse gases** Nature 433 (2005) 403.

1.8 Singhal S C, Kendall K, **"High Temperature Solid Oxide Fuel Cells:Fundamentals, Design and Applications"** Elsevier Advanced Technology,Oxford, UK p. 1 (2003).

1.9 Vielstich W, **Fuel Cells; Modern Processes for the Electrochemical Production of Energy**. New York : Wiley (1970)

1.10 Minh N Q, **"Ceramic Fuel Cells"**, Journal of the American Ceramic Society, 76,563-88 (1993).

1.11 Yamamoto O, **Solid oxide fuel cells: fundamental aspects and prospects**, Electrochimica Acta, 45 (2000) 2423.

1.12 L. Xianguo, **Solid Oxide Fuel Cells: Materials, Properties and Performance**, CRC Press, (2009).

1.13 H. Davy, Nicholson's Journal of Nature Philosophy 144, 1802

1.14 Grove W R, **XXIV. On voltaic series and the combination of gases by platinum**, Philosophical Magazine series3, 14, 127, 1839

1.15 Nernst W, **Über die elektrolytische Leitung fester Körper bei sehr hohen Temperaturen**, Z. Elektrochem., 6 (1899) 41

1.16 Baur E and Preis H Z, **Über Brennstoff-ketten mit FestLeitern**, Z. Electrochem, 43 (1937) 727-32

1.17 Williams K R, **Francis Thomas Bacon, 21 December 1904-24 May 1992** Biographical Memoirs of the Fellows of the Royal Society, 39 (1994), 3-18

1.18 Steele B C H, Heinzel A, **Materials for Fuel-Cell Technologies**, *Nature*, 414, (2001) 345-52

1.19 Laminie J, Dicks A L, **Fuel cell systems Explained**. Wiley, New York, (2000) 308

1.20 Blomen L, & Mugerwa M, **Fuel Cell Systems** ,Plenum Press, New York (1993)

1.21 Williams M C, **Status of Solid Oxide Fuel Cell Development in Japan**, In: Proceedings of the 4th International Symposium On SOFC-IV, (Yokohama, Japan) (1995) 3-9.

1.22 Nishikawa M, **Status of Solid Oxide Fuel Cell Development in the United States**, In: Proceedings of the 4th International Symposium On SOFC-IV, (Yokohama, Japan, (1995) 10-19

1.23 Zegers P, **Status of Solid Oxide Fuel Cell Development in Europe**, In: Proceedings of the 3th Internationl Symposium On SOFC-III, (Honolulu, Hawaii, 1993),16-20

1.24 Yamaguchi T, Shimizu S, *et al* , **Design and Fabrication of a Novel Electrode-Supported Honeycomb SOFC**, Journal of American Ceramic Society 92 (2009) 107–111

1.25 Dennes T J and Schwartz J,**A Nanoscale Adhesion Layer to Promote Cell Attachment on PEEK,** Journal of American Chemical Society 131 (2009) 3456–3457

1.26 Francisco J; Jose S, **Development of the Solid Oxide Fuel Cell**, Energy Sources, 26 (2004) 177–188

1.27 Kee R J, Zhu H, *et al* **Solid Oxide Fuel Cells: Operating Principles, Current Challenges, And The Role Of Syngas** , Combustion Science and Technology, 180(2008) 1207–1244
1.28 Haile S M**, Fuel cell materials and components**, Acta Materilia, 51(19) (2003) 5981-6000.
1.29 Zhu W Z, Deevi S C, **A review on the status of anode materials for solid oxide fuel cells.** Materials Science and Engineering A. 362 (1-2) (2003) 228-239
1.30 Arachi Y, Sakai H, *et al* , **Electrical conductivity of the ZrO_2-Ln_2O_3 (Ln=Lanthanides) system**, Solid State Ionics, 122 (1999) 133
1.31 Wang, S, Kobayashi T, *et al*, **Electrical and ionic conductivity of Gd-doped ceria**, Journal of Electrochemical Society 147 (10) (2000) 3606
1.32 Tu H, Stimming U, **Advances, aging mechanisms and lifetime in solid-oxide fuel cells,** Journal of Power Sources 127(1-2) (2004) 284-293
1.33 Kharton VV, Marques FMB, Atkinson A. **Transport properties of solid oxide electrolyte ceramics: a brief review**. Solid State Ionics 174 (2004) 135-49.
1.34 Ishihara T. **Development of new fast oxide ion conductor and application for intermediate temperature solid oxide fuel cells.** Bulletin of Chemical Society of Japan 79 (2006) 1155-66
1.35 Badwal SPS. **Zirconia-based solid electrolytes -microstructure, stability and ionic-Conductivity** Solid State Ionics 52 (1992) 23-32.
1.36 Baumann F S, Maier J, *et al* **The polarization resistance of mixed conducting SOFC cathodes: A comparative study using thin film model electrodes** Solid State Ionics 179 (2008) 1198–1204
1.37 Simner S P, Anderson M D, *et al* , **Performance of a novel La(Sr)Fe(Co)O_3-Ag SOFC cathode**, Journal of Power Sources, 2006
1.38 Kenjo K, Nishiya M, **$LaMnO_3$ air cathodes containing ZrO_2 electrolyte for high temperature solid oxide fuel cells**, Solid State Ionics., 57(3-4) (1992) 295-302
1.39 Hammouche A, Siebert E, *et al*, **Crystallographic, thermal and electrochemical properties of the system $La_{1-x}Sr_xMnO_3$ for hightemperature solid electrolyte fuel-cells,** Materials Research Bulletin, , 24 (3) (1989) 367-380
1.40 Ostergard M J L, Clausen C, *et al*, **Manganitezirconia composite cathodes for SOFC: Influence of structure and composition,** Electrochem Acta. 40(12) (1995) 1971-1981
1.41 O. Yamamoto, et al., **Perovskite-type oxides as oxygen electrodes for high temperature oxide fuel cells.** Solid State Ionics, 22(2-3) (1987) 241-246
1.42 Petric A, Huang P, *et al* **Evaluation of La-Sr-Co-Fe-O perovskites for solid oxide fuel cells and gas separation membranes.** Solid State Ionics, 135, (2000) 719-725
1.43 K. Prater, **The renaissance of the solid polymer fuel cell**, Journal of power sources, 29 (1990) 239-250
1.44 Lv H, Zhao B Y, et al, **Effect of B-site doping on $Sm_{0.5}Sr_{0.5}M_xCo_{1-x}O_{3-\delta}$ properties for IT-SOFC cathode material (M = Fe, Mn)**. Materials Research Bulletin, 42(12) (2007) 1999-2012
1.45 Wang S, Zou Y, **High performance $Sm_{0.5}Sr_{0.5}CoO_{3-d}$ $La_{0.8}Sr_{0.2}Ga_{0.8}Mg_{0.15}Co_{0.05}O_3$ composite cathodes.** Electrochemistry Communications,8(6), (2006) 927-931
1.46 H. Fukunaga, **Reaction model of dense Sm0.5Sr0.5CoO3 as SOFC cathode**, Solid State Ionics, 132(3-4) (2000) 279-285.
1.47 Bae J M, Steele B C H, **Properties of Pyrochlore Ruthenate Cathodes for Intermediate Temperature Solid Oxide Fuel Cells**. Journal of Electroceramics, 3 (1999) 37-46
1.48 Yu H C, Fung K Z, **Electrode properties of $La_{1-x}Sr_xCuO_{2.5-\delta}$ as new cathode materials for intermediate-temperature SOFCs**. Journal of Power Sources,133,(2004) 162-168.
1.49 Tai L W, Nasrallah M M, *et al* **Structure and electrical properties of $La_{1-x}Sr_xCo_{1-y}Fe_yO_3$ Part 2. The system $La_{1-x}Sr_xCo_{0.2}Fe_{0.83}O_3$,** Solid State Ionics 76 (1995) 273-283

1.50 Ge L, Zhou W, *et al* / **Facile autocombustion synthesis of $La_{0.6}Sr_{0.4}Co_{0.2}Fe_{0.8}O_{3-\delta}$ (LSCF) perovskite via a modified complexing sol–gel process with NH4NO3 as combustion aid** Journal of Alloys and Compounds 450 (2008) 338–347

1.51 Zhao H, Shen W, *et al* / **Preparation and properties of $Ba_xSr_{1-x}Co_yFe_{1-y}O_{3-l}$ cathode material for intermediate temperature solid oxide fuel cells,** Journal of Power Sources 182 (2008) 503–509

1.52 Lee S, Lim Y, *et al*, **$Ba_{0.5}Sr_{0.5}Co_{0.8}Fe_{0.2}O_{3-\delta}$ (BSCF) and $La_{0.6}Ba_{0.4}Co_{0.2}Fe_{0.8}O_{3-\delta}$ (LBCF) cathodes prepared by combined citrate-EDTA method for IT-SOFCs** Journal of Power Sources 157(2006) 848–854

1.53 Hirschenhofer JH, **Status of commercialization effort**, American power conference, Chicago, IL, April 1993.

1.54 Kostogloudis G.C, Tsiniarakis G, *et al* / **Chemical reactivity of perovskite oxide SOFC cathodes and yttria stabilized zirconia** Solid State Ionics 135 (2000)529–535

1.55 Xu Q, Huang D, *et al* / **Structure, electrical conducting and thermal expansion properties of $Ln_{0.6}Sr_{0.4}Co_{0.2}Fe_{0.8}O_3$ (Ln = La, Pr, Nd, Sm) perovskite-type complex oxides** Journal of Alloys and Compounds 429 (2007) 34–39

1.56 Zhang S, Bi L, *et al*, **Fabrication of cathode supported solid oxide fuel cell by multi-layer tape casting and co-firing method** International journal of hydrogen energy 34 (2009) 7789-7794.

1.57 Plonczak P, Gazda M, *et al*, **Fabrication of solid oxide fuel cell supported on specially performed ferrite-based perovskite cathode** ,Journal of Power Sources 181 (2008) 1–7

1.58 Simner S P, Shelton J P, *et al*, **Interaction between La(Sr)FeO_3 SOFC cathode and YSZ electrolyte,** Solid State Ionics 161 (2003) 11 – 18.

1.59 Perez-Ramirez J, Vigeland B, **Lanthanum ferrite membranes in ammonia oxidation Opportunities for 'pocket-sized' nitric acid plants**, Catalysis Today 105 (2005) 436–442.

1.60 Swierczek K, Marzec J, *et al* , **LFN and LSCFN perovskites-structure and transport properties** Solid State Ionics 177 (2006) 1811–1817.

1.61 Garcia-Belmonte G, Bisquert J, *et al* , **Grain boundary role in the electrical properties of $La_{1-x}Sr_xCo_{0.8}Fe_{0.2}O$ perovskites**, Solid State Ionics 107 (1998) 203–211

1.62 Wang S, Katsuki M, *et al*, **High temperature properties of $La_{0.6}Sr_{0.4}Co_{0.8}Fe_{0.2}O_{3-\delta}$ phase structure and electrical conductivity** , Solid State Ionics 159 (2003) 71– 78

1.63 Tu HY, Takeda Y, *et al*, **$Ln_{0.4}Sr_{0.6}Co_{0.8}Fe_{0.2}O_{3-\delta}$ (Ln=La, Pr, Nd, Sm, Gd) for the electrode in solid oxide fuel cells** Solid State Ionics 117 (1999) 277–281.

1.64 Hartley A, Sahibzada M, *et al*, **$La_{0.6}Sr_{0.4}Co_{0.2}Fe_{0.8}O_3$ as the anode and cathode for intermediate temperature solid oxide fuel cells** ,Catalysis Today 55 (2000) 197–204

1.65 Ge L, Ran Ran , *et al* / **Low-temperature synthesis of $La_{0.6}Sr_{0.4}Co_{0.2}Fe_{0.8}O_{3-\delta}$ perovskite powder via asymmetric sol–gel process and catalytic auto-combustion,** Ceramics International 35 (2009) 2809–2815

1.66 Zhou W, Shao Z, *et al,* **LSCF Nanopowder from Cellulose–Glycine-Nitrate Process and its Application in Intermediate-Temperature Solid-Oxide Fuel Cells** , Journal of American Ceramic Society 27 (2008)

1.67 Gupta R K, Kim E Y, *et al,* **Mechanical, electrical and micro-structural properties of $La_{0.6}Sr_{0.4}Co_{0.2}Fe_{0.8}O_{3-\delta}$ perovskite-based ceramic foams** Journal of Physics D: Applied Physics 41 (2008) 032003

1.68 Zhao K, Xu Q,*et al*, **Microstructure and electrode properties of $La_{0.6}Sr_{0.4}Co_{0.2}Fe_{0.8}O_{3-\delta}$ spin-coated on Ce0.8Sm0.2O2−δ electrolyte** Ionics 17 (2011) 247–254

1.69 Zhao F, Wang Z, *et al*, **Novel nano-network cathodes for solid oxide fuel cells** Journal of Power Sources 185 (2008) 13–18

1.70 Serra J M, Uhlenbruck S, *et al*, **Nano-structuring of solid oxide fuel cells cathodes** Topics in Catalysis Vol. 40, Nos. 1–4, 2006

1.71 Ge L, Zhou W, et al,**Facile autocombustion synthesis of $La_{0.6}Sr_{0.4}Co_{0.2}Fe_{0.8}O_{3-\delta}$ (LSCF) perovskite via a modified complexing sol-gel process with NH_4NO_3 as combustion aid,** Journal of Alloys and Compounds 450 (2008) 338–347

1.72 Marinha D, Rossignol C, *et al*, **Influence of electrospraying parameters on the microstructure of $La_{0.6}Sr_{0.4}Co_{0.2}Fe_{0.8}O_{3-\delta}$ films for SOFCs** Journal of Solid State Chemistry 182 (2009) 1742–1748

1.73 Lei Z, Zhu Q, *et al,* **Low temperature processing of interlayer-free $La_{0.6}Sr_{0.4}Co_{0.2}Fe_{0.8}O_{3-d}$ cathodes for intermediate temperature solid oxide fuel cells** Journal of Power Sources 161 (2006) 1169–1175

Chapter-2

2.1 Singhal S C, Kendall K. "**High Temperature Solid Oxide Fuel Cells: Fundamentals, Design and Applications**" Elsevier Advanced Technology, Oxford, UK (2003) p.1

2.2 Adler S B, Lane J A, *et al*, **Electrode kinetics of porous mixed conducting oxygen electrodes**. Journal of Electrochemical Society 143 (1996) 3554-64

2.3 Ge L, Zhou W, *et al*, **Facile autocombustion synthesis of $La_{0.6}Sr_{0.4}Co_{0.2}Fe_{0.8}O_{3-\delta}$ (LSCF) perovskite via a modified complexing sol–gel process with NH_4NO_3 as combustion aid,** Journal of Alloys and Compounds 450 (2008) 338–347

2.4 Steele BCH. **Interfacial reactions associated with ceramic ion transport membranes**. Solid State Ionics 75(1995)157-65

2.5 Yasuda I, Ogasawara K, *et al*, Hishinuma M, Kawada T, Dokiya M.,**Oxygen tracer diffusion coefficient of (La, Sr)$MnO_{3-\delta}$**. Solid State Ionics 86-88 (1996)1197-201

2.6 Lee S, Song HS, *et al*, **Interlayer-free nanostructured $La_{0.58}Sr_{0.4}Co_{0.2}Fe_{0.8}O_{3-\delta}$ cathode on scandium stabilized zirconia electrolyte for intermediate temperature solid oxide fuel cells.** Journal of Power Sources 187 (2009)74-90

2.7 Liu M, Ding D, *et al*, **Enhanced performance of LSCF cathode through surface modification**.International Journal of Hydrogen Energy 37 (2012) 8613-20

2.8 Fossdal A, Menon M, *et al*, **Crystal Structure and Thermal Expansion of $La_{1-x}Sr_xFeO_{3-\delta}$ Materials** Journal of American Ceramic Society 87 [10] (2004) 1952–1958

2.9 Li J, Kou X, *et al*, **Density Functional Study of Electronic Properties of Perovskite Systems $La_{1-x}Sr_xFeO_3$** Journal of Materials Science and Engineering B 2 (2) (2012) 131-135

2.10 Xiwei Q, Zhou J, *et al*, **Auto-combustion synthesis of nanocrystalline $LaFeO_3$** Materials Chemistry and Physics 78 (2002) 25–29

2.11 Mostafavi E, Babaei A, *et al*, **Synthesis of nanostructured $Ln_{0.6}Sr_{0.4}Co_{0.2}Fe_{0.8}O_3$ perovskite by co-precipitation method** Journal of ultrafine grained and nanostructure materiasl 48 (2015) 45-52

2.12 Popa M, Frantti J, *et al*, **Lanthanum ferrite LaFeO3+d nanopowders obtained by the polymerizable complex method** Solid State Ionics 154–155 (2002) 437–445

2.13 Li X, Zhang H, *et al*, **Preparation of nanocrystalline LaFeO, using reverse drop coprecipitation with polyvinyl alcohol as protecting agent** Materials Chemistry and Physics 37 (1994) 132-135

2.14 Wang J, Liu Q, *et al*. **Synthesis and characterization of $LaFeO_3$ nano particles** Journal Of Materials Science Letters 21 (2002) 1059–1062

2.15 Patrakeev M V, Bahteeva H A, *et al*, **Electron/hole and ion transport in $La_{1-x}Sr_xFeO_{3-\delta}$** Journal of Solid State Chemistry 172 (2003) 219–231

2.16 Zheng W, Liu R, *et al*, **Hydrothermal synthesis of LaFeO3 under carbonate-containing medium,** Materials Letters 43 (2000) 19–22

2.17 Li X, Zhang H, *et al*, **Synthetic studies of nanocrystalline composite oxides with the perovskite structure based on LaFeO,** Materials Letters 15 (1992) 175-179

2.18 Kindermann L, Das D, *et al*, **Chemical compatibility of the $LaFeO_3$ base perovskites $(La_{0.6}Sr_{0.4})zFe_{0.8}M_{0.2}$ (z = 1, 0.9; M = Cr, Mn, Co, Ni) with yttria stabilized zirconia** Solid State Ionics 89 (1996) 215-220

2.19 Tietz F, Raj A, *et al*, **Electrical conductivity and thermal expansion of $La_{0.8}Sr_{0.2}(Mn,Fe,Co)O_{3-y}$ perovskites** Solid State Ionics 177 (2006) 1753 – 1756

2.20 Kilner J A, De Souza R A, *et al*, **Surface exchange of oxygen in mixed conducting perovskite oxides** Solid State Ionics 86-88 (1996) 703-709

2.21 Tanasescu S, Totir N D, *et al*, **Thermodynamic properties of some perovskite type oxides used as SOFC cathode materials** Solid State Ionics 119 (1999) 311–315

2.22 Lin J, Co A C, *et al*, **Oxygen reduction at sol-gel derived $La_{0.8}Sr_{0.2}Co_{0.8}Fe_{0.2}O_3$ cathodes** Solid state ionics 77 (2006) 377-387

2.23 Kim M C, Park S J, *et al*, **High Temperature Electrical Conductivity Of $La_{1-x}Sr_xFe0_{3-\delta}$ (x> 0.5)** Solid State Ionics 40141 (1990) 239-243

2.24 Li J, Kou X, *et al*, **Microstructure and Magnetic Properties of $La_{1-x}Sr_xFeO_3$ Nanoparticles**, physica status solidi (a) 191, (1) (2002) 255–259

2.25 Xiaojing Z, Huaju L, *et al*, **Structural Properties and Catalytic Activity of Sr-Substituted $LaFeO_3$ Perovskite** Chinese Journal Of Catalysis 7 (2012) 33

2.26 Striker T, Ruud J A, *et al*, **A-site deficiency, phase purity and crystal structure in lanthanum strontium ferrite powders**, Solid State Ionics 178 (2007) 1326–1336.

2.27 Zhang S, Bi L, *et al*, **Fabrication of cathode supported solid oxide fuel cell by multi-layer tape casting and co-firing method** International journal of hydrogen energy 34 (2009) 7789-7794.

2.28 Swierczek K, Marzec J, *et al* , **LFN and LSCFN perovskites - structure and transport properties,** Solid State Ionics 177 (2006) 1811–1817.

2.29 Perez-Ramirez J, Vigeland B. **Lanthanum ferrite membranes in ammonia oxidation Opportunities for 'pocket-sized' nitric acid plants,** Catalysis Today 105 (2005) 436–442.

2.30 Swierczek K, Marzec J, *et al*, **LFN and LSCFN perovskites - : structure and transport properties** solid state ionics solidi 177 (19-25) (2006) (1811-1817)

2.31 Sagdahl L T, Einarsrud M, *et al*, **Sintering behaviour of $La_{1-x}Sr_xFeO_{3-\delta}$ mixed conductors,** Journal of the European Ceramic Society 26 (2006) 3665–3673

2.32 Søgaard M, Hendriksen P V, *et al*, **Oxygen nonstoichiometry and transport properties of strontium substituted lanthanum ferrite** Journal of Solid State Chemistry 180 (2007) 1489–1503

2.33 Yao P J, Wang J, *et al*, **Preparation and characterization of $La_{1-x}Sr_xFeO_3$ materials and their formaldehyde gas-sensing properties,** Journal of Materials Science, 48(2013) 441-450

2.34 Wang W, Gross M D, *et al*, **The Stability of LSF-YSZ Electrodes Prepared by Infiltration,** Journal of The Electrochemical Society, 154 5 (2007) B439-B445

2.35 Suresh K, Panchapagesan T S , *et al*, **Synthesis and properties of $La_{1-x}Sr_xFeO_{3-\delta}$**, Solid State Ionics 126 (1999) 299–305.

2.36 Garcia-Belmonte G, Bisquert J, *et al*, **Grain boundary role in the electrical properties of $La_{1-x}Sr_xCo_{0.8}Fe_{0.2}O$ perovskites,** Solid State Ionics 107 (1998) 203–211

2.37 Wang S, Katsuki M, *et al*, **High temperature properties of $La_{0.6}Sr_{0.4}Co_{0.8}Fe_{0.2}O_{3-d}$ phase structure and electrical conductivity** , Solid State Ionics 159 (2003) 71– 78

2.38 Tu H Y, Takeda Y, *et al*, **$Ln_{0.4}Sr_{0.6}Co_{0.8}Fe_{0.2}O_{3-d}$ (Ln=La, Pr, Nd, Sm, Gd) for the electrode in solid oxide fuel cells** Solid State Ionics 117 (1999) 277–281.

2.39 Athanasiou C, Marnellos G, *et al*, **Methane Activation on a $La_{0.6}Sr_{0.4}Co_{0.8}Fe_{0.2}O_3$ Perovsksite; Catalytic and Electrocatalytic Results,** Ionics 3 (1997)

2.40 Liu J, Co A C, *et al*, **Oxygen reduction at sol–gel derived $La_{0.8}Sr_{0.2}Co_{0.8}Fe_{0.2}O_3$ cathodes,** Solid State Ionics 177 (2006) 377-387

2.41 Chanquía C M, Mogni L, *et al*, **Highly active $La_{0.4}Sr_{0.6}Co_{0.8}Fe_{0.2}O_{3-\delta}$ nanocatalyst for oxygen reduction in intermediate temperature-solid oxide fuel cells,** Journal of Power Sources, 270 (2014) 457-467

2.42 Baumann F S, Maier J, *et al*, **The polarization resistance of mixed conducting SOFC cathodes: A comparative study using thin film model electrodes,** Solid State Ionics 179 (2008) 1198–1204
2.43 Baumann F S, Fleig J, *et al*, **Impedance spectroscopic study on well-defined (La,Sr)(Co,Fe)$O_{3-\delta}$ model electrodes**, Solid State Ionics 177 (2006) 1071–1081
2.44 Ding C, Lin H, *et al*, **Synthesis of $La_{0.8}Sr_{0.2}Co_{0.8}Fe_{0.2}O_3$ nano powders and their application in solid oxide fuel cells,** Journal of Fuel Cell Science and Technology, 8 (5), (2011) art no. 051016
2.45 Ushkalov L M, Vasylyev O D, *et al*, **Synthesis and study of LSCF perovskites for IT SOFC cathode application,** ECS Transactions, 25 (2 PART 3), (2009) 2421-2426.
2.46 Baqué L, Djurado E, *et al*, **Electrochemical performance of nanostructured IT-SOFC cathodes with different morphologies,** ECS Transactions, 25 (2 PART 3), (2009) 2473-2480.
2.47 Ried P, Holtappels P, *et al*, **Synthesis and characterization of $La_{0.6}Sr_{0.4}Co_{0.2}Fe_{0.8}O_{3-\delta}$ and $Ba_{0.5}Sr_{0.5}Co_{0.8}Fe_{0.2}O_{3-\delta}$,** Journal of the Electrochemical Society, 155 (10), (2008) 1029-B1035.
2.48 Taheri Z, Nazari K, *et al*, **Oxygen permeation and oxidative coupling of methane in membrane reactor: A new facile synthesis method for selective perovskite catalyst** Journal of Molecular Catalysis A: Chemical, 286 (1-2) (2008) 79-86.
2.49 Jena H, Rambabu B, *et al*, **Effect of sonochemical, regenerative sol gel, and microwave assisted synthesis techniques on the formation of dense electrolytes and porous electrodes for all perovskite IT-SOFCs,** Proceedings of 4th International ASME Conference on Fuel Cell Science, Engineering and Technology, FUELCELL, (2006), 27
2.50 Mogni, LV, Yakal-Kremski K, *et al*, **Study of electrode performance for nanosized La0.4Sr0.6Co0.8Fe0.2O3-δ IT-SOFC cathode** ECS Transactions, 66 (2) (2015) 169-176
2.51 Kim-Lohsoontorn, P, Bae J. **Electrochemical performance of solid oxide electrolysis cell electrodes under high-temperature co electrolysis of steam and carbon dioxide** Journal of Power Sources, 196 (17) (2011) 7161-7168
2.52 Li S, Jin W, *et al*, **Synthesis and oxygen permeation properties of $La_{0.2}Sr_{0.8}Co_{0.2}Fe_{0.8}O_{3-\delta}$ membranes** Solid State Ionics, 124 (1999) 161-170
2.53 Zawadzki M, Gabowska H, *et al*, **Effect of synthesis method of LSCF perovskite on its catalytic properties for phenol methylation,** Solid State Ionics 181 (2010) 1131–1139
2.54 Xu Q, Huang D P, *et al*, **Structure, electrical conducting and thermal expansion properties of $Ln_{0.6}Sr_{0.4}Co_{0.2}Fe_{0.8}O_{3-\delta}$ (Ln = La, Pr, Nd, Sm) perovskite-type complex oxides** Journal of Alloys and Compounds 429 (2007) 34-39
2.55 Marinha D, Rossignol C, *et al*, **Influence of electrospraying parameters on the microstructure of $La_{0.6}Sr_{0.4}Co_{0.2}F_{0.8}O_{3-\delta}$ films for SOFCs** Journal of Solid State Chemistry 182 (2009) 1742–1748
2.56 Hartley A, Sahibzada M, *et al*, **$La_{0.6}Sr_{0.4}Co_{0.2}Fe_{0.8}O_{3-\delta}$ as the anode and cathode for intermediate temperature solid oxide fuel cells** ,Catalysis Today 55 (2000) 197–204
2.57 Ge L, Ran Ran, *et al*, **Low-temperature synthesis of $La_{0.6}Sr_{0.4}Co_{0.2}Fe_{0.8}O_{3-\delta}$ perovskite powder via asymmetric sol–gel process and catalytic auto-combustion**,Ceramics International 35 (2009) 2809–2815
2.58 Zhou W, Shao Z, *et al*, **LSCF Nano powder from Cellulose–Glycine-Nitrate Process and its Application in Intermediate-Temperature Solid-Oxide Fuel Cells** , Journal of American Ceramic Society, 27 (2008)
2.59 Gupta R K, Kim E Y, *et al*, **Mechanical, electrical and micro-structural properties of $La_{0.6}Sr_{0.4}Co_{0.2}Fe_{0.8}O_3$ perovskite-based ceramic foams,** Journal of Applied Physics 41 (2008) 032003 -8

2.60 Zhao K, Xu Q, *et al*, **Microstructure and electrode properties of $La_{0.6}Sr_{0.4}Co_{0.2}Fe_{0.8}O_{3-\delta}$ spin-coated on $Ce_{0.8}Sm_{0.2}O_{2-\delta}$ electrolyte,** Ionics 17 (2011) 247–254

2.61 Akbari-Fakhrabadi A, Sathishkumar P, *et al*, **Low frequency ultrasound assisted synthesis of $La_{0.6}Sr_{0.4}Co_{0.2}Fe_{0.8}O_{3-\delta}$ (LSCF) perovskite nanostructures,** Powder Technology, 276, (2015) 200-203.

2.62 Xi X, Kondo A, *et al*, **A simple mechanical process to synthesize $La_{0.6}Sr_{0.4}Co_{0.2}Fe_{0.8}O_3$ perovskite for solid oxide fuel cells cathode,** Materials Letters, 145 (2015) 212-215

2.63 Mimuro S, Makinose Y, *et al*, **Low-temperature synthesis of lanthanum strontium cobalt ferrite by the citrate complex method adding oleic acid,** Advanced Powder Technology, 26 (4)(2014)1245-1249.

2.64 Garcia L M P, Souza G L, *et al*, **Citrate-hydrothermal synthesis and electrochemical characterization of $La_{0.6}Sr_{0.4}Co_{0.2}Fe_{0.8}O_3$ for intermediate temperature SOFC** Materials Science Forum, 775-776 (2014) 673-677

2.65 Côrte D, Conceição R V Da, *et al*, **Structural and electrical properties of $La_{0.7}Sr_{0.3}Co_{0.5}Fe_{0.5}O_3$ powders synthesized by solid state reaction,** Ceramics International, 39 (7), (2013) 7975-7982

2.66 Garcia L M P, Macedo D A, *et al*, **Citrate-hydrothermal synthesis, structure and electrochemical performance of $La_{0.6}Sr_{0.4}Co_{0.2}Fe_{0.8}O_3$ cathodes for IT-SOFCs** Ceramics International, 39 (7), (2013) 8385-8392.

2.67 Jin H W, Kim J H, *et al*, **Lanthanum based iron and cobalt-containing perovskite using an inorganic nano-dispersants aqueous solution,** Journal of Ceramic Processing Research, 13 (SPL. ISS.2) (2012) s286-s290.

2.68 Zhou W, Ran R, *et al*, **Synthesis of nano-particle and highly porous conducting perovskites from simple in situ sol-gel derived carbon templating process,** Bulletin of Materials Science, 33 (4), (2010) 371-376

2.69 Ge L, Zhu Z, *et al*, **Effects of preparation methods on the oxygen nonstoichiometry, B-site cation valences and catalytic efficiency of perovskite $La_{0.6}Sr_{0.4}Co_{0.2}Fe_{0.8}O_{3-\delta}$** Ceramics International, 35 (8) (2009) 3201-3206

2.70 Ge L, Ran R, *et al*, **Facile auto-combustion synthesis for oxygen separation membrane application,** Journal of Membrane Science, 329 (1-2) (2009) 219-227.

2.71 Ge L, Zhou W, *et al*, **Facile autocombustion synthesis of $La_{0.6}Sr_{0.4}Co_{0.2}Fe_{0.8}O_{3-\delta}$ (LSCF) perovskite via a modified complexing sol-gel process with NH_4NO_3 as combustion aid,** Journal of Alloys and Compounds, 450 (1-2) (2008) 338-347

2.72 Lei Z, Zhu Q S, **Solution combustion synthesis and characterization of nanocrystalline $La_{0.6}Sr_{0.4}Co_{0.2}Fe_{0.8}O_{3-\delta}$ cathode powders,** Wuli Huaxue Xuebao/ Acta Physico - Chimica Sinica, 23 (2) (2007) 232-236

2.73 Liu S, Qian X, *et al*, **Synthesis and characterization of $La_{0.8}Sr_{0.2}Co_{0.5}Fe_{0.5}O_{3\pm\delta}$ nano powders by microwave assisted sol-gel route** Journal of Sol-Gel Science and Technology, 44 (3), (2007) 187-193

2.74 Song X, Wang Z, *et al*, **Synthesis and Characterization of $La_{0.8}Sr_{0.2}Cu_{0.95}$ $Fe_{0.05}O_{2.5-\delta}$** Journal of Rare Earths, 24 (SUPPL. 3), (2006) 14-17

2.75 Wu Z, Zhou W, *et al*, **Effect of pH on synthesis and properties of perovskite oxide via a citrate process,** AI ChE Journal, 52 (2), (2006) 769-776

2.76 Murata K, Fukui T, *et al*, **Morphology control of La(Sr)Fe(Co)O_{3-a} cathodes for IT-SOFCs,** Journal of Power Sources 145 (2) (2005) 257-261

2.77 Liu S, Xing C, *et al*, **Synthesis of $La_{0.8}Sr_{0.2}Co_{0.5}Fe_{0.5}O_{3-\delta}$ nanometer-size powders and its characterization,** Journal of Huazhong University of Science and Technology (Natural Science Edition), 33 (1) (2005) 81-83

2.78 Ghouse M, Al-Yousef Y, *et al*, **Preparation of $La_{0.6}Sr_{0.4}Co_{0.2}Fe_{0.8}O_{3-\delta}$ nanoceramic cathode powders for solid oxide fuel cell (SOFC) application,** International journal of hydrogen energy 35 (2010) 9411-9419

2.79 Jiang S P, **A comparison of O_2 reduction reactions on porous (La,Sr)MnO_3 and (La,Sr)(Co,Fe)O_3 electrodes,** Solid State Ionics, 146 (1-2) (2002) 1-22

2.80 Kammer K, **Studies of Fe–Co based perovskite cathodes with different A-site cations** Solid State Ionics 177 (2006) 1047–1051
2.81 Mai A, Tietz F, *et al*, **Partial reduction and re-oxidation of iron-and cobalt-containing perovskites using catalyst characterisation measurements** ,Solid State Ionics 173 (2004) 35–40
2.82 Kostogloudis G C, Ftikos C, **Properties of A-site-deficient $La_{0.6}Sr_{0.4}Co_{0.2}Fe_{0.8}O_{3-d}$ based perovskite oxides,** Solid State Ionics 126 (1999) 143–151
2.83 Tai L W, Nasrallah M M, *et al*, **Structure and electrical properties of $La_{1-x}Sr_xCo_{1-y}Fe_yO_3$ Part 2. The system $La_{1-x}Sr_xCo_{0.2}Fe_{0.8}3O_3$,** Solid State Ionics 76 (1995) 273-283
2.84 Waller D, Lane J A, *et al*, **The structure of and reaction of A-site deficient $La_{0.6}Sr_{0.4-x}Co_{0.2}Fe_{0.8}O_{3-\delta}$ perovskites,** Materials Letters 27 (1996) 225-228
2.85 Wailer D, Lane J A, *et al,* **The effect of thermal treatment on the resistance of LSCF electrodes on gadolinia doped ceria electrolytes** ,Solid State Ionics 86-88 (1996) 767-772
2.86 Lei Z, Zhu Q, *et al,* **Low temperature processing of interlayer-free $La_{0.6}Sr_{0.4}Co_{0.2}F_{0.8}O_{3-d}$ cathodes for intermediate temperature solid oxide fuel cells,** Journal of Power Sources 161 (2006) 1169–1175
2.87 Cesário M R, MacEdo D A, *et al,* **Synthesis, structure and electrochemical performance of cobaltite-based composite cathodes for IT-SOFC,** Crystal Research and Technology, 47 (7) (2012) 723-730
2.88 Kim J H, Park Y M, *et al,* **Nano-structured cathodes based on $La_{0.6}Sr_{0.4}Co_{0.2}Fe_{0.8}O_{3-\delta}$ for solid oxide fuel cells** Journal of Power Sources, 196 (7), (2011) 3544-3547
2.89 Da Conceião L, Silva A M, *et al,* **Combustion synthesis of $La_{0.7}Sr_{0.3}Co_{0.5}Fe_{0.5}O_3$ (LSCF) porous materials for application as cathode in IT-SOFC,** Materials Research Bulletin, 46 (2), (2011) 308-314
2.90 Chen J, Liu L N, *et al,* **The preparation of $La_{0.8}Sr_{0.2}Co_{0.5}$ $Fe_{0.5}O_{3-\delta}$ nano-powders by a polymer-assisted synthesis method Cailiao Kexue yu Gongyi/Material Science and Technology**, 19 (1), (2011) 71-75
2.91 Kwon H T, Kim J, *et al,* **Synthesis and characterization of porous $La_{1-x}Sr_xCo_{1-y}Fe_yO_{3-\delta}$ membranes fabricated using by electrostatic spray deposition,** Journal of the Korean Physical Society, 54 (3), (2009) 1223-1227
2.92 Zhou W, Shao Z P, *et al.,* **Functional nano-composite oxides synthesized by environmental-friendly auto-combustion within a micro-bioreactor,** Materials Research Bulletin, 43 (8-9), (2008) 2248-2259
2.93 Mineshige A, I zutsu J, *et al,* **Introduction of A-site deficiency into $La_{0.6}Sr_{0.4}Co_{0.2}Fe_{0.8}O_{3-\delta}$ and its effect on structure and conductivity,** Solid State Ionics, 176 (11-12) (2005) 1145-1149
2.94 Richardson R A, Cotton J W, *et al,* **Influence of synthesis route on the properties of doped lanthanum cobaltite and its performance as an electrochemical reactor for the partial oxidation of natural gas,** Dalton Transactions, 19 (2004) 3110-3115.
2.95 Lu K, Shen F, *et al,* **Long term behaviors of $La_{0.8}Sr_{0.2}MnO_3$ and $La_{0.6}Sr_{0.4}Co_{0.2}Fe_{0.8}O_3$ as cathodes for solid oxide fuel cells,** International Journal of Hydrogen Energy, 39 (15), (2014) 7963-7971.
2.96 Zhao Z, Liu L, *et al,* **High and low temperature behaviors of $La_{0.6}Sr_{0.4}Co_{0.2}Fe_{0.8}O_{3-\delta}$ cathode operating under CO_2/H_2O-containing atmosphere,** International Journal of Hydrogen Energy, 38 (35), (2013) 15361-15370
2.97 Mitsui T, Mineshige A, *et al,* **Electrochemical behavior of mixed conducting oxide cathode on oxygen excess-type solid electrolyte,** Journal of Power Sources 217 (2012) 170-174
2.98 Marinha D, Dessemond L, *et al,* **Electrochemical investigation of oxygen reduction reaction on $La_{0.6}Sr_{0.4}Co_{0.2}Fe_{0.8}O_{3-\delta}$ cathodes deposited by Electrostatic Spray Deposition,** Journal of Power Sources, 197 (2012) 80-87.

2.99 Marinha D, Dessemond L, *et al,* **Comparison of electrochemical performances of electrosprayed LSCF cathode films for IT-SOFCs for different morphologies and cobalt contents,** ECS Transactions, 35 (3), (2011) 2283-2294

2.100 Kuhn M, Fukuda Y, *et al.,* **Oxygen nonstoichiometry of perovskite-type $La_{0.6}Sr_{0.4}Co_{1-y}Fe_yO_{3-\delta}$ (y=0.2, 0.4, 0.5, 0.6, 0.8, 1) SOFC cathode materials,** ECS Transactions, 35 (3), (2011) 1881-1890

2.101 Angoua B F, Cantwell P R, *et al.,* **Crystallization and electrochemical performance of $La_{0.6}Sr_{0.4}Co_{0.2}Fe_{0.8}O_3$ $Ce_{0.8}Gd_{0.2}O_{1.9}$ thin film cathodes processed by single solution spray pyrolysis** Solid State Ionics, 203 (1), (2011) 62-68

2.102 Fan B, Yan J, *et al.,* **The ionic conductivity, thermal expansion behavior, and chemical compatibility of $La_{0.54}Sr_{0.44}Co_{0.2}Fe_{0.8}O_{3-\delta}$ as SOFC cathode material** Solid State Sciences, 13 (10), (2011) 1835-1839

2.103 Kournoutis V C, Tietz F, *et al.,* **Cyclic voltammetry characterization of a $La_{0.8}Sr_{0.2}Co_{0.2}Fe_{0.8}O_{3-\delta}$ electrode interfaced to CGO/YSZ** Solid State Ionics, 197 (1), (2011) 13-17

2.104 Digiuseppe G, Sun L, **Electrochemical performance of a solid oxide fuel cell with an LSCF cathode under different oxygen concentrations,** International Journal of Hydrogen Energy, 36 (8), (2011) 5076-5087

2.105 Lee S, Lim Y, *et al.,* **$Ba_{0.5}Sr_{0.5}Co_{0.8}Fe_{0.2}O_{3-\delta}$ (BSCF) and $La_{0.6}Ba_{0.4}Co_{0.2}Fe_{0.8}O_{3-\delta}$ (LBCF) cathodes prepared by combined citrate-EDTA method for IT-SOFCs,** Journal of Power Sources, 157 (2) (2006) 848-854.

2.106 Esquirol A, Brandon N P, *et al.,* M. **Electrochemical characterization of $La_{0.6}Sr_{0.4}Co_{0.2}Fe_{0.8}O_3$ cathodes for intermediate- temperature SOFCs** Journal of the Electrochemical Society, 151 (11), (2004) A1847-A1855.

2.107 Zeng P, Ran R, *et al.,* **Significant effects of sintering temperature on the performance of $La_{0.6}Sr_{0.4}Co_{0.2}Fe_{0.8}O_{3-\delta}$ oxygen selective membranes,** Journal of Membrane Science 302 (2007) 171–179

2.108 Park Y M, Kim J H, *et al.,* **In situ sinterable cathode with nanocrystalline $La_{0.6}Sr_{0.4}Co_{0.2}Fe_{0.8}O_{3-\delta}$ for solid oxide fuel cells,** international journal of hydrogen energy 36(2011) 5617-5623

2.109 Lu Z, Hardy J, *et al.,* **New insights in the polarization resistance of anode-supported solid oxide fuel cells with $La_{0.6}Sr_{0.4}Co_{0.2}Fe_{0.8}O_{3-\delta}$ cathodes,** Journal of Power Sources 196 (2011) 39–45

2.110 Shah M, Barnett S A, **Solid oxide fuel cell cathodes by infiltration of $La_{0.6}Sr_{0.4}Co_{0.2}Fe_{0.8}O_{3-\delta}$ into Gd-Doped Ceria,** Solid State Ionics 179 (2008) 2059–2064

2.111 Dutta A, Mukhopadhyay J, *et al.,* **Combustion synthesis and characterization of LSCF-based materials as cathode of intermediate temperature solid oxide fuel cells,** Journal of the European Ceramic Society, 29 (10), (2009) 2003-2011

2.112 Zhang Y L, Zha S W, *et al.,* **Dual cell porous electrodes for solid oxide fuel cells from polymer foams,** Advanced Materials 17 (2005) 487–491

2.113 Zhang G Y, Chen J, **Synthesis and applications of $La_{0.59}Ca_{0.4}1CoO_3$ nanotubes,** Journal of Electrochemical Society 152 (2005) A2069–A2073

2.114 Raming T P, Winnubst A I A, *et al.,* **Densification of zirconia-haematitie nanopowders,** Journal of European Ceramic Society 23 (2003) 1053–1060

2.115 Zhou W, Shao Z, *et al.,* **Synthesis of nanocrystalline conducting composite oxides based on a non-ion selective combined complexing process for functional applications,** Journal of Alloys and Compounds 426 (2006) 368–374

2.116 Kim J H, Park Y M, *et al.,* **Nano-structured cathodes based on $La_{0.6}Sr_{0.4}Co_{0.2}Fe_{0.8}O_{3-\delta}$ for solid oxide fuel cells,** Journal of Power Sources 196 (2011) 3544–3547

2.117 Yoon B Y, Bae J, **Characteristics of nano $La_{0.6}Sr_{0.4}Co_{0.2}Fe_{0.8}O_{3-\delta}$ infiltrated $La_{0.8}Sr_{0.2}Ga_{0.8}Mg_{0.2}O_{3-\delta}$ scaffold cathode for enhanced oxygen reduction,** International journal of hydrogen energy 38 (2013) 13399-13407

2.118 Zhao F, Wang Z, *et al.,* **Novel nano-network cathodes for solid oxide fuel cells,** Journal of Power Sources 185 (2008) 13–18

2.119 Jiang S P, **Nanoscale and nano-structured electrodes of solid oxide fuel cells by infiltration: Advances and challenges,** International journal of hydrogen energy 37 (2012) 449-470
2.120 Serra J M, Uhlenbruck S, *et al.,* **Nano-structuring of solid oxide fuel cells cathodes,** Topics in Catalysis 40 (2006) 1–4
2.121 Lai B K, Kerman K, *et al.,* **Nanostructured $La_{0.6}Sr_{0.4}Co_{0.8}Fe_{0.2}O_{3-\delta}$ /$Y_{0.08}Zr_{0.92}O_{1.96}$/ $La_{0.6}Sr_{0.4}Co_{0.8}Fe_{0.2}O_{3-\delta}$ (LSCF/YSZ/LSCF) symmetric thin film solid oxide fuel cells,** Journal of Power Sources 196 (2011) 1826–1832
2.122 Pathak L C, Singh T B, *et al.,* **Effect of pH on the combustion synthesis of nano-crystalline alumina powder,** Materials Letters 57 (2002) 380–385
2.123 Shukla S, Seal S, *et al.,* **Reduced activation energy for grain growth in nanocrystalline yttria stabilized zirconia,** Nano Lett. 3 (2003) 397–401
2.124 Zhu Q S, Fan B A, **Low temperature sintering of 8YSZ electrolyte film for Intermediate temperature Solis Oxide Fuel Cells**, Solid State Ionics 176 (2005) 889–894
2.125 Bellino M G, Lamas D G, *et al.,* **Enhanced ionic conductivity in nanostructured heavily doped ceria ceramics,** Advanced Functional Maters 16 (2006) 107–113
2.126 Simner S P, Shelton J P, *et al.,* **Interaction between La(Sr)FeO_3 SOFC cathode and YSZ electrolyte,** Solid State Ionics 161 (2003) 11 – 18

Chapter-3

3.1 Patil K C, Aruna S T, *et al.,* **Combustion synthesis: an update,** Current Opinion in Solid State and Materials Science 6 (2002) 507–512
3.2 Liu S, Xiu Z, *et al.,* **Feng Combustion synthesis and characterization of perovskite $SrTiO_3$ nanopowders** Journal of Alloys and Compounds 457 (2008) L12–L14
3.3 Qi X, Zhou J, *et al.,* **A simple way to prepare nanosized $LaFeO_3$ powders at room temperature** Ceramics International 29 (2003) 347–349
3.4 Jain S R, Adigav K C, *et al.,* **A New Approach to Thermochemical Calculations of Condensed Fuel-Oxidizer Mixtures** Combustion And Flame 40 (1981)71-79
3.5 Bakhman N N, **A Stoichiometric Coefficient Reflecting The Elemental Composition of Fuel And Oxidizer,** Fizika Goreniya i Vzryva, 4, 1 (1968) 16-19,
3.6 Civera A, Pavese M, *et al.,* **Combustion synthesis of perovskite-type catalysts for natural gas combustion,** Catalysis Today 83 (2003) 199–211
3.7 Yi S B, Chung H T, *et al.,* **A novel preparation method of active materials for the lithium secondary battery**, Electrochemistry Communications 9 (2007) 591–595
3.8. Speyer R F, **Thermal Analysis of Materials**, Marcel Dekker, Inc, 1994
3.9 Cullity B D, **Elements of X-Ray Diffraction**, 2nd Ed, Addison-Wesley. INC, (1978).
3.10 Tan L, Gu X, *et al.,* **Oxygen permeation performance of $Ba_{0.5}Sr_{0.5}Co_{0.8}Fe_{0.2}O_3$ perovskite type membranes** Journal of membrane science, 212 (2003) 157
3.11 Zheng Y, Zhang C, *et al.,* **A new symmetric solid-oxide fuel cell with $La_{0.8}Sr_{0.2S}Sc_{0.2}Mn_{0.8}O_{3-\delta}$ perovskite oxide as both the anode and cathode**, Acta materilia 57(4)(2009)1165-1175

Chapter-4

4.1 Peng-Jun Y, Jing W, *et al* **Preparation and characterization of $La_{1-x}Sr_xFeO_3$ materials and their formaldehyde gas-sensing properties,** Journal of Materials Science, 48 (2013) 441-450
4.2 Augustin C O, Kalai S R, *et al*, **Effect of La3+ substitution on the structural, electrical and electrochemical,properties of strontium ferrite by citrate combustion method**, Materials Chemistry and Physics 89 (2005) 406–411
4.3 Xiaojing Z, Huaju L, *et al.* **Structural Properties and Catalytic Activity of Sr-Substituted $LaFeO_3$ Perovskite** Chin. Journal of Catalysis, 33(2012)1109–1114.

4.4 Roth R S, **Classification of perovskite and other ABO_3-type compounds,** Journal of Research Natural Bureau Standards 58 (1957) 75.

4.5 Tai L W, Nasrallah M M, *et al.*, **Structure and electrical properties of $La_{1-x}Sr_xCo_{1-y}Fe_yO_3$. Part 2. The system $La_{1-x}Sr_xCo_{0.2}Fe_{0.8}0_{3-\delta}$,** Solid State Ionics 76 (1995) 273-283

4.6 Shannon R D, **Revised effective ionic radii and systematic studies of interatomic distances in halides and chalcogenides,** Acta Crystallography A32 (1976) 75 1.

4.7 Pauling L, **Nature of the Chemical Bond**, 3rd. Ed. (Cornell University Press, Ithaca, N.Y., 1960

4.9 Shimony U, Knudsen J M,*et al.*, **Mossbauer studies on Iron perovskite: $La_{1-x}Sr_xFeO_3$ (0<x<1),** Physical Review 144(1966)361,

4.10 Huang C Y, Huang T J, **Effect of Co substitution for Mn on $Y_{1-x}Sr_xMnO_3$ properties for SOFC cathode material,** Journal of Materials Science, 37 (2002) 4581.

4.11 Abbate M, de Groot F M F, *et al.*, **Controlled-valence properties of $La_{1-x}Sr_xFeO_3$ and $La_{1-x}Sr_xMnO_3$ studied by soft-x-ray absorption spectroscopy**, Physical Review B 46 (8), 4511 - 4519 (1992

4.12 Grenier J C, Ea N, *et al.* , **Proprietes electriques et magnetiques des ferrites oxides $La_{1-x}Sr_xFeO_{3-y}$,** Materials Research Bulletine 19(1984)1301-1309,.

4.13 Park S K, Ishikawa T, *et al*, **Variation of charge ordering transitions in $R_{1/3}Sr_{2/3}FeO_3$ (R=La, Pr, Nd, Sm, and Gd),** Physical Review B 60 (1999)10788 - 10795.

4.14 Patrakeev M V, Bahteeva J A, *et al,* **Electron/hole and ion transport in $La_{1-x}Sr_xFeO_{3-\delta}$,** J. Solid State Chemistry 172 (2003) 219-231.

4.15 Tai L W, Nasrallah M M, *et al.,* **Structure and electrical properties of $La_{1-x}Sr_x,Co_{1-y}Fe_yO_3$. Part 1. The system $La_{0.8}Sr_{0.2}Co_{1-y}Fe_y0_3$,** Solid State Ionics 76 (1995) 273-283

4.16 Zhou X D, Cai Q, *et al.*, **Coupled electrical and magnetic properties in (La,Sr)$FeO_{3-\delta}$,** Journal of Applied Physics 97(2005)10C314,.

4.17 Hombo J, Matsumoto Y, *et al.,* **Electrical Conductivities of $SrFeO_{3-\delta}$ and $BaFeO_{3-\delta}$ Perovskites,** Journal of Solid State Chemistry 84 (1990)138-143

4.18 Brown I D, **Influence of Chemical and Spatial Constraints on the Structures of Inorganic Compounds,** Acta Crystallographia B53 (1997), 381-393

4.19 Lian J S, Zhang X Y, *et al,* **Synthesis of nanocrystalline NiO/doped CeO_2 compound powders through combustion of citrate/nitrate gel,** Materials Letters 58 (2004) 1183.

4.20 Civera A, Pavese M, *et al.***Combustion synthesis of perovskite-type catalysts for natural gas combustion** Catalysis Today 83 (2003) 199–211

4.21 Yi S B, Chung H T, *et al.***A novel preparation method of active materials for the lithium secondary battery,** Electrochemistry Communications 9 (2007) 591–595

4.22 Ge L, Zhou W, *et al.,* **Facile autocombustion synthesis of $La_{0.6}Sr_{0.4}Co_{0.2}Fe_{0.8}O_{3-\delta}$ (LSCF) perovskite via a modified complexing sol-gel process with NH_4NO_3 as combustion aid,** Journal of Alloys & Compounds, 450 (2008) 338.

4.23 Zhou W, Shao Z, *et al* **Synthesis of nanocrystalline conducting composite oxides based on a non-ion selective combined complexing process for functional applications,** Journal of Alloys & Compounds 426 (2006) 368.

4.24 Xu Q, Huang D, *et al.,* **Influence of sintering temperature on microstructure and mixed electronic–ionic conduction properties of perovskite-type La0.6Sr0.4Co0.8Fe0.2O3 ceramics,** Ceramics International 30 (2004) 429–433

4.25 Purohit R D, Sharma B P, *et al.*, **Ultrafine ceria powders via glycine-nitrate combustion,** Mater Res Bull 36 (2001) 2711

4.26 Deganello F, Marc G, *et al.,* **Citrate–nitrate auto-combustion synthesis of perovskite-type nanopowders: A systematic approach,** Journal of European Ceramic Society 29 (2009) 439

4.27 Pathak L C, Singh T B, *et al.,* **Effect of pH on the combustion synthesis of nano-crystalline alumina powder,** Materials Letters 57(2002) 380

4.28 Patra H, Rout S K, *et al.*, **Effect of process parameters on combined EDTA–citrate synthesis of $Ba_{0.5}Sr_{0.5}Co_{0.8}Fe_{0.2}O_{3-\delta}$ perovskite,** Powder Technology 209 (2011) 98.

4.29 Xu G, Ma H, *et al.,* **Influence of pH on characteristics of $BaFe_{12}O_{19}$ powder prepared by sol–gel auto-combustion,** Journal of Magnetism and Magnetic Materials, 301 (2006) 383–388

4.30 Azad J. Darbandi, *et al.,* **Nanoparticulate cathode thin films with high electrochemical activity for low temperature SOFC applications,** Solid State Ionics 180 (2009) 1379–1387

4.31 Zeng P, Ran R, *et al.,* **FTIR spectra of gaseous products from the combustion of pyrotechnic mixtures containing carbon,** Fuel, 70 (1991) 667

4.32 Diznek V, Urbanov M, *et al*, **IR Laser Induced Chemical Vapour Depostition of Carbonaceous Phases from 3-Butyn-2-One,** Carbon 36(1998) 521-524.

4.33 Badini C, Saracco G, *et al.,* **Combustion of carbonaceous materials by Cu-K-V based catalysts I. Role of copper and potassium vanadates,** Applied Catalysis B: Environmental 11 (1997) 307-328

4.34 Hwang C C, Wu T Y, *et al.,* **Development of a novel combustion synthesis method for synthesizing of ceramic oxide powders,** Materials Science and Engineering B 111 (2004) 49–56

4.35 Conceic L, Silva A, *et al*, **Combustion synthesis of $La_{0.7}Sr_{0.3}Co_{0.5}Fe_{0.5}O_{3-\delta}$ (LSCF) porous materials for application as cathode in IT-SOFC,** Materials Research Bulletine 46 (2011) 308–314

4.36 Zhou W., Shao Z, *et al* **LSCF Nanopowder from Cellulose–Glycine-Nitrate Process and its Application in Intermediate-Temperature Solid-Oxide Fuel Cells,** Journal of American Ceramic Society 91(2008)1155-1162

4.37 Chick L A, Pederson L R, *et al.*, **Glycine-nitrate combustion synthesis of oxide ceramic powders,** Materials Letter 10 (1990) 6

4.38 Ge L, Zhou W, *et al.,* **Facile auto-combustion synthesis of $La_{0.6}Sr_{0.4}Co_{0.2}Fe_{0.8}O_{3-\delta}$ (LSCF) perovskite via a modified complexing sol–gel process with NH_4NO_3 as combustion aid**. Journal of Alloys & Compounds 450(2008) 338–347

4.39 Lanon R, Silvana R, *et al.,* **Single-step combustion synthesis of $LaAlO_3$ powders andtheir sintering behavior,** Ceramics International40(2014)7561–7565

4.40 Jayalakshmi I M, Palaniappa M, *et al.,* **Single Step Solution Combustion Synthesis of ZnO/carbon Composite and its Electrochemical Characterization for Supercapacitor Application,** International Journal of Electrochemical Sciences, 3 (2008) 96 – 103

4.41 Padma Kumar H, Vijayakumar C, *et al.,* **Characterization and sintering of BaZrO3 anoparticles synthesized through a single-step combustion process,** Journal of Alloys and Compounds 458 (2008) 528–531.

4.42 Deganello F, Marc G, *et al.*, **Citrate–nitrate auto-combustion synthesis of perovskite-type nanopowders:A systematic approach,** Journal European Ceramic Society 29 (2009) 439–450

4.43 Peng W, Liu G, Atlas of Infrared Spectroscopy for minerals, (1982) Science Press

4.44 Ze L, Zhu Q, **Low temperature processing of interlayer-free $La_{0.6}Sr_{0.4}Co_{0.2}Fe_{0.8}O_{3-\delta}$ cathodes for intermediate temperature solid oxide fuel cells,** Journal of Power Sources 161 (2006) 1169–1175

4.45 Zeng Pingying , Ran R, *et al* **Significant effects of sintering temperature on the performance of $La_{0.6}Sr_{0.4}Co_{0.2}Fe_{0.8}O_{3-\delta}$ oxygen selective membranes** Journal of Membrane Science, 302 (2007) 171–179

4.46 Aller D, Lane J A, *et al.,* **The effect of thermal treatment on the resistance of LSCF electrodes on gadollina doped ceria electrolytes,** Solid State Ionics 86–88 (1996) 767.

4.47 Tai LW, Nasrallah MM, *et al.,* **Structure and electrical properties of $La_{1-x}Sr_xCo_{1-y}Fe_yO_{3-\delta}$ Part -1: The system $La_{1-x}Sr_xCo_{0.2}Fe_{0.8}O_3$,** Solid State Ionics 76 (1995) 273.

4.48 Kostogloudis G H, Ftikos C, **Properties of A-site-deficient La0.6Sr0.4Co0.2Fe0.8O3−δ-based perovskite oxides**, Solid State Ionics 126 (1999) 143.
4.49 Garcia M P, Macedo D A, *et al.,* **Citrate–hydrothermal synthesis, structure and electrochemical performance of $La_{0.6}Sr_{0.4}Co_{0.2}Fe_{0.8}O_{3-\delta}$ cathodes for IT-SOFCs** Ceramics International, 39(2013)8385–8392
4.50 Xu Q, Huang D, *et al.,* **Structure, electrical conducting and thermal expansion properties of $Ln_{0.6}Sr_{0.4}Co_{0.2}Fe_{0.8}O_{3-\delta}$ (Ln = La, Pr, Nd, Sm) perovskite-type complex oxides.** Journal of Alloys and Compounds 429 (2007) 34–39
4.51 Rahman M N, **Ceramic Processing and Sintering**, Marcel Dekker, Inc., 1995
4.52 Shao Z, Xiong G, **Ba effect in doped $Sr(Co_{0.8}Fe_{0.2})O_{3-\delta}$ on the phase structure and oxygen permeation properties of the dense ceramic membranes,** Separation and Purification Technology, 25 (2001) 419
4.53 Alexander K B, Becher P F, **Grain growth kinetics in alumina–zirconia (CeZTA) composites,** Journal of American Ceramic Society, 77 (1994) 939
4.54 Young S, Cutler I B, **Initial sintering with constant rates of heating,** Journal of American Ceramic Society, 53 (1970) 659
4.55 McIntosh S, Vente J F, **Structure and oxygen stoichiometry of $SrCo_{0.8}$ $Fe_{0.2}O_{3-\delta}$ and $Ba_{0.5}Sr_{0.5}Co_{0.8}Fe_{0.2}O_{3-\delta}$,** Solid State Ionics, 177 (2006) 1737
4.56 Wei B, Lu Z, *et al.,* **Thermal and electrical properties of new cathode material $Ba_{0.5}Sr_{0.5}Co_{0.8}Fe_{0.2}O_{3-\delta}$ for solid oxide fuel cells,** Electrochemical Solid-State Letters, 8 (2005) A428.
4.57 Itoh T, Nishida Y, *et al.,* **Determination of the crystal structure and charge density of $(Ba_{0.5}Sr_{0.5})$ $(Co_{0.8}Fe_{0.2})O_{2.33}$ by Rietveld refinement and maximum entropy method analysis,** Solid State Communications, 149 (2009) 41.
4.58 Ullmann H, Trofimenko N, *et al.,* **Correlation between thermal expansion and oxide ion transport in mixed conducting perovskite-type oxides for SOFC cathodes,** Solid State Ionics 138 (2000) 79–90
4.59 Xu Q, Huang D, *et al.*, **Influence of sintering temperature on microstructure and mixed electronic–ionic conduction properties of perovskite-type $La_{0.6}Sr_{0.4}Co_{0.8}Fe_{0.2}O_3$** ceramics Ceramics International 30 (2004) 429–433
4.60 Belmonte G G, Bisquert J, **Grain boundary role in the electrical properties of $La_{1-x}Sr_xCo_{0.8}Fe_{0.2}O_{3-\delta}$ perovskites,** Solid State Ionics 107 (1998) 203–211
4.61 Hannink R H J, Kelly P M, *et al.,* **Transformation toughening in Zirconia containing ceramics,** Journal of American Ceramic Society 83 (3)(2000) 461–487
4.62 Mazaheri M, Razavi H Z, *et al.*, **The effect of confirmation method and sintering technique on the densification and grain growth of nano crystalline 8 mol% yttria stabilized zirconia,** Journal of American Ceramic Society 92(5) (2009)990-995.
4.63 Singh K A, Pathak L C , *et al* **Effect of citric acid on the synthesis of nano-crystalline yttria stabilized zirconia powders by nitrate–citrate process,** Ceramics International 33 (2007) 1463–1468
4.64 Yahiro H., Eguchi K., *et al.,* **Electrical properties and reducibilities of ceria-rare earth oxide systems and their application to solid oxide fuel cell,** Solid State Ionics 36 (1989) 71–75
4.65 Wu W C, Huang T, *et al.*, **Synthesis and properties of samaria-doped ceria electrolyte for IT-SOFCs by EDTA-citrate complexing method,** Journal of Power Sources 195 (2010) 5868–5874
4.66 Yahiro H, Ohuchi T, **Electrical properties and microstructure in the system ceria-alkaline earth oxide,** Journal of Materials Science 23 (1988) 1036-1041
4.67 Lin B, Sun W, *et al.,* **A cathode-supported SOFC with thin $Ce_{0.8}Sm_{0.2}O_{1.9}$ electrolyte prepared by a suspension spray** J of Alloys and Compounds 465 (2008) 285–290,
4.68 Zhang X, Decs-Petit C, *et al.,* **A study on sintering aids for $Sm_{0.2}Ce_{0.8}O_{1.9}$ electrolyte,** Journal of Power Sources 162 (2006) 480–485

4.69 Hartley A, Sahibzada M, *et al.,* **$La_{0.6}Sr_{0.4}Co_{0.2}Fe_{0.8}O_3$ as the anode and cathode for intermediate temperature solid oxide fuel cells,** Catalysis Today 55 (2000) 197-204

4.70 Qiu L, Ichikawa T, *et al* **$Ln_{1-x}Sr_xCo_{1-y}Fe_yO_{3-\delta}$ (Ln = Pr, Nd, Gd; x = 0.2, 0.3) for the electrodes of solid oxide fuel cells.** Solid State Ionics 158(2003)55-65.

4.71 Kostogloudis GC, Tsiniarakis G, *et al* **Chemical reactivity of perovskite oxide SOFC cathodes and yttria stabilized zirconia,** Solid State Ionics 135(20005)29-35

4.72 Esquirol A, Brandon N P, *et al.,* **Electrochemical characterization of $La_{0.6}Sr_{0.4}Co_{0.2}Fe_{0.8}O_{3-\delta}$ cathodes for intermediate-temperature SOFCs,** Journal of Electrochemical Society 151 (2004) 1847-55.

4.73 Świerczek K, Marzec J, *et al.,* **LFN and LSCFN perovskites — structure and transport properties,** Solid State Ionics 177 (2006) 1811–1817.

4.74 Chen M, Moon B H *et al.,* **Characterization of $La_{0.6}Sr_{0.4}Co_{0.2}Fe_{0.8}O_{3-\delta}$ + $La_2NiO_{4+\delta}$ Composite Cathode Materials for Solid Oxide Fuel Cells**, FUEL CELLS 12 (2012) 86–96

4.75 Beckel D, Ulrich P, *et al.,* **Electrochemical performance of LSCF based thin film cathodes prepared by spray pyrolysis,** Solid State Ionics 178 (2007) 407–415

4.76 Zhao K, Xu Q, *et al.,* **Microstructure and electrode properties of $La_{0.6}Sr_{0.4}Co_{0.2}Fe_{0.8}O_{3-\delta}$ spin-coated on $Ce_{0.8}Sm_{0.2}O_{2-\delta}$ electrolyte,** Ionics 17 (2011) 247–254

4.77 Baumann F S, Maier J, *et al.,* **The polarization resistance of mixed conducting SOFC cathodes: A comparative study using thin film model electrodes**, solid state ionics 179 (2008) 1198-1204

4.78 Xi X , Kondo A *et al.,* **A simple mechanical process to synthesize $La_{0.6}Sr_{0.4}Co_{0.2}Fe_{0.8}O_{3-\delta}$ perovskite for solid oxide fuel cells cathode Materials,** Letters 145 (2015) 212–215

4.79 Lei Z, Zhu Q, **Low temperature processing of interlayer-free $La_{0.6}Sr_{0.4}Co_{0.2}Fe_{0.8}O_{3-\delta}$ cathodes for intermediate temperature solid oxide fuel cells,** Journal of Power Sources 161 (2006) 1169–1175

4.80 Liu Y, Zhang L, **Oxygen reduction mechanism at $Ba_{0.5}Sr_{0.5}Co_{0.8}Fe_{0.2}O_{3-\delta}$ cathode for solid oxide fuel cell,** International Journal of Hydrogen Energy, 34 (2009) 1008